Università degli Studi di Ferrara

UCA | Universidad de Cádiz

International Ph.D. Course
in
Earth and Marine Sciences

CYCLE XXXI

DIRECTOR Prof. Massimo Coltorti

Thermobarometry, geochronology and

petrological evolution of the Middle-Late Triassic

magmatic products in the Dolomitic Area (Southern Alps)

Scientific/Disciplinary Sector (SDS) GEO/07

Candidate

Supervisor

Years 2015/2018

Table of contents

Abstract

The Middle Triassic magmatic event in the Dolomitic Area is represented by huge amounts of basaltic/trachybasaltic to trachytic volcanic and volcanoclastic rocks surrounding three main intrusive bodies (Predazzo, Mt. Monzoni and Cima Pape), with pyroxenitic/gabbroic to syenitic and syenogranitic composition. Geochemically, both the volcanic and the plutonic rocks are characterized by orogenic-like (high-K calc-alkaline to shoshonitic) affinity. Lamprophyric dykes with alkaline affinity constitute an additional and volumetrically limited pulse, thought to represent the ultimate stage of the magmatic event. Notwithstanding the large number of petrographic, petrologic and tectono-magmatic studies developed in the last decades, many features related to the magmatism of the Dolomitic Area are still poorly constrained. They are, for example: i) the physico-chemical conditions of emplacement of the plutonic bodies; ii) the interaction between ascending magmas and crust; iii) the precise temporal sequences (and the absolute radiometric ages) that characterize the multi-pulse intrusive complexes; iv) the geodynamic framework of the whole Dolomitic Area.

A detailed fieldwork, together with a complete geochemical, petrological and geochronological study was performed on the hypabyssal/intrusive rocks belonging to the Predazzo, Mt. Monzoni and Cima Pape plutons. Results showed that the emplacement of the various intrusive batches occurred in a shallow crustal context (< 4-6 km), in great accordance with the field evidence. An articulated thermobarometric approach enabled also to retrieve the temperature, oxygen fugacity conditions and water content of the less differentiated magmas intruded in the shallow crustal environment. Moreover, the Sr-Nd isotopic signature of Predazzo, Mt. Monzoni and Cima Pape rocks suggests that the interaction between magmas and the crustal components was limited (5-6% assimilation); on the other side, local contamination processes, mainly occurring at the intrusions edges, slightly modified the isotopic signature of some rocks, as in case of Mt. Monzoni intrusion. The existence of multiple magma pulses with different geochemical signature was documented in the Predazzo intrusion, where three main magmatic suites with orogenic-like affinity but different silica saturation degree emplaced over a short time span, and evolved along independent geochemical trends. Their Sr-Nd isotopes signature reflects a time-related depletion of the mantle source, moving from a "pure" EM I (with subduction-related components) to a slightly more $^{143}Nd/^{144}Nd$-enriched one.

The geochemical and geochronological study of the alkaline lamprophyric dykes, thought to represent a "fourth" pulse of the Middle Triassic magmatic event, revealed many unexpected points. Their emplacement, in fact, was dated at 219.22 ± 0.46/0.73 Ma ($^{40}Ar/^{39}Ar$; 2σ;

analytical/full systematic uncertainties), suggesting an origin unrelated to the short-lived high-K calc-alkaline to shoshonitic magmatism of the Predazzo-Mt. Monzoni-Cima Pape intrusions. The textural, geochemical and isotopic features of lamprophyres showed that: i) a carbonatitic melt was intimately associated to the alkaline lamprophyric one; ii) a depleted mantle component was involved in their genesis; iii) small scale mixing dynamics characterized the lamprophyric melt during ascent and fractionation. According to these results, Predazzo lamprophyres did not represent a late-stage pulse of the Middle Triassic magmatism, but instead a precursor of the Alpine Tethys rifting stage, together with the Late Triassic (215-225 Ma) alkaline-carbonatitic magmatic expressions cropping out in several districts of the Southern Alps-Carpathians area.

Introduction

Introduction

The present thesis is focused on the geochemical, petrological and geochronological study of the intrusive and hypabyssal manifestations of the Middle Triassic magmatism in the Dolomitic Area (Southern Alps). Among the huge amount of Middle Triassic igneous products that can be found throughout the whole Southalpine and Austroalpine domains, the plutonic bodies of the Dolomitic Area (cropping out at Predazzo, Mt. Monzoni and Cima Pape) constitute the most intriguing and well-preserved portion. Their compositional variability and geochemical affinity, together with the articulated tectonic/geodynamic framework of the area, attracted the interest of the scientific community since the beginning of the 19th century, when the relationships between the intrusive bodies and the surrounding limestones were documented and interpreted for the first time (Marzari Pencati, 1820). By the way, Mt. Monzoni and Predazzo intrusions played also a predominant role in the birth of the petrography, constituting the type locality of the monzonitic rocks themselves. After having been at the heart of the petrographic debates for decades, the study of these intrusive complexes was abandoned in the '90s, notwithstanding the various geological problems remained unsolved. Among them, the main outstanding topics are those related to the emplacement conditions of the intrusive bodies and the relationships between tectonics, magmatism and sedimentation, both at local and at geodynamic scale (Vardabasso, 1929; 1930; Leonardi, 1968; Castellarin *et al.*, 1982; Doglioni 1984; 1987; Sloman, 1989; Gasparotto & Simboli, 1991; Abbas *et al.*, 2018).

Predazzo, Mt. Monzoni and Cima Pape plutons are composed of single or multi-pulse intrusive batches with orogenic-like (high-K calc-alkaline to shoshonitic) affinity, ranging in composition from pyroxenitic/gabbroic to syenitic and syenogranitic. Their emplacement age, indirectly constrained by geochronological data from the tuff layers interbedded in the volcanic sequences of the Dolomitic Area, results between 238.0±0.05 and 237.579±0.0042 Ma (< 0.7 Ma; Mietto *et al.*, 2012; Abbas *et al.*, 2018; Storck *et al.*, 2018; Wotzlaw *et al.*, 2018). Recently, Storck *et al.* (2018) reported ages of 238.190±0.055 and 238.075±0.087 for the Mt. Monzoni and Predazzo intrusions, respectively.

These intrusions represent ideal "petrologic laboratories" for investigating and reconstructing the features of the Middle Triassic magmatism, since they offer the possibility to constrain the theoretical and experimental modeling by means of field evidence. However, few thermobarometric and isotopic data are reported in literature for these complexes, preventing the possibility to understand the main spatial and temporal dynamics of magma emplacement and differentiation.

Aim of this thesis is therefore the reconstruction of the chemico-physical features and temporal evolution of the Middle Triassic intrusive/hypabyssal bodies of the Dolomitic Area. To address these topics, particular attention was given to the Predazzo multi-pulse intrusion, in which different magmatic pulses, as well as their cross-cutting relationships, are recorded.

The following rational scheme was adopted in this thesis to shed light on the geochemical/temporal evolution of the magmatism in the Dolomitic Area:

Chapter 1: brief summary of the geodynamic and geological framework of the Dolomitic Area during Middle Triassic.

Chapter 2: list of the analytical methods, including: i) whole rock major and trace element analyses (XRF); ii) whole rock trace element analyses (ICP-MS); iii) mineral phase major element analyses (EMP); iv) mineral phase trace element analyses (LA-ICP-MS); v) whole rock $^{87}Sr/^{86}Sr$ and $^{143}Nd/^{144}Nd$ isotopic analyses (TIMS); vi) $^{40}Ar/^{39}Ar$ geochronology on mineral separates.

Chapter 3: field and petrological study of the Predazzo intrusion, with particular attention to the identification of the different magmatic suites and their differentiation processes.

Chapter 4: thermobarometric, oxybarometric, hygrometric and isotopic study of the Predazzo intrusion, aimed at the reconstruction of the emplacement conditions of the Middle Triassic plutonic bodies and their interaction with the crust.

Chapter 5: petrological, geochemical and thermobarometric study of the Mt. Monzoni and Cima Pape plutonic bodies, and review of the emplacement conditions of the intrusive bodies of the Dolomitic Area during Middle Triassic.

Chapter 6: petrological, geochemical and geochronological study of the alkaline lamprophyric dykes intruded in the plutonic bodies, and comparison between them and the previous high-K calc-alkaline to shoshonitic magmatism.

Chapter 7: final remarks, with a general overview of the main outcomes of this study.

Chapter 1

Geological and geodynamic setting

Chapter 1. Geological and geodynamic setting

1.1. Geodynamic framework

The geodynamic framework of the Austroalpine-Southalpine domains during Middle-Late Triassic is a challenging topic, mainly because of the variety of magmas erupted over a short time span in a relatively limited area, whose tectonic features have been also subsequently obscured by the Alpine orogenesis. Between 239±3 and 227±6 Ma, magmas with calc-alkaline/shoshonitic affinity intruded in several localities of the Southern Alps, Dynarides and Hellenides (Bébien *et al.*, 1978; Barbieri *et al.*, 1982; Pe-Piper, 1982; 1983; Pamić, 1984; Gianolla, 1992; Mundil *et al.*, 1996; Armienti *et al.*, 2003; Beccaluva *et al.*, 2005; Cassinis *et al.*, 2008; Bellieni *et al.*, 2010; Beltràn-Trivino *et al.*, 2016; Bianchini *et al.*, 2018; Storck *et al.*, 2018; Wotzlaw *et al.*, 2018). Almost simultaneously, scattered intrusions of alkaline magmas emplaced between 231±1 and 227±7 Ma along the Periadriatic lineament (Karawanken) and in the Carpathians (Ditrau) area (Lippolt & Pidgeon, 1974; Dallmeyer *et al.*, 1997; Morogan *et al.*, 2000; Visonà & Zanferrari, 2000; Batki *et al.*, 2014; Pál-Molnár *et al.*, 2015).

The magmatism of the Southern Alps domain is represented by volcano-plutonic sequences cropping out in the Brescian Alps, Alto Vicentino-Valsugana, Dolomites, Carnia areas (Italy) and the Karawanken region (Austria, Fig. 1).

Most of the igneous products are volcanic and volcanoclastic rocks, with subordinated dyke swarms. Intrusive bodies are instead rare and mainly located in the Karawanken and the Dolomitic Area (Predazzo -Mt. Monzoni-Cima Pape; Gasparotto & Simboli ,1991; Gianolla, 1992; Bonadiman *et al.*, 1994; Visonà & Zanferrari, 2000; Brack *et al.*, 2005; Cassinis *et al.*, 2008; Bellieni *et al.*, 2010).

The concomitance between the orogenic signature of the magmatism and the onset of extensional-transtensional tectonic regimes (Doglioni, 1984; 1987; 2007; Stampfli & Borel, 2002; 2004) led many authors to propose several possible geodynamic scenarios for the Southern Alps during Middle Triassic. They include: i) aborted rifting in a passive margin (Bernoulli & Lemoine, 1980); ii) active mantle upwelling (Stähle *et al.*, 2001); iii) arc system at the Paleo-Tethys NW limb (Castellarin *et al.*, 1988); iv) back-arc development connected to the subduction of the Paleo-Tethys (Ziegler & Stampfli, 2001; Stampfli & Borel, 2002; 2004; Stampfli *et al.*, 2002; Armienti *et al.*, 2003; Stampfli, 2005; Cassinis *et al.*, 2008; Schmid *et al.*, 2008; Zanetti *et al.*, 2013); v) anorogenic rifting with subduction signature inherited from the Hercynian orogeny (Sloman, 1989; Bonadiman *et al.*, 1994; Pe-Piper, 1998; Beltràn-Trivino *et al.*, 2016). This last hypothesis was supported by the similar Sr-Nd

isotopic signature of the Middle Triassic magmas in the Southern Alps and the Permian igneous products (260-290 Ma), whose expression was found along the Western and in the Eastern Alps sectors (Barth *et al.*, 1993; Rottura *et al.*, 1998; Monjoie *et al.*, 2007; Schaltegger & Brack, 2007; Marocchi *et al.*, 2008; Quick *et al.*, 2009; Willcock *et al.*, 2015; Dal Piaz *et al.*, 2015; Sinigoi *et al.*, 2016; Manzotti *et al.*, 2017). This kind of analogy led to speculate that similar mantle sources, and/or similar melting conditions, could have generated the Middle Triassic and the Permian magmatic episodes. In the Dolomitic Area, thick sequences of basaltic andesitic-to-rhyolitic ignimbrites associated with the Permian Atesina Volcanic District are also the main constituent of the crustal basement of the Dolomitic Area where magmas intruded during Middle Triassic.

To interpret the distribution of the Permo-Triassic orogenic and anorogenic magmatism, Visonà & Zanferrari (2000) hypothesized that the mantle portions beneath the Southalpine-Austroalpine and the Carnian-Dinaric plates experienced different Palaeozoic evolutions, being affected by subduction-related and plume-related processes, respectively. Alternatively, Bianchini *et al.* (2018) proposed the existence of a Palaeozoic oceanic basin between the Southalpine and Austroalpine domains, closed by a subduction dipping beneath the former. In such a scenario, the mantle beneath the Southalpine domain was fluxed by subduction-related components, whereas its Austroalpine counterpart was affected by mantle upwelling dynamics.

1.2. The magmatic sequences of the Dolomitic Area

The volcano-plutonic rocks of the Dolomitic Area constitute the most intriguing and spectacular portion of the Middle Triassic magmatic event in the Southern Alps. In this area, thick sequences of volcanites, intrusive bodies and dykes emplaced in a ±shallow marine environment, which was characterized by the presence of isolated carbonate platforms elevated over deep marine basins (Salomon, 1895; Cornelius & Cornelius-Furlani, 1924; Vardabasso, 1929; 1930; Leonardi, 1968; Calanchi *et al.*, 1977; 1978; Pisa *et al.*, 1979; Castellarin *et al.*, 1980; Lucchini *et al.*, 1982; Sloman, 1989; Bonadiman *et al.*, 1994; Coltorti *et al.*, 1996; Beccaluva *et al.*, 2005; Gianolla *et al.*, 2010).

1.2.1. The volcanic/volcanoclastic products

The earlier phase of the Middle Triassic volcanism was characterized by predominant explosive activity in result of water-magma interaction, as testified by the coarse and fine lapilli tuff and tuff deposits located at the base of the volcanic deposits sequence. These

products are constituted by a glass (± ash) matrix enclosing volcanic lapilli, bombs, as well as several dm-sized fragments of carbonate rocks (Nemeth *et al.*, 2009).

After this first phreatomagmatic episode, the eruption style moved towards a more effusive nature, characterized by the production of submarine pillow lavas, pillow breccias, lava breccias and hyaloclastites, as well as of subaerial lava flows. Volcanoclastic sandstones, probably formed during the quiescent stages of the activity, are often intercalated in the effusive sequences. Despite a clear stratigraphic organization is usually difficult to recognize, pillow lavas, pillow breccias, lava breccias and hyaloclastites seem to constitute the base of the volcanic sequence, whereas lava flows usually represent its upper portions. All the volcanic products are characterized by high-K calc-alkaline to shoshonitic affinity, and range in composition from basaltic/trachybasaltic to latitic.

1.2.2. The intrusive bodies and the dyke swarm

In contrast to the large amount of volcanic rocks and dykes cropping out from the Schlern/Seiser Alm (NW) to the Cadore (NE) regions, the intrusive bodies are rare and limited in volume (Fig. 1). They are, in order of increasing areal extension, Cima Pape (< 3 km^2), Mt. Monzoni (~8 km^2) and Predazzo Intrusive Complex (25 km^2).

The Mt. Monzoni body (dated at 238.190±0.05 Ma; Storck *et al.*, 2018) and the Cima Pape sill are composed of biotite ± amphibole-bearing gabbroic/clinopyroxenitic to syenitic rocks with orogenic affinity, generated by fractional crystallization processes from parental basaltic/trachybasaltic magmas (Gasparotto & Simboli, 1991; Bonadiman *et al.*, 1994; Della Lucia, 1997). Mt. Monzoni is a NE-SW elongated pluton, intruded into the Permo-Triassic volcanic and sedimentary formations (Atesina Volcanic District ignimbrites; Val Gardena Sandstones; Bellerophon Fm. marls and evaporites; Werfen Fm. carbonates; Richtofen to Contrin Fm. carbonate-siliciclastics units; Sciliar carbonate platforms; Buchenstein Fm. limestones). Its emplacement is thought to be controlled by a syn-genetic ESE–WNW trascurrent tectonics, which created the conditions for a shallow-level intrusion and the subsequent magma differentiation (Bonadiman *et al.*, 1994; Abbas *et al.*, 2018).

The Cima Pape body is a 50-70 to 300 m thick sill intruded into the Buchenstein Fm. limestones, as well as in the overlying volcanic/volcanoclastic deposits (Gasparotto & Simboli, 1991). The gradual textural transition, locally organized in columnar structures, between the Cima Pape sill and the overlying lavas led many authors to speculate about its shallow depth of emplacement (Sommavilla, 1970; Sarti & Ardizzoni, 1984).
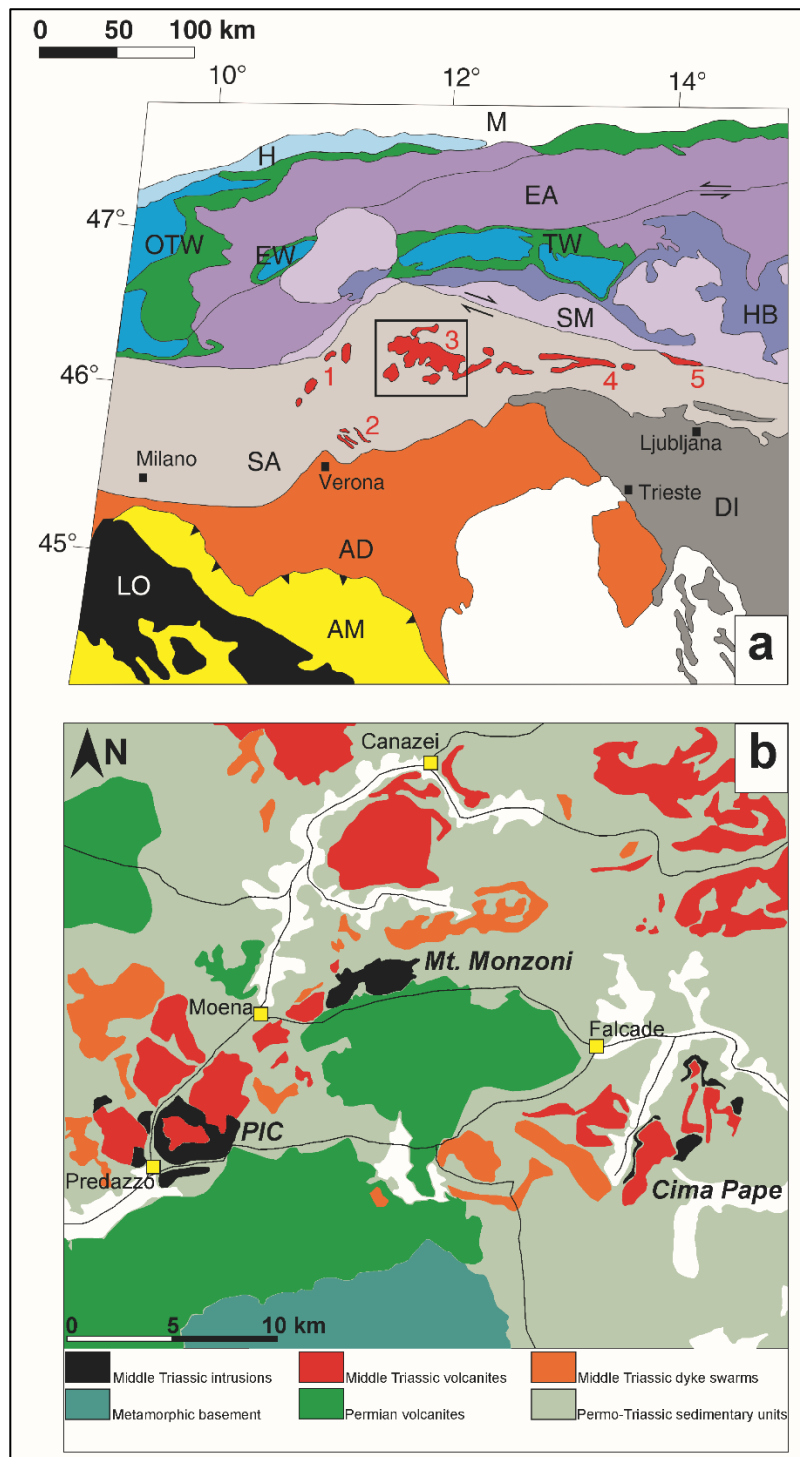
Fig. 1. (a) Distribution of the Triassic magmatism in the Alps. The tectonic units of the eastern portion of the Alps are partly modified from Dal Piaz et al. (2003) and Schmid et al. (2016). LO: Ligurian Ophiolites; AM: deformed Adriatic margin; AD: Adriatic Microplate; SA: Southern Alps; DI: Dinarides; SM: Southern margin of Meliata; HB: Eoalpine High-Pressure Belt; TW: Tauern tectonic Window; EW: Engadine tectonic Window; OTW: Ossola-Tessin tectonic Window; EA: Eastern Austroalpine; H: Helvetic domain; M: Molasse foredeep. In the Southern Alps domain the Triassic igneous bodies (see also Castellarin et al. 1988) are evidenced: (1) Brescian Alps (Cassinis et al. 2008); (2) Alto Vicentino (Bellieni et al. 2010); (3) Dolomitic Area; (4) Carnia region (Gianolla 1992; Brack et al. 2005); (5) Karawanken, Austria (Lippolt and Pidgeon, 1974; Bellieni et al. 2010). (b) Sketch of the distribution of the Middle Triassic intrusive bodies (Predazzo Intrusive Complex = PIC, Mt. Monzoni and Cima Pape), volcanic/volcanoclastic sequences and dyke swarms in the Dolomitic Area (modified from Abbas et al., 2018).

The Predazzo Intrusive Complex (PIC) is a ring-like shaped pluton composed of biotite- and amphibole-bearing pyroxenitic/gabbroic to syenitic/syenogranitic rocks. Zircon U-Pb age data from the syenogranitic and monzodioritic rocks suggest that PIC crystallization occurred between 237.3 ± 1.0 Ma and 238.075 ± 0.087 Ma (Mundil *et al.*, 1996; Storck *et al.*, 2018). PIC intrudes the Permian Atesina Volcanic District rhyolitic ignimbrites, the above-cited Permo-Triassic sedimentary formations, and the overlying volcanic sequences (Brack *et al.*, 1996, 1997, 2005; Mietto *et al.*, 2012), forming well-defined metamorphic aureoles (Princivalle *et al.*, 1999; Ferry *et al.*, 2002; Povoden *et al.*, 2002; Gallien *et al.*, 2007). Several authors identified the multi-pulse nature of PIC intrusion and the high variability of lithotypes of which it is composed (Vardabasso, 1930; Paganelli & Tiburtini, 1964; Petersen *et al.*, 1980; Castellarin *et al.*, 1982; Lucchini *et al.*, 1982; Menegazzo Vitturi *et al.*, 1995; Coltorti *et al.*, 1996; Visonà, 1997). Commonly accepted is the trachybasaltic nature of PIC parental magmas and their orogenic affinity (Marrocchino *et al.*, 2002), whereas the presence of both quartz- and nepheline-bearing rocks created a large number of debates on the petrogenesis of this complex (Vardabasso, 1930; Lucchini *et al.*, 1982; Menegazzo Vitturi *et al.*, 1995; Coltorti *et al.*, 1996; Visonà, 1997).

An articulated swarm of dykes, decimetric to metric in thickness, cut both the PIC, Mt. Monzoni and Cima Pape intrusions, the overlying volcanic/volcanoclastic sequences and the Permo-Triassic host rocks. These dykes range in composition from basanitic/basaltic to trachytic, and show the same orogenic-like (high-K calc-alkaline to shoshonitic) affinity as the corresponding plutonic bodies.

A minor portion of the dyke swarm, mainly cropping out in the Predazzo-Mt. Monzoni area, is constituted by grey to greenish lamprophyric dykes, 0.2-2.0 m in thickness, with alkaline affinity. As the majority of the dykes of the Dolomitic Area, lamprophyres are intruded into the plutonic bodies (especially PIC) and the surrounding volcanites; only one sample has been found within the Permian Val Gardena Sandstones Fm. (Lucchini *et al.*, 1969).

Chapter 2

Analytical methods

Chapter 2. Analytical methods

2.1. Wavelength Dispersive X-Ray Fluorescence Spectrometry (WDXRF)

Whole-rock major and trace element analyses of Mt. Monzoni, Cima Pape and PIC rocks were carried out at the Department of Physics and Earth Sciences (University of Ferrara, Italy), using an ARL Advant-XP automated X-Ray Fluorescence Spectrometer (WDXRF). Full matrix correction procedure and intensities were elaborated following Traill & Lachance (1966). Accuracy and precision are better than 2-5% for major elements and 5-10% for trace elements. The detection limits are 0.01 wt% and 1-3 ppm for most of the major and trace element concentrations, respectively (see also Allahyari *et al.*, 2014).

2.2. Inductively coupled plasma–mass spectrometry (ICP-MS)

Rb, Sr, Y, Zr, Nb, Hf, Ta, Th, U, and rare-earth elements (REE) concentration of Mt. Monzoni, Cima Pape and PIC rocks were analysed by inductively coupled plasma-mass spectrometry (ICP-MS) using a Thermo Series X spectrometer hosted at the Department of Physics and Earth Sciences (University of Ferrara, Italy). Precision and accuracy are better than 10% for all elements, well above the detection limits (see also Allahyari *et al.*, 2014).

2.3. Electron Microprobe (EMP)

Mineral phase major element compositions of representative samples of Mt. Monzoni, Cima Pape and PIC were analysed at the Department of Lithospheric Research, University of Wien (Austria), using a CAMECA SX100 electron microprobe equipped with four WD and one ED spectrometers. The operating conditions were as follows: 15 kV accelerating voltage, 20 nA beam current, and 20 s counting time on peak position. Natural and synthetic standards were used for calibration, and PAP corrections were applied to the intensity data (Pouchou & Pichoir, 1991). The following standards were used for the various elements: jadeite (Si and Na), corundum (Al), forsterite (Mg), andradite (Fe), rutile (Ti), orthoclase (K), apatite (P), and chromite (Cr).

2.4. Laser Ablation Inductively Coupled Plasma Mass Spectrometry (LA-ICP-MS)

Trace element concentration of pyroxene and amphibole crystals from selected Predazzo lamprophyres was carried out at the CNR - Istituto di Georisorse of Pavia by laser ablation microprobe-inductively coupled plasma-mass spectrometry (LAM-ICP-MS). The basic set and protocol were described by Tiepolo *et al.* (2003). NIST 610 and NIST 612 standard glasses were used to calibrate relative element sensitivity. Precision and accuracy for trace

element analyses were assessed by standard sample BCR-2 (reference values from USGS Geochemical Reference Materials Database). Each analysis was corrected with internal standards using CaO for both clinopyroxene and amphibole. The detection limit was function of the ablation volume and counting time and was therefore calculated for each analysis; indeed, ablation volume greatly dependes on instrument configuration. As a consequence, the detection limit reduces if spot size, beam power and cell gas flow are decreased. A 40-100 μm beam diameter and 20 μm s1 scanning rate were used. The theoretical detection limit ranges from 10 to 20 ppb for REE, Ba, Th, U, Zr and are about 2 ppm for Ti.

2.5. Thermal Ionization Mass Spectrometer (TIMS)

Whole-rock $^{87}Sr/^{86}Sr$ and $^{143}Nd/^{144}Nd$ isotopic analyses were performed at the Radiogenic Laboratory of the Scottish Universities Environmental Research Centre (SUERC) of Glasgow by means of a Sector-54 TIMS instrument.

Between 150-300 mg of powdered sample (some mixed with enriched Rb and Sr tracers for isotope dilution) were dissolved in sealed PFA fluoropolymer vials in a mixture of 2 ml HNO_3 and 5 ml HF at 150°C for 24 hours, evaporated to dryness, taken up in 2 ml HNO_3 at 150°C for >2 hours to eliminate fluorides, evaporated to dryness, taken up in 6 ml 6.2 M HCl at 150°C for 24 hours, visually inspected for complete dissolution, then evaporated to dryness before being taken up in 2 ml of 2.5 M HCl for ion exchange chemistry.

Strontium, Nd, and when necessary, Rb, were initially separated from matrix elements with a 12 ml quartz-glass cation exchange column with a sintered glass frit (AG50W-X8, 200-400 mesh, hydrogen form; 14.5 cm height, 1.2 cm diameter). The columns were cleaned with 90 ml of 6 M HCl, backwashed with H_2O, and 30 ml 2.5 M HCl. They were then conditioned with 10 ml of 2.5 M HCl. Sample was added, along with additional 2 x 1 ml 2.5 M HCl to ensure loading. A calibrated 2.5 M HCl + 3 M HNO_3 scheme was used to elute major elements and to collect purified Rb and fractions containing Sr and Sm+Nd, which were then evaporated to dryness. The Sr fraction was subsequently purified with a 0.7 ml glass crown ether coated, polymer bead anion exchange column and polymer frit (Sr.Spec, 100-150 μm; 5 cm long, 0.7 cm diameter).

The resin was single use, and cleaned prior to use by gently agitating fluoropolymer bottles of resin in alternating acid and water. Columns were cleaned with 12 ml of 0.01 M HNO_3 and conditioned with 1 ml 8 M HNO_3. Samples were taken up in 0.1 ml 8 M HNO_3 and washed onto the resin with an additional 1 ml HNO_3. Calcium and Ba were eluted with 5 ml of 8 M HNO_3 and 10 ml of 3 M HNO_3, followed by Sr elution with 5 ml of 0.01 M HNO_3 and evaporation to dryness. The Sm-Nd fraction was purified using the same type of 5 cm

glass column, with 0.7 ml of HDEHP coated, polymer bead anion exchange column (Ln.Spec). The resin was cleaned on the column by addition of 6 ml 6 M HCl, and then conditioned with 6 ml 0.18 M HCl. Samples were taken up in 0.2 ml 0.18 M HCl. Neodymium was eluted with 4 ml of 0.3 M HCl, Sm was eluted with 2.5 ml 0.7 M HCl, and then they were evaporated to dryness.

Strontium was loaded onto outgassed single Re filaments with a Ta-activator solution and ran on a Sector-54 TIMS instrument housed at SUERC using a multi-dynamic routine, with a typical signal intensity on ^{88}Sr of ~$1 \cdot 10$-11A. Mass fractionation was corrected with an exponential law to $^{86}Sr/^{88}Sr = 0.1194$. Eight measurements of SRM987 during the course of this analytical programme yielded a mean value of 0.710244 ± 0.000016 (2 SD), consistent with the consensus value of ~0.71025.

Neodymium was loaded onto the side of a triple Ta-Re-Ta filament assembly in H_2O and ran as Nd+ on the same Sector-54 TIMS instrument, using a multi-dynamic routine, and a typical signal intensity on ^{144}Nd of 0.5-$1 \cdot 10^{-11}$A. Mass fractionation was corrected with an exponential law to $^{146}Nd/^{144}Nd = 0.7219$, and 12 measurements of JNdi during the course of this analytical programme yielded a mean value of 0.512079 ± 0.000018 (2 SD), consistent with consensus value of 0.51210.

2.6. Analytical procedure for $^{40}Ar/^{39}Ar$ dating

$^{40}Ar/^{39}Ar$ datings were performed at the Radiogenic Laboratory of the Scottish Universities Environmental Research Centre (SUERC) of Glasgow. Samples (amphibole and plagioclase separates) for $^{40}Ar/^{39}Ar$ dating were prepared using the methods described in Mark *et al.* (2011a). All samples were subsequently cleaned in de-ionised water. They were parcelled in high purity Al discs for irradiation. International standards Fish Canyon sanidine (FCs) (28.294 ± 0.036 Ma, Renne *et al.*, 2011; Morgan *et al.*, 2014) and GA1550 biotite (99.738 ± 0.104 Ma, Renne *et al.*, 2011) were loaded adjacent to the samples to permit accurate characterisation of the neutron flux (J parameter). Samples were irradiated for 50 hours in the Cd-lined facility of the CLICIT Facility at the OSU TRIGA reactor. Standards were analysed on a MAP 215-50 system (described below briefly and in more detail by Ellis *et al.*, 2012) - FCs was analysed by CO_2 laser total fusion as single crystals (n = 20). GA1550 (n = 20) was also analysed by CO_2 laser total fusion and step-heated using a CO_2 scanning laser (n = 5) (Barfod *et al.*, 2014). Using GA1550 the J-parameter was determined to a precision approaching 0.1% uncertainty.

Wafers were loaded into an Ultra-High-Vacuum (UHV) laser cell with a SiO_2 window. In situ UVLAMP Ar extraction was conducted using a New Wave UP-213 nm UV laser system

(described in Moore *et al.*, 2011). 50 x 50 x 5 μm^3 (amounts of ablated material approximately 1250 μm^3) raster pits were made in mineral surfaces to extract the Ar isotopes. All gas fractions were subjected to 180 seconds of purification by exposure to two SAES GP50 getters (one maintained at room temperature, the other held at ca. 450˚C). A cold finger was maintained at -95.5˚C using a mixture of dry ice ($CO_{2[S]}$) and acetone. Ion beam intensities (i.e., Ar isotope intensities and hence ratios) were measured using a MAP 215-50 mass spectrometer in peak jumping mode. Measurements were made using a Balzers SEV-217 electron multiplier. The system had a measured sensitivity of 1.12 x 10^{-13} moles/Volt. The extraction and cleanup, as well as mass spectrometer inlet and measurement protocols and data acquisition were automated. Blanks (full extraction line and mass spectrometer) were made following every two analyses of unknowns. The average blank ± standard deviation (n = 28) from the entire blank run sequence was used to correct raw isotope measurements from unknowns. Mass discrimination was monitored by analysis of air pipette aliquots after every five analyses of unknowns (n = 13, 7.21 x 10^{-14} moles ^{40}Ar, $^{40}Ar/^{36}Ar$ = 289.67 ± 0.63).

The samples were step-heated using a CO_2 laser (approximately 500-1500˚C, optical pyrometer measurements). Extracted gases were subjected to 300 seconds of purification by exposure to two SAES GP50 getters (one maintained at room temperature, the other held at ca. 450˚C). A cold finger was maintained at -95.5˚C using a mixture of dry ice ($CO_{2[S]}$) and acetone. Ion beam intensities were measured using a MAP 215-50 mass spectrometer in peak jumping mode. Measurements were made using a Balzers SEV-217 electron multiplier. The system had a measured sensitivity of 1.12 x 10^{-13} moles/Volt. The extraction and cleanup, as well as mass spectrometer inlet and measurement protocols and data acquisition were automated. Blanks (full extraction line and mass spectrometer) were made following every analysis of an unknown. The average blank ± standard deviation for each experiment (n = 14) from the entire blank run sequence was used to correct raw isotope measurements from unknowns. Mass discrimination was monitored by analysis of air pipette aliquots after every three analyses. All Ar isotope data were corrected for backgrounds, mass discrimination, and reactor-produced nuclides and processed using standard data reduction protocols and reported according to the criteria of Renne *et al.* (2009). The atmospheric argon isotope ratios of Lee *et al.* (2006), which have been independently verified by Mark *et al.* (2011b), were employed. The $^{40}Ar/^{39}Ar$ ages for were determined relative to the statistical optimization model of Renne *et al.* (2010; 2011) and are reported including analytical and full systematic uncertainties at the 2 sigma level.

Chapter 3

The Predazzo Intrusive Complex (PIC): field characters and petrological evolution

Chapter 3. The Predazzo Intrusive Complex (PIC): field characters and petrological evolution

3.1. Introduction

The Predazzo Intrusive Complex (PIC), together with Mt. Monzoni and Cima Pape areas, represents one of the main intrusive expressions of the Triassic magmatism within the Dolomites (Southern Alps domain, Italy), which is strongly dominated by the presence of volcanics and dykes throughout all the Schlern/Seiser Alm (NW) and the Cadore (NE) regions.

Many petrological studies were carried out in order to explain the orogenic character of these complexes and the intrusion sequence: the clearly shoshonitic affinity of the Middle Triassic magmatism, in effusive, subvolcanic and intrusive terms, is in fact concomitant with the general anorogenic tectonic regime of the region during the Ladinian (Rossi *et al.*, 1976; Castellarin, 1983; Bonin, 1988; Zanetti *et al.*, 2013). The origin of this magmatic event was afterwards linked to an extensional tectonic regime, dominated by vertical differential movements and subsidence (Gianolla *et al.*, 2010), which were able to generate shoshonitic magmas by decompression melting of a subduction-related, previously metasomatized mantle source (Sloman, 1989; Bonadiman *et al.*, 1994).

After having been at the heart of the petrographic debate for decades, the study of PIC was abandoned, despite its key role in the interpretation of the Southern Alps Triassic magmatism. This volcano-plutonic complex has been in fact almost completely preserved, in both its intrusive and volcanic portions, from the action of the alpine tectonic event, resulting in one of the rare places worldwide where the relationship between an ancient magma chamber, its volcanic products and the host rocks could be observed. PIC, unlike Mt. Monzoni and Cima Pape, is characterized by the presence of multiple shoshonitic silica saturated, oversaturated and undersaturated plutons, whose genetic relationships gave rise to various debates (Sloman, 1989; Bonadiman *et al.*, 1994; Menegazzo Vitturi *et al.*, 1995; Visonà, 1997; Marrocchino *et al.*, 2002).

The present study is aiming at a complete geological and petrological reconstruction of the complex, which can also foster a deeper understanding of the Triassic magmatism in the Southern Alps. A detailed field survey and sampling, together with an accurate petrological investigation (whole rock and mineral major/trace element analyses) on more than 180 samples, were carried out in order to define i) the differentiation processes occurring within the feeding system, ii) the relationships between the various intrusive bodies and iii) their petrological signature.

3.2. Field characters and volume estimation

The main part of PIC is made up of a monzogabbroic to syenitic external ring-shaped body (with minor gabbros and clinopyroxenites) and by subordinated more differentiated intrusions, outcropping in the central (granites to syenogranites) and in the eastern part of the ancient magma chamber (Fig. 2). A huge amount of volcanic and volcanoclastic products, ranging in composition from basalts to latites, surrounds the intrusive portion, outcropping mainly in the northern and western sectors of the magmatic complex. A dyke swarm, basaltic to trachytic in composition, variable in width from tens of centimetres to few metres and with two prevalent strike directions (NNW-SSE and E-W), cut sedimentary, volcanic and intrusive rocks.
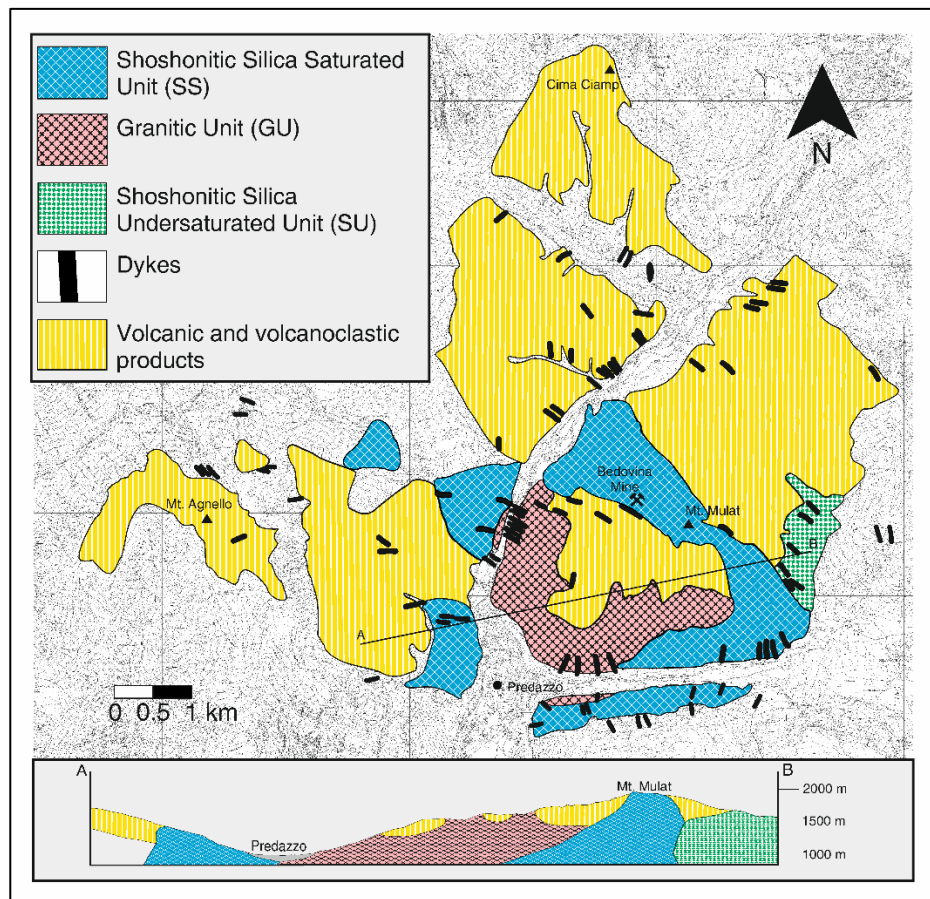
Fig. 2. Simplified geological map and cross-section of the Predazzo Intrusive Complex.

The entire complex is nowadays largely covered by vegetation, whereas during the XX century it was famous for the syenogranite quarries, as well as for the Bedovina Mine, a W, Mo, Sn, Bi, Cu, Pb, Zn, Ag, Te, Co and Ni mineralization (Frizzo *et al.*, 2010) lying at the north-eastern contact between PIC and the volcanic products (Fig. 2). A detailed geological survey together with an extensive sampling of the Predazzo area allowed the reconstruction

of the outcrop geometries for the entire PIC, as well as the mapping of the volcanic and volcanoclastic deposits. As shown further on, this field work defined the existence of three different magmatic units. In an overall view, both intrusive and volcanic portions are exposed to the surface, making possible to study the relationship between the ancient magma chamber and the overlying extrusive rocks, mainly in the central and in the eastern parts (Fig. 2). Here, in fact, the intrusion outcrops almost continuously over about 1000 m of vertical gap, preserving both its inner portions and its upper edges, where the contact with the corresponding volcanic products and the host rocks is clearly delineated. At the bottom of the PIC (about 900 m a.s.l.) the contact between the various lithotypes is well preserved: the relationships between the portions of the intrusion, as well as between them and the widespread dyke swarm, contributed also to constrain the intrusive sequence that formed the magmatic complex.

In addition, the intrusion shows a gradual transition to the volcanic rocks over a distance of hundred metres, marked by the presence of relatively fine-grained monzogabbroic to monzonitic lithotypes, with a hypabyssal texture (Fig. 3b). These rocks crop out almost symmetrically above the Bedovina Mine (Mt. Mulat) on the eastern side of the complex and at the Malga Gardoné on its western side, suggesting the presence of a transitional, magmatic contact between the intrusion and the volcanics, i.e. the absence of a tectonic contact between these two lithotypes (straight lines in the lower frame of Fig. 3). The widespread vegetation covering the whole complex, together with the length of such transition, makes not possible to show these contacts. For decades one of the most debated topics linked to the PIC has been the relationship between the intrusive and the volcanic portions. Due to its ring-like shape the historical definition of 'Predazzo caldera' was introduced, suggesting a highly explosive volcanic event (Leonardi, 1968; Castellarin *et al.*, 1982; Doglioni, 1984; Gianolla *et al.*, 2010). The above-mentioned transitional contact (Fig. 3), together with the absence of large caldera-fill deposits (Quick *et al.*, 2009; Sinigoi *et al.*, 2011), as clearly evidenced in the cross-section of Fig. 2, cast however some doubts on the presence of a caldera structure for the Predazzo magmatic complex.
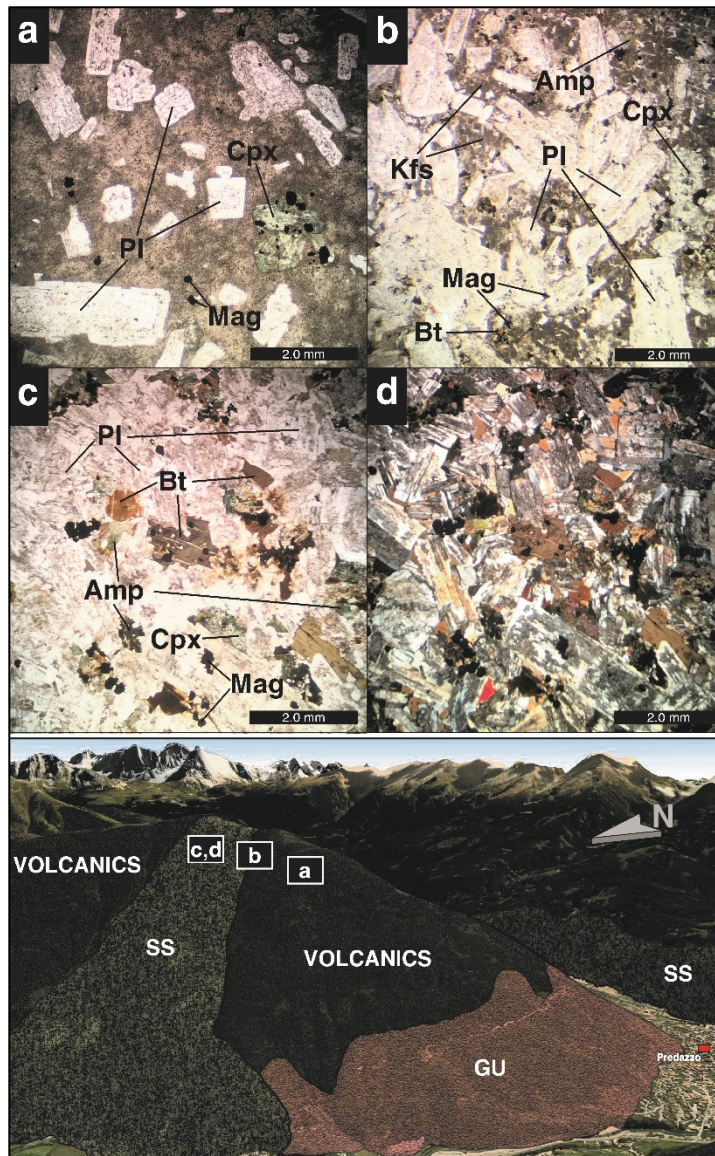
Fig. 3. Photomicrographs and field reconstruction (modified from Google Earth) reporting the grain size gradual transition from volcanic to intrusive rocks of the Shoshonitic Silica Saturated Unit at the eastern edge of Predazzo Intrusive Complex. (a) Porphyritic trachyandesite (1850 m a.s.l., M.te Mulat) comprising large plagioclase (Pl) and clinopyroxene (Cpx) phenocrysts embedded in a microcrystalline plagioclase + clinopyroxene + magnetite (Mag) groundmass (transmitted plane-polarized light). (b) Hypabyssal monzonite (1900 m a.s.l., M.te Mulat) characterized by large plagioclase over a microcrystalline assemblage of quartz (Qz) + K-feldspar (Kfs) + biotite (Bt) + plagioclase + clinopyroxene + amphibole (Amp) (transmitted plane-polarized light). (c, d) Holocrystalline monzodiorite (1900 m a.s.l., M.te Mulat) composed of plagioclase + clinopyroxene + biotite + amphibole + magnetite (c: transmitted plane-polarized light; d: cross-polarized light).

After the field survey, the use of QGis 2D and Polyworks (InnovMetrics) 3D software enabled us to convert the field relationships in a 3D surface model for the estimate of the volume of each portion of the complex. Due to the large volume of magmatic rocks that characterize the Predazzo complex, which is over 10 km^3 for an area of about 25 km^2, the edges of each magmatic unit within the complex were geometrically simplified to get a processable data, with an accuracy adequate for the focus of the present study. Such

estimations were in fact aimed to obtain an order of magnitude for the volume of the different portions of the intrusion, as well as to develop a volumetric comparison between the intrusives and the volcanics. The results from the 3D modelling show that the entire PIC volume is $4.51 \pm 0.136 \times 10^9$ m^3, i.e. about 4.5 km^3; by contrast, the volume of the volcanic deposits (lava flows, pillow lavas, lava breccias and explosive breccias) resulted slightly larger, being $5.97 \pm 0.179 \times 10^9$ m^3, i.e. about 6 km^3.

3.3. Petrography and whole rock geochemistry

Previous works on PIC (Visonà, 1997; Marrocchino *et al.*, 2002) proposed a subdivision into four units, named M1 (shoshonitic silica-saturated series), M2 (shoshonitic silica oversaturated series), M3 (potassic-alkaline series) and calc-alkaline series, this latter made up only by granitic and syenogranitic lithotypes. The improvement of the sample collection carried out in the present study, as well as new petrographic and geochemical data, suggest the subdivision of PIC into three main units (Fig. 2), based on the silica saturation degree and the mineral assemblages, in which M1 and M2 have been merged into a single saturated (SS) series. According to our sampling, in fact, the rare oversaturated rocks that were found scattered within the complex do not support the existence of a clearly independent series (M2), which is also in contrast with the general overlap of the petrographic and geochemical features of the two previously defined M1 and M2 series. Silica saturation, resulting in the modal and normative presence of quartz, well displayed in the QAPF diagram (Fig. 4), is in fact an important discriminating factor between the three units that constitute the PIC. The Shoshonitic Silica Saturated Unit (SS) is composed of a noticeable amount of quartz (up to 15–20%) from the less differentiated monzogabbroic to the evolved syenitic terms, while the Granitic Unit (GU) is constituted by granites and syenogranites with up to 35–40% of quartz. On the other side, the Shoshonitic Silica Undersaturated Unit (SU) suite is nepheline-normative along the entire differentiation trend.
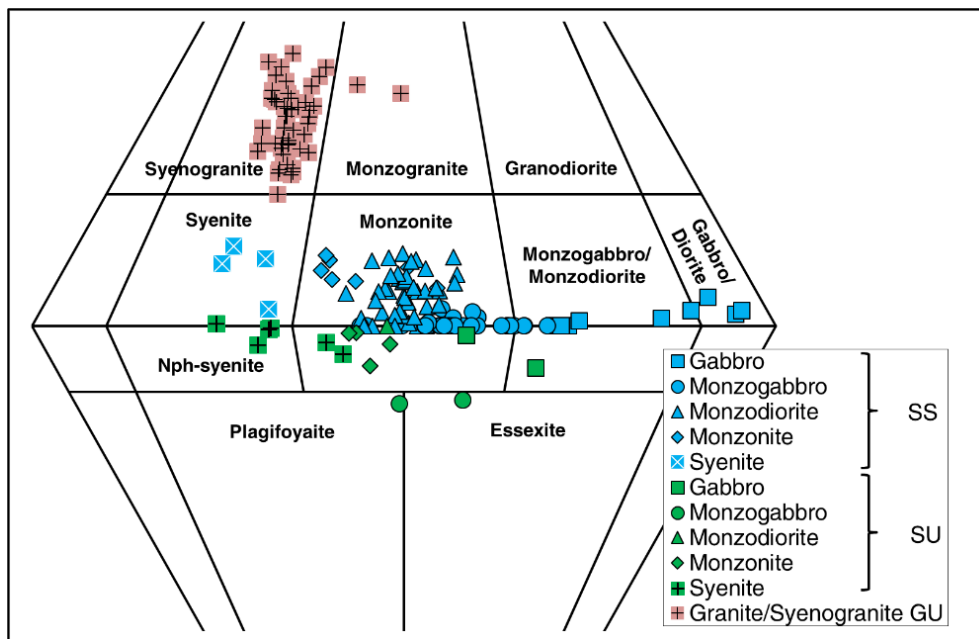
Fig. 4. QAPF diagram showing the distribution of rocks from the Predazzo Intrusive Complex.

3.3.1. Petrography

3.3.1.1. Shoshonitic Silica Saturated unit (SS)

It represents the main portion of the intrusion (67% of PIC, with a volume of about 3.1 km^3), outcropping in the external part of the plutonic ring. This unit is mainly constituted by gabbros, monzogabbros, monzodiorites, monzonites and syenites, and is thought to be derived from the first magmatic pulse. The gabbros crop out at the western border of the intrusion, dark-coloured, with medium to large grain size (1.2-6.8 mm) and, in some cases, mesocumulitc texture. The most common mineral phases are slightly zoned, light green and sometimes twinned augitic clinopyroxene (Cpx), olivine (Ol) and hypersthenic orthopyroxene (Opx; mineral abbreviations are hereinafter reported according to Whitney & Evans, 2010).The intercumulus assemblage is composed of zoned plagioclase (Pl), magnetite (Mag), quartz (Qz) and poikilitic biotite (Bt). The monzogabbros represent the most abundant lithotype, with fine to large grain size (0.3-6.8 mm), hypidiomorphic texture and low colour index. Peculiar is the presence of augitic Cpx showing, in some cases, incipient local replacement by brown amphibole (Amp). The primary Amp are hornblende in composition, while Ol and Opx are absent. Other common phases are Pl, minor alkali feldspar (Kfs), Bt, sometimes altered to chlorite (Chl), and Mag. Monzodiorites are characterized by a grain size comparable to that of monzogabbros, and by a slightly higher colour index. Monzonites show fine to medium grain size (0.3–4.5 mm), with large Kfs, often characterized by perthitic structure, containing other mineral phases, (i.e. Bt and Pl).

The augitic Cpx is often altered, while Amp is characterized by a compositional range from hornblende (primary formed terms) to actinolite-tremolite (replacing Cpx). Qz is also present, in an amount generally between 5 and 20%. Syenites are pink coloured, with granular structure: strongly perthitic Kfs is common, even if clouded by clay alteration; Qz and Pl are smaller in size and less abundant. The only mafic phases are represented by rare Cpx, Amp and Bt. Sphene (Spn), apatite (Ap) and zircon (Zrn), considered as accessory phases in almost all lithotypes, become quite abundant in syenites.

At the southern border of the intrusion, directly in contact with the SS unit, outcrops a small dark-coloured mesocumulitic clinopyroxenitic body, with grain size ranging from medium to large (1.1–6.2 mm). It is mainly constituted by Cpx, Ol, Bt, Mag and Pl. Its cumulitic nature, together with its marginal position, suggest that these rocks represent the first minerals crystallized at the border of the SS intrusion.

The SS hypabyssal monzogabbros and monzonites are mainly constituted by large Pl and Cpx embedded in a microcrystalline assemblage of Kfs, Bt, Pl, Cpx and Amp. They gradually pass into the volcanic lithotypes at the eastern and western side of the complex, as it is evident in the photomicrographs of Fig 3.

3.3.1.2. Granitic unit (GU)

It outcrops in the central part of PIC, where forms a half-ring of about 2 km^2 in extension and about 1.1 km^3 in volume (25% of the intrusion). Its contact towards the SS rocks is sub-vertical in the western portion of the complex, whereas in the eastern part it becames nearly sub-horizontal, where the GU body "overcomes" the SS one. The contact between GU and overlying volcanites is not gradual (as for SS rocks) and is locally characterized by the presence of thermometamorphic structures, further testifying the subsequent emplacement of the Granitic Unit with respect to the SS one (Fig. 2). The GU is constituted by pink granites to syenogranites, sometimes with pegmatitic facies. The most abundant phase in such rocks is large sized perthitic Kfs, with Pl, Qz and Fe-rich Bt in decreasing order of abundance. Accessory minerals are fluorite, allanite, Ap and Zrn, these two latters being often hosted in Qz crystals. Some samples are characterized by the presence of secondary Chl crystals, formed over Bt, as well as centimetric black aggregates of tourmaline. Paganelli & Tiburtini (1964) and Menegazzo Vitturi *et al.* (1995) reported also the presence, in some cases, of small amounts of Amp intergrew with Bt. The relationships between granites and the SS series, suggest that the GU unit was intruded after SS, representing the second magmatic pulse of the PIC.

3.3.1.3. Shoshonitic Silica Undersaturated unit (SU)

This series, about 0.3 km^3 in volume (8% of the PIC), outcrops in the easternmost part of the intrusion. It is characterized by the abundant presence of differentiated products, with subordinate gabbros, monzogabbros and monzonites, all of them nepheline (*nph*)-normative in composition. The most mafic rocks (gabbros and monzogabbros) are characterized by the presence of Pl, Kfs, salitic/aegirinaugitic Cpx, hastingsitic/Fe-pargasitic Amp, and minor Bt and Mag. Peculiar is also the presence of ugranditic-melanitic garnet (Grt). Monzonites are characterized by the absence of Qz, and by the presence of some altered Pl and Kfs, as well as rare altered Cpx, Amp and Bt. Syenites are grey coloured, with glomeroporphiric texture, where Kfs, melanitic Grt and minor altered Pl are the dominant phases. Small crystals of dark green Cpx and brown Amp are rarely present, embedded in a fine matrix constituted by Kfs, Pl, and dark green Cpx. Spn, ilmenite, Mag, Ap and epidote are present in the less differentiated lithotypes, while in the most differentiated rocks the accessory phases are Ti-Mag and Spn. In some differentiated samples the presence of Nph has been documented (Vardabasso, 1930; Visonà, 1997). The finding of dyke with similar undersaturated affinity cutting the GU unit suggests that the SU unit was the last pulse to enter the magma chamber.

3.3.2. Major element geochemistry

The three main units of the PIC (SS, SU and GU) show independent geochemical behaviour, well discriminated in QAPF (Fig. 4), TAS (Fig. 5) and K_2O vs. SiO_2 (Fig. 6) diagrams. The entire dataset is characterized by a potassic affinity (Fig. 7), only a few extremely differentiated syenogranites and syenites lie in the high-K affinity field.

The SS series is composed of gabbroic (mg# = 58-59) to monzogabbroic (mg# = 46-64), monzodioritic, monzonitic and syenitic samples, with SiO_2 and K_2O contents ranging from 42 to 68 wt% and 0.3 to 8.4 wt%, respectively, and Na_2O content up to 4.3 wt% in the most differentiated samples (Table A4.1). Clinopyroxenites and cumulitic gabbros are characterized by a lower silica and potassium contents, ranging from 39 to 46 wt% and from 0.3 to 0.8 wt%, respectively (Table A4.1). Their affinity is potassic and fits well with the SS series, although the abundant presence of Bt results in a normative (CIPW) silica undersaturation. These cumulitic samples are characterized by the highest MgO, TiO_2, CaO, FeO and contents (Fig. 8); except for the MgO/SiO_2 ratio, all diagrams confirm their affinity to the SS series. It is very likely that they could be derived from the early stage of fractional crystallization of the SS magma (Fig. 8; see also discussion below).

Rocks belonging to the GU are highly differentiated granitic to syenogranitic lithotypes, with high silica (up to 76 wt%) and alkali (7 to 11 Na_2O+K_2O wt%) contents; their K/Na ratio is

generally similar to that of SS series, except for few samples showing a low-K content (Table A4.1). Granites and syenogranites are also characterized by TiO_2 and CaO contents comparable to those of the SS syenites, whereas their low MgO/SiO_2 and high FeO/SiO_2 ratios (Fig. 8) highlight their peculiar petrological behaviour.

The SU series is composed of silica-undersaturated *nph*-normative lithotypes, with K_2O (from 2.2 to 9.2 wt%) and Na_2O (0.4 up to 6.3 wt%) contents higher than those of SS rocks (Table A4.1). A few gabbroic (mg# = 46-56) to monzogabbroic (mg# = 44) rocks belong to this series, that is generally composed of more differentiated terms (monzonites and syenites) with respect to the SS series, where the entire fractionation sequence is commonly represented. In Fig. 8, the CaO and FeO contents of the entire dataset are plotted against silica and the parallel SS and SU differentiation patterns are clearly distinguishable. At comparable differentiation degree, SU samples are in fact characterized by higher Na_2O, but lower MgO, CaO, FeO and TiO_2 contents, further supporting their origin from an independent magmatic pulse, whose fractionation trend is related to the subtraction of compositionally and modally different mineral phases (see discussion below).
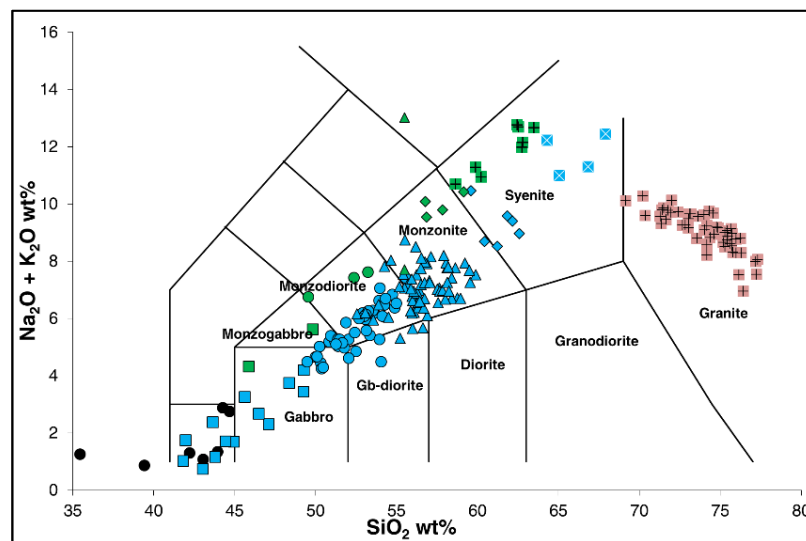
Fig. 5. Total alkali vs. silica (TAS) classification diagram (Le Maitre et al. 1989) showing whole rock compositions from the Predazzo Intrusive Complex. Symbols as in Fig. 4; black circles = pyroxenites.
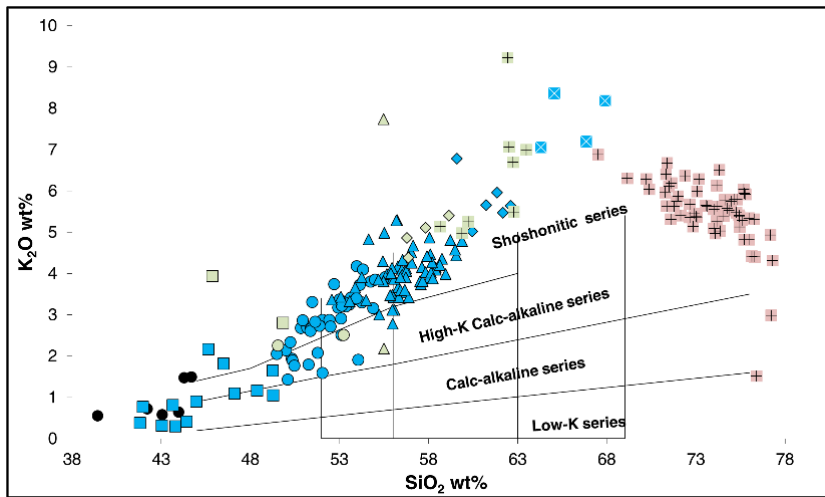
Fig. 6. K₂O vs. SiO₂ classification diagram (Ewart, 1982) showing whole rock compositions from the Predazzo Intrusive Complex. Symbols as in Fig. 4; black circles = pyroxenites.
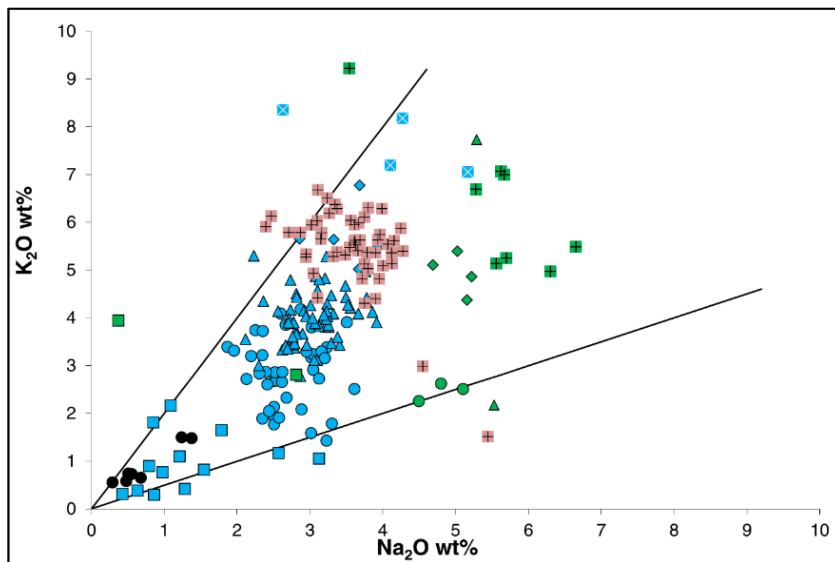
Fig. 7. K₂O vs. Na₂O classification diagram showing whole rock compositions from the Predazzo Intrusive Complex. Symbols as in Fig. 4; black circles = pyroxenites.
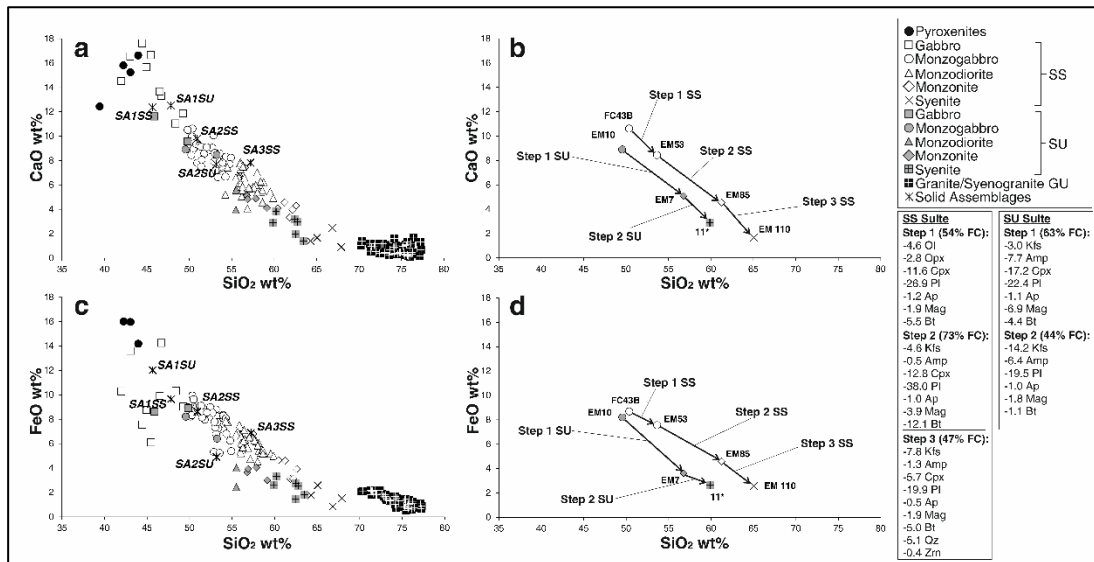
Fig. 8. (a, b) CaO and (c, d) FeO vs. SiO$_2$ variation diagrams showing whole rock compositions from the Predazzo Intrusive Complex. (a, c) Shoshonitic Silica Saturated, Granitic Unit, and Shoshonitic Silica Undersaturated suites are plotted together with the composition of the solid assemblages derived by the FC modelling. SA1SS = Gabbroic Solid Assemblage 1 with SS affinity; SA2SS = Monzogabbroic Solid Assemblage 2 with SS affinity; SA3SS = Monzodioritic Solid Assemblage 3 with SS affinity; SA1SU = Gabbroic Solid Assemblage 1 with SU affinity; SA2SU = Monzodioritic Solid Assemblage 2 with SU affinity. (b, d) FC vectors derived for the SS and SU suites using as starting compositions the monzogabbros (samples FC43B and EM10 respectively). The final compositions are syenites (samples EM110 and 11* respectively). For each step is also reported the relative percentage of the fractionating mineral phases, translating to the compositions of the subtracted solid assemblages. Ol: olivine; Opx: orthopyroxene; Cpx: clinopyroxene; Pl: plagioclase; Ap: apatite; Mag: magnetite; Bt: biotite; Kfs: K-feldspar; Amp: amphibole; Qz: quartz; Zrn: zircon.

3.3.3. Trace element geochemistry

N-MORB-normalized (Sun & McDonough, 1989) trace element distributions for PIC lithotypes are reported in Fig. 9. They show a general enrichment in large-ion lithophile elements (LILE), Th, U, and marked negative Nb and Ti anomalies. These features, together with the late Mag crystallization and the consequent absence of Fe-Ti enrichment trend, as well as with Bt, Amp and Kfs modal abundances, support the affinity to the shoshonitic series from active continental margins (Ewart, 1982).

All lithotypes show a marked enrichment in Pb, which ranges in composition from 20 up to about 90 ppm. Irrespective of lithotypes, this trace element represents a discrimination feature between SS and SU series, being slightly higher in the latter. Such a large positive anomaly is peculiar of the Triassic magmatism of the Dolomitic Area, which is often accompanied by small polymetallic copper-bearing deposits (Nimis *et al.*, 2012). Bedovina Mine represents in fact one of the most famous copper-wolfram deposits of the area, where the presence of a 'sulphide copper phase', i.e. chalcopyrite, pyrite, sphalerite and galena,

was genetically related to the effect of late magmatic lead-enriched fluids (Frizzo *et al.*, 2010). Together with Pb, all HFSE are generally enriched in SU suite with respect to SS one. Clinopyroxenites and gabbros display normalized patterns lower than monzogabbros, monzodiorites and monzonites, in agreement with their cumulitic nature. Sr and Ba show a behaviour shifting from incompatible in mafic and intermediate lithotypes to more compatible in sialic rocks, where the content of these elements decreases, in relation to Pl and Kfs fractionation, still maintaining a slight positive anomaly. Similarly, from clinopyroxenites and gabbros to syenites a negative P anomaly is recorded, probably due to Ap fractionation. Extremely differentiated syenites are characterized by the highest content of incompatible elements (Rb, Th and Nb), but show moderate to strong Ba, Sr, P, Zr, Ti and Y depletions, suggesting a considerable removal of Kfs, Mag, Ap and Zrn (see discussion below).

N-MORB-normalized REE spidergrams (Sun & McDonough, 1989) show that PIC rocks are characterized by parallel but higher REE distribution (Fig. 9, Table A4.1) from clinopyroxenites and gabbros throughout monzogabbros, monzodiorites, monzonites and syenites, as it would be expected by a normal fractionation trend. $(La/Yb)_N$ ratio for the SS suite ranges from 5 to 7 in clinopyroxenites, up to 9 in gabbros, from 9 to 12 in monzogabbros and from 10 to 22 in monzodiorites, monzonites and syenites. The SU lithotypes are extremely enriched in LREE, with $(La/Yb)_N$ reaching the highest values of 15-29. GU samples show a general REE enrichment, with $(La/Yb)_N$ ranging between 8 and 21. Almost all SS and SU lithotypes, except for gabbros and clinopyroxenites, are also characterized by a negative Eu anomaly, probably related to feldspar fractionation: this anomaly, more evident in the differentiated syenites, is extremely marked in all GU samples.
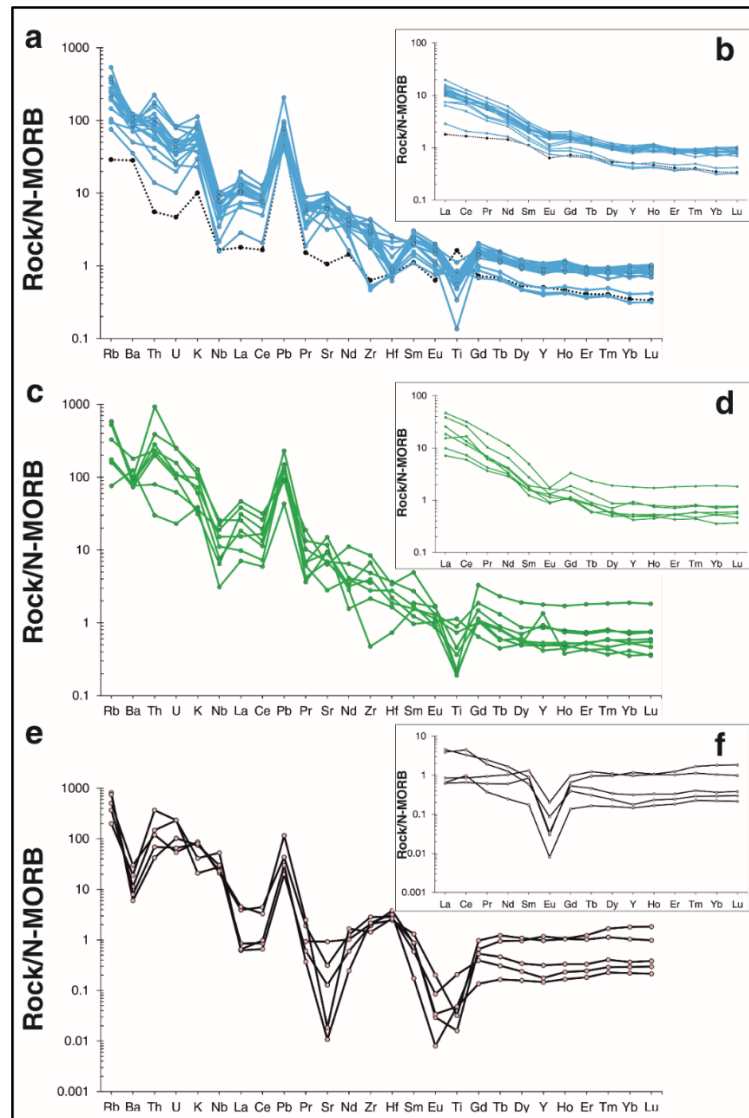
Fig. 9. N-MORB-normalized trace element and REE patterns for representative Predazzo Intrusive Complex (a, b) SS rocks, (c, d) SU rocks, (e, f) GU rocks. Normalizing values from Sun & McDonough (1989). The dashed patterns in (a) and (b) are referred to the pyroxenitic rocks.

The consistent increase of incompatible elements, like Rb, Nb, Zr, Th, Y, La, Ce, at increasing the differentiation index (SiO$_2$; Fig. 10), is well evident. A gradual enrichment in Rb, Zr and Nb are observed both with increasing silica content and varying the serial alkalinity from SS to SU series. The highest values of Rb (ca. 330 ppm) and Zr (ca. 640 ppm) are observed in the syenitic rocks of the SU series. In Rb and Zr vs. SiO$_2$ diagrams (Fig. 10), GU samples and clinopyroxenites plot in well separated fields. Clinopyroxenites are characterized by a Rb content below 50 ppm, while GU granites and syenogranites display higher concentrations (up to 440 ppm). At comparable SiO$_2$, Rb content is generally higher in the SU suite with respect to SS one. On the other hand, Zr content increases markedly from the less evolved monzogabbros (< 100 ppm) to SS and SU syenites, being the SU suite characterized by an average higher content. In GU lithotypes, the Zr content

decreases markedly from 360 to 80 ppm with increasing silica content up to 77 wt%, probably due to Zrn fractionation.
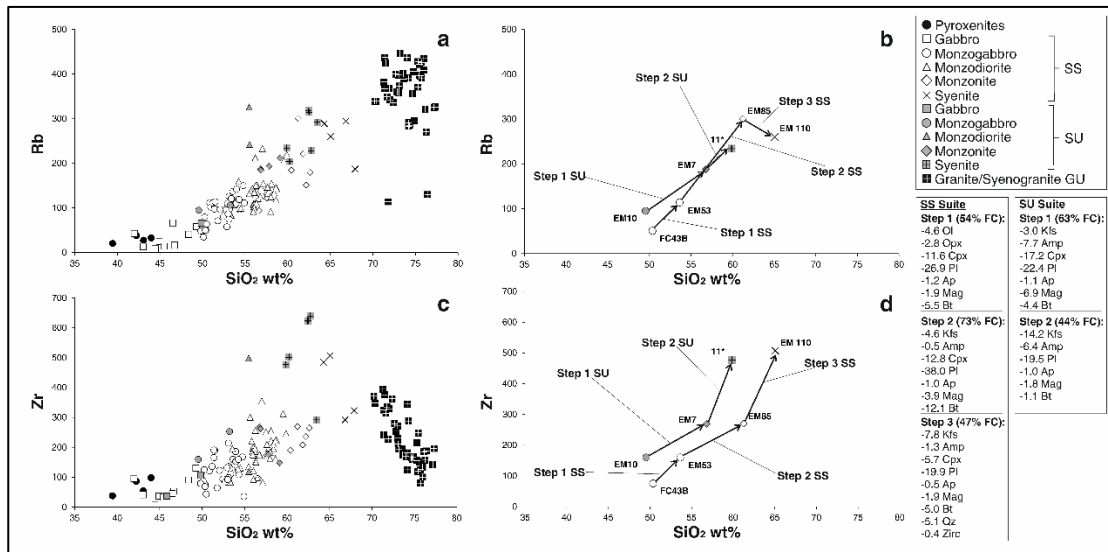
Fig. 10. (a, c) Rb and (b, d) Zr vs. SiO2 variation diagrams of rocks from the Predazzo Intrusive Complex. (a, c) Shoshonitic Silica Saturated, Granitic Unit and Shoshonitic Silica Undersaturated suites. (b, d) FC vectors derived for the SS and SU suites using as starting compositions the monzogabbros (samples FC43B and EM10 respectively). The final compositions are syenites (samples EM110 and 11* respectively). For each step is also reported the relative percentage of the fractionating mineral phases, translating to the compositions of the subtracted solid assemblages. Ol: olivine; Opx: orthopyroxene; Cpx: clinopyroxene; Pl: plagioclase; Ap: apatite; Mag: magnetite; Bt: biotite; Kfs: K-feldspar; Amp: amphibole; Qz: quartz; Zrn: zircon.

3.4. Mineral chemistry

The composition of the most representative PIC mineral phases was carried out to better characterize the geochemical features of SS, SU and GU suites and to develop the mass balance fractionation model illustrated below (see also Fig. 8 and Fig. 10). Fe^{2+}/Fe^{3+} ratio was stoichiometrically determined for the anhydrous phases, whereas for Amp and Bt it was calculated according to the models of Leake *et al.* (1997) and Dymek (1983) respectively.

Olivine, often altered to iddingsite, is present only in a few mafic samples of the SS series, like clinopyroxenites, gabbros and rare monzogabbros. Its compositional range varies from Fo_{62} to Fo_{38} in both gabbros and clinopyroxenites.

Magnetite (Fig. 11; Table A4.2) is characterized by an almost homogeneous composition among the three magmatic suites. The TiO_2 content is in fact always below 5 wt%, reaching its lowest values in the more differentiated samples (i.e. monzonites) as well as in the GU syenogranites, where is slightly above zero.

As for Ol, Opx (Fig. 11) is present only in a few mafic samples of the SS series. It occurs in reaction relationship with Ol in clinopyroxenites and gabbros, and in a few cases it is also

present in monzonites. Its composition ranges from En_{71-61} in clinopyroxenites, En_{69-63} in gabbros to En_{60-52} in monzonites.

Cpx (Fig. 11; Table A4.3) is reported from both SS and SU suites, with different composition for the two suites. Cpx from SS series are quite homogeneous, being diopsidic and augitic in composition with a Wo content < 50. On the other hand, SU Cpx show a generally higher CaO content, with Wo > 50, ranging from salitic to ferro-salitic in composition, almost comparable to Cpx from alkaline rocks as described by Dal Negro *et al.* (1986).

Analogously to Cpx, Amp (Fig. 12; Table A4.4) is very different between the two series, the alkali content is a peculiar feature of the SU lithotypes. Amphibole from SS gabbros to syenites are mainly Mg-hornblende to actinolite in composition, followed by edenite and Fe-edenite terms. In this series, actinolite is a reaction product upon primary Mg-hornblende and Cpx. On the other hand, Amp from SU gabbros to syenites range in composition between hastingsite, Mg-hastingsite and Fe-pargasite. At comparable evolution degree (from gabbros to syenites), Amp composition show a remarkable differences between the two suites (Fig. 12), SS Amp being higher in SiO_2, as well as lower in K_2O, Na_2O and Al_2O_3 contents with respect to Amp from SU series. In this latter, Na_2O and K_2O contents of Amp can reach up to 2.6 and 2.2 wt%, respectively.

Biotite (Fig. 12; Table A4.5) occurs in SS, SU and GU lithotypes, testifying to the K-affinity of the PIC magmas. This phase is generally characterized by a high TiO_2 (0.9–6.1 wt%) content, except for granites and syenogranites of the GU suite ($TiO_2 \leq 3.3$ wt%), where Bt have also low Al_2O_3 and SiO_2 contents. At comparable SiO_2 content, Bt from SU monzogabbros are slightly enriched in Al_2O_3 with respect to those from SS monzogabbros (Fig. 12). Discriminating feature is also the FeO content of Bt, separating the iron-rich GU Bt (FeO content up to 28.5 wt%) from the SS and SU ones. On the base of the FeO vs. SiO_2 content, SS Bt plot into two distinct fields: a first one is characterized by a lower Fe/Si ratio, and a second one, is described by an higher Fe content. Both of them are representative for Bt from gabbros to monzonites. SU Bt composition, whose iron content range from 10.0 to 11.4 wt%, fall within the second compositional spectrum (Fig. 12).

Plagioclase (Fig. 11; Table A4.6) is a common phase in all PIC rocks, often characterized by oscillatory zoning. In SS samples, Pl shows a compositional range of An_{81-56} in clinopyroxenites, An_{78-49} in monzogabbros, An_{50-43} in monzonites, down to An_7 in syenites. In the SU series, the average composition is about An_{48-29} in monzogabbros and monzonites. Orthoclase content in more differentiated lithotypes generally reaches values up to about 7%. Kfs (Fig. 11; Table A4.7), one of the main phases that characterize GU granites and

syenogranites, has an almost negligible albite content, as the orthoclase term increases up to 90%.
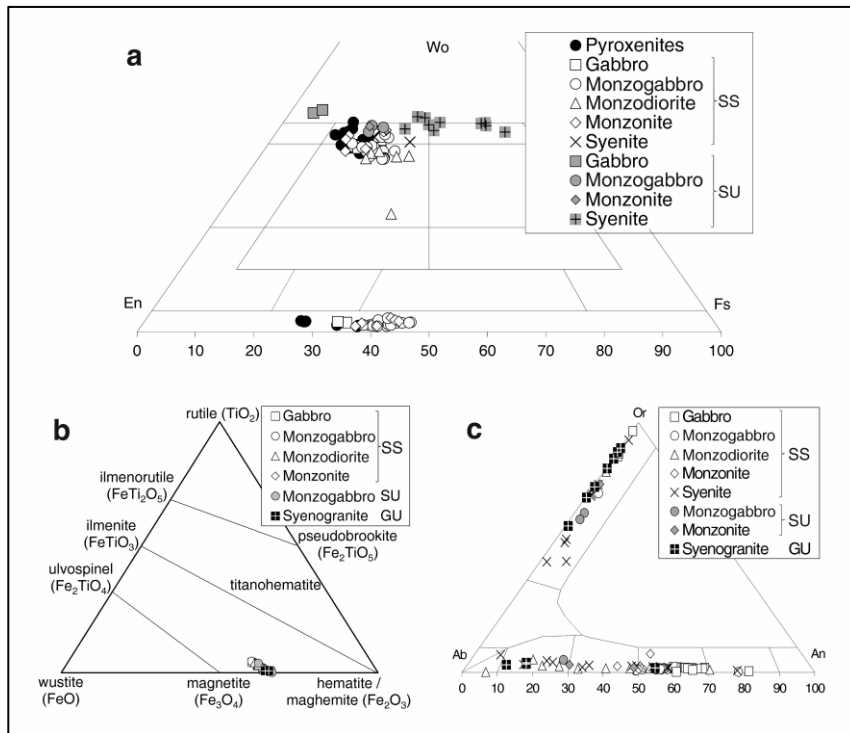
Fig. 11. (a) Pyroxene, (b) magnetite, and (c) feldspar classification diagrams showing the mineral phases composition of PIC lithotypes.
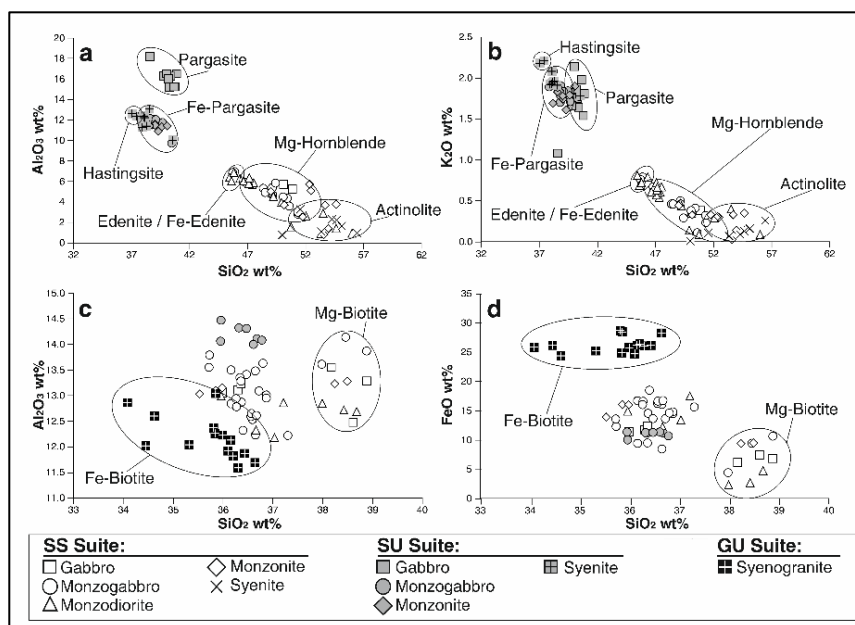
Fig. 12. (a) Al_2O_3 vs. SiO_2 and (b) K_2O vs. SiO_2 diagrams for Shoshonitic Silica Saturated and Shoshonitic Silica Undersaturated amphiboles. (c) Al_2O_3 vs. SiO_2 and (d) FeO vs. SiO_2 diagrams for Shoshonitic Silica Saturated, Shoshonitic Silica Undersaturated and Granitic Unit biotite. Field labels are based on amphibole and biotite classification from Leake et al. (1997) and Dymek (1983), respectively.

3.5. FC processes in the magma chamber

Petersen *et al.* (1980), Gasparotto & Simboli (1991), and Bonadiman *et al.* (1994) hypothesized the derivation of the intrusive rocks of the Dolomites from a monzogabbroic magma that mainly experienced fractional crystallization (FC) processes in an almost closed system, with subsequent generation of Cpx cumulates. PIC is the only multi-pulse intrusion of the Dolomitic Area in which more than one geochemical suite can be identified. Thus, major/trace element whole rock compositions, as well as major element mineral chemistry, were used for develop a mass balance calculation for modelling the main differentiation trends for the geochemical suites of the PIC (SS, GU and SU). This model is typically applied to effusive rocks. However, in closed system crystallization, assuming equilibrium conditions, intrusive rocks are able to resemble the differentiation trend of magmatic liquids. According to the previous studies on this area (Petersen *et al.*, 1980; Gasparotto & Simboli, 1991; Bonadiman *et al.*, 1994) and on the petrographic features above mentioned, PIC rocks crystallization occurred in closed system-like conditions, making it possible to model their genesis via "simple" FC processes. This statement is also strengthen by the comparison with the very similar composition of basaltic and hypabyssal rocks outcropping in the area.

Aim of our model is to better constrain the genetic relationships between the various lithotypes. In this respect, for example, the link between clinopyroxenites and gabbros or monzogabbros of both SS and SU series is not well defined. Thus, two FC models were developed, for both SS and SU suites. FC calculations have been firstly attempted by using MELTS and Rhyolite-MELTS software: however, being the SS and SU magmatic suites enriched in Amp and Bt, no reliable results have been produced. In fact, application of such software to magmas fractionating under wet conditions is limited by the lack of appropriate thermodynamic models for hydrous mafic silicates, particularly Amp and Bt (Gualda *et al.*, 2012). As a consequence, least squares mass balance calculations have been computed to simulate the FC processes that generated the PIC.

Monzogabbros were taken as starting material, while the final products were syenites. Accuracy on the major element mass balance model has been evaluated by means of the least squares error (r^2) between natural and calculated compositions. Trace element distribution in the calculated compositions was obtained using the partition coefficients (Kd) extracted by the GERM Database (earthref.org/KDD, Table 1) and using the formulation of Shaw (1970) for Rayleigh fractionation, $C_L = C_0 \times F^{(D-1)}$, where: C_0 is the amount of the chosen element in the starting (natural) magma; C_L the amount of trace element calculated in the arrival magma; F the residual melt percentage; D the partition coefficients weighted for the percentage of fractionated minerals obtained by the mass balance calculation.

3.5.1. SS series

Monzogabbro FC43B was chosen as the nearest composition to a primary magma for this series (Table 2) for its low SiO_2 and high mg#, Ni and Co amounts.

The first step towards the more differentiated monzogabbro EM53 (Fig. 13) accounts for the removal of 54% of a solid assemblage (SA1SS, $r^2 = 0.89$) made up of Ol (8.3%), Opx (5.1%), Cpx (21.3%), Pl (49.4%), Ap (2.3%), Mag (3.5%) and Bt (10.1%) with an overall gabbroic composition. The errors in the model for most of the trace elements are lower than 2% (Table 2), except for Th and La, due to their low concentrations in the primary sample. The second stage from monzogabbro EM53 to monzonite EM85 is modelled by removing 73% of a monzogabbroic assemblage (SA2SS, $r^2 = 0.68$), constituted by Kfs (6.2%), Amp (0.7%), Cpx (17.6%), Pl (52.2%), Ap (1.4%), Mag (5.3%) and Bt (16.6%), with errors on trace element contents lower than 14%. The last step from monzonite EM85 to syenite EM110 is derived by removal of 47% of a solid assemblage (SA3SS, $r^2 = 0.26$) of Kfs (16.3%), Amp (2.6%), Cpx (12.1%), Pl (41.9%), Ap (1.1%), Mag (4.1%), Bt (10.5%), Qz (10.6%), and Zrn (0.8%), with monzodioritic composition. Having Qz and Zrn the same effect on SiO_2 balance, Zrn modal fractionation (0.8%) was calculated based on Zr trace element modelling. Trace element composition of theoretical melt match very well with that of the natural magma, resulting in an error lower than 2% for all the elements except for Th (20%), due to its low concentration in the syenitic sample (9 ppm), and La (16%). Syenite is the result of 94% fractionation (Fig. 13) corresponding to a solid residuum made up of gabbroic to monzogabbroic and monzodioritic lithotypes. The compositions calculated for the three solid assemblages (Fig. 8, Fig. 10 and Fig. 13) are similar to those of natural clinopyroxenitic and gabbroic to monzodioritic lithotypes found within the SS suite, lending further support to the theoretical results.

Moreover, several FC modelling attempts have been made to find a link between the SS suite and the GU granites and syenogranites. However, the mass balance calculation did not explain the genesis of the GU rocks via simple FC trends belonging to the SS suite.

3.5.2. SU series

The parent magma chosen as starting point for the modelling of the fractionation of this suite (Table 3) was the *nph*-normative monzogabbro EM10, characterized by high mg#, Ni and Co amounts (Fig. 13). Monzogabbro EM10 can reach the monzonite EM7 by 63% fractionation of a solid assemblage (SA1SU, $r^2 = 0.98$), constituted by Kfs (4.7%), Amp (12.2%), Cpx (27.5%), Pl (35.9%), Ap (1.7%), Mag (11.0%) and Bt (7.0%), with gabbroic

composition. The trace element (Rb, Ba, Th, Nb, La, Ce, Pb, Sr, Nd, Zr and Y) distribution for this first step has an errors < 4%. The second stage from monzonite EM7 to syenite 11* can be modelled by removal of 44% of a monzodioritic assemblage (SA2SU, r^2 = 0.73) constituted by Kfs (32.1%), Amp (14.6%), Pl (44.2%), Ap (2.4%), Mag (4.1%) and Bt (2.6%). Trace element distribution errors are <1%, except for Pb and Th, whose errors are respectively 14% and 23%, being this latter due to the high amount of Th in the more differentiated rock. SU Syenite is the result of 79% fractionation corresponding to a solid residuum made up of gabbroic to monzodioritic rocks (Fig. 13), that fits well with the compositional spectrum of the similar lithotypes found within this portion of the complex, as highlighted also by the variation diagrams of Fig. 8 and Fig. 10.
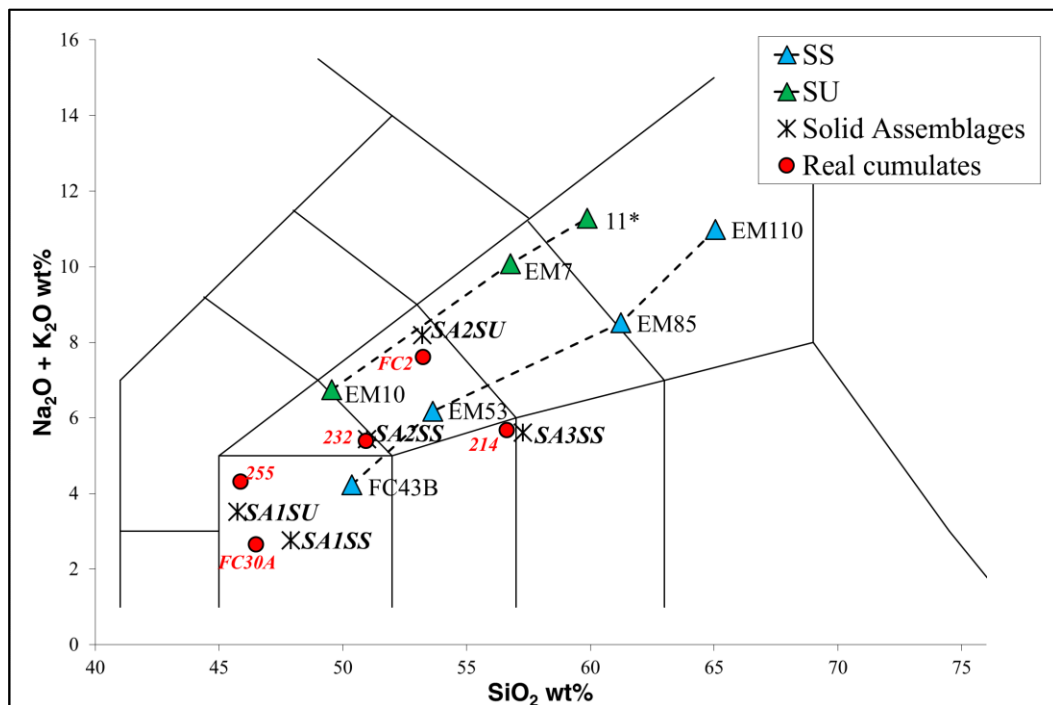
Fig. 13. Total alkali vs. silica (TAS) classification diagram (Le Maitre et al., 1989) illustrating the fractional crystallization modelling of selected PIC rock samples, as well as the compositions of the cumulate assemblages calculated from the model compared to the natural cumulate lithotypes. SA1SS: Gabbroic Solid Assemblage 1 with SS affinity; SA2SS: Monzogabbroic Solid Assemblage 2 with SS affinity; SA3SS: Monzodioritic Solid Assemblage 3 with SS affinity; SA1SU: Gabbroic Solid Assemblage 1 with SU affinity; SA2SU: Monzodioritic Solid Assemblage 2 with SU affinity.

Table 1. Trace elements partition coefficients (Kd) used in the FC model for the SS and SU suites. Values and references extracted by the GERM Database (earthref.org/KDD).

SS SUITE											
STEP 1	**Kfs**	**Ol**	**Amp**	**Opx**	**Cpx**	**Pl**	**Ap**	**Mag**	**Bt**	**Qz**	**Zrn**
Rb	-	0.000179	-	0.0004	$8*10^{-5}$	0.008	-	0.011	-	-	-
Ba	-	0.05	-	0.0003	0.14	0.39	0.05	0.028	0.03	-	-
Th	-	$2.4*10^{-6}$	-	0.0002	0.00026	0.004	-	0.05	0.0014	-	-
Nb	-	$7*10^{-5}$	-	0.0001	1.24	1.3	-	1.8	0.088	-	-
La	-	0.03	-	0.0001	0.77	0.3017	21.7	0.45	0.7	-	-
Ce	-	0.01	-	0.005	0.53	0.167	11.2	0.016	-	-	-
Pb	-	0.0001	-	0.0001	0.008	0.94	-	0.38	0.1	-	-
Sr	-	0.00019	-	0.0001	0.56	2.48	1.3	0.11	0.7	-	-
Zr	-	0.00068	-	0.0005	0.16	0.0009	0.636	0.02	0.017	-	-
Y	-	0.009	-	0.003	0.245	0.16	-	0.0039	0.018	-	-
STEP 2	**Kfs**	**Ol**	**Amp**	**Opx**	**Cpx**	**Pl**	**Ap**	**Mag**	**Bt**	**Qz**	**Zrn**
Rb	0.11	-	0.0077	-	$8*10^{-5}$	0.008	-	0.011	1.52	-	-
Ba	-	-	0.044	-	0.00011	0.1	0.05	0.4	5.35	-	-
Th	0.02	-	0.5	-	0.29	0.19	17.1	0.42	0.31	-	-
Nb	-	-	0.006	-	0.0008	0.002	-	0.01	0.088	-	-
La	0.08	-	0.54	-	0.19	0.28	4.4	0.29	0.318	-	-
Ce	-	-	0.094	-	0.04	0.241	48	0.35	0.377	-	-
Pb	0.98	-	0.53	-	0.32	1.3	-	0.38	0.89	-	-
Sr	3.87	-	0.01	-	0.02	1.8	1.4	0.53	0.363	-	-
Zr	0.003	-	1.79	-	0.95	0.55	0.906	0.38	0.59	-	-
Y	0.5	-	0.4	-	3.28	0.51	-	0.84	0.6	-	-
STEP 3	**Kfs**	**Ol**	**Amp**	**Opx**	**Cpx**	**Pl**	**Ap**	**Mag**	**Bt**	**Qz**	**Zrn**
Rb	2.4	-	1	-	0.15	0.97	0.4	0.043	3.5	-	-
Ba	1.07	-	0.07	-	0.05	1.2	0.45	0.4	4.04	-	-
Th	0.3	-	0.45	-	3.44	0.382	41	13.1	2	-	22.1
Nb	3.4	-	1.25	-	0.03	0.88	-	-	4.6	-	-
La	0.026	-	2.06	-	21.7	0.0007	23.5	0.0029	0.76	-	1.4
Ce	0.02	-	0.094	-	0.044	0.15	52.5	26	11	-	23.5
Pb	1.37	-	0.53	-	0.13	0.4	0.03	2.9	0.1	-	7.5
Sr	6.7	-	3.56	-	0.0432	0.94	8	0.01	0.29	-	-
Zr	0.003	-	0.8	-	0.02	0.0009	0.636	0.02	0.09	-	-
Y	0.017	-	0.4	-	0.66	0.21	162	0.95	1.4	-	71.4

Table 1. (continued)

SU SUITE										
STEP 1	Kfs		Amp		Cpx	Pl	Ap	Mag	Bt	
Rb	0.659		0.58		0.3	0.3	0.4	0.15	2.48	
Ba	-		0.6		0.15	0.56	0.3	0.12	3.68	
Th	-		0.5		0.23	0.05	17.1	0.42	0.12	
Nb	-		0.8		2.1	0.008	-	0.7	0.088	
La	-		0.7219		0.77	0.49	21.7	0.45	0.7	
Ce	-		0.98		1.31	0.57	52.5	0.42	0.377	
Pb	-		0.12		0.008	2.453	-	2.9	0.1	
Sr	-		0.188		0.5	3.2	1.3	0.11	0.7	
Zr	-		0.127		1.53	0.27	0.636	1.78	0.017	
Y	-		11.3		1.05	0.1	-	0.64	0.018	
STEP 2	Kfs		Amp		Cpx	Pl	Ap	Mag	Bt	
Rb	1.57		5.58		-	0.17	0.4	0.01	0.936	
Ba	9.7		0.07		-	3.4	0.45	0.1	52	
Th	0.007		0.06		-	0.001	-	0.01	0.03	
Nb	0.16		4		-	2.5	-	-	4	
La	0.1		2.06		-	0.23	27	29.6	15.1	
Ce	0.06		4.23		-	0.34	31	9.7	4	
Pb	4.1		9.77		-	2.2	-	1.3	2.1	
Sr	7.3		0.01		-	10.89	8	0.01	0.2	
Zr	0.003		0.047		-	0.0009	0.636	0.02	0.09	
Y	0.017		4		-	0.022	-	3.21	1	
Rb	Philpotts & Schnetzler (1970); Nagasawa & Schnetzler (1971); Hart & Brooks (1974); Ronov & Yaroshevskiy (1976); Matsui *et al.* (1977); Nash & Crecraft (1985); Villemant (1988); Mahood & Stimac (1990); McKenzie & O'Nions (1991); Green *et al.* (1993); Dunn & Sen (1994); Ewart & Griffin (1994); Latourrette *et al.* (1995); Bindeman *et al.* (1998); Marks *et al.* (2004); Adam & Green (2006)									
Ba	Nagasawa & Schnetzler (1971); Ewart *et al.* (1973); Paster *et al.* (1974); Drake & Weill (1975); Okamoto (1979); Luhr & Carmichael (1980); Mahood & Hildreth (1983); Villemant (1988); Mahood & Stimac (1990); Beattie (1993); Green *et al.* (1993); Ewart & Griffin (1994); Skulski *et al.* (1994); Latourrette *et al.* (1995); Schmidt *et al.* (1999); Marks *et al.* (2004); Adam & Green (2006)									
Th	Matsui *et al.* (1977); Larsen (1979); Luhr & Carmichael (1980); Villemant *et al.* (1981); Dostal *et al.* (1983); Mahood & Hildreth (1983); Luhr *et al.* (1984); Nash & Crecraft (1985); Bacon & Druitt (1988); Villemant (1988); Mahood & Stimac (1990); Stix & Gorton (1990); McKenzie & O'Nions (1991); Beattie (1993); Bea *et al.* (1994); Dunn & Sen (1994); Ewart & Griffin (1994); Latourrette *et al.* (1995); Salters & Longhi (1999); Wood & Trigila (2001); Marks *et al.* (2004); Adam & Green (2006)									
Nb	Haskin *et al.* (1966); Nash & Crecraft (1985); McKenzie & O'Nions (1991); Nielsen (1992); Dalpe & Baker (1994); Dunn & Sen (1994); Ewart & Griffin (1994); Latourrette *et al.* (1995); Bindeman *et al.* (1998); Green *et al.* (2000); Johnson & Schwab (2004); Marks *et al.* (2004); Adam & Green (2006)									
La	Dudas *et al.* (1971); Matsui *et al.* (1977); Luhr & Carmichael (1980); Watson (1980); Villemant *et al.* (1981); Mahood & Hildreth (1983); Fujimaki *et al.* (1984); Luhr *et al.* (1984); Nash & Crecraft (1985); Villemant (1988); Mahood & Stimac (1990); Stix & Gorton (1990); Nielsen *et al.* (1992); Wood & Trigila (2001); Marks *et al.* (2004); Adam & Green (2006)									
Ce	Nagasawa (1970); Schnetzler & Philpotts (1970); Nagasawa (1973); Paster *et al.* (1974); Matsui *et al.* (1977); Luhr & Carmichael (1980); Reid (1983); Mahood & Hildreth (1983); Fujimaki *et al.* (1984); Luhr *et al.* (1984); Nash & Crecraft (1985); Lemarchand *et al.* (1987); Mahood & Stimac (1990); Stix & Gorton (1990); Bindeman & Davis (2000); Sisson (1994); Salters & Longhi (1999); Wood & Trigila (2001)									
Pb	Leeman (1979); Nash & Crecraft (1985); McKenzie & O'Nions (1991); Bea *et al.* (1994); Dunn & Sen (1994); Ewart & Griffin (1994); Brenan *et al*. (1995); Latourrette *et al.* (1995); Marks *et al.* (2004); Adam & Green (2006); Aignertorres *et al.* (2007)									
Sr	Philpotts & Schnetzler (1970); Nagasawa (1973); Villemant *et al.* (1981); Watson & Green (1981); Nash & Crecraft (1985); Bacon & Druitt (1988); Villemant (1988); Mahood & Stimac (1990); McKenzie & O'Nions (1991); Dunn & Sen (1994); Ewart & Griffin (1994); Vannucci *et al.* (1998); Marks *et al.* (2004); Adam & Green (2006)									
Zr	Larsen (1979); Villemant *et al.* (1981); Fujimaki *et al.* (1984); Fujimaki (1986); Villemant (1988); Nielsen (1992); Kennedy *et al.* (1993); Dunn & Sen (1994); Ewart & Griffin (1994); Latourrette *et al.* (1995); Marks *et al.* (2004); Adam & Green (2006)									
Y	Larsen (1979); Ronov & Yaroshevskiy (1976); Nash & Crecraft (1985); Nielsen *et al.* (1992); Green *et al.* (1993); Bea *et al.* (1994); Ewart & Griffin (1994); Hack *et al.* (1994); Latourrette *et al.* (1995); Sobolev *et al.* (1996); Nikogosian & Sobolev (1997); Wood & Trigila (2001); Adam & Green (2006)									

Table 2. Mass balance calculation and FC modelling for SS suite.

	STEP 1	r² =	0.89		STEP 2	r² =	0.68		STEP 3	r² =	0.26	
	FROM	TO	S.A.	NATURAL	FROM	TO	S.A.	NATURAL	FROM	TO	S.A.	NATURAL
	Mzgb	Mzgb	Gb	Gb	Mzgb	Mz	Mzgb	Mzgb	Mz	Sy	Mzdr	Mzdr
% Oxides	FC43B	EM53	SA1SS	FC30A	EM53	EM85	SA2SS	232	EM85	EM110	SA3SS	214
SiO$_2$	50.44	53.71	47.89	46.66	53.71	61.28	50.98	51.10	61.28	65.08	57.27	56.77
TiO$_2$	1.09	0.84	0.72	1.10	0.84	0.70	0.95	1.46	0.70	0.57	0.77	0.78
Al$_2$O$_3$	16.59	17.46	16.10	16.51	17.46	17.06	17.57	17.76	17.06	17.45	16.74	18.94
FeOtot	9.87	8.59	10.96	11.29	8.59	5.22	9.78	10.06	5.22	2.92	7.82	7.15
MgO	6.15	4.12	8.05	8.01	4.12	2.29	4.83	5.79	2.29	1.20	3.49	2.78
CaO	10.63	8.45	12.53	13.71	8.45	4.56	9.80	7.82	4.56	1.67	7.83	7.45
Na$_2$O	2.35	2.77	1.81	0.85	2.77	2.86	2.91	2.53	2.86	2.63	2.88	2.12
K$_2$O	1.89	3.42	0.94	1.81	3.42	5.66	2.53	2.87	5.66	8.36	2.73	3.56
P$_2$O$_5$	0.77	0.49	0.97	0.06	0.49	0.26	0.62	0.60	0.26	0.07	0.46	0.45
tot	100	100	100	100	100	100	100	100	100	100	100	100
	SA1SS (Gb)				SA2SS (Mzgb)				SA3SS (Mzdr)			
Kfs	0.00	0.00			4.55	6.24			7.75	16.32		
Ol	4.54	8.33			0.00	0.00			0.00	0.00		
Amp	0.00	0.00			0.49	0.67			1.26	2.65		
Opx	2.76	5.07			0.00	0.00			0.00	0.00		
Cpx	11.61	21.31			12.80	17.57			5.73	12.07		
Pl	26.90	49.38			38.03	52.19			19.90	41.90		
Ap	1.24	2.28			1.01	1.39			0.51	1.07		
Mag	1.92	3.52			3.89	5.34			1.93	4.06		
Bt	5.50	10.10			12.10	16.60			5.00	10.53		
Qz	0.00	0.00			0.00	0.00			5.05	10.63		
Zrn	0.00	0.00			0.00	0.00			0.36	0.76		
tot	54.47	100.00			72.87	100.00			47.49	100.00		
	C$_0$	C$_L$ nat.	C$_L$ calc.	Err %	C$_0$	C$_L$ nat.	C$_L$ calc.	Err %	C$_0$	C$_L$ nat.	C$_L$ calc.	Err %
Rb	51	114	111	-2.32	114	301	304	0.94	301	260	262	0.86
Ba	275	504	504	-0.09	504	530	530	0.07	530	481	487	1.16
Th	3	12	7	-41.43	12	21	24	13.26	21	9	11	20.08
Nb	8	8	8	1.69	8	31	29	-6.27	31	24	24	0.10
La	16	14	17	24.01	14	32	34	6.63	32	8	9	15.90
Ce	39	60	60	0.29	60	70	70	0.32	70	19	19	-0.05
Pb	16	24	24	0.05	24	26	27	1.55	26	34	34	0.11
Sr	1140	801	801	0.00	801	554	547	-1.32	554	350	352	0.62
Zr	75	160	161	0.36	160	270	271	0.21	270	507	504	-0.55
Y	14	28	28	0.25	28	24	27	13.85	24	8	8	0.75

Gb: gabbro; Mzgb: monzogabbro; Mzdr: monzodiorite; Mz: monzonite; Sy: syenite

S.A.: subtracted solid assemblage; NATURAL: sampled PIC lithotype; r²: least squares error

C$_0$: trace element starting concentration; C$_L$ nat.: trace element arrive natural concentration

C$_L$ calc.: trace element arrive calculated concentration; Err %: percentage of error

Table 3. Mass balance calculation FC modelling for SU suite.

	STEP 1	$r^2 =$	0.98		STEP 2	$r^2 =$	0.73	
	FROM	TO	S.A.	NATURAL	FROM	TO	S.A.	NATURAL
	Mzgb	Mz	Gb	Gb	Mz	Sy	Mzdr	Mzdr
% Oxides	EM10	EM7	SA1SU	255	EM7	11*	SA2SU	FC2
SiO_2	49.90	56.81	45.76	46.00	56.81	59.90	53.22	53.51
TiO_2	0.93	0.59	1.10	0.87	0.59	0.38	0.25	1.16
Al_2O_3	17.93	21.42	15.86	21.07	21.42	21.77	21.24	16.38
FeOtot	10.12	4.11	13.65	9.82	4.11	2.98	5.57	7.31
MgO	4.98	1.39	6.98	6.19	1.39	0.42	2.80	5.14
CaO	9.57	5.11	12.36	11.65	5.11	2.90	7.70	8.51
Na_2O	2.82	5.22	1.73	0.37	5.22	6.31	3.56	5.13
K_2O	2.81	4.86	1.80	3.95	4.86	4.98	4.63	2.52
P_2O_5	0.76	0.25	0.73	0.07	0.25	0.06	1.01	0.33
tot	100	100	100	100	100	100	100	100
	SA1SU (Gb)				SA2SU (Mzdr)			
Kfs	2.98	4.76			14.15	32.12		
Amp	7.65	12.23			6.44	14.62		
Cpx	17.20	27.49			0.00	0.00		
Pl	22.43	35.85			19.49	44.25		
Ap	1.06	1.69			1.04	2.36		
Mag	6.85	10.95			1.79	4.06		
Bt	4.39	7.02			1.14	2.59		
tot	62.56	100.00			44.05	100.00		
	C_0	C_L nat.	C_L calc.	Err %	C_0	C_L nat.	C_L calc.	Err %
Rb	95	188	188	-0.10	188	234	233	-0.38
Ba	459	853	852	-0.10	853	329	329	0.00
Th	23	44	46	3.54	44	102	79	-22.90
Nb	15	26	25	-3.46	26	29	29	-0.07
La	78	113	117	3.35	113	102	102	0.11
Ce	179	171	174	1.64	171	182	182	0.22
Pb	69	88	87	-1.11	88	52	59	13.67
Sr	1054	1194	1197	0.28	1194	325	325	-0.06
Zr	160	269	271	0.82	269	477	481	0.79
Y	36	31	32	4.02	31	46	46	-0.57
Gb: gabbro; Mzgb: monzogabbro; Mzdr: monzodiorite; Mz: monzonite; Sy: syenite								
S.A.: subtracted solid assemblage; NATURAL: sampled PIC lithotype; r^2: least squares error								
C_0: trace element starting concentration; C_L nat.: trace element arrive natural concentration								
C_L calc.: trace element arrive calculated concentration; Err %: percentage of error								

3.6. Discussion

Whole rock major and trace element composition, as well as mineral chemistry and detailed field surveys, allowed to discriminate between the three magmatic suites that compose the PIC, after a re-evaluation of the petrogenetic subdivision proposed by Visonà (1997) and Marrocchino *et al.* (2002). All the three suites, namely SS, SU and GU are characterized marked Nb and Ti negative anomalies and a high positive Pb anomaly. Modal abundance of Bt, Amp and Kfs, as well as late Mag crystallization, leading to the lack of a Fe-Ti enrichment trend, support the by K-affinity of the magmas, typical of the shoshonitic series from active continental margins (Ewart, 1982). The progressive differentiation trend for both SS and SU series is marked by the appearance of a significant Eu negative anomaly,

particularly in the more evolved syenites. On the other side, SU suite is characterized by lower K/Na ratios, as well as by higher HFSE and LREE content than SS and GU. Amp, absent in GU lithotypes, is markedly enriched in Al_2O_3, Na_2O and K_2O in the SU with respect to the SS suite, while iron-rich Bt is a peculiar feature of GU rocks. All these features lead to speculate about the belonging of the SU suite to a magma pulse different to that of the SS one, likely related to spatial and/or temporal heterogeneities of their sources.

By means of this discrimination, mass balance calculations have been developed for both SS and SU series in order to model the FC processes in an almost closed system (Petersen *et al.*, 1980; Gasparotto & Simboli, 1991; Bonadiman *et al.*, 1994) responsible for the genesis of all PIC lithotypes (Fig. 8, Fig. 10 and Fig. 13). The calculated subtracted solids are quite similar in composition to the natural pyroxenitic and gabbroic to monzodioritic samples found within the complex, further supporting the accuracy of the model and suggesting that FC is the main differentiation process controlling the magmatic evolution. Still unsolved remains the relationship between the GU granites and syenogranites and the SS-SU suites, because of the independent geochemical behaviour of the formers. The alkali and silica content of the GU body, together with a marked Eu negative anomaly, may indicate a differentiation from a silica-oversaturated series, but the lack of any differentiated volcanic rock with similar features in the area surrounding PIC, as well as of any petrological relationships with the intrusive rocks of the complex, does not allow to put forward a robust cogenetic mechanism. Visonà (1997) proposed the existence of a calc-alkaline and/or oversaturated trend able to generate the granites and syenogranites. However, several attempts to reconstruct the geochemical features of the GU lithotypes via FC processes from the SS suite have been unsuccessful. It has also to be noted that no rhyolitic products are found within the volcanics, thus, contrary of what occurs for the other two series, there would not be a correspondence between GU and its effusive counterpart.

Together with the petrological distinction of the three suites, an accurate study of the field relationships of the intrusive portions, the volcanics, and the dyke swarm outlines a detailed PIC temporal evolution (Fig. 14) and defines the relationships with the effusive portions of the complex.
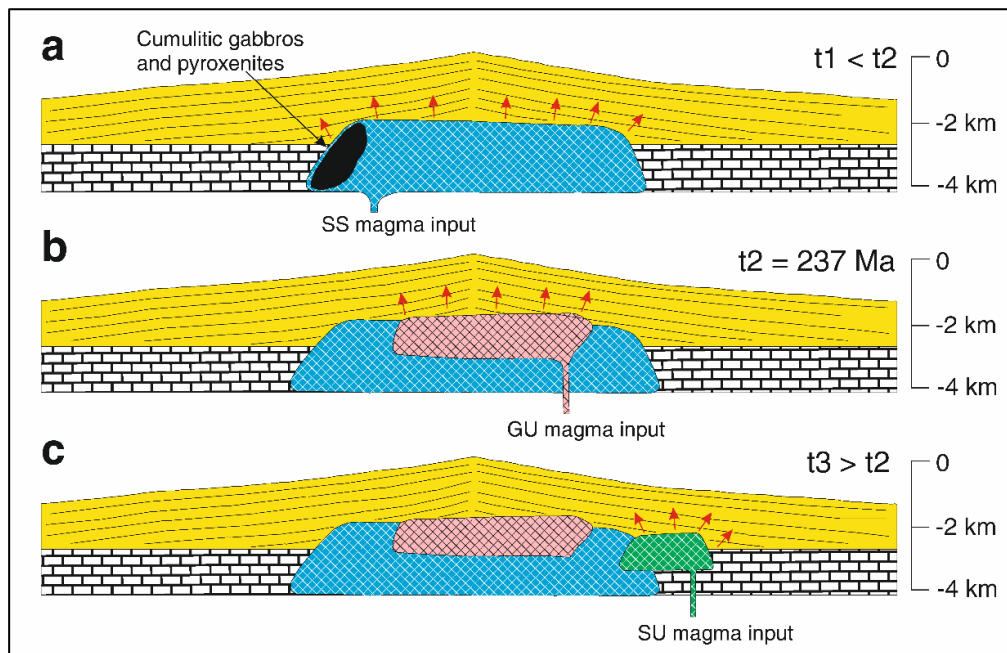
Fig. 14. Interpretative sketch of the evolutionary sequence of rocks from the Predazzo Intrusive Complex. The first pulse at t1 (a) is characterized by Shoshonitic Silica Saturated affinity; the second pulse at t2 (b) is represented by the intrusion of the Granitic Unit granites and syenogranites; the final pulse at t3 (c), outcropping in the eastern part of the complex, is constituted by Shoshonitic Silica Undersaturated terms. t2 (237 Ma) is from Mundil et al. (1996). The cumulitic gabbros and pyroxenites are also shown at the border of the Shoshonitic Silica Saturated intrusion.

According to our findings, PIC evolution is characterized by the emplacement of three magma batches with different petrological affinities in a relatively short time. The first most voluminous SS pulse (3.1 km^3) was emplaced as what nowadays appears as an external ring. It was followed by the GU intrusion (1.1 km^3) in the central part of the complex, and then by the alkaline SU batch (0.3 km^3) in the eastern portion of the PIC. From field survey and volume estimates, it is evident that the SU series represents a minor contribution to the whole PIC: it likely constitutes the ultimate melt produced in the vanishing stage of the magmatic intrusion. During this last stage, several undersaturated dykes intruded the SS and GU lithotypes, indirectly constraining the temporal relationships between the three intrusive bodies by means of these cross-cutting relationships.

The presence of a fourth silica-oversaturated suite, identified by Visonà (1997) and Marrocchino *et al.* (2002) has been furthermore ruled out because of the paucity of oversaturated rocks scattered within the PIC, and of the overlap of their petrographic and geochemical features with the SS suite, in case of both whole rock and mineral chemistry. The origin of such rocks, whose Qz modal content lies between 4 and 15%, could be instead explained by the last stage of the FC processes for the SS suite (Fig. 13). In this, the genesis of a SS syenite from a monzonitic material results by the removal of a monzodioritic solid

assemblage with up to 11% Qz content (Table 2), that is close to the natural monzodiorites defined as 'oversaturated' by Visonà (1997) and Marrocchino *et al.* (2002). This evidence suggests that the rare oversaturated rocks in PIC are fractionation products of the SS suite, making unlikely the existence of an independent oversaturated suite from which the GU lithotypes could have been derived.

The extended fieldwork along the contact between the PIC and the surrounding volcanites provided also important constraints about the so-called 'Predazzo caldera' definition, introduced by Leonardi (1968), Castellarin *et al.* (1982), Doglioni (1984) and Gianolla *et al.* (2010) to take somehow into account the ring-shape of the PIC. In this context the transitional magmatic contact between the volcanics and the SS lithotypes (Fig. 3) that has been found on both the eastern and western part of the complex, as well as the lack of evolved caldera-filling materials, casts some doubts on the existence of a structure of this type.

3.7. Conclusions

Within the Dolomitic Area, the Predazzo magmatic complex is the most developed volcano-plutonic centre, being characterized by a 6 km^3 of volcanites surrounding 4.5 km^3 of intrusive rocks (PIC). This area is an entirely preserved magmatic complex, in which the relationships between the intrusion, the dyke swarm, the host rocks and the volcanic products are exposed onto the surface, making it a perfect petrographic and petrological laboratory. Moreover, the PIC multi-pulse nature and high petrological variability point out its key role in constraining the main features of the Triassic magmatism in the Dolomites and in the whole Southern Alps domain. The combination of field, petrographic and petrological studies leads to the following considerations:

1. The K-affinity, the marked Nb and Ti negative anomalies, as well as the widespread occurrence of Amp and Bt in almost all PIC rocks, indicate a relationship with the shoshonitic series from active continental margins, suggesting the presence of a subduction setting in the Southern Alps domain, as already hypothesized by Zanetti *et al.* (2013). However, the model of mixing between mantle-derived basic and crustal-derived acid magmas put forward by Sinigoi *et al.* (2011; 2016) for the Ivrea-Verbano magmatic complex and the related upper crustal section leaves the question still unanswered.

2. The PIC is a multi-pulse body, dominated by three main magmatic suites (SS, GU and SU), characterized by different HFSE and LREE contents, as well as by peculiar mineral assemblages, where Amp and Bt are a clear distinctive feature.

3. SS and SU differentiation trends explain the occurrence of cumulitic gabbros and pyroxenites within the complex, as well as the scattered presence of silica oversaturated lithotypes. The origin and nature of the GU suite remains uncertain, because of the absence of similar effusive products in the surrounding area and due to the impossibility to model the genesis of granites and syenogranites via simple FC process for the SS suite. Further studies are under way to investigate the relationships between such rocks, the PIC intrusive and effusive products.

4. The magmatic transitional contact identified between the PIC and the volcanites, as well as the lack of 'caldera-filling'-like materials, lead to exclude the presence of a calderic collapse structure in the area, invoked by several authors to explain the ring-shape of the complex. By means of these considerations, the outcropping relationships between the PIC, the volcanic products, and the host rocks have to be considered in a different light. Such a finding will constitute a fundamental starting point to develop future accurate models on the magma chamber emplacement history and timing, in one of the few worldwide examples of an entirely preserved and 'frozen' volcano-plutonic system.

Chapter 4

The Predazzo Intrusive Complex (PIC): thermobarometry, oxybarometry, hygrometry, and AFC modeling

Chapter 4. The Predazzo Intrusive Complex (PIC): thermobarometry, oxybarometry, hygrometry, and AFC modeling

4.1. Introduction

The Middle Triassic magmatic event in the Southern Alps is expressed in volcano-plutonic sequences outcropping from the Brescian Alps, Alto Vicentino, Dolomites and Carnia areas (Italy) to the Karawanken region (Austria). Most of the igneous products are volcanic and volcanoclastic rocks, with subordinated dyke swarms. Intrusive bodies are instead rare, and mainly located in the Dolomites (Predazzo-Mt. Monzoni-Cima Pape) and Karawanken areas (Gasparotto & Simboli, 1991; Gianolla, 1992; Bonadiman *et al.*, 1994; Visonà & Zanferrari, 2000; Brack *et al.*, 2005; Cassinis *et al.*, 2008; Bellieni *et al.*, 2010). These intrusions represent snapshots of magmatic plumbing systems, emplaced during and/or immediately after the eruption of the overlying volcanic products. There are several outstanding geological problems regarding the nature of these complexes, mainly related to their emplacement conditions, and to the relationships between tectonics and magmatism. The Predazzo Intrusive Complex (PIC) represents the ideal "petrologic laboratory" for investigating and reconstructing the features of the Middle Triassic feeding systems, since it offers the possibility to constrain the theoretical and experimental modeling by means of field evidence.

As in the case of the nearby Mt. Monzoni, the contact aureole between PIC and the surrounding sedimentary rocks enabled many authors to speculate about the geometry of the intrusive body and its field relationships to the shallow crust (Princivalle *et al.*, 1999; Ferry *et al.*, 2002; Povoden *et al.*, 2002; Gallien *et al.*, 2007). On the basis of petrological and field evidence, three different magma batches constituting the PIC were identified (see Chapter 3), interpreted as a multi-pulse body of shoshonitic affinity with variable alkalies and H_2O-content which led to differentiation from mafic to amphibole and biotite-bearing end-members. However, several issues are still unsolved, such as the (possible) interaction between PIC magmas and crust, and their chemical/physical conditions of emplacement. The latter resulting in a current uncertainty about the depth of the intrusion.

Few thermobarometric and oxybarometric data are reported in literature for the Middle Triassic magmatic systems of the Dolomitic Area. According to Bonadiman *et al.* (1994), the oxygen fugacity of the nearby Mt. Monzoni system was around the NNO buffer and the crystallization temperature range was between 1044 and 589°C. Despite the clear evidence of a predominant role of water during crystallization, as testified by the wide presence of hydrous phases in the intrusive rocks, no estimates of the H_2O contents and *P-T* conditions

of these Middle Triassic plumbing systems have been performed so far. Taking into account the Al^{tot} content of amphiboles, Menegazzo Vitturi *et al.* (1995) hypothesized a depth of 10-17 km for PIC emplacement, but their values appeared in stark contrast with both the field evidence and the data reported by Visonà & Zanferrari (2000) for the similar and coheval Karawanken pluton (5-9 km).

Therefore, in this paper we made new geochemical and isotopic ($^{87}Sr/^{86}Sr$-$^{143}Nd/^{144}Nd$) measurements on new samples from PIC that are representative of its main portions. A multiple thermobarometric and hygrometric approach, based on the interaction between distinct single mineral, mineral pairs and mineral-melt equations, corroborated by appropriate simulations by means of Rhyolite-MELTS software (Gualda *et al.*, 2012), enabled us to: (i) provide for the first time *P-T-f*O_2 estimates and H_2O evaluation of PIC system over its entire evolution; (ii) verify if the depth of the intrusion obtained by the previous petrologic approaches well fit the field evidence. The resulting *P-T-f*O_2 and H_2O values, together with the isotopic signatures of PIC rocks were then used as input to (iii) quantify the role of assimilation and fractional crystallization processes in the generation of the main PIC magmatic suites.

4.2. Whole-rock geochemistry

4.2.1. Major and trace element

Shoshonitic Silica Saturated (SS) suite (Fig. 15 and Fig. 16; Table A4.1) is mainly constituted by monzogabbros and monzodiorites, with Mg# (calculated as Mg/[Mg+Fe^{2+}] mol%) of 65-45, and by subordinated monzonites and syenites (Mg# of 53-26 and 45-20 respectively) randomly distributed within the unit (Fig. 1). Volumetrically limited pyroxenitic (Mg# 64-47) and gabbroic (Mg# 65-45) cumulates crop out in the southwestern sector of the intrusion. Shoshonitic Silica Undersaturated (SU) suite (Fig. 15 and Fig. 16; Table A4.1) is on average more evolved than the SS one, being dominated by the presence of nepheline-normative monzonites (Mg# 40-39) and syenites (Mg# 36-15), over a minority composed of cumulitic gabbros (Mg# 56-50), monzogabbros (Mg# 59-47) and monzodiorites (Mg# 55-27). Granitic Unit (GU, Fig. 15 and Fig. 16) is composed of highly evolved granites and syenogranites (69-77 SiO_2 wt%, Table A4.1) that, according to Chappell and White (2001) discriminating criteria, are ascribable to the I-type granitoids (Al/[Na + K + Ca] < 1.1; low P_2O_5 wt%; decreasing Zr, Sr and Al_2O_3 wt% with increasing SiO_2 wt%). Few samples show instead intermediate behaviour between I- and S-type rocks.

All SS, SU and GU rocks have K-affinity (Fig. 16), and their K_2O and SiO_2 contents led to classify them as belonging to shoshonitic (SS and SU) and high-K calc-alkaline (GU) series. Despite the general similarities, the major and trace element distribution in the SS, SU and GU rocks made it possible to pinpoint their origin from independent magmatic batches. At comparable differentiation degrees, main discriminating features between the SS and SU rocks are the relative enrichment in HFSE (Th, U, Pb), LREE and the higher Na_2O/K_2O ratio of the latters. Such differences are in accordance with the predominant presence of amphibole and other Na and REE-rich phases in the SU rocks (see Chapter 3).
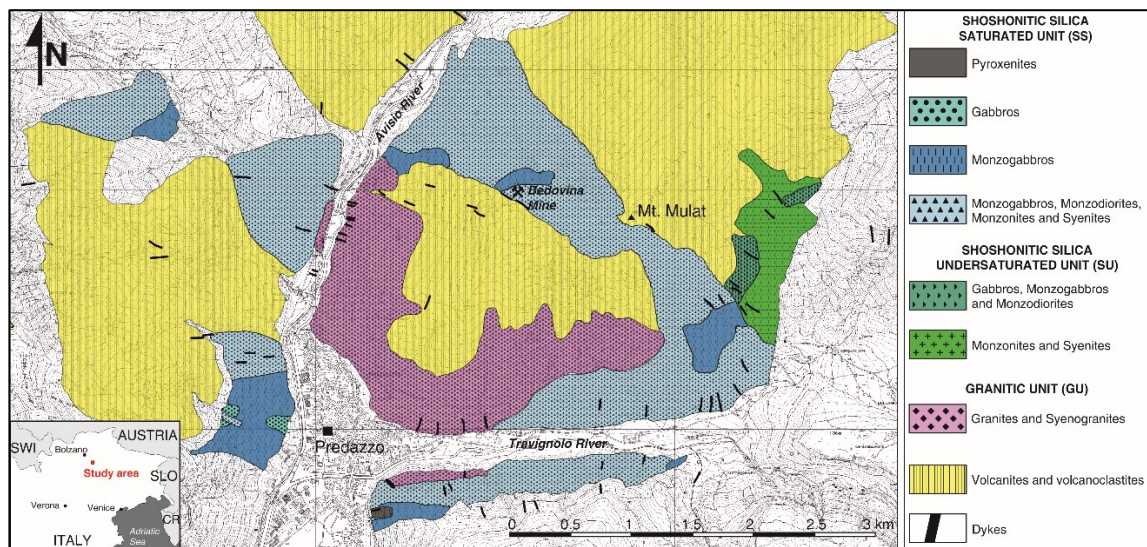
Fig. 15. Simplified geological map of the Predazzo Intrusive Complex (PIC). On the left bottom corner, the study area location with respect to the NE sector of Italy is shown.
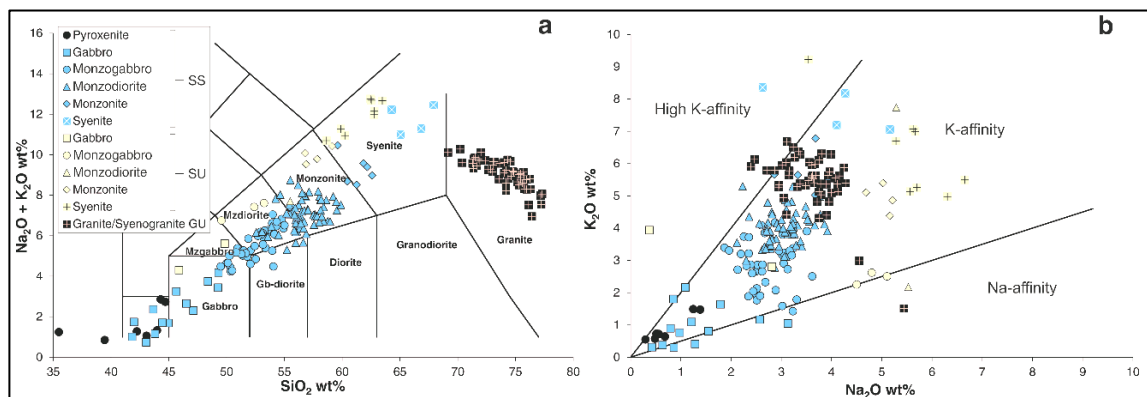
Fig. 16. (a) Total Alkali vs. Silica and (b) K_2O vs. Na_2O diagrams for Predazzo Intrusive Complex rocks (Le Maitre et al., 2002). SS shoshonitic silica saturated, SU shoshonitic silica undersaturated; GU granitic unit.

4.2.2. $^{87}Sr/^{86}Sr$ and $^{143}Nd/^{144}Nd$ isotopes

Whole-rock $^{87}Sr/^{86}Sr$ and $^{143}Nd/^{144}Nd$ isotopic ratios were analysed on representative samples of the SS, SU, and GU suites (Table A4.8). Shoshonitic Silica Saturated samples

have the initial Sr isotope composition from 0.7039 to 0.7052, whereas their initial Nd isotope compositions range from 0.512191 to 0.512247. Shoshonitic Silica Undersaturated rocks are characterized by a generally higher $^{143}Nd/^{144}Nd_i$ varying from 0.512261 to 0.512289 and by $^{87}Sr/^{86}Sr_i$ comparable with the SS samples (0.7047 to 0.7063). $^{143}Nd/^{144}Nd_i$ range of GU rocks is between 0.512206 and 0.512304, thus comparable to those of both SS and SU suites. High Rb/Sr of the GU rocks resulted in imprecise initial calculated $^{87}Sr/^{86}Sr$ preventing any correlation between the GU and the SS/SU bodies.

4.3. Crystallization sequences and mineral chemistry

To better focus on the P-T-fO_2 conditions and on the H_2O contents of the PIC system, some remarks on the mineral phase compositions and crystallization sequences of the various units is hereafter summarized. A more detailed description of the petrographic and mineral chemistry features of these rocks is reported in Chapter 3. The mineral phase analyses are reported in Tables A4.2 to A4.7.

Shoshonitic Silica Saturated rocks are dominated by the presence of clinopyroxene and plagioclase as cumulus phases; minor olivine and orthopyroxene can be found in gabbros and monzogabbros. The intercumulus assemblage is characterized by the ubiquitous presence of plagioclase and biotite, followed by the appearance of amphibole in gabbros to monzodiorites (Fig. 17). Magnetite and Ti-magnetite are often reported in association with biotite, whereas K-feldspar and accessory phases (quartz, apatite, ilmenite, sphene, and zircon) modally increase in more evolved rocks. The main alteration features of the SS rocks consist of sericite formation at the expenses of feldspars, chlorite growth over clinopyroxene, amphibole, and biotite, as well as epidote formation at the expenses of clinopyroxene and plagioclase. The following crystallization sequence can be deduced for SS rocks: olivine → clinopyroxene (± orthopyroxene) → Ti-magnetite/magnetite → plagioclase → biotite → amphibole → K-feldspar → quartz (± accessories).

The crystallization sequence of the SU magmatic suite mirrors its silica undersaturation and higher Na_2O content. Orthopyroxene and quartz are in fact absent, and an earlier appearance of amphibole at the expenses of biotite characterizes the intercumulus assemblage of the SU rocks (Fig. 17). Other Na-rich minerals like ferrosalitic clinopyroxene, abiotic plagioclase, and nepheline (Visonà, 1997) are variably present. Accessory phases are ugrandite group garnets, epidote, apatite, and titanite. As already highlighted by Visonà (1997), many portions of the SU body are hydrothermalized, showing the formation of kaoline, sericite and scapolite. Where this secondary assemblage does not occur, the primary differences between the SU and SS magmatic suites are evident. The likely crystallization sequence of

the SU rocks is: olivine → clinopyroxene → Ti-magnetite/magnetite → plagioclase → amphibole → biotite → K-feldspar → nepheline (± accessories).
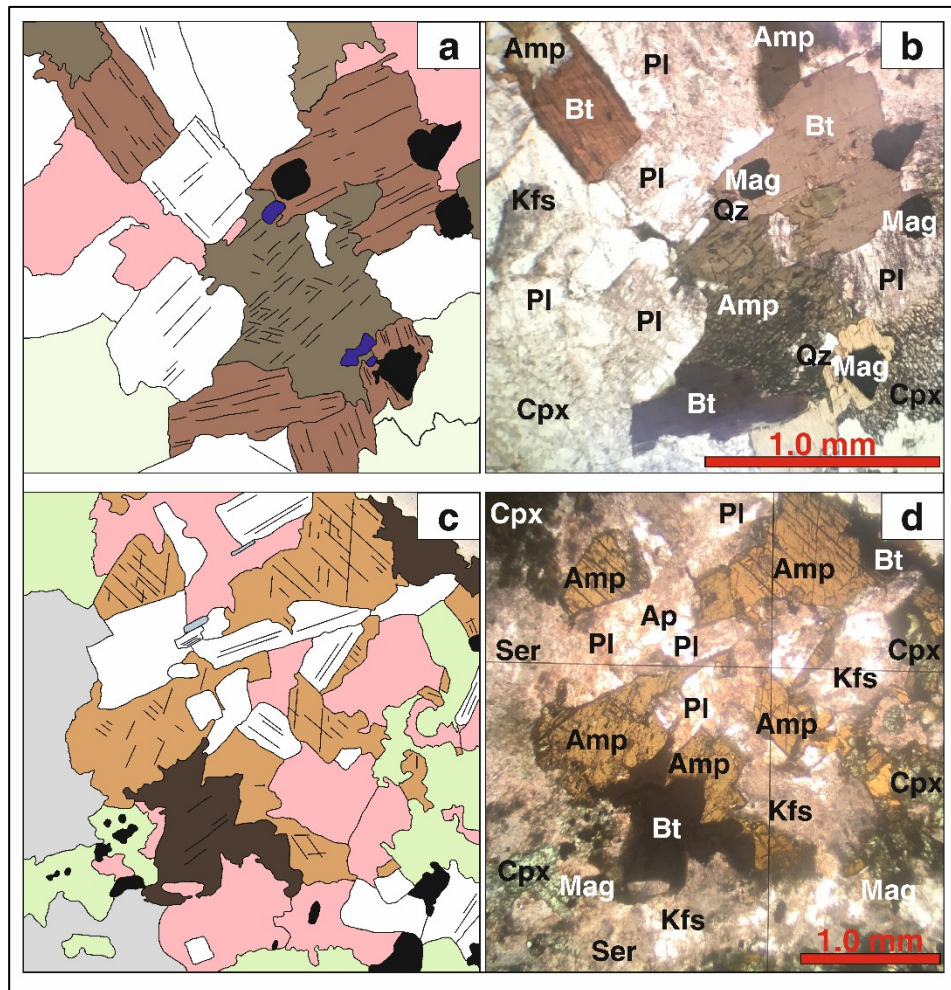
Fig. 17. Textural sketches of Predazzo Intrusive Complex rocks and corresponding photomicrographs showing the crystallization relationships between biotite and amphibole in the intercumulus assemblage of (a, b) Shoshonitic Silica Saturated monzodiorites and (c, d) Shoshonitic Silica Undersaturated monzogabbros. Each labeled mineral phase in the right photomicrographs is contraddistinct by a different colour in the left sketches. Amp: amphibole, Ap: apatite, Bt: biotite, Cpx: clinopyroxene, Kfs: K-feldspar, Mag: magnetite, Pl: plagioclase, Qz: quartz, Ser: sericite.

Syenogranites and granites of the GU are quite homogeneous in composition, being constituted by K-feldspar, plagioclase, and quartz, locally associated with several other minerals, among which Fe-rich biotite is the most common. Accessory phases are tourmaline, fluorite, sphene, magnetite, apatite, ilmenite, and zircon. Muscovite and chlorite are rare and always grow at the expenses of biotite and amphibole in the late hydrothermal stages, whereas the sericitization of feldspars is pervasive. Less common phases are ematite, allanite, scheelite, xenotime, gummite, thorite, uranium micas, molybdenite, and other sulphides, irregularly disseminated and generated in the later pneumatolytic and

65

hydrothermal stages (Marzocchi, 1987; Visonà, 1997). The main GU paragenesis is composed of: K-feldspar + plagioclase + quartz + fluorite + biotite (chlorite and/or muscovite) ± amphibole + accessories.

In the less altered samples, at comparable whole-rock differentiation degree, the composition of the most representative minerals clearly discriminates between the SS and SU magmatic suites. For instance, biotites and amphiboles are Al- and Na-enriched in the SU rocks with respect to the SS ones. Amphibole in fact varies from the hornblendic and actinolitic composition in the SS rocks (Na_2O < 1.5 wt%; Al_2O_3 < 8 wt%) to the hastingsitic/pargasitic composition (rare actinolitic hornblende, Leake *et al.*, 1997) in the SU ones (Na_2O up to ~ 2.5 wt%; Al_2O_3 up to ~ 18 wt%). Even the Na content of plagioclase differs between the two magmatic suites: it ranges from An_{84} to An_{34} in SS samples, and from An_{50} to $An_{<23}$ in SU rocks. Another discriminating feature is represented by the clinopyroxene composition, augitic/salitic (En_{43-33}) in the SS, and salitic/ferrosalitic (En_{37-24}) in the SU rocks (Morimoto, 1988). Furthermore, the manganese content of several phases is quite higher in the SU rocks: Ti-magnetite (0.2–1.9 wt% SU; 0.1–0.4 wt% SS), biotite (0.1–0.7 wt% SU; 0-0.4 wt% SS), amphibole (~ 0.7 wt% SU; ~0.5 wt% SS), and clinopyroxene (0.5–1.5 wt% SU; 0.2–0.8 wt% SS).

4.4. *P*, *T*, and H_2O estimates: thermobarometric evolution of the intrusion

4.4.1. Recover the initial equilibrium conditions

In this section, we apply several methods for estimating the *P*, *T*, and H_2O contents of PIC rocks, taking into account the coexistence of minerals used as thermometers, barometers, and/or hygrometers in both the SS and SU crystallization sequences. Apart from the Holland & Blundy (1994), Anderson & Smith (1995), Anderson (1996) and Henry *et al.* (2005) methods (see below) applied to amphibole-plagioclase pairs and biotite, and specific for intrusive rocks, the other equations used in this study are designed for volcanic samples. As often happens in intrusive contexts, the identification of the parental "melt" from which crystals formed is challenging (e.g. Skaergaard Intrusion; Nielsen, 2004; Namur & Humphreys, 2018). Intrusive rocks, in fact, rarely correspond to bulk melt composition, representing a variable mixture of cumulus and intercumulus minerals, removed by the crystallizing melts at various stages of fractionation, thus in equilibrium with different melts in different moments. As hypothesized in Chapter 3, cumulitic gabbros and pyroxenites, as well as most of the intermediately evolved rocks of the complex, can be generated by various

extent of fractional crystallization from a starting trachybasaltic magma in an almost closed system.

It is modelled that the mineral assemblages constituting the PIC rocks (e.g. clinopyroxenes of SS gabbro) showed partial equilibrium with a more evolved melt (e.g. SS trachybasalt), from which then segregated to form the cumulates. The cumulitic nature of a rock itself incorporates the concept that its composition (e.g. Mg# of clinopyroxene) represents an independent physico-chemical system with respect to the deriving melt. Consequently, if we try to consider the intrusive (cumulitic) rock of PIC as a bulk representative of a melt (e.g. in terms of Mg# or CaO/Al_2O_3), it is reasonable to find that its mineral constituents (e.g. clinopyroxene or plagioclase), are in evident disequilibrium with the bulk composition (Fig. 18 and Fig. 19). They are instead compositionally coherent with a segregation process from a more evolved melt. On the other side, by taking into account more evolved rocks (e.g. monzogabbros to syenites), the amount of crystal disequilibrium progressively decreases (Fig. 18 and Fig. 19). This because the ultimate products of the SS/SU fractional crystallization processes, syenitic in composition, progressively approach the eutectic of the system and likely resemble a melt composition: this condition has been also proposed by Morse & Brady (2017) for the syenites of the 1300 Ma old Kiglapait Intrusion (Labrador).

Evidences of the reliability of this genetic model are the observed textural and mineral homogeneities of the SS/SU rocks: any kind of significant zoned texture would result from the introduction of additional magma chamber processes (i.e. mixing) during the formation of the PIC lithotypes, invalidating our assumptions. The unzoned texture, coupled with the crystal size of PIC rocks (e.g. clinopyroxenes up to 6-7 mm in pyroxenites and gabbros) and with the small volume of the intrusive body (4.5 km^3), speaks also against a considerable effect of syn- to post-crystallization diffusion processes, which can be a rate-limiting process for thermobarometric estimates. On the other side, thermometers involving clinopyroxene in upper crustal context, commencing cooling from relatively low T, hold the potential to record the peak temperature conditions, especially in large-sized grains (Müller $et~al.$, 2013). If we couple the euhedral unzoned texture of PIC clinopyroxenes with the diffusion rates proposed by several authors (e.g. at about 1000°C $logD^{(Ca)}$ = -21 m^2/s; $logD^{(Ti)}$ = -22 m^2/s; $logD^{(Fe)}$ = -21 m^2/s, where D indicates the diffusion coefficient; see Brady & McCallister, 1983; Dimanov $et~al.$, 1996; Cherniak & Lyiang, 2012; Müller $et~al.$, 2013 and references therein), we can argue that the crystal compositions were nearly unmodified by significant diffusion processes. Similar remarks can be made for plagioclase, whose crystallization in plutonic rocks at relatively low T limit the efficiency of CaAl-NaSi diffusion to submicron length scales (Grove $et~al.$, 1984). The mineral compositions were therefore considered as

representative of the various stages of fractional crystallization of the magmas inside PIC, and were used to constrain the physical parameters of the magma chamber.
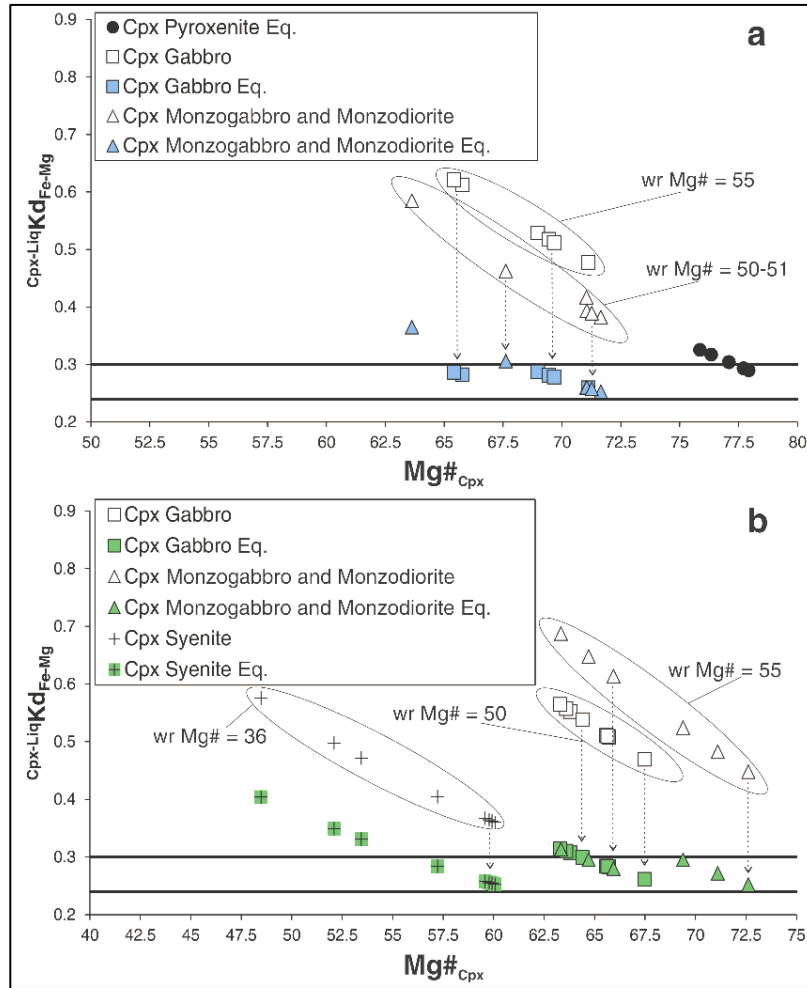
Fig. 18. Mg# vs. $^{Cpx-Liq}Kd_{Fe-Mg}$ of clinopyroxene from the (a) Shoshonitic Silica Saturated and (b) Shoshonitic Silica Undersaturated rocks. The white symbols represent the disequilibrium between crystals and their host rock composition, whose whole-rock Mg# (wr Mg#) is also reported. The filled symbols represent the attained equilibrium conditions after the calculation of melt composition in equilibrium. "Liq" indicates both the composition of the crystals host rocks (white symbols, prior to equilibration process) and that of the calculated "melt" (filled symbols, after equilibration process). The length of the dashed arrows is directly functioning of the amount of disequilibrium between the crystals and their host rock. The equilibrium range of $^{Cpx-Liq}Kd_{Fe-Mg}$ = 0.24–0.30 (black lines) is from Putirka et al. (2003).
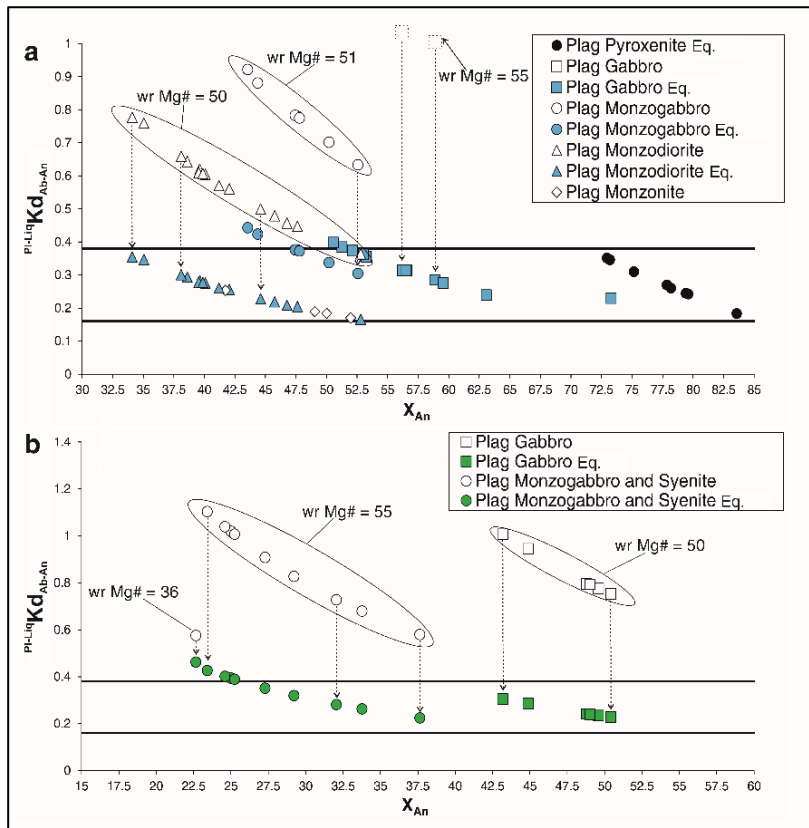
Fig. 19. Anorthite (X_{An}) vs. $^{Pl-Liq}Kd_{Ab-An}$ *of plagioclase from the (a) Shoshonitic Silica Saturated and (b) Shoshonitic Silica Undersaturated rocks. White symbols represent the disequilibrium between crystals and their host rock composition (whose Mg# is reported as "wr Mg#"), whereas filled symbols represent the attained equilibrium conditions after the equilibration processes. "Liq" indicates both the composition of the crystals host rocks (white symbols, prior to equilibration process) and that of the calculated "melt" (filled symbols, after equilibration process). The length of the dashed arrows is directly functioning of the amount of disequilibrium between the crystals and their host rock. The chosen equilibrium range of* $^{Pl-Liq}Kd_{Ab-An}$ *= 0.27 ± 0.11 (black lines) is from Putirka (2008).*

On the basis of these assumptions, we matched each mineral (e.g. clinopyroxene of SS cumulates) with an estimated "melt" following the crystal/melt equilibrium partitioning (e.g. $^{Cpx-Liq}Kd_{Fe-Mg}$, see below), to trace the *P-T* path of an hypothetical differentiation trend (e.g. SS suite, see Chapter 3). This operation enabled us to compute the "melt" composition, to skip the appearent disequilibrium between minerals and cumulitic rocks as a bulk and thus to constrain the *P, T* and H_2O parameters of the less evolved melts in the PIC feeding system. Afterwards, the application of the "traditional" thermobarometric equations for intrusive contexts (i.e. to amphibole-plagioclase pairs and biotite, see below) enabled us to verify the convergence between the various results as well as to unravel the *T-P-*H_2O conditions in the later stages of crystallization. A complete list of the applied equations, results, and corresponding errors is reported in Table A4.9 and discussed in detail in the following sections.

4.4.2. Clinopyroxene-melt thermobarometer and water content of primary magmas

Clinopyroxene is the dominant and ubiquitous phase in the SS and SU rocks, thus clinopyroxene-melt thermobarometry was considered as a valuable starting point to estimate the T-P intensive variables and H_2O content of PIC magmatic system since early stage of fractionation. Crystal-melt equilibrium conditions were tested by taking into account the experimentally determine range of $^{Cpx-Liq}Kd_{Fe-Mg} = 0.24$-$0.30$ at $T > 1050°C$ by Putirka et $al.$ (2003). First tests highlighted that all clinopyroxene crystals in the SS and SU units have $^{Cpx-Liq}Kd_{Fe-Mg} = 0.36$-$0.68$ (hereinafter the superscript "Liq" indicates the composition of the bulk rock), indicating a disequilibrium towards composition more evolved than their host rock (Fig. 18). The amount of disequilibrium, as said before, decreases with increasing the differentiation degree of the rock (Fig. 18). Such a decrease could be explained by the fact that more evolved lithotypes better approach the eutectic of the system and more likely simulate melt compositions.

Following the FC model of Chapter 3, clinopyroxenes of each lithotype were thus related to a calculated "melt" composition having the same chemical affinity of their host rock and a more evolved nature (Table A4.10), by which crystals retrieved their equilibrium conditions. As shown in the flow chart of Fig. 20, once chosen the clinopyroxene-melt couple of the SS suite, T-P pairs were extrapolated by means of the Putirka (2008) equations, assuming variable H_2O wt% contents of the melt. The water-dependant equations 32b and 33 (Putirka, 2008), derived from the P-independent thermometer and the T-dependent barometer of Putirka (1996), were firstly applied to constrain the crystallization conditions of clinopyroxene from the melt, obtaining several T-P-H_2O triplets. Since these triplets are strongly dependant on the chosen melt and on the inferred H_2O content, they were checked, together with the melt composition, by means of the Rhyolite-MELTS calibration (Gualda et $al.$, 2012). Iterated procedures (Fig. 20) were developed until a clinopyroxene composition analogous to the starting one was reproduced by Rhyolite-MELTS. In this way, the two independent approaches reinforce one to another, giving a more robust framework for the thermobarometric and water results. Since the only left starting parameter required by Rhyolite-MELTS was oxygen fugacity, we chose $fO_2 = NNO$ as proposed by Bonadiman et $al.$ (1994) for the Mt. Monzoni intrusion.

However, by increasing the differentiation degree of SS rocks, and/or considering the more alkaline SU magmas, the reliability of Rhyolite-MELTS decreases, as a function of the alkali-enrichment of the system and the related crystallization of amphibole and biotite, for whom thermodynamic parameters are not well constrained (Gualda et $al.$, 2012). Therefore, the use of Masotta et $al.$ (2013) thermobarometer was preferred for the SU suite and for the

more evolved SS rocks, and was cross-checked with Putirka (2008) equations (Fig. 20). As for SS rocks, once assessed the equilibrium between clinopyroxene and melt, T-P pairs at variable H_2O contents of the melt were extrapolated by means of the Putirka (2008) method. The resulting T-P-H_2O triplets were then inputed in Masotta $et\ al.$ (2013) equation until the resulting T and P were comparable to those obtained by Putirka (2008) method at similar water contents.

Some issues for handling this combination of modeling tools should be remarked: (i) since Rhyolite-MELTS is not suitable for amphibole and biotite-dominated rocks, it was only used to simulate the composition of clinopyroxene in equilibrium with the least evolved SS magmas, at the $P,\ T$ and H_2O conditions determined by the previous calculations; (ii) the alkaline nature of PIC (especially SU) differentiated rocks implies that clinopyroxene-melt behavior during crystallization and cooling depends not only on Fe and Mg, but also on Ca, Na and Al, so Masotta $et\ al.$ (2013) equations became progressively more reliable; (iii) iterated and cross-checked calculations using Putirka (2008), Rhyolite-MELTS and Masotta $et\ al.$ (2013) methods (Fig. 20) were proposed to unravel P-T-H_2O crystallization conditions avoiding circular relationships between the equations. The errors proposed for the thermobarometers, oxybarometers and hygrometers are reported in Table A4.9: while temperatures could be defined within a narrow error range (±10 to $\pm20°C$) with both Putirka $et\ al.$ (2008) and Masotta $et\ al.$ (2013) equations, the P estimates were affected by high uncertainties, varying from ±120 (Masotta $et\ al.$, 2013) to ±260 MPa (Putirka $et\ al.$, 2008).
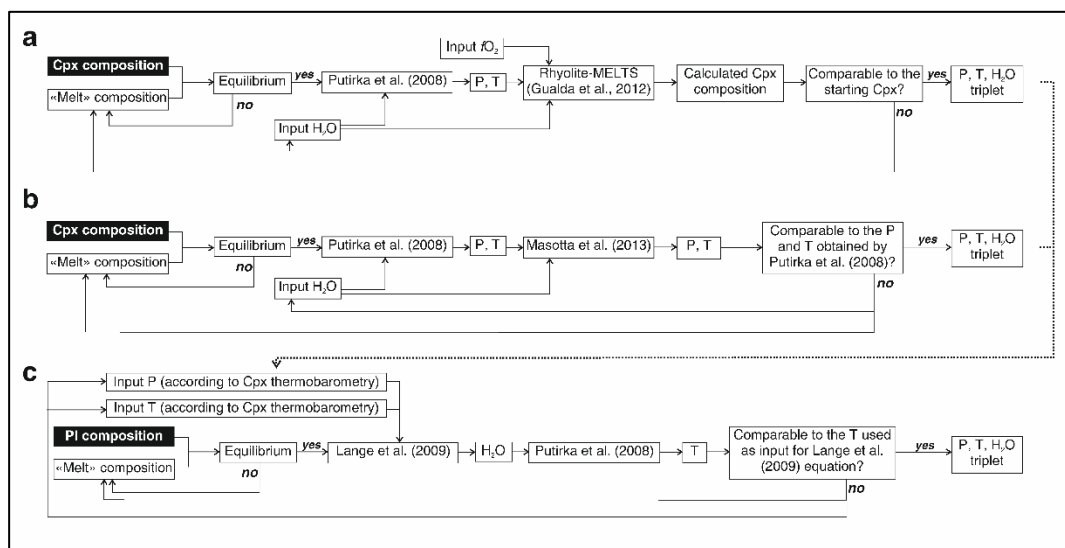
Fig. 20. Flowchart representing the rationality of our models for clinopyroxene (Cpx) and plagioclase (Pl) thermobarometry and hygrometry, from the starting mineral compositions (black squares) to the final P–T–H2O triplets. a) Model for clinopyroxenes in the less differentiated Shoshonitic Silica Saturated rocks; b) model for clinopyroxenes in the evolved Shoshonitic Silica Saturated and in the Shoshonitic Silica Undersaturated rocks; c) model for plagioclases in both Shoshonitic Silica Saturated and Shoshonitic Silica Undersaturated rocks.

4.4.2.1. Clinopyroxene crystallization conditions of Shoshonitic Silica Saturated rocks

The most magnesian clinopyroxene in SS rocks were found within pyroxenites (Mg#$_{Cpx}$ 76-78), whereas the less magnesian compositions (Mg#$_{Cpx}$ 63-71) were in the monzodiorites and monzonites. The early *T-P*-H_2O crystallization conditions were likely represented by the former, which attained equilibrium with a trachybasaltic melt (Mg# 51; Fig. 18; Table A4.10), further confirming the first FC step identified in Chapter 3. Clinopyroxene-melt thermobarometers indicated a *P-T* range of 160-230 MPa and 1070-1050°C, for water contents of 2.0-2.5 wt% (Table A4.9). The best fitting data in by Rhyolite-MELTS simulations were obtained at pressure of 150 MPa, temperature of 1060°C and 2.5 H_2O wt%. Consequently, 2.0-2.5 H_2O wt% could be assumed as the water contents of the first SS magmas intruding the PIC. Clinopyroxenes in the cumulitic gabbros were slightly less homogeneous and less magnesian (Mg#$_{Cpx}$ 69-71 cores; 65-66 rims), and resulted in equilibrium with melts varying in Mg# from 43 to 40 (cores) to about Mg# 36 (rims), as shown in Fig. 18 and Table A4.10. Pressure-temperature paths indicated that cores attained equilibrium in a *P* range of 50-190 MPa and *T* of 910-980°C, while rims formed at 30-120 MPa and 900-920°C, considering H_2O contents of 3.0-4.0 wt%. Clinopyroxenes in monzogabbros and monzodiorites were nearly unzoned although compositionally comparable to those in gabbros, showing Mg#$_{Cpx}$ of 68-72. As for gabbroic rocks, equilibrium was reached with intermediately evolved magmas (Mg# 40, Fig. 18; Table A4.10), by which thermobarometric equations indicated a *T* range of 940-990°C at *P* of 140-160 MPa, for a H_2O contents in the melt of 3.0-4.0 wt%. All results are reported in Fig. 21 and Table A4.9.

4.4.2.2. Clinopyroxene crystallization conditions of Shoshonitic Silica Undersaturated rocks

Clinopyroxenes from the SU suite are more alkaline than those of the SS rocks, ranging from salitic-aegirinaugitic to ferrosalitic compositions. The most magnesian compositions in gabbros and monzogabbros (Mg#$_{Cpx}$ 67-63) were in equilibrium with Mg# 36 melts (Fig. 18; Table A4.10). Pressure-temperature paths indicate a *P* range of 20-160 MPa and *T* of 920-940°C at water contents of about 1.0-1.5 wt%. Clinopyroxenes in syenites (Mg#$_{Cpx}$ 60-48) show composition close to the equilibrium with the whole rock (Fig. 18; Table A4.10), which represent a theoretical slightly evolved trachytic melt. Thermobarometers yielded a *P* of 20-160 MPa at *T* of 810-860°C at water contents between 4.0 and 5.0 wt%. Results are reported in Table A4.9 and shown in Fig. 21.

4.4.3. Amphibole and amphibole-plagioclase thermobarometer and hygrometer

Pressure, temperature and H_2O conditions for amphibole crystallization were estimated using amphibole-plagioclase Al-exchange thermobarometers (Holland & Blundy, 1994; Anderson & Smith, 1995; Anderson, 1996) and a single amphibole thermobarometers (Ridolfi *et al.*, 2010; Ridolfi & Renzulli, 2012). Amphibole-plagioclase equations were used for mineral pairs in both SS and SU suites, whereas the single amphibole thermobarometers were applied to all amphibole compositions in the SS rocks, but only for amphibole in gabbros in the SU suite. This because of the higher alkali content of SU differentiated magmas, well above the compositional ranges admitted for the calibration of the empirical geothermometers of Ridolfi *et al.* (2010) and Ridolfi & Renzulli (2012). For the SS and SU amphiboles, the single amphibole equations enabled also the calculation of the water content of the melt from which they crystallized. Contrary to the clinopyroxene-melt equations, the error range for the barometric estimates based on amphibole-plagioclase and single amphibole was lower, ranging between ±3 and ±60 MPa, whereas errors on *T* estimates were slightly higher (±23 to ±40°C, Table A4.9).

4.4.3.1. Amphibole crystallization conditions of Shoshonitic Silica Saturated and Shoshonitic Silica Undersaturated rocks

Pressure-temperature paths obtained from amphibole-plagioclase thermobarometers yielded a *T-P* range of 750-845°C and 10-120 MPa in SS gabbros to monzodiorites (Fig. 21; Table A4.9). Single amphibole calculations for the same lithotypes confirmed these values, indicating *P* = 70-140 MPa and *T* = 720-810°C. The estimated H_2O contents of melts in equilibrium with amphiboles of SS gabbros to monzodiorites was between 4.8 and 6.0 wt% Fig. 21; Table A4.9).

Amphibole-plagioclase estimates for the SU suite yielded similar *P* intervals (40-100 MPa) but at lower *T* (620-660°C) for gabbros, and *P-T* ranges of 160-190 MPa and 870-880°C taking into account the mineral pairs in the monzogabbroic rocks (Fig. 21; Table A4.9). The single amphibole method, applied only to the actinolitic hornblendes in SU gabbros, provided comparable pressures (50-60 MPa) and temperatures (700-720°C) with respect to the SS rocks (Fig. 21; Table A4.9). The calculated water contents of the melts were similar to those obtained for the SS suite (5.1-5.7 wt%, Fig. 21; Table A4.9).

As expected, the water contents calculated by these models were higher than those obtained from the clinopyroxene-melt calculations. Amphibole crystallization, in fact, occurred later than clinopyroxene, thus the melt from which amphibole precipitated should have undergone differentiation in some extent, and its water content should have increased. If we consider

the water enrichment linked to the fractional crystallization of the SS/SU magmas, together with the concomitant precipitation of volatile-bearing phases, the H_2O contents resulted from the single amphibole equations appear in line with the calculations proposed by the FC model shown in Chapter 3.

4.4.4. Biotite thermometer

Biotite is a ubiquitous phase occurring in the late inter-cumulus mineral assemblages of almost all SS, SU and GU rocks. Its presence enabled us to provide some estimates on the temperatures of these assemblages, by using of the empirical single-mineral thermometer of Henry *et al.* (2005), based on the Ti content of biotite.

4.4.4.1. Biotite crystallization conditions of Shoshonitic Silica Saturated, Shoshonitic Silica Undersaturated and Granitic Unit rocks

Temperature of biotite crystallization in SS pyroxenitic cumulates resulted between 690 and 740°C, whereas a *T* interval of 600-660°C was considered representative of SS gabbros to monzodiorites. Biotites from more differentiated SS monzonites yielded a *T* of about 540-580°C (Fig. 21; Table A4.9). Biotite in SU gabbros and monzogabbros indicated comparable temperatures, ranging between 640 and 660°C (Fig. 21; Table A4.9).

The thermometer was also applied to GU syenogranites, resulting in a *T* range of 420-570°C: the biotites in GU rocks are however iron-rich, with $Mg/(Mg+Fe_{tot}) < 0.275$, just out of the compositional field for which the thermometer was calibrated. Consequently, the resulting temperatures were not used for further modeling purposes.

4.4.5. Plagioclase-melt thermobarometer and hygrometer

Plagioclase appears in almost all PIC rocks, from the cumulitic pyroxenites, where it is part of the intercumulus assemblages, to the syenitic rocks, where, together with K-feldspar, dominates the paragenesis. Its ubiquitous presence made it an additional tool for investigating the *T* and H_2O content of PIC magmas along the entire SS and SU differentiation trends by means of Putirka (2008) and Lange *et al.* (2009) equations. Plagioclase from GU granites and syenogranites are compositionally close to the pure albitic end-member, probably because of hydrothermal/alteration processes. This made them unsuitable for the hygrometer application, being its calibration limited to An_{37} plagioclase (Lange *et al.*, 2009).

As for clinopyroxene, plagioclase equilibrium with its host rock was constrained by means of the experimentally determined values of $^{Pl-Liq}Kd_{Ab-An} = 0.10\pm0.05$ at $T < 1050$ °C and

0.27±0.11 at $T \geq 1050$ °C (Putirka 2008). However, Mollo *et al.* (2011) demonstrated that $^{Pl-Liq}Kd_{Ab-An}$ is highly sensitive to the cooling rate of the melts, being thus variable between 0.2±0.02 (cooling rate of 0.5°C/min) and 0.35±0.03 (cooling rate of 15°C/min). Thus, all plagioclase-melt equilibria (even at $T < 1050$°C) were considered following a $^{Pl-Liq}Kd_{Ab-An}$ in the range of 0.27±0.11 (Putirka, 2008), whose interval is also in accordance with the results obtained by Mollo *et al.* (2011). Cooling rate is in fact an essential factor for the crystallization dynamics of intrusive bodies, as testified by the plagioclase morphological variations in PIC rocks, where it appears as both cumulus and intercumulus phase throughout the entire SS/SU fractionation trends. According to crystallization sequences, plagioclase appeared after clinopyroxene and Fe-Ti oxides, just before or even contemporary to biotite and amphibole in the intercumulus assemblages. Consequently, we considered the thermobarometric values obtained by clinopyroxene, amphibole and biotite calculations for each magmatic suite (see above) to identify the P-T-H_2O interval in which plagioclase crystallized from the melt. As for clinopyroxene, plagioclase often appeared in disequilibrium with its whole rock composition (Fig. 19), and the amount of disequilibrium gradually decreases with increasing the differentiation degree of the corresponding whole rock. Plagioclase in monzodiorites were in fact closer to the equilibrium with respect to those of pyroxenites and gabbros, whereas most of the plagioclase from monzonites and syenites were in equilibrium with their host rock (Fig. 19). As previously mentioned for clinopyroxene, such a trend could be justified by considering that the more evolved rocks likely resemble melt compositions, being close to the eutectic of the system. Thus, plagioclase compositions were related to estimated melt compositions, according to the differentiation trends proposed in Chapter 3, to retrieve the equilibrium conditions. Once equilibrated, plagioclase and melt compositions were used as input for the Lange *et al.* (2009) hygrometer to calculate the amount of H_2O dissolved in the melt (see flow chart of Fig. 20). For each sample, input T and P required in Lange *et al.* (2009) equation were chosen in the T-P interval between those estimated by clinopyroxene-melt calculations and those resulted from amphibole and biotite.

Pressure, temperature and H_2O were calculated by iterating Lange *et al.* (2009) method and equation 24a of Putirka (2008) until a matching T was found. In any case, small variations of P scarcely affect the results of the hygrometers: ±100 MPa corresponds to ±0.1 wt% H_2O calculated in the melt (Giacomoni *et al.*, 2014). Since the P interval obtained by the previous (clinopyroxene and amphibole) barometers was roughly between 20 and 190 MPa for all PIC rocks, the H_2O estimates were almost entirely constrained by temperature changes. As a consequence, the match between T obtained with Lange *et al.* (2009) and equation 24a of

Putirka (2008) was considered a reliable cross-check and a robust constraint on our geothermal modelling (Fig. 20).

4.4.5.1. Plagioclase crystallization conditions of Shoshonitic Silica Saturated rocks

Data from clinopyroxene-melt simulations on pyroxenites indicated that SS primary magmas began crystallizing at about 150 MPa, 1060°C and 2.5 H_2O wt%. The more anorthitic plagioclase (An_{84-73}) were analyzed in the pyroxenites intercumulus assemblage, following clinopyroxene and preceding biotite, thus the *T* range of plagioclase crystallization is constrained by the temperatures of crystallization of these two phases. Since pressure does not sensitively affect the calculations, a pressure of 150 MPa was used according to the results from clinopyroxene-melt calculations (Fig. 20). Results indicated that the most anorthitic plagioclase (An_{84-73}) crystallized in equilibrium with a trachybasaltic melt (Mg# 51; Fig. 19, Table A4.10): at *P* = 150 MPa, *T* of crystallization resulted of 1060-1081°C for a H_2O content of 3.0 wt%.

Plagioclase in SS gabbros were in compositional continuity with those of pyroxenites, varying between An_{73} and An_{51} in both the cumulus and intercumulus assemblages. As for plagioclase inside pyroxenites, the marked disequilibrium (Fig. 19) was probably related to the cumulitic nature of gabbros and/or a variable cooling rate of the magma. The crystallization sequence and the comparison with the *T* ranges obtained from clinopyroxene, amphibole and biotite suggested that plagioclase crystallized in a temperature interval of 980 to 740°C. Plagioclase with An_{73} reached the equilibrium with a Mg# 49 melt (Fig. 19): at *P* of 150 MPa, *T* and H_2O content resulted of 1016-1053°C and 3.1 wt% respectively. An_{63-51} plagioclases were equilibrated with a basaltic trachyandesitic melt (Fig. 19; Table A4.10), yielding *T* of 920-1021°C and a water content of 3.2-3.4 wt% at pressures of 120-150 MPa (Fig. 21; Table A4.9). It is worth noting that for these temperatures, Putirka (2008) proposed a potential partitioning $^{Pl-Liq}Kd_{Ab-An} = 0.05-0.15$ to attest equilibrium. However, after several iterations, the modelled *P*-*T*-H_2O terns for PIC magmas were attained only within a $^{Pl-Liq}Kd_{Ab-An}$ of 0.27±0.11. Such appearent discrepancies could be explained considering the dependency of Ab-An equilibrium coefficient with the cooling rate (Mollo *et al.*, 2011).

Plagioclase from monzogabbros to monzonites were in a compositional range from An_{53} to An_{34}, resulting in equilibrium with basaltic trachyandesitic to trachyandesitic melts (Fig. 19; Table A4.10). At *P* of 120 MPa, *T* resulted between 917 and 989°C, for water contents of 3.9-4.8 wt%, progressively increasing with the differentiation degree of the samples (Fig. 21; Table A4.9).

4.4.5.2. Plagioclase crystallization conditions of Shoshonitic Silica Undersaturated rocks

Plagioclase in SU rocks range from An_{50-43} in gabbros to An_{38-23} in monzogabbros and monzodiorites, and reach the more albitic compositions in syenites, where anorthite content is low (An_{23}-An_2). Plagioclase in gabbros were equilibrated by an intermediately evolved melt, trachyandesitic in composition (Fig. 19; Table A4.10). According to the thermobarometric data obtained by multiple geothermometers (clinopyroxene, amphibole and biotite), the temperature crystallization interval of plagioclase ranges between 940 and 720°C. Plagioclase-melt thermometers and hygrometers yielded a *T* range of 975-990°C at *P* of 150 MPa, for a water content of 4.1 wt%.

Apart from the nearly pure albitic compositions (likely effects of secondary processes), plagioclase in monzogabbros to syenites vary from An_{38} to An_{23}. They were equilibrated with an evolved trachytic melt (Fig. 19; Table A4.10), thought to be the final product of the SU differentiation trend (see Chapter 3). At *T-P* space of 920-936°C and 120 MPa, the estimated water contents of melt in equilibrium with An_{38} plagioclases was about 4.4 wt%, progressively increasing with the differentiation of the samples (Fig. 21; Table A4.9).

4.4.6. K-Feldspar-melt hygrometer

Except for pyroxenites, K-feldspar is present in all PIC rocks, where it occurs as intercumulus (gabbros to monzodiorites) and cumulus (monzonites/syenites) phase. Its composition was used to constrain the amount of H_2O dissolved in the co-existing melt by means of the equation proposed by Mollo *et al.* (2015). Such method, based on the Or-Ab exchange between K-feldspar and melt is calibrated for alkaline differentiated magmas, thus proper for the SS, SU and GU rocks compositions. Together with the data obtained by the previous equations, such estimates enabled to "track" the H_2O contents in the progressively differentiating melts. According to Mollo *et al.* (2015), this method can be applied only to K-feldspar with Or_{44-86}, whereas no reliable results were produced for $Or_{>86}$ as it extended outside the range of calibrated compositions. K-feldspar and whole rock equilibrium evaluation was attained by minimizing the difference between predicted and measured $^{Kfs-Liq}Kd_{Or-Ab}$, following equation 2 of the Mollo *et al.* (2015) model. These conditions were satisfied only by considering K-feldspar compositions in equilibrium with trachyandesitic to trachytic melts (Table A4.10), further confirming the correspondence between the crystallization sequence and the progressive differentiation model proposed in Chapter 3.

According to the equilibration temperatures recorded by clinopyroxene, amphibole, biotite and plagioclase, a *T* of 900-800°C was used as input for all samples of the SS and SU suites, whereas lower temperatures (800-700°C) were considered for GU syenogranites.

4.4.6.1. K-Feldspar crystallization conditions of Shoshonitic Silica Saturated, Shoshonitic Silica Undersaturated and Granitic Unit rocks

Water concentration of melts in equilibrium with K-feldspar in SS gabbros to monzogabbros were in the range of 4.4-5.3 wt% and 5.6-6.5 wt% respectively, whereas higher H_2O contents (6.1-7.3 wt%) were recorded in monzodiorites. The highest water values were calculated in SS syenites, that in turn show a larger variability of values (H_2O = 4.6-7.3 wt%; Fig. 21; Table A4.9).
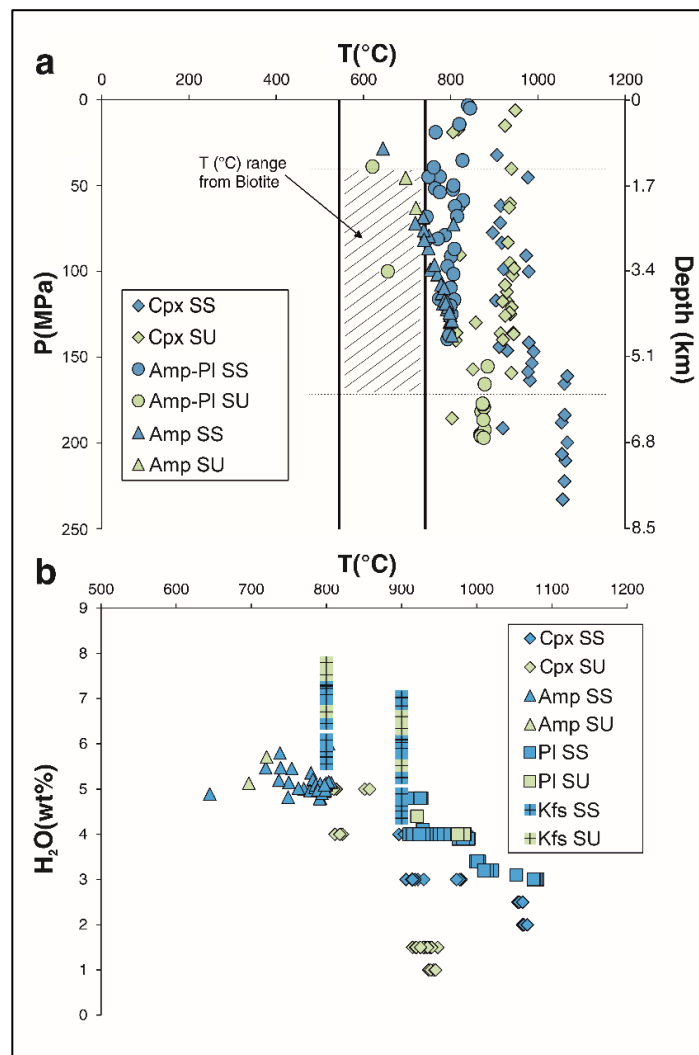
Fig. 21. (a) Temperature vs. pressure and (b) temperature vs. water content diagrams for Predazzo Intrusive Complex rocks. SS Shoshonitic Silica Saturated, SU Shoshonitic Silica Undersaturated. The reported values were obtained from the several thermobarometric approaches explained in text. Cpx: clinopyroxene; Amp: amphibole, Pl: plagioclase, Kfs: K-feldspar. Dashed interval in (a) represents the best-fit pressure range between the various estimates, whereas the shaded field represents the temperature interval resulted from biotite thermometry. Depth was calculated by considering a ΔP/Δz of 29 MPa/km.

K-feldspar analysed in SU monzogabbros and monzonites indicated H_2O contents of the crystallizing melts between 5.5-6.3 wt% and 6.7-7.8 wt%, respectively. H_2O estimates for GU syenogranites range between 8 and 11 wt%, being however meaningless in the physical system compatible with the body emplacement. The solubility of water at $P < 250$ MPa for rhyolitic-trachytic melts in fact do not exceed 7 wt%, as experimentally and theoretically determined in the T range of 500-1000°C (Di Matteo *et al.*, 2004; Liu *et al.*, 2005). These values were therefore discharged in the discussion.

4.5. Oxygen fugacity

The two main magmatic suites (SS and SU) are formed by the differentiation of melts which began crystallizing at pressures lower than 200 MPa and at similar T ranges (1050-1000°C). Main differences between the SS and SU suites could be found by taking into account the total amount of water of the crystallizing melts: SS primitive melts in fact were characterized by an higher water contents with respect to that of SU ones (2.0-2.5 wt% *vs.* 1.0-1.5 wt%, respectively). Classically, it is considered that dissolved molecular H_2O reacts with oxygens of the silicate network producing two OH^- groups (e.g. Stolper, 1982; Silver & Stolper, 1985; Kohn, 2000). The overall reaction reading as $H_2O + O^{-2} = 2OH^-$ may thus be considered as the counterpart of the water solubility in evaluating the redox conditions.

To effectively quantify such differences, we estimated the fO_2 conditions of each portion of PIC by means of the T-fO_2 model of Burkhard (1991), based on the biotite/K-feldspar/magnetite equilibrium in biotite-bearing intrusive rocks. Burkhard's (1991) empirical equation complements that of Kress & Carmichael (1988), enabling to calculate oxygen fugacity and temperature by two independent formulas. Water fugacity required in Burkhard's (1991) equation was calculated at a fixed P of 150 MPa following Burnham *et al.* (1969). Sanidine activity was considered according to Waldbaum & Thompson (1969), whereas magnetite activity was approximated at unity (Burkhard, 1991). Since this equation required as input the amount of Fe^{2+} in biotite, Fe^{2+}/Fe^{3+} ratios of SS, SU and GU biotites were calculated following Dymek (1983). Because the compositional spectrum of biotite and sanidine in each rock is slightly variable, we calculated two T-fO_2 pairs for each lithotype (Fig. 22; Table A4.9), to account for the possible oxygen fugacity ranges. According to Burkhard (1991), the error on each calculation was of ±0.3 log units.

As shown in Fig. 8, oxygen fugacity in SS rocks resulted in a range from -14.1 to -10.7 $logfO_2$, at temperatures comprised between 790 and 1000°C (Table A4.9). Such values plot between the FMQ and NNO buffers (+0.2 to +0.7 ΔFMQ, Fig. 22), and are well comparable to the values chosen as input for the Rhyolite-MELTS model above developed (-9.34 $logfO_2$

at 1060°C), further confirming the validity of the calculated parameters. Rocks from the SU and GU suites were characterized by values of -11.9 to -10.2 log$f$O$_2$ at T of 920-1050°C (-0.1 to +0.3 ΔFMQ, Fig. 22), and -12.9 to -11.8 log$f$O$_2$ at T of 850-920°C (around +0.4 ΔFMQ, Fig. 22), respectively (Table A4.9). Syenogranites of the GU suite were characterized by a behavior comparable to that of SS rocks, whereas SU rocks record slightly more reduced conditions.
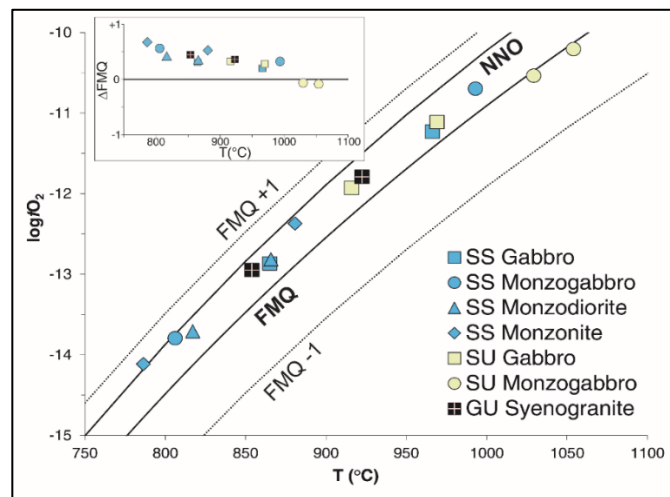
Fig. 22. Temperature vs. oxygen fugacity (expressed in log fO₂) diagram for Predazzo Intrusive Complex rocks. SS Shoshonitic Silica Saturated, SU Shoshonitic Silica Undersaturated. FMQ and NNO buffers are from Myers & Eugster (1983) and Huebner & Sato (1970), respectively. Up on the right, insert with the same oxygen fugacity data expressed in terms of ΔFMQ to facilitate the comparison between the various magmatic suites.

4.6. EC-AFC processes

As shown by the thermobarometric and hygrometric models, the two main magmatic suites (SS and SU) emplaced and crystallized at comparable pressures and temperatures conditions. The only differences can be identified when water content and oxygen fugacity are considered, being the SU system characterized by lower H$_2$O content and by more reduced conditions. Anyway, such slight divergences are not able to justify the marked geochemical variations between SS and SU magmas (see also Chapter 3). To account for the geochemical features of the SS and SU batches, we developed several Energy-Constrained Assimilation and Fractional Crystallization (EC-AFC) models (Bohrson & Spera, 2001; Spera & Bohrson, 2001), based on [87]Sr/[86]Sr and [143]Nd/[144]Nd. The purpose of this calculation was to discriminate between the original (i.e. mantle-derived) signature of SS/SU magmas and the effects of assimilation (and/or contamination) during the emplacement and differentiation of PIC magmas. Specifically, the main target of the models were: (i) verifying if the isotopic signature of SU rocks was generated an interaction between SS magmas and crust; (ii)

quantify the eventual (if any) crustal assimilation during the differentiation of the SS/SU magmatic suites; (iii) discriminate between assimilation and contamination processes.

A wide spectrum of Permo-Triassic crustal rock isotopic signatures from the literature were considered in the EC-AFC model as potential assimilants. These are Triassic carbonates (Martin & Macdougall, 1995; Blendiger *et al.*, 2015), Permian intrusives of Mt. Croce (central-eastern Southern Alps; Rottura *et al.*, 1997) and Serie dei Laghi (southwestern Alps; Sinigoi *et al.*, 2016, and references therein), Permian rhyolitic ignimbrites of the Atesina Volcanic District (Barth *et al.*, 1993), and the Kinzigite formation (southwestern Alps; Voshage *et al.*, 1990). Geothermobarometric and hygrometric results (Table A4.9) were used to to calculate assimilants and starting magmas' specific heat [J/(KgK)], heat of crystallization (J/Kg) and heat of fusion (J/Kg) according to Spera (2000), Bohrson & Spera (2001) and Spera & Bohrson (2001; Table 4). Specific heat [J/(KgK)] and liquidus T (°C) of carbonate assimilant (Table 4) were considered accordingly to Dallai *et al.* (2011) and Eppelbaum *et al.* (2014).

Table 4. Starting Shoshonitic Silica Saturated (SS) and Shoshonitic Silica Undersaturated (SU) magmas, assimilant end-members and input thermodynamic data used in the EC-AFC model. Calculated and absolute values are from Bohrson and Spera (2001) and Spera and Bohrson (2001) upper crustal case. Specific heat and liquidus T of carbonate assimilant were calculated according to Dallai et al. (2011) and Eppelbaum et al. (2014) respectively. References are also reported for all chosen assimilants compositions.

Starting magma	Liquidus T (°C)	Initial T (°C)	Solidus T(°C)	Specific Heat [J/(Kg K)]	Heat of Crystallization (J/Kg)	Heat of Fusion (J/Kg)
SS monzogabbro	1212	1100	600	1567	396000	270000
SU monzogabbro	1251.65	1100	600	1515	396000	270000
Assimilant	Liquidus T (°C)	Initial T (°C)	Specific Heat [J/(Kg K)]	Reference for isotopic $^{87}Sr/^{86}Sr$ and $^{143}Nd/^{144}Nd$ composition		
Carbonate	650	300	1170	Martin and Macdougall (1995); Blendiger et al. (2015)		
Rhyolitic Ignimbrite (AVD)	1077	300	1376	Barth et al. (1993)		
Mt. Croce Granodiorites	1111	300	1398	Rottura et al. (1997)		
Serie dei Laghi Granites	1026	300	1379	Sinigoi et al. (2016) and references therein		
Kinzigite Amphibolite	1196	300	1447	Voshage et al. (1990)		

The absence of $^{87}Sr/^{86}Sr$ and $^{143}Nd/^{144}Nd$ variations with increasing silica content for both SS and SU suites and the lack of overlap between SS and SU compositional fields suggested that the two suites have a different origin. A slight $^{87}Sr/^{86}Sr$ increase was however noted for both SS and SU samples while approaching the intrusion borders (Table A4.8). On the other side, the $^{143}Nd/^{144}Nd$ of both SS and SU rocks were not sensitive to the distance from intrusion edges, ruling out the occurrence of contamination processes during magma emplacement. Therefore, the Nd isotopic enrichment of the SU suite can be considered as a

primary feature, directly function of its mantle source or alternatively derived from assimilation of crustal components.

In this view, the EC-AFC equations were applied to the less contaminated compositions to better constrain the Sr and (especially) Nd isotopic variations among the magmatic suites.

The EC-AFC model from a starting SS composition (Fig. 23) showed that none of the chosen crustal components was able to drive the initial SS $^{87}Sr/^{86}Sr$ and $^{143}Nd/^{144}Nd$ ratios towards the SU field. This simulation reinforced the primary nature of the Nd isotopes enrichment of the SU body, ruling out the genesis of the SU rocks via crustal assimilation by an SS starting magma. The model was instead able to explain the isotopic variability of the SS samples. Almost all assimilation models well fitted the isotopic trend of SS rocks, suggesting that small amounts of crustal components were assimilated during magma storage. As shown in Fig. 23, the less depleted $^{143}Nd/^{144}Nd$ end-members were achieved by an interaction between magma and 2-10% of crust, represented by kinzigites (Voshage *et al.*, 1990), Mt. Croce granodiorites (Rottura *et al.*, 1997) and/or Atesina Volcanic District rhyolitic ignimbrites (Barth *et al.*, 1993). A 5% assimilation of carbonates (Martin & Macdougall, 1995; Blendiger *et al.*, 2015) and/or Serie dei Laghi-like granites (Sinigoi *et al.*, 2016) instead reproduced the more depleted $^{143}Nd/^{144}Nd$ ratios.

A second EC-AFC model was attempted to explain the isotopic variations of SU samples, but their scattered distribution prevented to retrace the assimilation path. Nevertheless, this model was used just to quantify the crustal contribution in the Nd isotopic variations of the SU samples. As a result, the $^{143}Nd/^{144}Nd$ range of the SU suite was achieved by a 2-7% assimilation of the crustal components (carbonates, Atesina Volcanic District rhyolitic ignimbrites, Mt. Croce granodiorites, Serie dei Laghi granites and amphibolitic kinzigites).

On the whole, the Nd isotopic ranges of both SS and SU suites could be explained by low amounts of assimilation, whereas Sr isotopic variability is more likely derived from contamination processes at the intrusion borders during magma emplacement, where fluid mobilization and local metamorphic reactions occurred (Ferry *et al.*, 2002; Gallien *et al.*, 2007).

As reported in Table A4.8, the Sr isotopic signature of PIC rocks appears to be more sensitive to their distance to the intrusion edges rather than to their degree of differentiation, being thus the $^{143}Nd/^{144}Nd$ ratio the best proxy to discriminate the two magmatic suites. Given this, the Sr variations of the SU suite at near constant $^{143}Nd/^{144}Nd$ could be also affected by i) slight alteration effects, unavoidable for such a small body and/or ii) the contact halo between PIC and the wall rocks.
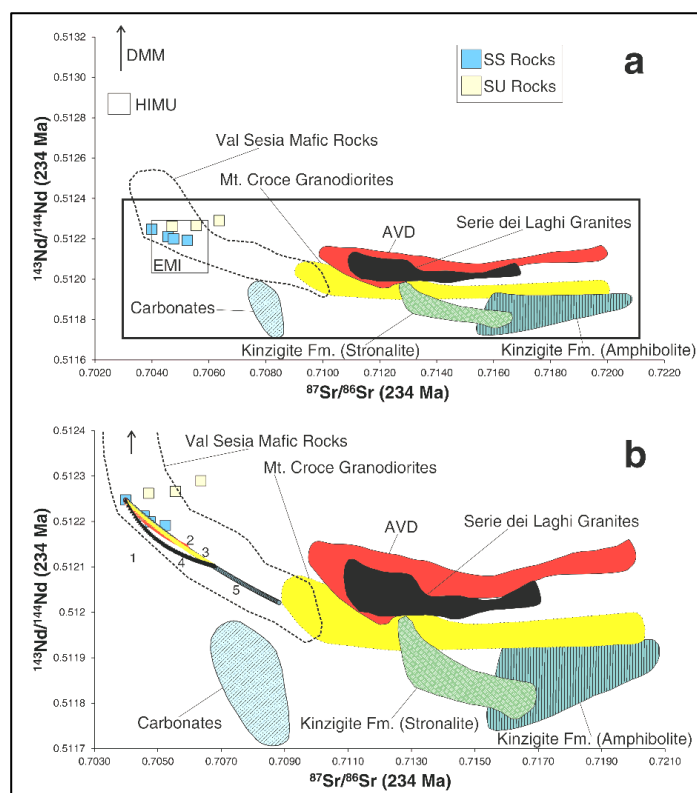
Fig. 23. Diagrams showing the $^{87}Sr/^{86}Sr$ vs. $^{143}Nd/^{144}Nd$ isotopic ratios of Predazzo Intrusive Complex rocks compared to those of Permo-Triassic crustal components (all values corrected to 234 Ma). SS Shoshonitic Silica Saturated, SU Shoshonitic Silica Undersaturated. Triassic carbonates field from Martin & Macdougall (1995) and Blendinger et al. (2015); Permian intrusives (Mt. Croce and Serie dei Laghi) field from Rottura et al. (1997) and Sinigoi et al. (2016, and references therein); Atesina Volcanic District (AVD) Permian ignimbrites field from Barth et al. (1993); Val Sesia Permian mafic rocks field from Voshage et al. (1990), Pin & Sills (1986) and Sinigoi et al. (2016); Kinzigite formation field from Voshage et al. (1990). a) Sr–Nd isotopic ratios of Predazzo Intrusive Complex rocks plotted against those of the Permo-Triassic crustal components, the enriched 1 (EMI), high-μ (HIMU, where μ = $^{238}U/^{204}Pb$), and depleted (DMM) mantle end-members (Zindler & Hart 1986); the insert corresponds to the area reported in diagram (b). b) EC-AFC trends (Bohrson & Spera 2001; Spera & Bohrson 2001) for the Shoshonitic Silica Saturated suite by considering variable crustal assimilants. 1-assimilation of Triassic carbonates; 2-assimilation of AVD ignimbrites; 3-assimilation of Mt. Croce granodiorites; 4-assimilation of Serie dei Laghi granites; 5-assimilation of Kinzigite formation amphibolites.

4.7. Discussion

4.7.1. Emplacement of the Shoshonitic Silica Saturated and Shoshonitic Silica Undersaturated magmas

The SS and SU intrusive bodies formed as result of fractional crystallization of two distinct trachybasaltic melts, which differentiated along two independent trends over a short time span. The result of this process was the generation of a large spectrum of intrusive rocks whose cumulus+intercumulus assemblages progressively vary in composition, reaching the most evolved nature in the syenitic rocks. The textural/compositional homogeneity of the

main cumulus phases of PIC rocks, together with the scarce efficiency of syn- to post-crystallization diffusion processes on such large-sized crystals, led us to hypothesize that their composition is directly function of the physical conditions at which they formed and segregated from the melt. In this scenario, clinopyroxene and plagioclase were considered as "snapshots" of the fractional crystallization processes, able to provide informations on the *T-P* conditions of the melts from which they generated.

If we compare the clinopyroxene and plagioclase compositions to that of their host rock, in fact, the disequilibrium is evident (Fig. 18 and Fig. 19). Clinopyroxene of SS gabbros (Mg# 55), for example, are characterized by Mg# of 65-71, ideally in equilibrium with melt with Mg# < 43, quite far from the bulk rock composition of the gabbro. The most magnesian ones (Mg#$_{Cpx}$ 76-78), in pyroxenites, are theoretically in equilibrium with a trachybasaltic melt (Mg# 51), further confirming that the mafic rocks of the complex are cumulates formed during the initial stages of fractionation of the trachybasaltic melt. On the other hand, the less magnesian clinopyroxene crystals tracked in syenites were almost in equilibrium with their host rocks, corroborating the assumption that the more differentiated rocks of the complex resemble the composition of melts and approach the eutectic of the system. On the basis of the results obtained by the proposed "equilibration model", in turn supporting the differentiation model of Chapter 3, PIC rocks were formed during progressive stages of fractional crystallization from starting trachybasaltic melts.

Once evaluated the disequilibrium conditions and reconducted the clinopyroxene/plagioclase compositions to their ideal equilibrium conditions, thermobarometric and hygrometric calculations enabled us to retrieve the *T-P*-H_2O parameters of the less evolved melts in the feeding system. The "classical" thermobarometric approach for intrusive rocks (amphibole-plagioclase and biotite equations) was then used to verify the previous results. These thermobarometers and hygrometers provided *T-P*-H_2O informations for the later crystallization stages.

According to our estimates, some differences between the emplacement conditions of SS and SU magmas can be highlighted. Oxygen fugacities of the PIC plumbing system are between -0.1 and +0.7 ΔFMQ (Fig. 22), confirming the oxidation conditions proposed by Bonadiman *et al.* (1994) for Mt. Monzoni intrusion at comparable temperature intervals, further highlighting the low to moderate oxidizing components that characterized the magmatic systems of the Dolomitic Area during Triassic.

On the basis of clinopyroxene-melt thermometric and hygrometric calculations, SS magmas result slightly water-enriched (H_2O = 2.0-2.5 wt%) with respect to SU ones (H_2O =1.0- 1.5 wt%), during the first crystallization stages (*T* ~1000-1100°C, Fig. 21; Table A4.9). With

increasing differentiation, the water content of PIC rocks increased up to 5-8 wt%, value compatible with the amount of fractionation (79-94%) proposed in Chapter 3, by taking into account the role of amphibole and biotite during differentiation.

The *T-P* estimates (Fig. 21; Table A4.9) indicated that both magma batches cooled from a starting *T* of ~1000-1100°C (cumulus assemblage) down to ~600°C (intercumulus assemblage), sharing a common thermal regime. The pressure obtained by applying various mineral-mineral and mineral-melt equilibria were subsequently used to estimate the emplacement depth of the PIC plumbing system, and all the pressures were filtered to extrapolate the best-fit from all models, taking into account the errors of the different methods (Table A4.9). The resulting pressure values were between 40 and 170 MPa for both SS and SU intrusive bodies, yielding a depth of about 1.4-5.6 km considering a *ΔP/Δz* of 29 MPa/km. With respect to the depth (10-17 km) proposed by Menegazzo Vitturi *et al.* (1995), our estimates suggested that PIC represents an intrusion in the shallow crust, with SS and SU magma batches emplaced within the same thermal regime. Despite the common geothermobarometric evolution and slightly different water contents, SS and SU bodies can be distinguished in terms of $^{87}Sr/^{86}Sr$ and $^{143}Nd/^{144}Nd$, reinforcing the preliminary PIC model that, on the basis of mineral and bulk rock elemental geochemistry (see Chapter 3) suggested that SS and SU series represent two independent magma pulses.

EC-AFC models (Bohrson & Spera, 2001; Spera & Bohrson, 2001) show that assimilation of various types of Permo-Triassic crustal components by a starting SS magma could not account for the higher $^{143}Nd/^{144}Nd$ of the SU batch, ruling out any possible derivation of the SU suite from the SS one. Therefore, the Nd isotopic enrichment of the SU suite could be interpreted as an original mantle signature or, alternatively, could be ascribed to assimilation processes occurring within the crust. We prefer the first hypothesis, since the second one would imply the existence of a common mantle-segregated magma with a $^{143}Nd/^{144}Nd$ ratio high enough to be able to "split" in the SS and SU trends by varying the nature of the assimilant, and such a magma has never been documented in the Dolomitic Area.

The same EC-AFC models demonstrated that both suites assimilated a small proportion of crustal components (5-6% on average, Fig. 23). That amount of assimilation is, however, able to explain the $^{143}Nd/^{144}Nd$ variation throughout SS/SU samples, being that the $^{87}Sr/^{86}Sr$ was affected by late contamination that occurred at the intrusion edges. The fit between PIC isotopic data and the crustal end-members of the Triassic carbonates, the Permian magmatic rocks and the metamorphic basement of the Ivrea Zone is consistent with a geochemical influence on the PIC of a basement that could be attributed to the Ivrea Zone. This hypothesis

was also suggested by Barth *et al.* (1993) to explain the Atesina Volcanic District-Cima d'Asta magma genesis.

In summary, both SS and SU batches are characterized by a strong contribution of an enriched mantle component, even if the lack of primitive products cannot directly quantify its role in the original source. Anyway, if examined in the light of their temporal relationships, the major, trace element and Sr-Nd isotopic signature of the SS and SU bodies enable to define the progressive evolution of the PIC magmatic suites. In turn, this geochemical evolution could be linked to a time-related (slight) variation of the mantle source, even if an accurate dating of the two single bodies would help in better deciphering the time scale of such process. On the other side, the magmatic evolution in the shallow crust for both the SS and SU batches was confined in the same thermal regime.

4.7.2. Origin of the Granitic Unit

The GU rocks (granites and syenogranites) differ from the other PIC magmatic suites (SS and SU), mainly in terms of silica saturation, FeO, MgO, K_2O and Rb contents (see Chapter 3). Moreover the estimated volume of the GU portion of the complex (1.1 km^3) is unrealistically larger than that of the SS/SU syenites (≤ 0.25 km^3) if we consider the already high ($> 90\%$) fractionation degrees from which these latters generated. This means that, if the GU portion was the result of ~95% fractionation of a SS/SU magma, ~20 km^3 of SS/SU rocks should be intruded somewhere. This fact is in stark contrast to what is observable on field.

The GU magmas evolved at redox states comparable to SS/SU ones (about +0.4 ΔFMQ) and record temperatures down to 800-850°C (Fig. 8). Put this all together, it is reasonable to hypothesize that the GU granites/syenogranites were generated by magmatic differentiation from a calc-alkaline parental melt, the primitive/intermediate products of which are not exposed in the PIC area. It should be emphasized that GU rocks are similar to the Middle Triassic calc-alkaline/high-K calc-alkaline rhyolites found in Carnia (Tarvisio area, Julian Alps; Gianolla, 1992) and Alto Vicentino regions (Recoaro-Schio area, Southern Alps; De Vecchi *et al.*, 1974; Barbieri *et al.*, 1982). In these latters, the entire high-K calc-alkaline trend is documented, further highlighting the existence of a similar differentiation suite during the Triassic magmatic event. In such a context, GU rocks could represent the corresponding intrusives of the rhyolites of these areas, even if further studies are needed to better investigate this comparison.

4.7.3. Solidification time of PIC

According to Bonadiman *et al.* (1994) the solidification time of Mt. Monzoni intrusion, emplaced at *P-T*-z conditions similar to those of PIC, was about 300 ka. The thermobarometric results obtained for PIC magmas and their subsequent application to the Spera (2000), Bohrson & Spera (2001) and Spera & Bohrson (2001) equations, enabled to model the cooling time of PIC, expected to be slightly higher than that of Mt. Monzoni, due to its larger volume (4.5 km^3 *vs.* 1.0-1.5 km^3).

In order to make an accurate comparison with Bonadiman *et al.* (1994), Spera (1980) equation was applied to PIC by assuming the thermal estimates already used for the EC-AFC calculations and/or derived from Rhyolite-MELTS modelling (see Table 4). By taking into account the whole volume of PIC, the solidification time resulted about 700 ka. Even if this time value was obtained without discriminating the single volumes of the SS, SU and GU bodies, it was considered reliable taking into account the similar thermal regimes calculated for the SS, SU and GU suites and the limited re-heating effects provided by the subsequent magma pulses.

4.8. Conclusions

A coupled thermobarometric and isotopic study of the main magmatic suites of the Predazzo Intrusive Complex enabled us to set out some remarkable points on the emplacement conditions of the Middle Triassic magmas in the Dolomitic Area. They can be summarized as:

1. Predazzo Intrusive Complex emplacement occurred at a depth of 1.4-5.6 km (40-165 MPa), consistent with the field relationships suggesting consanguinity with the overlying effusive rocks. Its solidification time was about 700 ka, slightly higher but comparable to that proposed by Bonadiman *et al.* (1994) for the near Mt. Monzoni intrusion.

2. Despite similar *T-P* of magma emplacement of the three unites, H_2O and fO_2 data indicated that SU primary magmas were characterized by lower water contents and oxidizing conditions than the SS ones (1.0-1.5 *vs.* 2.0-2.5 H_2O wt%; -0.1/+0.33 *vs.* +0.2/+0.7 ΔFMQ, respectively). Plagioclase-melt, amphibole and K-feldspar-melt hygrometers indicated highly hydrated conditions of magmas and progressive H_2O enrichment during differentiation.

3. The $^{87}Sr/^{86}Sr$ and $^{143}Nd/^{144}Nd$ of PIC magmas plot in the enriched mantle source field. This feature speaks in favour of the presence of a subduction-signature in the mantle beneath Southern Alps during Triassic, as already proposed by Bonadiman *et*

al. (1994) and Zanetti *et al.* (2013). Even if the absence of primary products in the Dolomitic Area prevents to exactly quantify the role of the enriched mantle component in the magma genesis, its contribution was undoubtedly high.

4. The EC-AFC models cannot account for the genesis of SU rocks via crustal assimilation starting from a SS magma, thus indicating two distinct geochemical signatures for SS and SU magmas. In turn, this difference could be ascribed to a time-related change in the mantle source, slightly moving towards a more $^{143}Nd/^{144}Nd$ enriched component.

5. A low degree of crustal assimilation (5-6%) was able to explain the Nd isotopic variability of both SS and SU magmas, whereas the Sr isotopic variations were more likely the results of contamination processes at PIC edges. Fractional crystallization was the major (and almost only) process acting during the differentiation of SS and SU magmas, confirming what hypothesized by Petersen *et al.* (1980) and proposed in Chapter 3. The signature of the Triassic magmas is consistent with an Ivrea-like basement beneath the Dolomitic Area.

6. Despite petrography, whole-rock and mineral chemistry suggested an I-type affinity for GU granites/syenogranites, the wide range and the uncertainty on their isotopic signature leaves the question on the origin of GU suite still unsolved. However, the geochemical and petrographic similarities with the coheval calc-alkaline/high-K calc-alkaline rhyolites found in Carnia (Gianolla, 1992) and Alto Vicentino (De Vecchi *et al.*, 1974; Barbieri *et al.*, 1982; Bellieni *et al.*, 2010) suggest the presence of a high-K calc-alkaline series also in the Dolomitic Area.

Appendix A4

Table A4.1. Major and trace element whole rock composition of selected Shoshonitic Silica Saturated (SS), Shoshonitic Silica Undersaturated (SU) and Granitic Unit (GU) rocks. Px: pyroxenite; Gb: gabbro; Mzgb: monzogabbro; Mzdr: monzodiorite; Mz: monzonite; Sy: syenite; Gr: granite; Sygr: syenogranite. Fe_2O_3 and FeO were calculated by considering a Fe_2O_3/FeO ratio of 0.15, in agreement with a fO_2 around FMQ buffer (Kress & Carmichael, 1991). Mg# = Mg/[Mg Fe^{2+}] mol%; n.d. = not detected. All trace element (ppm) were analysed by ICP-MS except Pb, Zn, Ni, Co, Cr, V, Cu and Ba (XRF).

Suite	SS	SS	SS	SS	SS	SS	SU	SU	SU	SU	SU	SU	SU	GU	GU
Lithology	Px	Gb	Mzgb	Mzdr	Mz	Sy	Gb	Mzgb	Mzdr	Mz	Sy	Sy	Gr	Sygr
Sample	FC31E	FC30C	FC43D	FC37B	EM79	EM64	EM15	FC2B	EM9	EM6	EM5	EM107	EM90B	EM31
Oxide (wt%)															
SiO₂	35.48	45.64	52.56	55.43	61.84	67.91	49.83	52.39	55.48	56.86	60.22	62.44	76.41	70.21
TiO₂	2.07	1.08	0.85	0.80	0.43	0.17	0.93	1.13	0.24	0.58	0.46	0.28	0.04	0.26
Al₂O₃	6.20	16.78	18.92	17.30	19.82	16.54	17.91	17.08	23.80	21.71	19.58	18.68	13.79	15.58
Fe₂O₃	3.74	1.55	1.03	1.01	0.47	0.22	1.34	1.06	0.37	0.59	0.49	0.21	0.11	0.31
FeO	24.90	10.34	6.88	6.74	3.11	1.51	8.91	7.05	2.44	3.94	3.31	1.44	0.74	2.07
MnO	0.25	0.18	0.19	0.20	0.07	0.07	0.18	0.41	0.18	0.19	0.16	0.11	0.02	0.03
MgO	12.54	6.97	4.03	3.73	1.14	0.22	4.97	4.80	0.51	1.50	0.84	0.45	0.28	0.24
CaO	13.57	14.16	8.68	6.71	3.34	0.90	9.56	8.28	3.94	4.81	3.80	3.20	1.65	1.01
Na₂O	0.51	1.09	2.79	3.24	3.62	4.27	2.81	4.80	5.29	5.16	5.70	3.54	5.44	3.99
K₂O	0.73	2.16	3.37	4.30	5.96	8.18	2.80	2.62	7.73	4.38	5.25	9.22	1.51	6.29
P₂O₅	0.02	0.05	0.68	0.54	0.20	0.00	0.76	0.38	0.02	0.28	0.18	0.43	0.00	0.00
Tot.	100	100	100	100	100	100	100	100	100	100	100	100	100	100
LOI	0.00	2.57	1.33	1.09	1.72	0.99	1.21	1.57	4.33	1.13	0.60	1.20	1.53	1.23
Mg#	**47.29**	**54.56**	**51.08**	**49.65**	**39.48**	**20.72**	**49.86**	**54.81**	**27.26**	**40.34**	**31.01**	**35.57**	**40.60**	**17.33**
Trace element (ppm)															
Pb	14.8	14.2	17.8	27.5	21.0	23.0	13.0	44.1	45.0	37.0	28.0	27.0	n.d.	13.0
Zn	148	72.3	103	107	51.0	54.0	115	202	147	148	86.0	50.0	8.00	30.0
Ni	69.3	32.0	5.90	5.90	6.00	5.00	15.0	5.90	11.0	5.00	8.00	6.00	4.00	7.00
Co	62.9	52.7	27.2	24.4	9.00	6.00	40.0	29.5	4.00	9.00	7.00	3.00	n.d.	2.00
Cr	61.7	68.6	6.9	11.2	9.00	5.00	23.0	58.9	9.00	3.00	5.00	1.00	5.00	3.00
V	1600	565	153	144	32.0	15.0	239	165	36.0	80.0	67.0	29.0	13.0	9.00
Cu	13.0	17.3	85.7	79.4	n.d.	n.d.	n.d.	35.3	n.d.	n.d.	n.d.	n.d.	n.d.	n.d.
Rb	16.2	42.3	52.7	81.4	221	187	42.5	89.1	326	184	97.9	318	112	284
Ba	178	223	479	546	772	553	782	482	506	1129	498	616	121	190
Sr	95.4	440	676	556	755	284	849	621	818	1351	254	569	83.4	28.2
Nb	3.83	3.68	10.5	13.4	18.0	24.0	7.22	44.4	60.0	18.0	35.3	52.0	64.7	48.7
Zr	47.0	39.0	38.0	34.5	208	323	35.1	359	499	262	206	623	153	211
Hf	1.60	1.48	1.54	1.67	1.71	5.31	1.51	7.48	4.54	n.d.	5.66	6.95	5.05	5.81
U	0.22	0.48	0.93	1.59	2.46	3.89	1.08	2.92	11.8	7.39	5.26	11.6	11.0	2.55
Th	0.66	1.67	3.68	6.56	12.5	27.0	3.60	9.57	46.7	27.8	33.7	112	44.3	14.4
Y	14.1	11.1	11.9	13.7	21.9	24.5	13.6	23.8	13.7	26.0	14.8	49.9	27.1	5.0
Ta	0.26	0.30	0.52	0.68	n.d.	n.d.	0.51	1.57	n.d.	n.d.	1.34	n.d.	1.51	1.06
La	4.49	7.16	15.9	18.5	26.6	24.3	17.7	95.6	63.9	45.9	38.4	117	2.12	9.75
Ce	12.4	15.5	37.2	49.6	59.5	56.8	44.5	195	99.5	85.1	125	237	6.44	33.6
Pr	2.01	2.47	4.34	4.96	7.10	6.96	4.80	13.6	8.99	8.95	8.04	24.9	1.24	2.51
Nd	10.5	11.9	18.6	20.8	27.2	27.1	20.8	47.3	24.3	30.1	28.9	81.8	7.46	9.21
Sm	2.92	2.87	3.63	4.11	5.60	5.34	4.11	7.18	3.24	4.94	4.49	12.9	3.46	1.55
Eu	0.65	0.77	0.89	0.96	1.70	1.07	1.16	1.33	0.89	1.68	0.93	1.75	0.21	0.09
Gd	2.67	2.50	3.19	3.66	5.20	4.74	3.71	6.86	4.18	5.46	4.03	12.2	3.57	1.44
Tb	0.46	0.43	0.47	0.55	0.78	0.76	0.54	0.88	0.41	0.60	0.56	1.55	0.82	0.21
Dy	2.41	2.12	2.17	2.58	4.16	4.35	2.47	3.93	2.24	3.18	2.55	8.67	4.95	1.08
Ho	0.47	0.42	0.43	0.52	0.89	0.92	0.49	0.80	0.52	0.75	0.54	1.72	1.06	0.23
Er	1.22	1.08	1.12	1.38	2.25	2.57	1.27	2.22	1.59	2.09	1.53	5.34	3.04	0.73
Tm	0.18	0.17	0.18	0.22	0.38	0.44	0.20	0.37	0.26	0.35	0.27	0.84	0.52	0.13
Yb	1.06	0.96	0.95	1.25	2.51	3.08	1.08	2.16	1.78	2.30	1.61	5.78	3.17	0.89
Lu	0.15	0.14	0.15	0.19	0.35	0.47	0.17	0.34	0.27	0.35	0.25	0.83	0.45	0.14

Table A4.2. Major element analyses of representative Fe-Ti oxides from Shoshonitic Silica Saturated (SS) and Shoshonitic Silica Undersaturated (SU) rocks. Px: pyroxenite; Gb: gabbro; Mzgb: monzogabbro; Mzdr: monzodiorite; Mz: monzonite; Sy: syenite; Gr: granite; Sygr: syenogranite.

Suite	SS	SS	SS	SS	SS	SS	SS	SS	SS	SS	SU	SU	SU	SU	SU	SU
Sample	FC31E	FC31E	FC30C	FC30C	FC43D	FC43D	FC37B	FC37B	EM79	EM79	EM15	EM15	FC2B	FC2B	EM107	EM107
Lithology	Px	Px	Gb	Gb	Mzgb	Mzgb	Mzdr	Mzdr	Mz	Mz	Gb	Gb	Mzgb	Mzgb	Sy	Sy
Name	Ox1	Ox2	Ox4	Ox6	Ox1	Ox3	Ox2	Ox3	Ox1	Ox2	Ox3	Ox4	Ox4	Ox5	Ox1	Ox2
SiO_2	0.043	0.039	0.054	0.075	0.075	0.041	0.040	0.038	0.073	0.061	0.048	0.063	0.033	0.050	0.065	0.048
TiO_2	3.983	4.645	1.841	2.204	0.652	0.936	1.100	13.238	0.544	0.302	2.944	3.401	6.038	4.989	1.161	1.126
Al_2O_3	1.982	2.284	0.656	0.578	0.398	0.472	0.229	2.167	0.378	0.337	1.048	1.363	1.211	1.194	0.107	0.406
Cr_2O_3	0.078	0.116	0.141	0.154	0.058	0.065	0.059	0.032	0.042	0.077	0.097	0.082	0.044	0.024	0.054	0.019
FeO_{TOT}	86.418	85.247	89.073	85.525	91.295	90.555	90.945	76.377	90.922	91.237	88.367	85.814	84.140	85.304	90.306	90.672
MnO	0.233	0.287	0.184	0.394	0.086	0.141	0.110	0.356	0.069	0.022	0.334	0.334	1.727	1.543	0.407	0.434
MgO	0.553	0.389	0.043	0.025	0.000	0.038	0.005	0.039	0.002	0.000	0.141	0.235	0.048	0.103	0.008	0.042
CaO	0.001	0.001	0.007	0.107	0.013	0.064	0.023	0.057	0.043	0.016	0.028	0.022	0.002	0.015	0.073	0.007
NiO	0.036	0.048	0.000	0.016	0.000	0.003	0.023	0.000	0.031	0.000	0.000	0.008	0.023	0.000	0.000	0.000
V_2O_3	0.558	0.593	0.704	0.646	0.531	0.527	0.693	0.590	0.226	0.234	0.506	0.528	0.323	0.322	0.208	0.412
ZnO	0.080	0.091	0.109	0.490	0.056	0.043	0.021	0.059	0.021	0.009	0.132	0.109	0.554	0.447	0.025	0.109
Total	93.966	93.742	92.813	90.215	93.166	92.885	93.247	92.953	92.351	92.295	93.646	91.958	94.144	93.991	92.415	93.276
A.F.U.																
Si	0.002	0.001	0.002	0.003	0.003	0.002	0.002	0.001	0.003	0.002	0.002	0.002	0.001	0.002	0.003	0.002
Ti	0.114	0.134	0.054	0.067	0.019	0.027	0.032	0.389	0.016	0.009	0.085	0.100	0.175	0.144	0.034	0.033
Al	0.089	0.103	0.030	0.027	0.018	0.022	0.010	0.100	0.017	0.015	0.048	0.063	0.055	0.054	0.005	0.018
Cr	0.002	0.004	0.004	0.005	0.002	0.002	0.002	0.001	0.001	0.002	0.003	0.003	0.001	0.001	0.002	0.001
Fe^{3+}	1.677	1.623	1.854	1.828	1.936	1.919	1.920	1.119	1.944	1.960	1.775	1.730	1.592	1.653	1.920	1.912
Fe^{2+}	1.077	1.104	1.047	1.055	1.019	1.022	1.030	1.376	1.016	1.010	1.068	1.078	1.117	1.090	1.023	1.018
Mn	0.008	0.009	0.006	0.013	0.003	0.005	0.004	0.012	0.002	0.001	0.011	0.011	0.056	0.050	0.013	0.014
Mg	0.031	0.022	0.002	0.002	0.000	0.002	0.000	0.002	0.000	0.000	0.008	0.014	0.003	0.006	0.000	0.002
Tot. Cat.	3.000	3.000	3.000	3.000	3.000	3.000	3.000	3.000	3.000	3.000	3.000	3.000	3.000	3.000	3.000	3.000
Tot. Oxy.	4.000	4.000	4.000	4.000	4.000	4.000	4.000	4.000	4.000	4.000	4.000	4.000	4.000	4.000	4.000	4.000

Table A4.3. Major element analyses of representative clinopyroxene from Shoshonitic Silica Saturated (SS) and Shoshonitic Silica Undersaturated (SU) rocks. Px: pyroxenite; Gb: gabbro; Mzgb: monzogabbro; Mzdr: monzodiorite; Sy: syenite.

Suite	SS	SS	SS	SS	SS	SS	SS	SS	SS	SU	SU	SU	SU	SU	SU
Sample	FC31E	FC31E	FC30C	FC30C	FC30C	FC43D	FC43D	FC37B	FC37B	EM15	EM15	FC2B	FC2B	EM107	EM107
Lithology	Px	Px	Gb	Gb	Gb	Mzgb	Mzgb	Mzdr	Mzdr	Gb	Gb	Mzgb	Mzgb	Sy	Sy
Name	Cpx1	Cpx4	Cpx5	Cpx7 core	Cpx7 rim	Cpx1	Cpx2	Cpx1	Cpx 3	Cpx2	Cpx 3	Cpx2	Cpx 6	Cpx1	Cpx3
SiO_2	52.625	51.811	51.879	52.408	52.500	52.198	51.129	50.820	51.150	51.097	52.640	50.321	50.954	51.495	50.536
TiO_2	0.296	0.307	0.235	0.053	0.126	0.046	0.444	0.549	0.445	0.461	0.041	0.714	0.590	0.084	0.140
Al_2O_3	1.688	2.103	1.202	0.680	0.661	0.401	2.232	2.886	2.257	2.204	0.407	2.870	2.370	0.814	1.241
FeO_{TOT}	7.860	7.583	10.849	10.286	11.802	11.720	10.098	10.171	9.806	11.690	10.805	8.424	8.854	12.063	14.221
MnO	0.265	0.239	0.484	0.508	0.511	0.751	0.480	0.422	0.443	0.531	0.614	0.509	0.598	1.236	1.487
MgO	14.843	14.850	13.536	13.260	12.530	11.506	13.899	14.008	13.648	12.505	12.579	12.532	12.225	10.061	8.680
CaO	22.279	22.289	21.437	22.181	21.790	22.856	20.626	20.329	21.238	20.875	22.521	22.953	22.689	23.700	22.733
Na_2O	0.260	0.287	0.229	0.232	0.211	0.186	0.294	0.258	0.287	0.288	0.175	0.806	0.818	0.335	0.574
Total	100.117	99.469	99.861	99.611	100.145	99.672	99.220	99.447	99.274	99.689	99.798	99.129	99.103	99.811	99.450
A.F.U.															
Si	1.949	1.935	1.957	1.979	1.982	1.989	1.929	1.908	1.930	1.934	1.989	1.904	1.930	1.973	1.960
Ti	0.008	0.009	0.007	0.002	0.004	0.001	0.013	0.016	0.013	0.013	0.001	0.020	0.017	0.002	0.004
IV Al	0.051	0.065	0.043	0.021	0.018	0.011	0.071	0.092	0.070	0.066	0.011	0.096	0.070	0.027	0.040
VI Al	0.023	0.028	0.010	0.009	0.012	0.007	0.028	0.036	0.030	0.033	0.007	0.032	0.036	0.010	0.017
Fe_{TOT}	0.244	0.237	0.342	0.325	0.373	0.374	0.319	0.319	0.309	0.370	0.341	0.267	0.280	0.387	0.461
Mn	0.008	0.008	0.015	0.016	0.016	0.024	0.015	0.013	0.014	0.017	0.020	0.016	0.019	0.040	0.049
Mg	0.820	0.827	0.761	0.746	0.705	0.654	0.782	0.784	0.768	0.706	0.708	0.707	0.690	0.575	0.502
Ca	0.884	0.892	0.866	0.897	0.882	0.933	0.834	0.818	0.859	0.847	0.912	0.931	0.921	0.973	0.945
Na	0.019	0.021	0.017	0.017	0.015	0.014	0.022	0.019	0.021	0.021	0.013	0.059	0.060	0.025	0.043
Tot. Cat.	4.012	4.020	4.018	4.013	4.007	4.007	4.017	4.016	4.016	4.011	4.006	4.038	4.028	4.016	4.026
End Members															
Wo	45.4	45.6	44.0	45.6	45.0	47.6	43.1	42.6	44.4	44.0	46.5	48.9	48.7	50.3	49.5
En	42.1	42.3	38.6	37.9	36.0	33.3	40.4	40.8	39.7	36.7	36.1	37.1	36.5	29.7	26.3
Fs	12.5	12.1	17.4	16.5	19.0	19.1	16.5	16.6	16.0	19.3	17.4	14.0	14.8	20.0	24.2
Tot.	100	100	100	100	100	100	100	100	100	100	100	100	100	100	100

Table A4.4. Major element analyses of representative amphibole from Shoshonitic Silica Saturated (SS) and Shoshonitic Silica Undersaturated (SU) rocks. Px: pyroxenite; Gb: gabbro; Mzgb: monzogabbro; Mzdr: monzodiorite; Mz: monzonite; Sy: syenite; Gr: granite; Sygr: syenogranite.

Suite	SS	SS	SS	SS	SS	SS	SU	SU	SU	SU
Sample	FC30C	FC30C	FC43D	FC43D	FC37B	FC37B	EM15	EM15	FC2B	FC2B
Lithology	Gb	Gb	Mzgb	Mzgb	Mzdr	Mzdr	Gb	Gb	Mzgb	Mzgb
Name	Amph4	Amph5	Amph1	Amph2	Amph1	Amph3	Amph4	Amph5	Amph3	Amph4
SiO_2	45.226	49.122	46.395	45.644	44.471	44.691	51.335	50.497	38.846	39.323
TiO_2	1.021	0.841	0.800	1.099	1.491	1.519	0.065	0.044	3.327	3.135
Al_2O_3	7.698	5.108	6.485	6.978	6.707	7.007	3.504	4.014	12.046	11.628
FeO_{TOT}	19.262	15.929	19.541	19.819	19.801	20.216	17.004	19.362	17.221	16.135
MnO	0.341	0.301	0.591	0.581	0.530	0.458	0.471	0.514	0.810	0.839
MgO	9.883	12.885	10.516	10.133	9.573	9.462	13.130	10.808	9.078	9.764
CaO	11.903	11.864	10.562	11.023	11.011	10.839	10.965	11.798	11.296	11.453
Na_2O	0.990	0.755	1.130	1.298	1.368	1.467	0.475	0.393	2.395	2.545
K_2O	0.872	0.418	0.651	0.722	0.733	0.767	0.118	0.213	1.835	1.816
F	-	-	-	-	0.221	0.270	-	-	-	-
Cl	-	-	-	-	0.257	0.285	-	-	-	-
Total	**97.221**	**97.249**	**96.683**	**97.317**	**96.163**	**96.975**	**97.076**	**97.643**	**96.853**	**96.642**
A.F.U.										
IV Si	6.819	7.210	6.919	6.831	6.819	6.796	7.439	7.460	6.000	6.075
IV Al	1.181	0.790	1.081	1.169	1.181	1.204	0.561	0.540	2.000	1.925
VI Al	0.187	0.094	0.059	0.061	0.032	0.051	0.037	0.159	0.193	0.192
VI Ti	0.116	0.093	0.090	0.124	0.172	0.174	0.007	0.005	0.387	0.364
VI Cr	0.003	0.001	0.001	0.000	0.000	0.000	0.001	0.000	0.000	0.000
VI Fe^{3+}	0.456	0.485	1.015	0.811	0.637	0.692	0.949	0.485	0.217	0.092
VI Fe^{2+}	1.973	1.471	1.422	1.669	1.902	1.878	1.112	1.908	2.008	1.993
VI Mn	0.044	0.037	0.075	0.074	0.069	0.059	0.058	0.064	0.106	0.110
VI Mg	2.221	2.819	2.338	2.261	2.188	2.145	2.836	2.380	2.090	2.249
A Ca	1.923	1.866	1.688	1.767	1.809	1.766	1.702	1.867	1.869	1.896
A Na	0.289	0.215	0.327	0.377	0.407	0.433	0.133	0.113	0.717	0.762
A K	0.168	0.078	0.124	0.138	0.143	0.149	0.022	0.040	0.362	0.358
Tot. Cat.	15.380	15.159	15.138	15.282	17.359	17.347	14.858	15.020	15.948	16.016
Tot. Oxy.	23	23	23	23	23	23	23	23	23	23
Amphibole group	Ca	Ca	Ca	Ca	Ca	Ca	Ca	Ca	Ca	Ca
(Ca+Na) (B)	2.000	2.000	2.000	2.000	2.000	2.000	1.836	1.980	2.00	2.02
Na (B)	0.077	0.134	0.312	0.233	0.191	0.234	0.133	0.113	0.13	0.12
(Na+K) (A)	0.380	0.159	0.138	0.282	0.359	0.347	0.022	0.040	0.95	1.00
$Mg/(Mg+Fe^{2+})$	0.530	0.657	0.622	0.575	0.535	0.533	0.718	0.555	0.51	0.53
$Fe^{3+}/(Fe^{3+}+Al\ VI)$	0.709	0.838	0.945	0.930	0.953	0.931	0.962	0.753	0.53	0.32
Sum of S2	13	13	13	13	13	13	13	13	13	13

Table A4.5. Major element analyses of representative biotite from Shoshonitic Silica Saturated (SS), Shoshonitic Silica Undersaturated (SU) and Granitic Unit (GU) rocks. Px: pyroxenite; Gb: gabbro; Mzgb: monzogabbro; Mzdr: monzodiorite; Mz: monzonite; Sy: syenite; Gr: granite; Sygr: syenogranite.

Suite	SS	SS	SS	SS	SS	SS	SS	SS	SS	SS	SU	SU	SU	SU	GU	GU
Sample	FC31E	FC31E	FC30C	FC30C	FC43D	FC43D	FC37B	FC37B	EM79	EM79	EM15	EM15	FC2B	FC2B	EM31	EM31
Lithology	Px	Px	Gb	Gb	Mzgb	Mzgb	Mzdr	Mzdr	Mz	Mz	Gb	Gb	Mzgb	Mzgb	Sygr	Sygr
Name	Bt1	Bt3	Bt1	Bt8	Bt1	Bt2	Bt1	Bt2	Bt4	Bt5	Bt10	Bt11	Bt2	Bt3	Bt4	Bt8
SiO_2	37.724	38.118	36.207	35.771	35.782	34.358	36.093	35.818	36.434	34.846	36.043	35.855	35.616	36.211	30.073	31.488
TiO_2	4.627	4.413	4.875	5.01	4.142	3.653	4.593	4.694	3.027	4.737	4.328	4.473	4.453	4.555	2.241	3.44
Al_2O_3	15	15.036	13.373	13.49	13.43	13.27	12.819	12.775	11.494	13.38	13.722	13.693	14.615	14.398	15.145	14.213
FeO_{TOT}	8.558	9.028	22.175	19.999	22.814	25.66	22.607	23.188	25.44	24.231	19.559	20.016	17.268	17.256	34.62	32.02
MnO	0.061	0.044	0.17	0.152	0.298	0.413	0.314	0.27	0.323	0.297	0.172	0.203	0.657	0.606	0.464	0.426
MgO	18.939	19.126	9.87	11.128	9.849	7.734	9.261	8.89	8.919	8.276	11.708	11.699	12.5	12.583	4.849	4.96
CaO	0.058	0.029	0.028	0.006	0.074	0.494	0.038	0.088	0.027	0.017	0.022	0.154	0.036	0.005	0.069	0.086
Na_2O	0.432	0.394	0.142	0.156	0.145	0.07	0.195	0.136	0.088	0.231	0.174	0.094	0.401	0.426	0.045	0.047
K_2O	9.105	8.928	9.168	9.335	9.088	8.035	8.346	8.132	8.765	8.883	9.198	8.822	8.889	9.067	4.418	6.025
Cl	0.103	0.221	0.332	0.331	0.319	0.623	0.372	0.461	1.197	0.404	0.265	0.32	0.053	0.041	0.373	0.434
F	-	-	-	-	-	-	0.296	0.298	-	-	-	-	-	-	-	-
Total	94.821	95.458	96.482	95.468	95.943	94.392	94.935	94.754	95.772	95.976	95.268	95.396	94.965	95.308	92.308	93.151
A.F.U. (all Fe assumed as Fe^{2+}).																
Si	2.754	2.765	2.789	2.762	2.780	2.764	2.830	2.823	2.898	2.753	2.775	2.760	2.730	2.754	2.549	2.628
Ti	0.254	0.241	0.282	0.291	0.242	0.221	0.271	0.278	0.181	0.282	0.251	0.259	0.257	0.261	0.143	0.216
Al	1.291	1.285	1.214	1.227	1.230	1.258	1.185	1.187	1.078	1.246	1.245	1.242	1.320	1.291	1.513	1.398
Fe^{2+}	0.523	0.548	1.428	1.291	1.482	1.726	1.482	1.528	1.692	1.601	1.259	1.289	1.107	1.098	2.454	2.235
Mn	0.004	0.003	0.011	0.010	0.020	0.028	0.021	0.018	0.022	0.020	0.011	0.013	0.043	0.039	0.033	0.030
Mg	2.061	2.068	1.133	1.281	1.141	0.928	1.083	1.045	1.058	0.975	1.344	1.343	1.428	1.427	0.613	0.617
Ca	0.005	0.002	0.002	0.000	0.006	0.043	0.003	0.007	0.002	0.001	0.002	0.013	0.003	0.000	0.006	0.008
Na	0.061	0.055	0.021	0.023	0.022	0.011	0.030	0.021	0.014	0.035	0.026	0.014	0.060	0.063	0.007	0.008
K	0.848	0.826	0.901	0.919	0.901	0.825	0.835	0.818	0.889	0.895	0.903	0.866	0.869	0.880	0.478	0.642
Tot Cat.	7.801	7.793	7.783	7.805	7.824	7.804	7.739	7.725	7.834	7.808	7.816	7.800	7.817	7.811	7.795	7.781
Tot. Oxy.	11	11	11	11	11	11	11	11	11	11	11	11	11	11	11	11

Table A4.6. Major element analyses of representative plagioclase from Shoshonitic Silica Saturated (SS), Shoshonitic Silica Undersaturated (SU) and Granitic Unit (GU) rocks. Px: pyroxenite; Gb: gabbro; Mzgb: monzogabbro; Mzdr: monzodiorite; Mz: monzonite; Sy: syenite; Gr: granite; Sygr: syenogranite.

Suite	SS	SS	SS	SS	SS	SS	SS	SS	SS	SS	SU	SU	SU	SU	SU	SU	GU	GU
Sample	FC31E	FC31E	FC30C	FC30C	FC43D	FC43D	FC37B	FC37B	EM79	EM79	EM15	EM15	FC2B	FC2B	EM107	EM107	EM88	EM88
Lithology	Px	Px	Gb	Gb	Mzgb	Mzgb	Mzdr	Mzdr	Mz	Mz	Gb	Gb	Mzgb	Mzgb	Sy	Sy	Sygr	Sygr
Name	Plag2	Plag6	Plag3	Plag4	Plag2	Plag3	Plag1	Plag6	Plag1	Plag2	Plag5	Plag6	Plag2	Plag3	Plag1	Plag2	Plag1	Plag2
SiO_2	49.17	46.79	55.34	53.03	57.44	55.59	57.16	55.73	57.54	54.86	55.46	57.36	61.24	59.31	61.89	67.63	68.30	67.37
TiO_2	0.021	0.008	0.018	0.031	0.016	0.017	0.025	0.039	0.017	0.022	0.035	0.009	0.040	0.048	0.031	0.000	0.000	0.000
Al_2O_3	31.67	33.54	28.17	29.69	27.115	28.07	26.72	27.50	26.72	28.19	28.23	26.81	23.33	25.56	23.29	20.02	19.76	20.61
FeO_{TOT}	0.584	0.544	0.351	0.369	0.260	0.259	0.246	0.330	0.287	0.250	0.237	0.272	0.432	0.197	0.361	0.055	0.080	0.100
MgO	0.028	0.028	0.024	0.029	0.013	0.025	0.017	0.026	0.023	0.020	0.010	0.025	0.000	0.003	0.011	0.000	0.005	0.000
CaO	14.99	16.83	10.52	12.03	9.022	10.19	8.668	9.523	8.533	10.42	10.05	8.854	4.875	6.999	4.650	0.507	0.118	0.968
Na_2O	2.958	1.758	5.306	4.497	6.296	5.410	6.381	5.709	6.219	5.511	5.541	6.199	8.119	7.174	8.404	11.16	11.44	10.85
K_2O	0.116	0.106	0.332	0.229	0.255	0.264	0.339	0.43	0.564	0.363	0.354	0.361	1.048	0.624	0.556	0.054	0.149	0.315
Total	99.54	99.60	100.1	99.91	100.4	99.82	99.55	99.29	99.91	99.62	99.91	99.90	99.09	99.91	99.20	99.43	99.85	100.2
A.F.U.																		
Si	2.256	2.158	2.496	2.404	2.568	2.511	2.575	2.526	2.586	2.479	2.500	2.579	2.748	2.651	2.771	2.979	2.991	2.950
Ti	0.001	0.000	0.001	0.001	0.001	0.001	0.001	0.001	0.001	0.001	0.001	0.000	0.001	0.002	0.001	0.000	0.000	0.000
Al	1.712	1.823	1.497	1.586	1.429	1.494	1.419	1.469	1.416	1.501	1.500	1.421	1.234	1.347	1.229	1.039	1.020	1.063
Fe_{TOT}	0.022	0.021	0.013	0.014	0.010	0.010	0.009	0.013	0.011	0.009	0.009	0.010	0.016	0.007	0.014	0.002	0.003	0.004
Mn	0.000	0.000	0.000	0.000	0.000	0.000	0.000	0.000	0.000	0.000	0.000	0.000	0.000	0.000	0.000	0.000	0.000	0.000
Mg	0.002	0.002	0.002	0.002	0.001	0.002	0.001	0.002	0.002	0.001	0.001	0.002	0.000	0.000	0.001	0.000	0.000	0.000
Ca	0.737	0.832	0.508	0.584	0.432	0.493	0.418	0.462	0.411	0.504	0.485	0.427	0.234	0.335	0.223	0.024	0.006	0.045
Na	0.263	0.157	0.464	0.395	0.546	0.474	0.557	0.502	0.542	0.483	0.484	0.540	0.706	0.622	0.730	0.953	0.972	0.921
K	0.007	0.006	0.019	0.013	0.015	0.015	0.019	0.025	0.032	0.021	0.020	0.021	0.060	0.036	0.032	0.003	0.008	0.018
Tot. Cat.	5.000	5.000	5.000	5.000	5.000	5.000	5.000	5.000	5.000	5.000	5.000	5.000	5.000	5.000	5.000	5.000	5.000	5.000
Tot. Oxy.	7.978	7.988	8.004	7.994	8.003	8.015	7.997	7.999	8.008	7.979	7.998	8.009	7.983	7.998	8.006	8.020	8.011	8.012
End Members																		
An	73.2	83.6	51.3	58.9	43.5	50.2	42.0	46.8	41.7	50.0	49.0	43.2	23.4	33.8	22.7	2.4	0.6	4.6
Ab	26.1	15.8	46.8	39.8	55.0	48.2	56.0	50.7	55.0	47.9	48.9	54.7	70.6	62.6	74.1	97.2	98.6	93.6
Or	0.7	0.6	1.9	1.3	1.5	1.5	2.0	2.5	3.3	2.1	2.1	2.1	6.0	3.6	3.2	0.3	0.8	1.8
Tot.	100	100	100	100	100	100	100	100	100	100	100	100	100	100	100	100	100	100

Table A4.7. Major element analyses of representative K-feldspar from Shoshonitic Silica Saturated (SS), Shoshonitic Silica Undersaturated (SU) and Granitic Unit (GU) rocks. Px: pyroxenite; Gb: gabbro; Mzgb: monzogabbro; Mzdr: monzodiorite; Mz: monzonite; Sy: syenite; Gr: granite; Sygr: syenogranite.

Suite	SS	SS	SS	SS	SS	SU	GU	GU	GU	GU
Sample	FC30C	FC30C	FC43D	FC37B	EM79	FC2B	EM31	EM31	EM88	EM88
Lithology	Gb	Gb	Mzgb	Mzdr	Mz	Mzgb	Sygr	Sygr	Sygr	Sygr
Name	K-Feld1	K-Feld2	K-Feld1	K-Feld1	K-Feld2	K-Feld5	K-Feld9	K-Feld10	K-Feld3	K-Feld4
SiO_2	64.825	64.007	64.586	64.679	64.160	64.603	64.934	65.018	64.718	64.681
TiO_2	0.021	0.048	0.013	0.036	0.015	0.057	0.004	0.027	0.002	0.012
Al_2O_3	18.942	19.318	18.952	19.484	18.569	19.717	18.575	18.834	18.570	18.749
FeO_{TOT}	0.087	0.324	0.151	0.159	0.027	0.157	0.049	0.080	0.040	0.015
MgO	0.000	0.000	0.000	0.004	0.022	0.013	0.000	0.022	0.003	0.016
BaO	0.309	0.344	0.090	0.690	0.059	0.623	0.023	0.061	0.014	0.000
CaO	0.096	0.144	0.000	0.202	0.051	0.208	0.000	0.000	0.000	0.000
Na_2O	1.869	2.033	1.601	3.552	0.593	3.796	0.641	1.199	0.745	0.571
K_2O	13.543	13.103	14.342	10.911	15.758	10.522	15.840	14.982	15.818	16.038
Total	**99.693**	**99.321**	**99.734**	**99.718**	**99.253**	**99.696**	**100.103**	**100.223**	**99.912**	**100.082**
A.F.U.										
Si	2.987	2.959	2.975	2.955	2.986	2.948	2.997	2.987	2.988	2.984
Ti	0.001	0.002	0.000	0.001	0.001	0.002	0.000	0.001	0.000	0.000
Al	1.029	1.052	1.029	1.049	1.018	1.060	1.010	1.020	1.011	1.019
Cr	0.000	0.000	0.000	0.000	0.000	0.000	0.000	0.000	0.000	0.000
Fe_{TOT}	0.003	0.013	0.006	0.006	0.001	0.006	0.002	0.003	0.002	0.001
Mn	0.000	0.000	0.000	0.000	0.000	0.000	0.000	0.000	0.000	0.000
Mg	0.000	0.000	0.000	0.000	0.002	0.001	0.000	0.002	0.000	0.001
Ca	0.015	0.017	0.004	0.034	0.003	0.030	0.001	0.003	0.001	0.000
Ba	0.002	0.003	0.000	0.004	0.001	0.004	0.000	0.000	0.000	0.000
Na	0.167	0.182	0.143	0.315	0.054	0.336	0.057	0.107	0.067	0.051
K	0.796	0.773	0.843	0.636	0.935	0.613	0.933	0.878	0.932	0.944
Tot. Cat.	5.000	5.000	5.000	5.000	5.000	5.000	5.000	5.000	5.000	5.000
Tot. Oxy.	8.021	8.009	7.997	8.006	8.001	8.006	8.007	8.005	7.995	7.996
End Members										
An	1.56	1.75	0.45	3.43	0.30	3.11	0.11	0.30	0.07	0.00
Ab	17.07	18.75	14.44	31.96	5.39	34.31	5.79	10.81	6.68	5.13
Or	81.37	79.50	85.11	64.60	94.31	62.58	94.10	88.89	93.26	94.87
Tot.	100	100	100	100	100	100	100	100	100	100

Table A4.8. Whole rock $^{87}Sr/^{86}Sr$ and $^{143}Nd/^{144}Nd$ isotopes of Shoshonitic Silica Saturated (SS), Shoshonitic Silica Undersaturated (SU) and Granitic Unit (GU) rocks. Samples were corrected for 234 Ma (Laurenzi & Visonà, 1996; Mundil *et al.*, 1996) of radiogenic ingrowth using the trace element abundances determined by ICP-MS, the decay rates of Rotenberg *et al.* (2012) and Lugmair & Marti (1978). Initial ratios (i) and uncertainties (2σ) were propagated according to Ickert (2013).

Sample	Lithology	Suite	Age (Ma)	Rb (ppm)	Sr (ppm)	$^{87}Sr/^{86}Sr$	$^{87}Rb/^{86}Sr$	$^{87}Sr/^{86}Sr$(i)	2σ
FC31E	Pyroxenite	SS	234	16.19	95.45	0.706630	0.4907	0.705024	0.000025
FC30C	Gabbro	SS	234	42.27	440.27	0.706149	0.2777	0.705240	0.000020
FC43D	Monzogabbro	SS	234	52.73	675.82	0.705304	0.2257	0.704565	0.000022
EM79	Monzonite	SS	234	220.50	754.80	0.707524	0.8452	0.704757	0.000032
EM64	Syenite	SS	234	186.70	284.10	0.710211	1.9018	0.703985	0.000065
EM15	Gabbro	SU	234	42.55	849.41	0.705182	0.1449	0.704707	0.000018
FC2B	Monzogabbro	SU	234	89.14	620.85	0.707719	0.4154	0.706359	0.000028
EM107	Syenite	SU	234	318.30	569.10	0.710856	1.6187	0.705556	0.000055
EM5	Syenite	SU	234	97.87	253.65	0.709851	1.1166	0.706196	0.000042
EM31	Syenogranite	GU	234	324.50	148.19	-	-	-	-
EM88	Syenogranite	GU	234	371.86	15.99	-	-	-	-

Table A4.8. (continued)

Sample	Lithology	Suite	Age (Ma)	Sm (ppm)	Nd (ppm)	$^{143}Nd/^{144}Nd$	$^{147}Sm/^{144}Nd$	$^{143}Nd/^{144}Nd$(i)	2σ	Distance to edge (m)
FC31E	Pyroxenite	SS	234	2.92	10.46	-	0.1483	-	-	170
FC30C	Gabbro	SS	234	2.87	11.86	0.512415	0.1463	0.512191	0.000007	420
FC43D	Monzogabbro	SS	234	3.63	18.60	0.512392	0.1180	0.512211	0.000007	565
EM79	Monzonite	SS	234	5.60	27.16	0.512389	0.1246	0.512198	-	740
EM64	Syenite	SS	234	5.34	27.12	0.512429	0.1189	0.512247	0.000006	1000
EM15	Gabbro	SU	234	4.11	20.83	0.512444	0.1192	0.512261	0.000008	385
FC2B	Monzogabbro	SU	234	7.18	47.25	0.512430	0.0918	0.512289	0.000005	135
EM107	Syenite	SU	234	12.94	81.78	0.512412	0.0956	0.512266	0.000006	300
EM5	Syenite	SU	234	4.49	28.87	-	0.0826	-	-	158
EM31	Syenogranite	GU	234	9.69	62.08	0.512350	0.0942	0.512206	0.000007	376
EM88	Syenogranite	GU	234	8.43	39.41	0.512502	0.1291	0.512304	0.000016	735

Table A4.9. Pressure, temperature, *f*O₂ and H₂O parameters obtained by mineral pairs, mineral-melt and single mineral calculations on Shoshonitic Silica Saturated (SS), Shoshonitic Silica Undersaturated (SU) and Granitic Unit (GU) rocks. For each applied method, the corresponding reference, target and error on the single parameters are reported. Values used as input for each calculation are marked with (*); n.r. indicates a parameter that was not required as input by the chosen equation. Cpx: clinopyroxene; Amp: amphibole; Pl: plagioclase; Bt: biotite; Kfs: K-feldspar; Mag: magnetite. Py: pyroxenite; Gb: gabbro; Mzgb: monzogabbro; Mzdr: monzodiorite; Mz: monzonite; Sy: syenite; Sygr: syenogranite.

Suite and sample	Method	Target	Reference	T(°C)	Error (°C)	P (MPa)	Error (MPa)	H₂O (wt%)	Error (wt%)	log *f*O₂	Error (log *f*O₂)
SS Py	Cpx-melt	*P, T*	Putirka (2008), eq. 32b, 33	1050-1070	±10-20	160-230	±260	2-2.5 (*)	-	n.r.	-
SS Py	Cpx-melt	Cpx compos.	Rhyolite-MELTS (Gualda et al. 2012)	1060 (*)	-	150 (*)	-	2.5 (*)	-	-9.3 (*)	-
SS Gb	Cpx-melt	*P,T*	Putirka (2008), eq. 32b, 33	910-930°C	±10-20	100-190	±260	3-4 (*)	-	n.r.	-
SS Gb	Cpx-melt	*P, T*	Masotta et al. (2013), eq. Talk and Palk2012	910-980	±18	50-140	±120	3-4 (*)	-	n.r.	-
SS Mzgb/Mzdr	Cpx-melt	*P, T*	Masotta et al. (2013), eq. Talk and Palk2012	940-990	±18	140-160	±120	3-4 (*)	-	n.r.	-
SU Gb/Mzgb	Cpx-melt	*P, T*	Putirka (2008), eq. 32b, 33	930-940	±10-20	40-160	±260	1-1.5 (*)	-	n.r.	-
SU Gb/Mzgb	Cpx-melt	*P, T*	Masotta et al. (2013), eq. Talk and Palk2012	920-940	±18	20-140	±120	1.5 (*)	-	n.r.	-
SU Sy	Cpx-melt	*P, T*	Putirka (2008), eq. 32b, 33	810-820	±10-20	20-140	±260	4-5 (*)	-	n.r.	-
SU Sy	Cpx-melt	P, T	Masotta et al. (2013), eq. Talk and Palk2012	850-860	±18	130-160	±120	4-5 (*)	-	n.r.	-
SS Gb to Mzdr	Amp-Pl	*T*	Holland and Blundy (1994)	750-845	±40	n.r.	-	n.r.	-	n.r.	-
SS Gb to Mzdr	Amp-Pl	*P*	Anderson and Smith (1995); Anderson (1996)	n.r.	-	10-120	±60	n.r.	-	n.r.	-
SS Gb to Mzdr	Amp	*P, T, H₂O*	Ridolfi et al. (2010); Ridolfi and Renzulli (2012)	720-810	±23-24	70-140	±5-15	4.8-6.0	±0.8	-	-
SU Gb/Mzgb	Amp-Pl	*T*	Holland and Blundy (1994)	620-880	±40	n.r.	-	n.r.	-	n.r.	-
SU Gb/Mzgb	Amp-Pl	*P*	Anderson and Smith (1995); Anderson (1996)	n.r.	-	40-190	±60	n.r.	-	n.r.	-
SU Gb	Amp	*P, T, H₂O*	Ridolfi et al. (2010); Ridolfi and Renzulli (2012)	700-720	±23-24	50-60	±5-15	5.1-5.7	±0.8	-	-
SS Py	Bt	*T*	Henry et al. (2005)	690-740	±12-24	n.r.	-	n.r.	-	n.r.	-
SS Gb to Mz	Bt	*T*	Henry et al. (2005)	540-660	±12-24	n.r.	-	n.r.	-	n.r.	-
SU Gb/Mzgb	Bt	*T*	Henry et al. (2005)	640-660	±12-24	n.r.	-	n.r.	-	n.r.	-
SS Py	Pl-melt	H₂O	Lange et al. (2009)	1060 (*)	-	150 (*)	-	3.0	±0.7	n.r.	-
SS Py	Pl-melt	P,T	Putirka (2008), eq. 24a	1076-1081	±36	150 (*)	-	3.0 (*)	-	n.r.	-
SS Gb	Pl-melt	H₂O	Lange et al. (2009)	920-1016 (*)	-	120-150 (*)	-	3.1-3.4	±0.7	n.r.	-
SS Gb	Pl-melt	*P, T*	Putirka (2008), eq. 24a	999-1053	±36	120-150 (*)	-	3.1-3.4 (*)	-	n.r.	-
SS Mzgb/Mzdr	Pl-melt	H₂O	Lange et al. (2009)	920 (*)	-	120 (*)	-	3.9-4.8	±0.7	n.r.	-
SS Mzgb/Mzdr	Pl-melt	*P, T*	Putirka (2008), eq. 24a	917-989	±36	120 (*)	-	3.9-4.8 (*)	-	n.r.	-
SU Gb	Pl-melt	H₂O	Lange et al. (2009)	990 (*)	-	150 (*)	-	4.1	±0.7	n.r.	-
SU Gb	Pl-melt	*P, T*	Putirka (2008), eq. 24a	975-990	±36	150 (*)	-	4.1 (*)	-	n.r.	-
SU Mzgb	Pl-melt	H₂O	Lange et al. (2009)	920 (*)	-	120 (*)	-	4.4	±1.0	n.r.	-
SU Mzgb	Pl-melt	*P, T*	Putirka (2008), eq. 24a	936	±36	120 (*)	-	4.4 (*)	-	n.r.	-
SS Gb/Mzgb	Kfs-melt	H₂O	Mollo et al. (2015)	800-900 (*)	-	n.r.	-	4.4-6.5	±0.94	n.r.	-
SS Mzdr to Sy	Kfs-melt	H₂O	Mollo et al. (2015)	800-900 (*)	-	n.r.	-	4.6-7.3	±0.94	n.r.	-
SU Mzgb to Mz	Kfs-melt	H₂O	Mollo et al. (2015)	800-900 (*)	-	n.r.	-	5.5-7.8	±0.94	n.r.	-
SS Gb	Bt/Kfs/Mag	*f*O₂	Burkhard (1991)	865-966	±7	150 (*)	-	n.r.	-	-11.2/-12.9	±0.3
SS Mzgb/Mzdr	Bt/Kfs/Mag	*f*O₂	Burkhard (1991)	806-993	±7	150 (*)	-	n.r.	-	-10.7/-13.8	±0.3
SS Mz	Bt/Kfs/Mag	*f*O₂	Burkhard (1991)	786-881	±7	150 (*)	-	n.r.	-	-12.4/-14.1	±0.3
SU Gb/Mzgb	Bt/Kfs/Mag	*f*O₂	Burkhard (1991)	916-1054	±7	150 (*)	-	n.r.	-	-10.2/-11.9	±0.3
GU Sygr	Bt/Kfs/Mag	*f*O₂	Burkhard (1991)	853-922	±7	150 (*)	-	n.r.	-	-11.8/-12.9	±0.3

Table A4.10. Major element composition of the calculated melts used to retrieve the equilibrium conditions for clinopyroxene and plagioclase thermobarometry and for K-feldspar hygrometry (see text for explanation). SS = Shoshonitic Silica Saturated; SU = Shoshonitic Silica Undersaturated; Mg# = Mg/[Mg Fe^{2+}] mol%.

Method	Suite	Crystal host rock	SiO$_2$ (wt%)	TiO$_2$	Al$_2$O$_3$	Fe$_2$O$_3$	FeO	MnO	MgO	CaO	Na$_2$O	K$_2$O	P$_2$O$_5$	Mg#	
Clinopyroxene-melt thermobarometer	SS	Pyroxenite	50.9	1.2	20.7	1.0	7.0	0.1	4.0	9.3	2.9	2.3	0.6	**50.8**	Trachybasalt
	SS	Gabbro	54.9	0.6	21.0	0.8	5.4	0.1	2.1	8.2	3.2	3.2	0.4	**41.4**	Basaltic trachyandesite
	SS	Gabbro	64.1	0.6	17.3	0.7	4.5	0.2	1.5	2.7	3.1	5.2	0.2	**36.6**	Trachyandesite
	SS	Monzogabbro/monzodiorite	62.6	0.6	17.2	0.6	3.9	0.1	1.5	4.3	3.3	5.6	0.3	**40.2**	Trachyandesite
	SU	Gabbro/monzogabbro	62.2	0.3	18.5	0.3	1.7	0.1	0.5	3.1	3.9	9.0	0.6	**36.4**	Trachyandesite
	SU	Syenite	63.5	0.3	19.7	0.3	1.8	0.1	0.4	1.4	5.7	7.0	0.0	**28.0**	Trachyte
Plagioclase-melt thermobarometer	SS	Pyroxenite	50.0	1.1	17.1	1.3	8.8	0.2	5.1	10.9	2.5	2.1	0.7	**50.7**	Trachybasalt
	SS	Gabbro	53.6	0.8	17.4	1.1	7.6	0.2	4.1	8.4	2.8	3.4	0.5	**49.3**	Basaltic trachyandesite
	SS	Monzogabbro	57.9	0.6	17.8	0.8	5.1	0.1	2.7	6.6	3.8	4.4	0.1	**48.5**	Basaltic trachyandesite
	SS	Monzodiorite/monzonite	62.6	0.6	17.2	0.6	3.9	0.1	1.5	4.3	3.3	5.6	0.3	**40.2**	Trachyandesite
	SU	Gabbro	57.8	0.7	20.2	0.6	4.0	0.2	1.5	4.9	4.7	5.1	0.4	**39.3**	Trachyandesite
	SU	Monzogabbro to syenite	62.7	0.4	18.4	0.4	2.5	0.1	0.5	3.0	5.3	6.7	0.0	**24.1**	Trachyte
K-Feldspar-melt hygrometer	SS	Gabbro/monzogabbro	62.6	0.6	17.2	0.6	3.9	0.1	1.5	4.3	3.3	5.6	0.3	**40.2**	Trachyandesite
	SS	Monzodiorite to syenite	64.3	0.3	19.5	0.3	1.8	0.1	0.3	1.4	5.2	7.1	0.0	**20.3**	Trachyte
	SU	Monzogabbro/monzodiorite	63.5	0.3	19.7	0.3	1.8	0.1	0.4	1.4	5.7	7.0	0.0	**28.0**	Trachyte

Chapter 5

Mt. Monzoni and Cima Pape intrusive bodies

Chapter 5. Mt. Monzoni and Cima Pape intrusive bodies

5.1. Introduction

The volcano-plutonic rocks of the Dolomitic Area represent a significant and intriguing portion of a widespread magmatic event that, during Middle-Late Triassic, affected several areas of the nowadays Europe, including Carpathians, Dinarides, Hellenides, Austroalpine and Southalpine domains (Castellarin *et al.*, 1988; Beccaluva *et al.*, 2005).

In the Dolomitic Area, this event was characterized by the emission of huge amounts of trachybasaltic to trachytic volcanites/volcanoclastites over an area of about 2000 km^2 in a relatively limited time span between 238.0±0.05 and 237.579±0.042 Ma (<0.7 Ma, Mietto *et al.*, 2012; Abbas *et al.*, 2018; Storck *et al.*, 2018; Wotzlaw *et al.*, 2018). Such massive effusive activity was accompanied by the concomitant and/or immediately subsequent emplacement of small and scattered pyroxenitic/gabbroic to syenitic/syenogranitic plutons. These plutons, characterized by an overall volume of <10 km^3, crop out at Predazzo, Mt. Monzoni and Cima Pape (Trento-Belluno provinces, NE Italy). The few geochronological data from these intrusions are in great accordance with what reported from the volcanites, yielding ages between 237.3 ± 1.0 and 238.075 ± 0.087 Ma (U-Pb on zircon; Mundil *et al.*, 1996; Storck *et al.*, 2018).

Petrological/geochemical studies on the Predazzo Intrusive Complex enabled to define the existence of three different magmatic suites, all of them showing orogenic affinity but having distinct petrological and geochemical behaviours (see Chapters 3 and 4). The emplacement of the Predazzo intrusion occurred at shallow depth (1.4-5.6 km), and the interaction between the less differentiated magmas and the crustal basement during ascent was limited, being fractional crystallization the main differentiation process to which magmas were subjected. Detailed petrographic/petrologic studies on the smaller intrusions of Mt. Monzoni and Cima Pape were carried out in the last decades, and particular attention was given to the main fractional crystallization trends (Sommavilla, 1970; Gasparotto & Simboli, 1991; Bonadiman *et al.*, 1994) and to the chemico-physical conditions of magmas during emplacement (Bonadiman *et al.*, 1994).

Notwithstanding the huge amount of data present in literature, a comprehensive treatment of the geochemical and petrological features of the Predazzo, Mt. Monzoni and Cima Pape intrusive bodies has never been performed so far. An unequivocal identification of the main magmatic suites which constitute the three plutons, as well as an accurate study of their emplacement depth and fractional differentiation processes is still required. The lack of isotopic data on the Cima Pape body, as well as the high contamination degree of most of

Mt. Monzoni rocks (Bonadiman *et al.*, 1994), for example, prevented any possible isotopic comparison between them and the Predazzo Intrusive Complex rocks. In the present study, whole rock major, trace element and Sr-Nd isotopic analyses were carried out on representative rocks from Mt. Monzoni and Cima Pape, with the purpose of deciphering the main chemico-physical features of the magmas that generated these smaller intrusive bodies, and evaluating their interaction with the crust during differentiation. A comparison with the geochemical/petrological features of the larger Predazzo Intrusive Complex (PIC) was also put forward to reconstruct the general framework of the intrusive/hypabyssal magmatism of the Dolomitic Area.

5.2. Field description and petrography

With respect to the Predazzo pluton, Mt. Monzoni and Cima Pape intrusions (Figg. 24 and 25) have a more elongated shape. While the aspect ratio of Mt. Monzoni (thickness 0.5-1 km; length 4-5 km) led to classify it as a pluton, Cima Pape shape tipically resembles that of a sill (thickness <0.3 km; length ~5 km; see Rocchi & Breitkreuz, 2018; Cruden *et al.*, 2018). Mt. Monzoni pluton is elongated ENE-WSW along a regional transcurrent system, and intrudes the Permo-Triassic volcanic and sedimentary rocks belonging to the Atesina Volcanic District, Val Gardena Sandstons Fm., Bellerophon Fm., Werfen Fm., Contrin Fm., Sciliar Fm. and Buchenstein Fm., which record significant contact metamorphism (Fig. 24; Bonadiman *et al.*, 1994; Ferry *et al.*, 2002; Gallien *et al.*, 2007; Abbas *et al.*, 2018). The Cima Pape sill, on the other side, is almost entirely intruded in the Buchenstein Fm., in turn overlied by thick sequences of volcanic and volcanoclastic products (Fig. 25; Gasparotto & Simboli, 1991). The degree of conservation of Mt. Monzoni and Cima Pape rocks is sensitively different, being these latters often affected by secondary alteration processes. With respect to Mt. Monzoni, the Cima Pape area suffered an intense tectonic activity during the Alpine orogenesis (Fig. 25).

According to Gasparotto & Simboli (1991), Bonadiman *et al.* (1994), Della Lucia (1997) and Nardini (2018), the intrusive rocks cropping out at Mt. Monzoni (Fig. 24) and Cima Pape (Fig. 25) are compositionally similar, and mainly range from gabbros to monzodiorites. Clinopyroxenitic and monzonitic rocks, absent in the Cima Pape sill, constitute an additional and substantial portion of the Mt. Monzoni pluton, where also rare quartz-syenitic dykes and apophyses have been documented. In contrast with the ENE-WSW differentiation trend recognized in the Mt. Monzoni intrusion (Bonadiman *et al.*, 1994), the arrangement of the Cima Pape sill is apparently vertical. Its "stratigraphic" organization is dominated by the presence of cumulitic gabbros and monzogabbros in the bottom part and by the appearance

of monzodioritic rocks in the upper portions (Fig. 26; see also Sommavilla, 1970). Here the occurrence of a grain size textural transition marks the magmatic contact between the monzodioritic rocks and the overlying basaltic trachyandesitic volcanites. Inside the monzodioritic body, the sporadic occurrence of centimetric to decimetric monzonitic to syenitic veins is also reported. Such veins, pink in colour, are constituted by K-feldspar, plagioclase, magnetite/Ti-magnetite and rare clinopyroxene, and are thought to represent ultimate melts segregated during the later crystallization stages of the monzodioritic rocks. In the following, a brief summary of the petrographic features of Mt. Monzoni and Cima Pape rocks is reported, according to what proposed by Gasparotto & Simboli (1991) and Bonadiman *et al.* (1994).
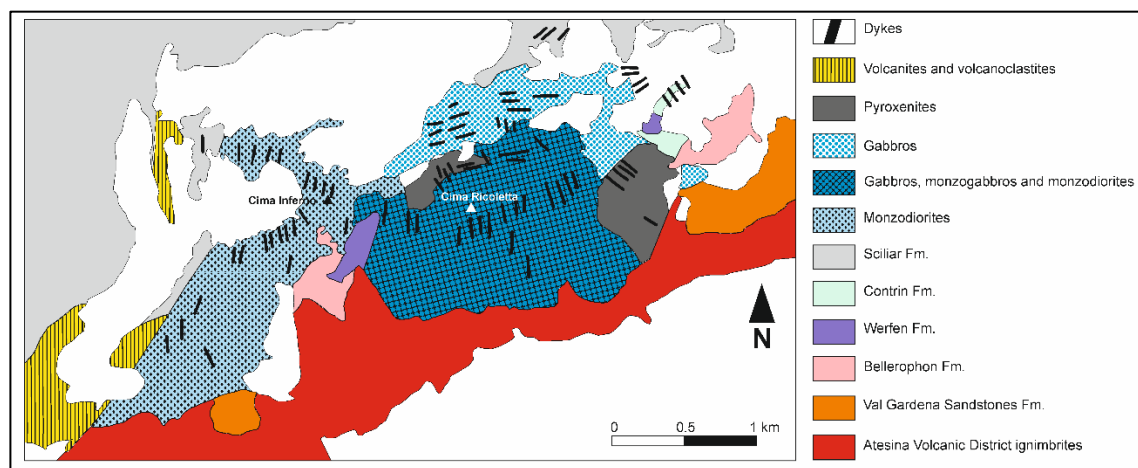
Fig. 24. Simplified geological map of the Mt. Monzoni intrusion (modified from Servizio Geologico - Provincia autonoma di Trento and Abbas et al., 2018).
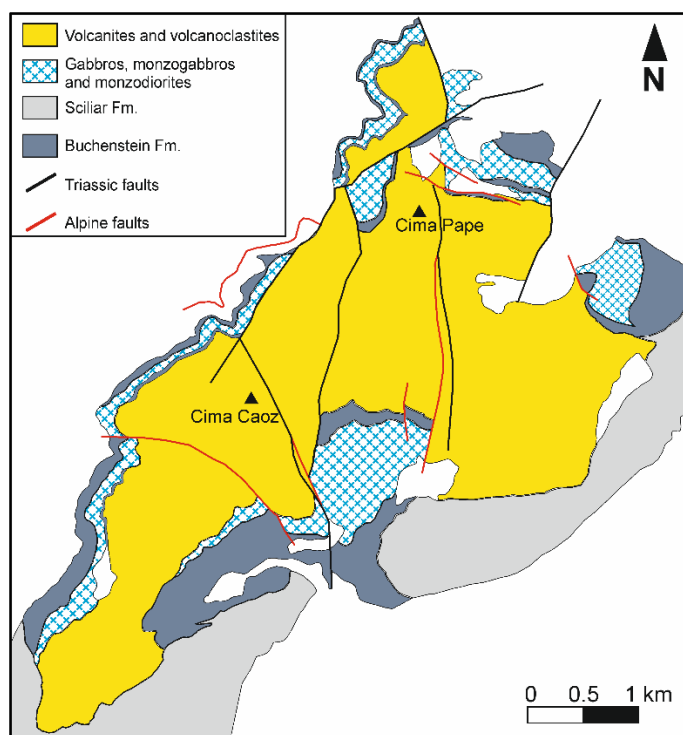
Fig. 25. Simplified geological map of the Cima Pape volcano-plutonic complex (modified from Sarti & Ardizzoni, 1984 and Gasparotto & Simboli, 1991).
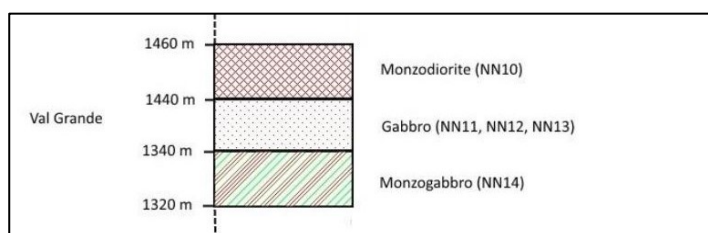
Fig. 26. Sketch of the stratigraphic organization of the Cima Pape sill in Val Grande locality (from Nardini, 2018).

5.2.1. Mt. Monzoni and Cima Pape intrusive rocks

Clinopyroxenites (Mt. Monzoni) show cumulitic textures, characterized by the presence of euhedral clinopyroxene (> 5 mm), magnetite/Ti-magnetite and olivine crystals in the cumulus, and biotite and plagioclase in the intercumulus assemblage. Biotite locally displays poikilitic texture (Fig. 27) around clinopyroxene and olivine grains.

Gabbros and olivine-gabbros (Mt. Monzoni - Cima Pape) are constituted by orthocumulitic to noncumulitic texture with, in order of appearance, olivine, clinopyroxene, orthopyroxene, magnetite/Ti-magnetite, plagioclase and biotite. K-feldspar (Or_{78}) is also present in small amounts, but only in the gabbroic rocks. The different degree of alteration between Mt. Monzoni and Cima Pape rocks is particularly evident in olivine crystals, generally fresh with limited iron oxide exsolution along fractures in Mt. Monzoni samples, whereas totally pseudomorphosed in iddingsite in Cima Pape rocks. Clinopyroxene crystals (Mg# = 61-75),

up to 8 mm in size, are generally euhedral, sometimes twinned, and often rich of oxides inclusions. Olivine grains, sometimes surrounded by the growth of large clinopyroxene (Fig. 27), range in composition from Fo_{60} to Fo_{49}. Intercumulus plagioclase (An_{52-73}) generally show subparallel alignment, due to magmatic flow (Fig. 27; Bonadiman *et al.*, 1994). Analogously to olivine, biotite is fresh in Mt. Monzoni gabbros, while is almost totally altered in Cima Pape ones. According to Bonadiman *et al.* (1994), the textural features and mineral assemblages of some Mt. Monzoni gabbros enable to interpret them as representative of the parental magmas of the intrusion.

Monzogabbros (Mt. Monzoni - Cima Pape) have coarse-grained hypidiomorphic texture, dominated by the presence of clinopyroxene (up to 5 mm; Mg# ~ 67-68), magnetite/Ti-magnetite (up to 1 mm) and plagioclase (An_{51-57}). Olivine (Fo_{41-52}) is rare and often altered in iddingsite. The late-stage crystallization matrix is composed, in addition to plagioclase, of K-feldspar (Or_{72-97}) and biotite, often with poikilitic texture. Rare are the amphibole crystals, often with actinolitic composition and formed at the expenses of clinopyroxene. Occasionally some primary amphiboles, hornblendic in composition, occur as last intercumulus phase (Fig. 27).

Monzodiorites (Mt. Monzoni - Cima Pape) are medium-grained, with hypidiomorphic texture characterized by the presence of, in order of appearance, clinopyroxene (Mg# ~ 60), plagioclase (An_{50-55}), K-feldspar (Or_{80}) and magnetite/Ti-magnetite. Biotite, often altered in chlorite, is the main intercumulus phase.

Monzonites (Mt. Monzoni; Fig. 27) have medium- to fine-grained texture, with, in order of decreasing abundance, plagioclase (An_{25-70}), K-feldspar (Or_{62-81}), biotite, magnetite/Ti-magnetite and clinopyroxene (Mg# = 66-75) crystals. Accessory phases include apatite and zircon. Some monzonitic rocks are characterized by holocrystalline hypabyssal texture, in which larger plagioclase phenocrysts (up to 1-2 cm, Fig. 27), are immersed in a fine-grained groundmass made by plagioclase, K-feldspar, magnetite/Ti-magnetite and biotite. These large plagioclase crystals display a large compositional variation between cores (An_{60-61}) and rims (An_{30-32}).

Quartz-syenitic dykes/apophyses (Mt. Monzoni) are fine-grained, hypidiomorphic, and characterized by the presence of perthitic K-feldspar (Or_{89}), quartz, plagioclase, biotites and magnetite/Ti-magnetite. Apatite and zircon are minor accessory phases (Fig. 27).
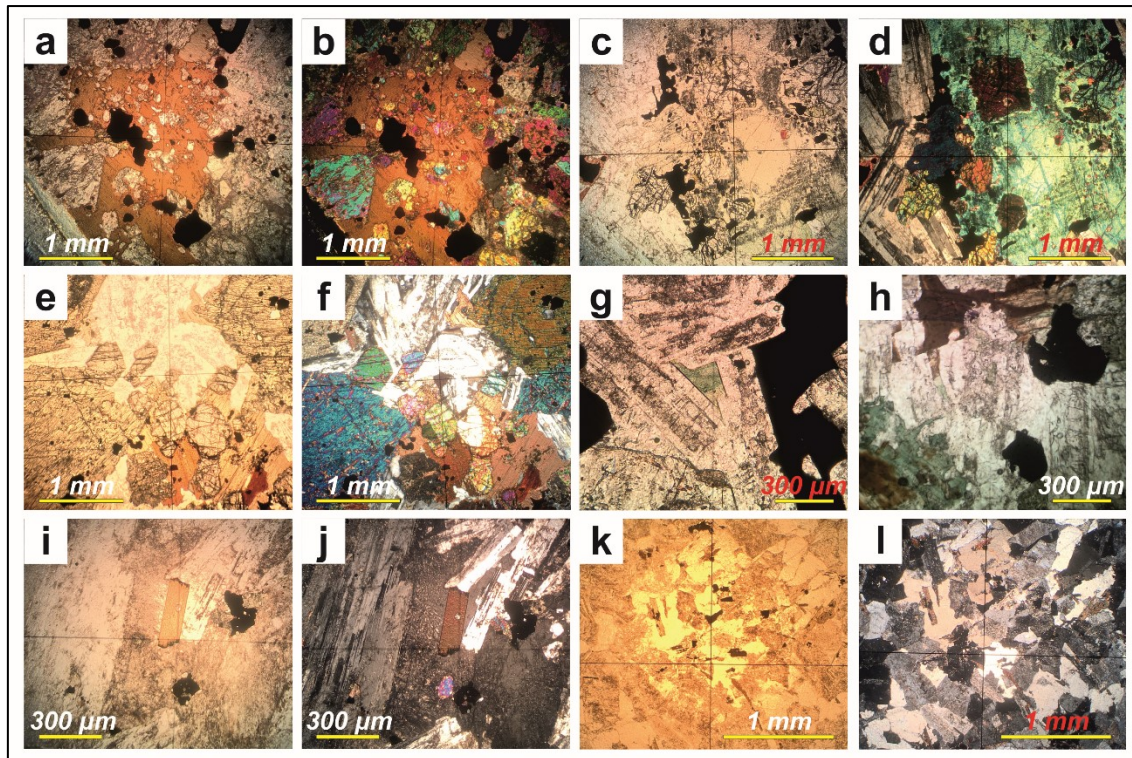
Fig. 27. Photomicrographs of (a, b) Mt. Monzoni biotite clinopyroxenites; (c, d, e, f) Mt. Monzoni gabbros; (g, h) Hornblende crystals inside Mt. Monzoni monzogabbros; (i, j) Mt. Monzoni monzonites; (k, l) Mt. Monzoni quartz-syenites. (a, c, e, g, h, i, k) are in plane-polarized light;(b, d, f, j, l) are in cross-polarized light.

The main crystallization sequence of both Mt. Monzoni and Cima Pape rocks, according to what proposed by Bonadiman *et al.* (1994), can be summarized as follows: olivine → magnetite/Ti-magnetite + clinopyroxene → orthopyroxene → plagioclase → biotite (± amphibole) → K-feldspar (± accessories).

5.2.2. Cima Pape volcanic rocks

The volcanic products of the Cima Pape complex, classified as pillow lavas, pillow breccias, lava flows and lava breccias, range in composition from trachybasaltic to basaltic trachyandesitic. Their texture is generally porphyritic (Porphyricity Index, P.I. = 30-60), with, in order of decreasing abundance, clinopyroxene, plagioclase, magnetite/Ti-magnetite and olivine phenocrysts immersed in a microcrystalline groundmass (Gasparotto & Simboli, 1991; Nardini, 2018). Clinopyroxene phenocrysts (up to 3 mm in size) are often zoned, and sometimes associated to magnetite/Ti-magnetite, forming aggregates up to 4-5 mm in size. Plagioclase crystals have usually smaller dimensions (< 2 mm) and are often sericitized. Olivine, rarely fresh (often altered in iddingsite/bowlingite) and limited to the trachybasaltic samples, do not exceed 1 mm in diameter. The groundmass is constituted by microcrysts of plagioclase and clinopyroxene, with subordinated magnetite/Ti-magnetite.

In accordance with the textual transition identified by Sommavilla (1970), some lava flows cropping out in the bottom part of the volcanic sequence are characterized by hypabyssal texture. They are constituted by larger phenocrysts of clinopyroxene (up to 3 mm), plagioclase (up to 2 mm), magnetite/Ti-magnetite (up to 0.5 mm) and olivine (up to 1 mm, always altered in iddingsite) immersed in a medium- to fine-grained groundmass made by the same mineral assemblage.

5.3. Whole rock geochemistry

5.3.1. Major and trace element

Mt. Monzoni and Cima Pape intrusive and volcanic rocks are characterized by K-alkaline affinity, with a SiO_2 content of 43-56 wt% and an alkali content ranging from 1 to 8 wt% (Fig. 28). An exception is constituted by the syenitic dykes/apophyses found in Mt. Monzoni body, which are characterized by higher silica (69-70 wt%) and alkali (9-11 wt%) contents. On the K_2O vs. SiO_2 diagram (Fig. 29), both Mt. Monzoni and Cima Pape samples plot in the shoshonitic series field, in accordance to what proposed by several authors (Sommavilla, 1970; Gasparotto & Simboli, 1991; Bonadiman *et al.*, 1994).

The less differentiated composition is displayed by Mt. Monzoni clinopyroxenites and cumulitic gabbros (Table A5.1). Cima Pape volcanites, trachybasaltic to basaltic trachyandesitic in composition, lie a narrower compositional interval, with SiO_2 and Na_2O+K_2O contents of 50-55 wt% and 5-7 wt%, respectively. A negative correlation between FeO and SiO_2 content is clearly displayed by all Mt. Monzoni and Cima Pape lithotypes. Intrusive rocks from both plutonic bodies are silica saturated to slightly undersaturated, except clinopyroxenites and cumulitic gabbros, whose degree of undersaturation is moderate, with up to 4-5% normative nepheline. Analogously, Cima Pape volcanites are generally silica saturated, sometimes showing small amounts of normative quartz (1%). The few quartz-syenitic dykes found on Mt. Monzoni are by definition silica oversaturated, with 13-22% of normative quartz.

Zirconium and Rb positively correlate with SiO_2, and range in concentration from 30 to 327 ppm and from 16 to 241 ppm, respectively, in the intrusive rocks. The concentration of Zr in Cima Pape volcanites is about 133-200 ppm, whereas Rb content is between 17 and 95 ppm (Fig. 30). Nickel highest content is reached in Mt. Monzoni clinopyroxenites and cumulitic gabbros (up to ~120 ppm) while in monzogabbros to Qz-syenites it progressively decreases down to 3 ppm. Cima Pape intrusives and volcanites are characterized by a Ni content decreasing from 67 to 7 ppm with increasing silica content.
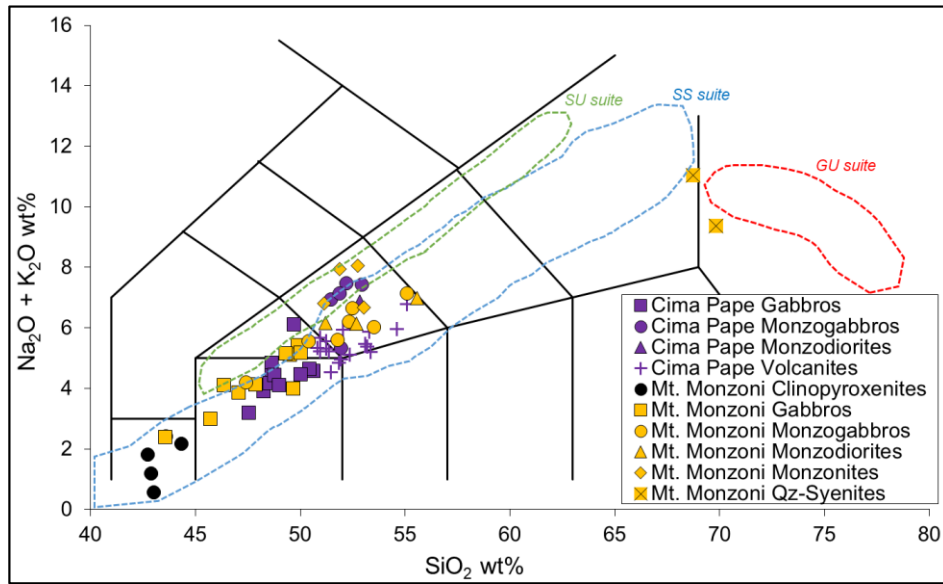
Fig. 28. Total Alkali vs. Silica diagram (Le Maitre et al., 2002) showing the composition of Mt. Monzoni and Cima Pape rocks. The compositional fields of the Shoshonitic Silica Saturated (SS), Shoshonitic Silica Undersaturated (SU) and Granitic Unit (GU) rocks of the Predazzo Intrusive Complex are shown for comparison.
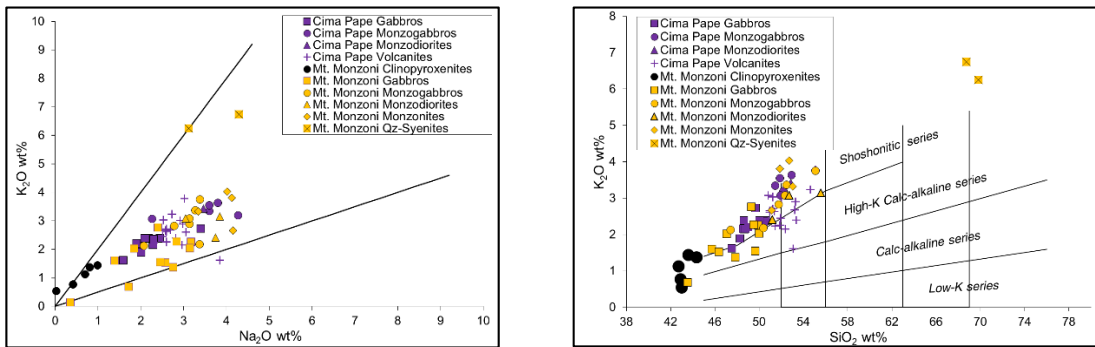
Fig. 29. K_2O vs. Na_2O (left) and K_2O vs. SiO_2 (Ewart 1982; right) diagrams showing the composition of Mt. Monzoni and Cima Pape rocks.
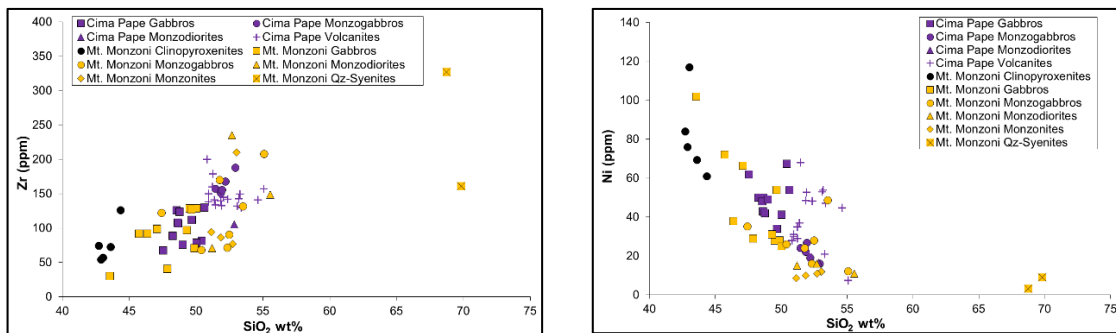
Fig. 30. Zr (left) and Ni (right) vs. SiO_2 diagrams showing the composition of Mt. Monzoni and Cima Pape rocks.

N-MORB-normalized (Sun & McDonough, 1989) trace element distribution of both Mt. Monzoni and Cima Pape rocks are characterized by the "typical" subduction-related pattern, with negative anomalies in Nb-Ta and Ti and LILE-enrichment (Fig. 31). Niobium content is in fact low in both Mt. Monzoni (4-24 ppm) and Cima Pape (7-12 ppm) intrusive rocks,

as well as in Cima Pape volcanites (8-14 ppm). Intrusive rocks N-MORB-normalized REE patterns are relatively LREE-enriched, with $(La/Yb)_N$ ratio progressively increasing from 8-11 in Mt. Monzoni clinopyroxenites to 10-20 in gabbros, 12-25 in monzogabbros/monzonites and ~33 in Mt. Monzoni quartz-syenitic rocks. REE patterns of Cima Pape volcanites are similar to those of the intrusive lithotypes, being characterized by $(La/Yb)_N$ ratios of 13 to 16 (Fig. 31).
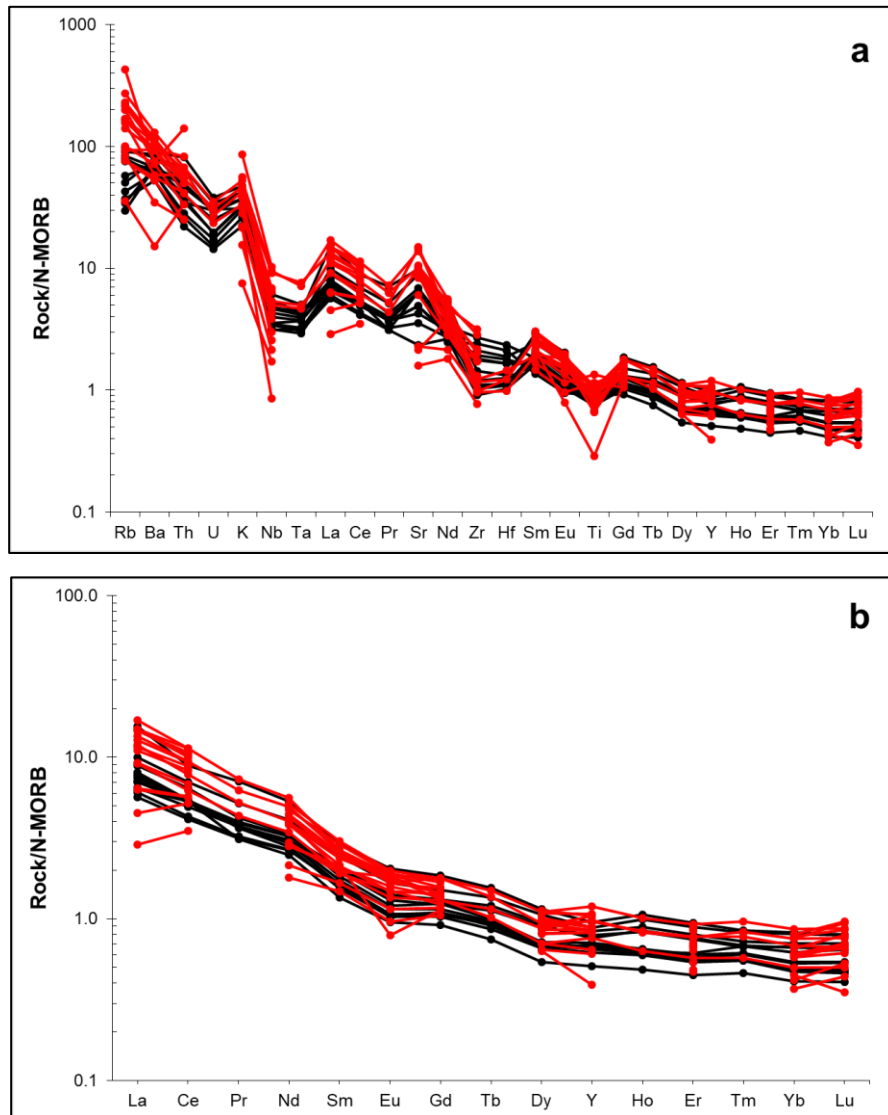
Fig. 31. N-MORB-normalized (Sun & McDonough, 1989) trace element (a) and REE (b) patterns of Mt. Monzoni (red) and Cima Pape (black) rocks.

5.3.2. Sr-Nd isotopes

Whole-rock $^{87}Sr/^{86}Sr$ and $^{143}Nd/^{144}Nd$ isotopic ratios were determined on representative samples of both Mt. Monzoni and Cima Pape bodies. All values were corrected to 234 Ma, in accordance with the age data proposed by Laurenzi & Visonà (1996) and Mundil *et al.*

(1996). Mt. Monzoni gabbros to monzonites are characterized by initial Sr (^{87}Sr/^{86}Sr$_i$) values of 0.7041 to 0.7044 and by initial Nd (^{143}Nd/^{144}Nd$_i$) ratios of 0.512249 to 0.512281. Cima Pape gabbros have slightly higher ^{87}Sr/^{86}Sr$_i$ (~0.7049) at comparable ^{143}Nd/^{144}Nd$_i$ ratios (0.512244-0.512252). The initial Sr values of Cima Pape trachybasalts is similar to those of the related intrusive rocks (0.7045-0.7050), whereas their initial Nd ratios range from 0.512231 to 0.512278. On the whole the isotopic signature of both Mt. Monzoni and Cima Pape rocks well fit the enriched mantle (EM I) field (Zindler & Hart, 1986).

5.4. The Middle Triassic intrusions of the Dolomitic Area

5.4.1. Emplacement conditions of the intrusions

A detailed estimation of the temperature and oxygen fugacity conditions of Mt. Monzoni magmas during emplacement was proposed by Bonadiman *et al.* (1994). Accordingly, a *T* interval of 1044-589°C at *f*O$_2$ around the NNO buffer was obtained to encompass the crystallization path of gabbros to syenites, assuming an input pressure of 150 MPa. Nevertheless, an exact quantification of the emplacement depth of Mt. Monzoni and Cima Pape bodies has never been proposed. In fact, primary amphibole crystals (by far the most suitable barometers in this kind of rocks), are rare in Mt. Monzoni rocks, where almost only secondary actinolite, grown at the expenses of clinopyroxene, can be found.

According to our findings, however, small relicts of magmatic magnesio-ferri-hornblende are present inside Mt. Monzoni monzogabbros, where they grow in contact with plagioclase during the latest crystallization stages, i.e. in the intercumulus assemblage (Fig. 27). The analyses of hornblende and plagioclase (Tables A5.2 and A5.3) enabled thus to retrieve the lowest *P* and *T* of crystallization of the Mt. Monzoni body, by means of the single-amphibole barometer of Hammarstrom & Zen (1986) and the amphibole-plagioclase thermobarometers of Holland & Blundy (1994), Anderson & Smith (1995) and Anderson (1996). Results yielded a *P* of about 30 to 70 MPa by applying the Hammarstrom & Zen (1986) barometer. *T-P* paths calculated by the Holland & Blundy (1994), Anderson & Smith (1995) and Anderson (1996) equations are in a range of 35-98 MPa and 719-747°C (Fig. 32).

To unravel the ultimate *T* of crystallization of the intercumulus assemblage, the single-mineral Ti-in biotite thermometer of Henry *et al.* (2005) was also applied to Mt. Monzoni rocks (Table A5.4). This thermometer yielded a *T* interval of 610-710 °C, generally decreasing with increasing the differentiation degree, thus from gabbros to quartz-syenites (Fig. 32).
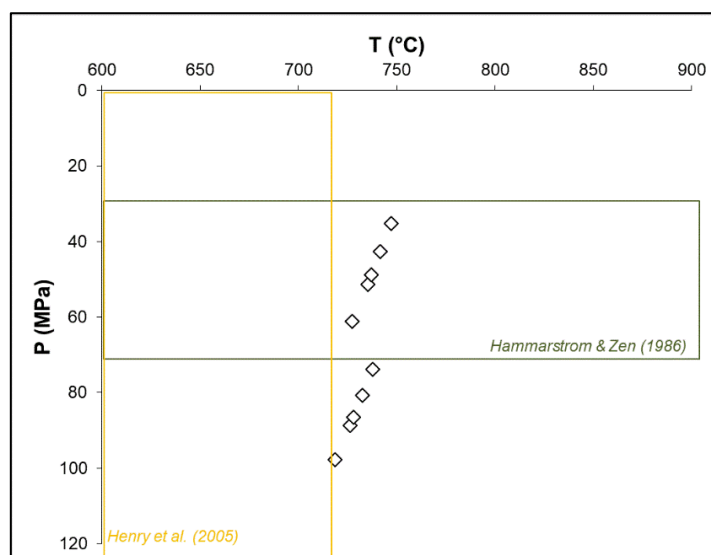
Fig. 32. Temperature (T °C) vs. pressure (P MPa) diagram for Mt. Monzoni rocks, showing the results of the amphibole-plagioclase thermobarometric equations (Holland & Blundy, 1994; Anderson & Smith, 1995; Anderson, 1996). Green field indicates the pressure range obtained by the single-amphibole barometer of Hammarstrom & Zen (1986). Yellow field indicates the temperature range obtained by the single-biotite thermometer of Henry et al. (2005).

By considering a $\Delta P/\Delta z$ of 27-29 MPa/km, the depth emplacement of Mt. Monzoni body results 1.0-3.6 km. Errors on pressure calculations are between ±60 and ±100 MPa.

These results are in great accordance with what proposed for the Predazzo Intrusive Complex (Chapter 4), whose emplacement depth resulted between 1.4 and 5.6 km. The intense state of alteration of both biotite and (the few) amphibole crystals in Cima Pape rocks prevented their analyses and therefore the application of the above mentioned thermobarometric equations. However, the concomitance between the data obtained for Mt. Monzoni and Predazzo intrusions, as well as the existence of a grain size gradual textural transition between the intrusive and effusive portions of both Predazzo and Cima Pape bodies can be considered as indirect evidence of the shallow nature of this latter.

5.4.2. Interaction with the crust and differentiation processes

According to Gasparotto & Simboli (1991) and Bonadiman *et al.* (1994), the differentiation of magmas at Mt. Monzoni and Cima Pape occurred in almost closed systems. A similar hypothesis was proposed by Petersen *et al.* (1980), and confirmed in Chapters 3 and 4 for PIC magmas. The Sr-Nd isotopic signature of both Mt. Monzoni and Cima Pape well fit that of Predazzo rocks, plotting in the EM I field. Notwithstanding similar $^{143}Nd/^{144}Nd_i$ ratios, Mt. Monzoni rocks are characterized by lower and constant $^{87}Sr/^{86}Sr_i$ values with respect to Cima Pape intrusives and volcanites (Fig. 33). With respect to the Sr-Nd isotopic ratios identified by Bonadiman *et al.* (1994), these samples plot in a narrower interval, characterized by quite lower $^{87}Sr/^{86}Sr_i$ and $^{143}Nd/^{144}Nd_i$ ratios. When compared to the

Shoshonitic Silica Saturated (SS) and Undersaturated (SU) units of the Predazzo Intrusive Complex (see Chapters 3 and 4), Mt. Monzoni intrusives clearly fit the SS isotopic signature, whereas the Cima Pape rocks seem to be more consistent with that of the SU rocks, especially in terms of $^{87}Sr/^{86}Sr_i$. It should be noted, that, even the discrimination between the SS and SU units is slight, neither Mt. Monzoni nor Cima Pape rocks reach the higher Nd_i values of SU rocks, predominant feature of this unit. The variability of the Sr isotopic signature, on the other side, is probably function of a syn-emplacement contamination process linked to the interaction between the magmas and the carbonate host rocks. In small intrusive bodies, like for example Mt. Monzoni and Cima Pape, this process could be significantly efficient.

To take into account the Sr-Nd isotopic variability of Mt. Monzoni and Cima Pape rocks, as well as to explain the gap between our samples and the isotopic ratios reported by Bonadiman *et al.* (1994), two main EC-AFC models (Bohrson & Spera, 2001; Spera & Bohrson, 2001) were put forward. Following the same rational scheme proposed in Chapter 4, the EC-AFC models were developed by using as starting composition that of a Mt. Monzoni monzogabbro. The averaged compositions of Middle Triassic carbonates (Martin & McDougall, 1995; Blendiger *et al.*, 2015) and Southern Alps crustal basement (Voshage *et al.*, 1990; Barth *et al.*, 1993; Rottura *et al.*, 1997; Sinigoi *et al.*, 2016, and references therein) were chosen as possible assimilants. Liquidus, solidus, initial temperature and specific heat of the starting magma were 1212°C, 600°C, 1100°C and 1567 J/(KgK), respectively. Heat of crystallization and heat of fusion values (J/Kg) were considered in accordance with the upper crustal case proposed by Bohrson & Spera (2001) and Spera & Bohrson (2001). Thermodynamic properties and composition of the carbonate assimilant were considered analogous to those adopted in the model of Chapter 4. Thermodynamic properties and composition of the Southern Alps crustal basement were considered as average of the single end-members reported in Chapter 4 (see Table 4).

Equations showed that small amounts of crustal components assimilation (3-4%) are able to explain the Sr-Nd isotopic variability of Mt. Monzoni and Cima Pape rocks. The isotopic variability of Bonadiman *et al.* (1994) Mt. Monzoni rocks can be explained, as already proposed by the authors themselves, by taking into account a considerable effect of contamination processes by the carbonate host rocks. The match between one of Mt. Monzoni samples and the Middle Triassic carbonates field (Fig. 33) confirms this hypothesis.

Our results confirm that, as already proposed for Predazzo Intrusive Complex, the main process acting during the differentiation of Mt. Monzoni and Cima Pape magmas was

fractional crystallization (Gasparotto & Simboli, 1991; Bonadiman *et al.*, 1994). The compositional spectrum of both Mt. Monzoni and Cima Pape rocks can be modelled by considering a ~60% fractional crystallization from a starting gabbroic/monzogabbroic magma (Mg# 52).
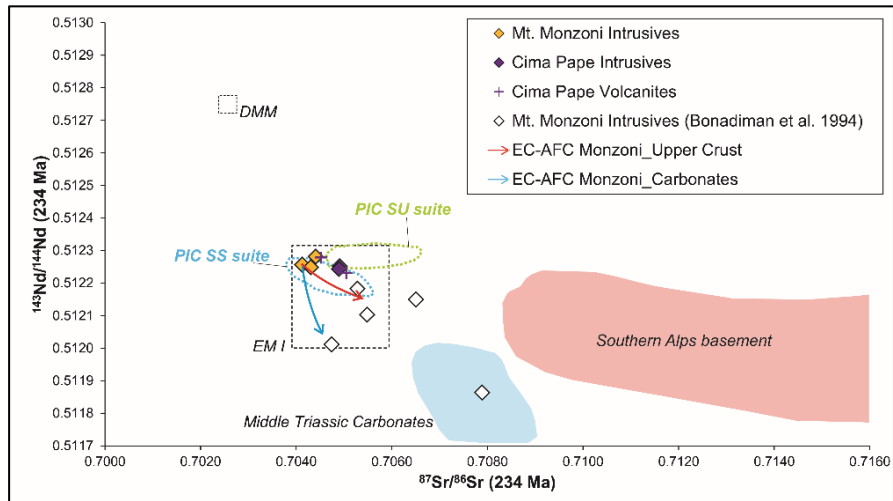
Fig. 33. Diagram showing the $^{87}Sr/^{86}Sr$ vs.$^{143}Nd/^{144}Nd$ isotopic ratios of Mt. Monzoni and Cima Pape rocks compared to those of the Predazzo Intrusive Complex (PIC) SS-SU rocks and the Southern Alps basement (all values corrected to 234 Ma; see also Chapter 4). Triassic carbonates field from Martin & Macdougall (1995) and Blendinger et al. (2015); Southern Alps basement field according to Voshage et al. (1990), Barth et al. (1993), Rottura et al. (1997), Sinigoi et al. (2016). The enriched 1 (EMI)and depleted (DMM) mantle end-members are in accordance to Zindler & Hart (1986) and Workman & Hart (2005).The blue and red arrows indicate the EC-AFC trends (Bohrson & Spera, 2001; Spera & Bohrson, 2001) for the Mt. Monzoni and Cima Pape rocks by considering assimilation of Triassic carbonates and Southern Alps basement, respectively.
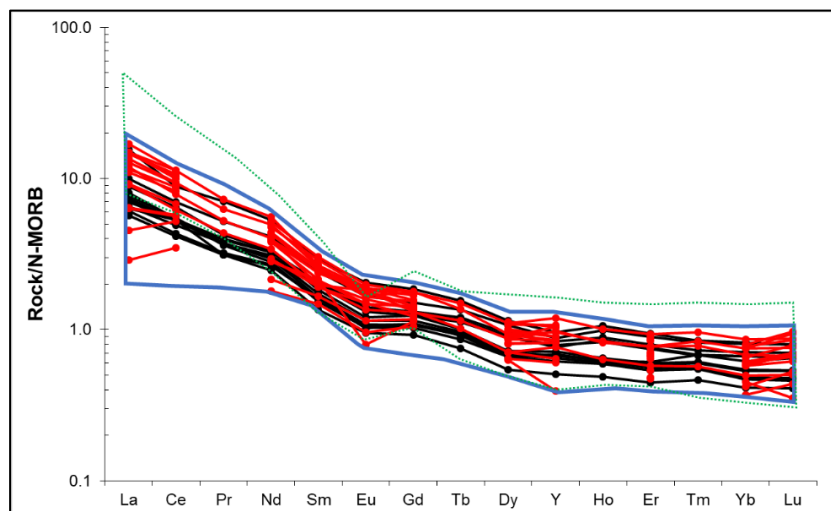
Fig. 34. Comparison between the N-MORB-normalized (Sun & McDonough, 1989) REE patterns of Mt. Monzoni (red) and Cima Pape (black) rocks and the compositional fields of the Predazzo Intrusive Complex SS (blue) and SU (green) rocks.

111

5.4.3. The Middle Triassic magmatic suites of the Dolomitic Area

Common petrological and geochemical features characterize the limited volume of Middle Triassic intrusions of the Predazzo, Mt. Monzoni and Cima Pape bodies. All these rocks display in fact a K-alkaline affinity, as well as major/trace element distribution consistent with the subduction-related (shoshonitic) series generated in active continental margins.

The lithological variability progressively decreases with decreasing the volume of the intrusive bodies, thus moving from the Predazzo Intrusive Complex to the Cima Pape sill. In the former, three different magmatic suites, silica-undersaturated to -oversaturated, can be found. The latter, as well as Mt. Monzoni body, is apparently constituted by only one silica-saturated suite, dominated by the presence of gabbroic, monzogabbroic and monzodioritic rocks. Analogously to PIC, a portion of Mt. Monzoni intrusion is composed of clinopyroxenitic and monzonitic/syenitic rocks.

The mineral paragenesis of Mt. Monzoni and Cima Pape rocks is consistent with that of the PIC Shoshonitic Silica Saturated (SS) body, as testified by the earlier appearance of biotite with respect to amphibole in the intercumulus assemblage, by the hornblendic composition of amphiboles and the diopsidic-augitic composition of clinopyroxenes. Whole rock geochemistry data seem to support such a comparison, especially in terms of REE, HFSE and, in minor extent, Sr-Nd isotopes distribution. As shown in Fig. 34, in fact, Mt. Monzoni-Cima Pape N-MORB-normalized REE patterns are well comparable to those of the Predazzo SS rocks, being on the other side LREE-depleted with respect to the SU compositional field. In addition, their Th-U concentration is consistent with those of SS rocks. $^{87}Sr/^{86}Sr_i$ and$^{143}Nd/^{144}Nd_i$ ratios are not analogously helpful in this discrimination, since the isotopic signature of Mt. Monzoni and Cima Pape rocks lies between the SS and SU compositional fields (Fig. 33). However, the overlap between the Sr-Nd signature of the less altered Mt. Monzoni rocks and the SS suite of the Predazzo Intrusive Complex is consistent with this parallelism.

5.5. Conclusions

The geochemical and thermobarometric study of Mt. Monzoni and Cima Pape rocks enabled to set out some remarkable points:

1. Mt. Monzoni, Cima Pape and Predazzo intrusions emplaced at similar depth (1.0-3.6 km Mt. Monzoni; 1.4-5.6 km Predazzo Intrusive Complex). Crystallization *T* ranges from 1000-1100°C to 589-610°C. In accordance with the field evidence, this data speaks in favour of a shallow nature of all the Middle Triassic intrusions of the Dolomitic Area.

2. The geochemical affinity of Mt. Monzoni and Cima Pape rocks almost totally overlaps with that of the Shoshonitic Silica Saturated rocks of the Predazzo Intrusive Complex. This suite represented the first and most volumetrically significant magmatic pulse of the Middle Triassic magmatism in the Dolomitic Area.

3. The $^{87}Sr/^{86}Sr$ and $^{143}Nd/^{144}Nd$ signature of all Mt. Monzoni, Cima Pape and Predazzo rocks plot in the enriched mantle (EM I) field. Together with the marked orogenic-like affinity of magmas, this feature highlights the predominant role of subduction-related components in the mantle source beneath the Southern Alps during Middle Triassic (Bonadiman *et al.*, 1994; Zanetti *et al.*, 2013).

4. Low degree of crustal assimilation are necessary to explain the restricted Sr-Nd isotopic range of all the Mt. Monzoni, Cima Pape and Predazzo magmas. On the other side, a significant role was played by syn-emplacement contamination processes by the carbonate host rocks, especially at Mt. Monzoni.

5. Together with the numerous field evidences, the obtained thermobarometric results for the Mt. Monzoni, Cima Pape and Predazzo intrusions highlight the importance of their study in a "volcanologic" perspective. They can be in fact considered as constituents of a shallow multi-pulse and multi-batch plumbing system, where the differentiation processes of H_2O and K-rich magmas can be determined.

Appendix A5

Table A5.1. Whole rock major, trace element composition and $^{87}Sr/^{86}Sr$ and $^{143}Nd/^{144}Nd$ isotopes of representative Mt. Monzoni and Cima Pape rocks. Fe_2O_3 and FeO were calculated by considering a Fe_2O_3/ FeO ratio of 0.15, in agreement with a fO_2 around FMQ buffer (Kress & Carmichael, 1991). Mg# = Mg/[Mg+Fe^{2+}] mol%; n.d. = not detected. All trace element (ppm) were analysed by ICP-MS except Pb, Zn, Ni, Co, Cr, V and Ba (XRF). The trace element composition of samples labelled with (*) was entirely determined by XRF. Sr-Nd isotopic ratios were corrected for 234 Ma of radiogenic ingrowth using the trace element abundances determined by ICP-MS, the decay rates of Rotenberg *et al.* (2012) and Lugmair & Marti (1978). Initial ratios (i) and uncertainties (2σ) were propagated according to Ickert (2013). Cpx: Clinopyroxenite; Ol-gb: Olivine gabbro; Gb: Gabbro; Mzgb: Monzogabbro; Mzdr: Monzodiorite; Mz: Monzonite; Qz-sy: Quartz-syenite; Tr-bas: Trachybasalt.

Locality	Cima Pape							
Lithology	Ol-gb	Ol-gb	Gb	Mzgb	Mzdr	Tr-bas	Tr-bas	Tr-bas
Sample	DL14	DL16	NN11	NN14	NN10	DL25	DL29	DL76
Oxide (wt%)								
SiO₂	48.25	47.53	50.43	51.95	52.85	50.82	53.20	51.24
TiO₂	1.10	1.27	1.05	0.92	0.85	1.07	0.95	1.15
Al₂O₃	14.02	11.12	12.81	14.63	16.38	16.79	15.55	17.50
Fe₂O₃	1.49	1.77	1.44	1.14	1.09	1.20	1.03	1.23
FeO	9.91	11.82	9.58	7.57	7.25	8.03	6.89	8.23
MnO	0.15	0.18	0.18	0.13	0.13	0.11	0.14	0.15
MgO	11.38	12.17	10.21	7.89	6.87	6.21	6.15	5.08
CaO	9.47	10.60	9.32	10.02	7.10	9.94	10.34	9.62
Na₂O	2.01	1.59	2.29	2.26	3.46	2.26	2.69	2.60
K₂O	1.90	1.62	2.36	3.07	3.42	3.07	2.68	2.71
P₂O₅	0.32	0.33	0.33	0.41	0.60	0.49	0.38	0.48
Tot.	100.00	100.00	100.00	100.00	100.00	100.00	100.00	100.00
LOI	2.93	2.98	2.20	1.80	2.15	1.84	1.95	1.68
Mg#	**67.18**	**64.72**	**65.51**	**64.98**	**62.82**	**57.95**	**61.37**	**52.39**
Trace element (ppm)								
Pb	11.0	10.0	16.2	15.2	16.6	13.0	14.0	12.0
Zn	156	103	92.8	63.5	56.1	117	196	93.0
Ni	50.0	62.0	67.4	26.7	16.4	28.0	54.0	35.0
Co	50.0	60.0	48.3	34.4	30.6	32.0	32.0	31.0
Cr	187	244	201	93.3	64.9	102	314	130
V	354	426	337	257	181	265	250	267
Rb	23.9	20.7	47.0	55.1	95.0	50.8	19.3	28.4
Ba	382	331	423	508	562	543	432	490
Sr	319	210	575	803	884	618	444	584
Nb	8.21	7.91	8.26	10.0	12.4	14.2	11.1	12.5
Zr	88.6	67.5	81.5	156	105	200	143	179
Hf	2.59	2.10	2.31	3.85	2.72	4.78	3.67	4.32
U	0.71	0.67	0.91	1.62	1.78	1.39	1.37	1.40
Th	3.13	2.65	4.46	7.99	9.76	5.56	6.02	4.19
Y	18.2	18.8	23.4	24.7	26.8	19.9	19.3	14.2
Ta	0.43	0.41	0.49	0.52	0.57	0.67	0.58	0.58
La	15.2	14.2	17.8	24.9	38.6	22.2	20.1	15.9
Ce	32.4	31.2	40.4	52.6	66.5	48.4	40.7	39.9
Pr	4.27	4.13	5.27	6.84	9.37	5.60	4.79	4.11
Nd	19.7	19.4	24.0	29.9	38.9	24.5	20.5	18.1
Sm	4.25	4.27	5.46	6.39	7.69	4.82	4.06	3.57
Eu	1.10	1.04	1.44	1.70	2.08	1.23	1.05	0.97
Gd	3.92	4.01	4.83	5.56	6.84	4.57	3.79	3.39
Tb	0.62	0.63	0.81	0.91	1.04	0.67	0.58	0.50
Dy	3.09	3.15	4.31	4.85	5.24	3.28	3.00	2.46
Ho	0.61	0.63	0.89	1.00	1.07	0.65	0.63	0.49
Er	1.60	1.66	2.36	2.65	2.81	1.78	1.81	1.33
Tm	0.25	0.26	0.33	0.37	0.39	0.28	0.31	0.21
Yb	1.43	1.48	2.15	2.46	2.51	1.65	1.89	1.26
Lu	0.21	0.22	0.32	0.36	0.36	0.25	0.29	0.19
$^{87}Sr/^{86}Sr$	0.705604	0.705837					0.705459	0.704980
$^{87}Rb/^{86}Sr$	0.2167	0.2844					0.1257	0.1408
$^{87}Sr/^{86}Sr(i)$	0.704895	0.704906					0.705047	0.704519
2σ	0.000020	0.000021					0.000019	0.000026
$^{143}Nd/^{144}Nd$	0.512444	0.512456					0.512415	0.512461
$^{147}Sm/^{144}Nd$	0.1305	0.1334					0.1199	0.1193
$^{143}Nd/^{144}Nd(i)$	0.512244	0.512252					0.512231	0.512278
2σ	0.000006	0.000006					0.000007	0.000007

Table A5.1. (continued)

Locality	Mt. Monzoni								
Lithology	Cpx	Ol-gb	Gb	Mzgb	Mzgb	Mzgb	Mz	Mz	Qz-sy
Sample	C12	C5	CB13	P38	C2	NCM	CB11	NCG	CB10
Oxide (wt%)									
SiO_2	43.03	45.72	49.51	52.33	52.48	51.19	52.73	51.87	69.82
TiO_2	1.45	1.45	1.37	0.85	1.05	1.01	0.96	1.30	0.37
Al_2O_3	5.99	12.63	18.71	19.80	17.01	22.27	21.41	21.12	15.05
Fe_2O_3	2.20	1.66	1.28	1.08	1.07	0.75	0.78	0.83	0.31
FeO	14.65	11.04	8.56	7.19	7.16	5.00	5.18	5.51	2.07
MnO	0.22	0.21	0.17	0.16	0.14	0.16	0.12	0.14	0.05
MgO	16.86	11.78	5.19	3.05	4.72	3.69	2.77	3.37	0.82
CaO	14.86	12.25	9.44	8.96	9.40	9.11	7.20	7.00	1.87
Na_2O	0.02	1.39	2.84	3.13	3.28	3.74	4.01	4.13	3.12
K_2O	0.54	1.60	2.27	3.08	3.37	2.41	4.03	3.81	6.25
P_2O_5	0.17	0.28	0.66	0.36	0.32	0.67	0.80	0.92	0.26
Tot.	100.00	100.00	100.00	100.00	100.00	100.00	100.00	100.00	100.00
LOI	2.05	1.23	1.01	0.98	1.08	0.00	1.56	1.88	1.78
Mg#	**67.22**	**65.53**	**51.96**	**43.04**	**54.04**	**56.79**	**48.83**	**52.20**	**41.53**
Trace element (ppm)									
Pb	n.d.	n.d.	n.d.	n.d.	n.d.	n.d.	n.d.	n.d.	n.d.
Zn	n.d.	n.d.	n.d.	n.d.	n.d.	n.d.	n.d.	n.d.	n.d.
Ni	117	72.0	28.0	16.0	28.0	15.0	11.0	10.0	9.00
Co	83.0	54.0	32.0	23.0	28.0	13.0	16.0	16.0	5.00
Cr	244	205	52.0	20.0	51.0	24.0	12.0	10.0	14.0
V	553	436	245	164	246	133	123	137	27.0
Rb	20.0	43.0	52.0	94.4	119	78.7	129	153	241
Ba	96.0	330	593	674	649	590	732	818	472
Sr	143	542	766	911	915	1321	1350	1248	192
Nb	4.00	7.00	11.0	21.4	12.5	11.7	10.0	22.3	24.0
Zr	57.0	92.0	129	71.5	90.3	70.7	77.0	86.7	161
Hf	n.d.	n.d.	n.d.	2.51	2.98	2.01	n.d.	2.52	n.d.
U	n.d.	n.d.	n.d.	1.27	1.46	1.10	n.d.	1.66	n.d.
Th	4.00	3.00	6.00	7.64	6.59	4.92	7.00	8.03	17.0
Y	17.0	24.0	25.0	33.5	27.5	21.4	23.0	26.9	11.0
Ta	n.d.	n.d.	n.d.	1.01	0.65	0.62	n.d.	0.94	n.d.
La	7.2	15.8	27.4	33.9	22.8	29.8	36.6	42.4	37.3
Ce	26.2	42.3	62.1	70.5	46.7	58.8	77.8	84.9	74.9
Pr	n.d.	n.d.	n.d.	8.28	5.76	6.94	n.d.	9.60	n.d.
Nd	13.2	20.7	28.9	36.1	25.0	29.4	31.2	40.7	27.8
Sm	3.88	5.62	6.59	6.89	5.06	5.17	6.47	7.02	5.65
Eu	0.98	1.51	1.91	1.72	1.38	1.86	1.86	1.92	0.81
Gd	3.87	5.26	5.79	6.53	4.78	4.83	5.28	6.58	4.19
Tb	n.d.	n.d.	n.d.	1.00	0.77	0.68	n.d.	0.92	n.d.
Dy	2.92	4.2	4.44	5.02	3.96	3.22	3.70	4.24	2.87
Ho	n.d.	n.d.	n.d.	1.02	0.83	0.64	n.d.	0.85	n.d.
Er	1.4	2.06	2.26	2.76	2.29	1.71	2.00	2.30	1.44
Tm	n.d.	n.d.	n.d.	0.44	0.38	0.26	n.d.	0.36	n.d.
Yb	1.13	1.86	2.00	2.63	2.29	1.52	1.76	2.08	1.37
Lu	0.2	0.32	0.36	0.40	0.35	0.23	0.28	0.30	0.16
$^{87}Sr/^{86}Sr$		0.705059		0.705107				0.705577	
$^{87}Rb/^{86}Sr$		0.2295		0.2997				0.3554	
$^{87}Sr/^{86}Sr(i)$		0.704308		0.704126				0.704413	
2σ		0.000021		0.000021				0.000028	
$^{143}Nd/^{144}Nd$		0.512500		0.512434				0.512441	
$^{147}Sm/^{144}Nd$		0.1641		0.1155				0.1043	
$^{143}Nd/^{144}Nd(i)$		0.512249		0.512257				0.512281	
2σ		0.000008		0.000007				0.000007	

Table A5.2. Major element analyses and a.p.f.u. calculation of representative amphibole (Amp) from Mt. Monzoni monzogabbros. A.p.f.u. were calculated using the Locock (2014) computation; the classification follows the recommendations of the IMA-CNMNC subcommittee on amphiboles (Hawthorne _et al._, 2012; Oberti _et al._, 2012).

Mineral	Amp	Amp	Amp	Amp
Sample	T1	T1	T1	T1
Lithology	Mzgb	Mzgb	Mzgb	Mzgb
Name	Amph1	Amph2	Amph3	Amph4
SiO$_2$	51.124	49.287	49.944	48.648
TiO$_2$	0.093	0.171	0.281	0.610
Al$_2$O$_3$	3.516	4.925	4.179	5.233
FeO$_{tot}$	14.835	13.901	18.545	15.323
MnO	0.528	0.278	0.297	0.276
MgO	14.850	14.627	10.902	12.985
CaO	10.441	11.577	12.123	12.101
Na$_2$O	0.388	0.602	0.407	0.573
K$_2$O	0.160	0.422	0.403	0.353
Cr$_2$O$_3$	0.004	0.013	0.000	0.012
F	0.155	0.185	0.028	0.016
Cl	0.015	0.180	0.337	0.085
Tot.	**96.109**	**96.167**	**97.443**	**96.215**
Fe3+/ΣFe used	0.170	0.323	0.083	0.247
Group	OH,F,Cl	OH,F,Cl	OH,F,Cl	OH,F,Cl
Subgroup of (OH,F,Cl)	Ca	Ca	Ca	Ca
Species	actinolite	magnesio-ferri-hornblende	actinolite	magnesio-ferri-hornblende
Formula Assignments				
(T) Si	7.525	7.256	7.470	7.230
(T) Al	0.475	0.744	0.530	0.770
(T) Ti				
(C) Ti	0.010	0.019	0.032	0.068
(C) Al	0.135	0.111	0.206	0.147
(C) Cr	0.000	0.002	0.000	0.001
(C) Fe^{3+}	0.310	0.552	0.192	0.471
(C) Ni	0.002	0.000	0.000	0.000
(C) Mn^{2+}	0.000	0.000	0.012	0.002
(C) Fe^{2+}	1.284	1.106	2.128	1.433
(C) Mg	3.258	3.210	2.431	2.877
(B) Mn^{2+}	0.066	0.035	0.026	0.032
(B) Fe^{2+}	0.232	0.053	0.000	0.000
(B) Ca	1.647	1.826	1.943	1.927
(B) Na	0.055	0.086	0.031	0.041
(A) Ca	0.000	0.000	0.000	0.000
(A) Na	0.055	0.086	0.087	0.125
(A) K	0.030	0.079	0.077	0.067
O (non-W)	22.000	22.000	22.000	22.000
(W) OH	1.903	1.831	1.838	1.834
(W) F	0.072	0.086	0.013	0.008
(W) Cl	0.004	0.045	0.085	0.021
(W) O	0.021	0.038	0.063	0.137
Sum T,C,B,A	15.084	15.165	15.165	15.191

Table A5.3. Major element analyses and a.p.f.u. calculation of representative plagioclase (Pl) and K-feldspar (Kfs) from Mt. Monzoni monzogabbros.

Mineral	Pl	Pl	Pl	Kfs	Kfs	Pl	Pl
Sample	T1	T1	T1	T1	T1	T1	T1
Lithology	Mzgb	Mzgb	Mzgb	Mzgb	Mzgb	Mzgb	Mzgb
Name	Plg1	Plg2	Plg3	Kf1	Kf2	Plg4	Plg5
SiO_2	53.472	53.632	52.94	63.781	63.709	54.236	53.957
TiO_2	0.016	0.014	0.017	0	0	0.015	0.024
Al_2O_3	29.011	28.799	29.186	18.489	18.666	28.215	28.784
FeO_{tot}	0.381	0.382	0.307	0.046	0.088	0.278	0.261
MnO	0.016	0	0.018	0.009	0	0.016	0.008
MgO	0.022	0.031	0.024	0	0.002	0.023	0.031
CaO	11.469	11.041	11.66	0	0	10.497	11.169
Na_2O	4.931	5.104	4.726	0.363	0.309	5.299	5.053
K_2O	0.175	0.267	0.276	15.413	15.405	0.358	0.266
BaO	0	0.038	0.012	0.152	0.173	0	0.022
Tot.	**99.489**	**99.3**	**99.166**	**98.226**	**98.339**	**98.903**	**99.574**
A.p.f.u.							
Si	2.431	2.442	2.418	2.993	2.986	2.474	2.449
Al	1.555	1.546	1.571	1.023	1.032	1.517	1.540
Fe^{3+}	0.014	0.015	0.012	0.002	0.003	0.011	0.010
Mg	0.000	0.000	0.000	0.000	0.000	0.000	0.000
Ca	0.559	0.539	0.571	0.000	0.000	0.513	0.543
Na	0.435	0.451	0.419	0.033	0.028	0.469	0.445
K	0.010	0.016	0.016	0.923	0.921	0.021	0.015
An	**55.67**	**53.61**	**56.76**	**0.00**	**0.00**	**51.17**	**54.14**
Ab	**43.32**	**44.85**	**41.64**	**3.46**	**2.96**	**46.75**	**44.32**
Or	**1.01**	**1.54**	**1.60**	**96.54**	**97.04**	**2.08**	**1.54**

Table A5.4. Major element analyses and a.p.f.u. calculation of representative biotite (Bt) from Mt. Monzoni monzogabbros.

Mineral	Bt	Bt	Bt	Bt
Sample	T1	T1	T1	T1
Lithology	Mzgb	Mzgb	Mzgb	Mzgb
Name	Bt1	Bt2	Bt3	Bt4
SiO_2	34.884	35.292	34.886	34.822
TiO_2	6.085	6.028	5.703	5.511
Al_2O_3	14.133	14.133	13.803	13.882
FeO_{tot}	18.255	18.294	20.016	19.735
MnO	0.136	0.128	0.140	0.128
MgO	11.405	11.022	10.298	10.504
CaO	0.034	0.033	0.026	0.047
Na_2O	0.168	0.169	0.135	0.126
K_2O	8.845	8.782	8.759	9.144
Cr_2O_3	0.000	0.007	0.014	0.023
F	0.123	0.187	0.068	0.114
Cl	0.266	0.295	0.298	0.273
Tot.	**94.334**	**94.370**	**94.146**	**94.309**
A.p.f.u.				
Si	2.700	2.729	2.727	2.721
Ti	0.354	0.351	0.335	0.324
Al	1.289	1.288	1.272	1.279
Fe^{3+}	0.000	0.000	0.000	0.000
Fe^{2+}	1.182	1.183	1.309	1.290
Mn	0.009	0.008	0.009	0.008
Mg	1.316	1.270	1.200	1.224
Ca	0.003	0.003	0.002	0.004
Na	0.025	0.025	0.020	0.019
K	0.873	0.866	0.874	0.912
Tot.	**7.751**	**7.723**	**7.749**	**7.781**

Chapter 6

The lamprophyric dykes

Enclosed manuscript:

Casetta, F., Ickert, R.B., Mark, D.F., Bonadiman, C., Giacomoni, P.P., Ntaflos, T., Coltorti, M., The alkaline lamprophyres of the Dolomitic Area (Southern Alps, Italy): markers of the Late Triassic change from orogenic-like to anorogenic magmatism. (*submitted*)

Chapter 6. The lamprophyric dykes

6.1. Introduction

The late-stage emplacement of lamprophyric dykes typifies a large number of plutonic complexes, providing important information of the local geodynamic evolution. According to Rock *et al.* (1987), Le Maitre *et al.* (1989), Rock (1991), Woolley *et al.* (1996) and Le Maitre *et al.* (2002), lamprophyres are defined as H_2O, CO_2 and alkali-rich rocks with a porphyritic texture, characterized by the essential presence of amphibole and/or phlogopite-biotite phenocrysts and the common occurrence of halides, carbonates, sulphides and zeolites. Feldspars and/or feldspathoids are often present as groundmass phases. Mineral chemistry is by far a key factor for the identification/classification of these rocks: high-Ti, -Ba and -F amphiboles and micas, high-Al clinopyroxenes, high-Zn spinels and Fe^{3+}-rich micas are in fact diagnostic phases of lamprophyres. The genesis of lamprophyres is commonly attributed to partial melting of a metasomatised mantle (Rock, 1991; Stoppa *et al.*, 2014; Pandey *et al.*, 2017*a*; 2017*b*; Soder & Romer, 2018), whereas their emplacement is usually associated to the onset of lithospheric extensional-transtensional tectonic regimes. Lamprophyres, in fact, are typically associated with strike-slip movements, and potentially act as markers of a change in the geodynamic regime and tectono-magmatic conditions (Scarrow *et al.*, 2011). Following Le Maitre *et al.* (2002), lamprophyric rocks are grouped, on the basis of their mineralogy, into three associations: i) minette-kersantite; ii) vogesite-spessartite; iii) sannaite-camptonite-monchiquite. This discrimination partially reflects what was originally proposed by Le Maitre *et al.* (1989) and Rock (1991), according to whom the first two associations belong to the "calc-alkaline (shoshonitic) lamprophyres", whereas the third to the "alkaline lamprophyres". While the calc-alkaline variety is commonly (but not exclusively) associated to convergent settings, alkaline lamprophyres are typical of divergent margins and continental intra-plate settings (Rock, 1991; Batki *et al.*, 2014; Stoppa *et al.*, 2014; Ubide *et al.*, 2014; Lu *et al.*, 2015; Pandey *et al.*, 2017*a*; 2017*b*), their composition resembling that of volatile-enriched alkali basalts, basanites and nephelinites. Several authors have investigated the main geochemical features of the Cretaceous (110 Ma) to Oligocenic (29 Ma) alkaline lamprophyres across Italy, speculating about their genesis by partial melting of the deep mantle portions metasomatized by alkaline carbonatitic components (Galassi *et al.*, 1994; Vichi *et al.*, 2005; Stoppa, 2008; Stoppa *et al.*, 2014). Lesser known are the alkaline lamprophyres of the Dolomitic Area (Southern Alps, NE Italy), intruded in and around the Middle Triassic Predazzo Intrusive Complex, to which they seem geochemically and temporally related (Lucchini *et al.*, 1969). This complex is one

of the few plutonic expressions of the high-K calc-alkaline to shoshonitic magmatism that shaped the Dolomitic Area between 237 and 238 Ma (Gasparotto & Simboli, 1991; Bonadiman *et al.*, 1994; Mundil *et al.*, 1996; Abbas *et al.*, 2018; Storck *et al.*, 2018; Wotzlaw *et al.*, 2018). Recent petrologic and Sr-Nd isotopic studies on the Predazzo pluton, complemented by field observations, revealed: i) the existence of three different SiO_2-saturated to -undersaturated magma batches and their precise emplacement sequence at shallow crustal depth (1.4-5.6 km); ii) the textural gradual transition between the intrusion and the overlying hypabyssal and volcanic (basaltic/latitic) deposits; iii) the EM I-like Sr-Nd isotopic signature of the intrusive rocks and the low degree of crustal assimilation experienced by Ladinian magmas during ascent; iv) the slight isotopic depletion of the mantle source with time, moving towards higher $^{143}Nd/^{144}Nd$ ratios from the SiO_2-saturated to -undersaturated batches (see Chapters 3 and 4).

The connection between the alkaline lamprophyres and the host volcano-plutonic complex, however, has never been investigated, remaining an intriguing topic and a key factor for deciphering the evolution of the magmatism of the Dolomitic Area. For this reason, whole-rock major, trace element and Sr-Nd isotopic determinations, together with mineral phases major and trace element chemistry, were used to characterize the Predazzo alkaline lamphrophyres and model their mantle source, on one side, and the main differentiation dynamics to which lamprophyric melts underwent at shallow depth, on the other side. Finally, $^{40}Ar/^{39}Ar$ dating on crystal separates enabled to frame for the first time their emplacement within the temporal evolution of the Dolomitic Area and the whole Southern Alps magmatism.

6.2. Petrography and whole rock geochemistry

6.2.1. Petrography

The lamprophyres of the Dolomitic Area are part of an articulated swarm of dykes which intrudes both the Predazzo Intrusive Complex, the overlying volcanites and the Permo-Triassic sedimentary host rocks (Fig. 35). These dykes, metric to decimetric in thickness, are mainly porphyritic basalts to trachytes with the same geochemical features of the intrusive rocks (i.e. high-K calc-alkaline to shoshonitic affinity, see Chapters 3 and 4). Lamprophyres are easily recognizable on field for their grey-greenish colour, which grades into a more green shade in the altered specimens, strongly contrasting with the pink granitic/syenogranitic body, in which are preferentially (even if not exclusively) intruded (Fig. 35; see also Lucchini *et al.*, 1969). The thickness of lamprophyric dykes ranges from

0.2 to 2.0 metres and their orientation is generally NNW-SSE to N-S. The contact between lamprophyres and country rocks is generally sharp and no significant thermometamorphic structures are present. The intense state of alteration of most of these dykes prevents the identification of any textural variation between their central and outer portions.

Distinctive feature of Predazzo lamprophyres is the abundant presence of carbonate-bearing ocelli, feldspar and amphibole megacrysts (up to 5 cm), and xenoliths (Fig. 35; Vardabasso, 1929; Lucchini *et al.*, 1969; 1982). These latters are mainly cumulitic clinopyroxenites (Morten, 1980) and/or feldspar+quartz xenoliths from the Triassic intrusive rocks and the Permian basement, but also a few spinel lherzolites can be found (Carraro & Visonà, 2003). The mineral paragenesis of Predazzo lamprophyres, together with their chemical composition, led Lucchini *et al.* (1969) to classify them as camptonites, an alkaline variety of lamprophyres characterized by abundant plagioclase (modally more abundant than K-feldspar), and the absence of leucite and Na-foids (Rock, 1991).

The texture of the analyzed samples is generally panidiomorphic, with, in order of decreasing abundance, amphibole, plagioclase, clinopyroxene and olivine phenocrysts, embedded in a microcrystalline assemblage made of amphibole, plagioclase, clinopyroxene, K-feldspar and Fe-Ti oxides (Fig. 36). Accessory phases include carbonate, ilmenite, titanite, apatite and analcime. The modal abundance of the main constituents can be summarized as: amphibole 35-55 vol.%, plagioclase 30-40 vol.%, clinopyroxene 0-10 vol.%, olivine 0-10 vol.%, K-feldspar 2-6 vol.%, Fe-Ti oxides 3-6 vol.%. Clinopyroxene ad olivine are totally absent only in the MA1 sample (Fig. 36), where the presence of plagioclase, K-feldspar and Fe-Ti oxides strongly increases. Carbonate is present as pseudomorphous phase in replacement of olivine, in secondary veins/fractures, or as major constituent of small (200-250 μm in diameter) spherical ocelli, variably distributed and surrounded by the tangential (orthogonal) growth of multiple small plagioclase, amphibole and/or clinopyroxene crystals (see the following section for a detailed discussion of these features). These features confirm the definition of camptonites proposed by the previous authors for all Predazzo lamprophyres.

Amphibole, pale brown to reddish in colour, always occurs with euhedral habitus and elongated shape in both the phenocrysts and the groundmass types. In the sample MA1, amphibole shape is often nearly acicular and its colour is pale brown to yellowish (Fig. 36). It ranges in size from 20-30 μm (groundmass) to 2.5 mm (phenocryst), excluding the exceptional dimensions reached by the megacrysts, whose colour ranges from dark brown to black.

Plagioclase crystals are generally euhedral and vary in size between 10-20 and 400-450 μm. Larger plagioclase xenocrysts, fragments and xenoliths (0.5-1 mm) of crustal origin can be

easily distinguished from the phenocrysts by their rounded shape and by the presence of well developed reaction rims made of Fe-Ti oxides, secondary feldspar and rare clinopyroxene. Clinopyroxene, pale brown in colour, is less abundant and smaller than amphibole, rarely exceeding 150-200 µm in size among the phenocrysts. Relicts of bigger euhedral crystals (1-2 mm) are almost totally replaced by plagioclase, amphibole and Fe-Ti oxides, resulting in an "atoll-like" shape, where only the outermost rim of clinopyroxene is preserved. The formation of secondary epidote and chlorite often occurs at the expense of clinopyroxene. Olivine phenocrysts (100-350 µm) are rare and usually pseudomorphosed by calcite and serpentine. This kind of alteration, typical in lamprophyres, is indicated by the general term pilite (Velde, 1968; Rock, 1991). K-feldspar and Fe-Ti oxides are present only in the groundmass, rarely exceeding 40-50 µm in size.
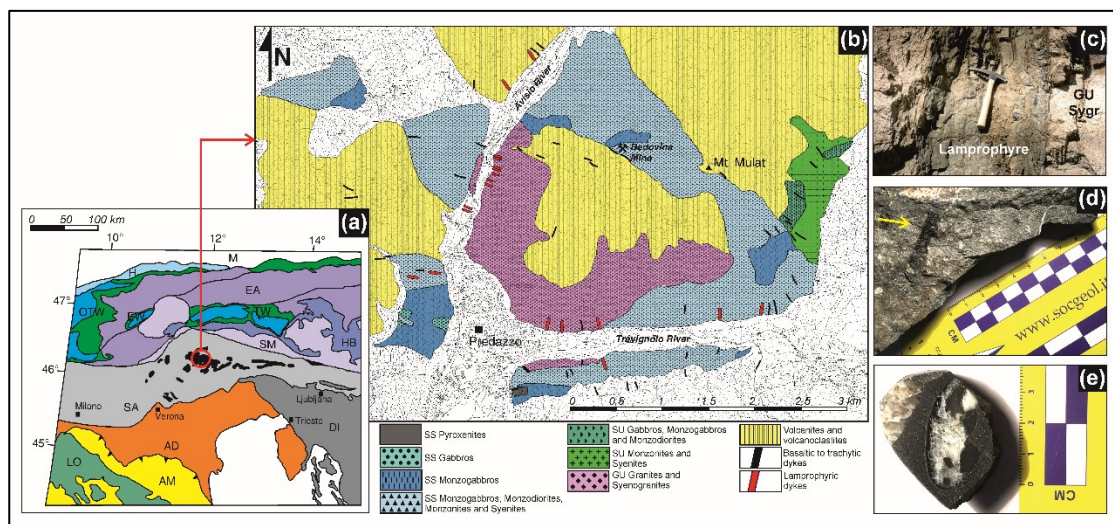
Fig. 35. (a) Map of the tectonic units of the eastern portion of the Alps (partly modified from Castellarin et al., 1988; Dal Piaz et al., 2003; Schmid et al., 2016). LO: Ligurian Ophiolites; AM: deformed Adriatic margin; AD: Adriatic Microplate; SA: Southern Alps; DI: Dinarides; SM: Southern margin of Meliata; HB: Eoalpine High-Pressure Belt; TW: Tauern tectonic Window; EW: Engadine tectonic Window; OTW: Ossola-Tessin tectonic Window; EA: Eastern Austroalpine; H: Helvetic domain; M: Molasse foredeep. The Middle Triassic magmatic occurrences in the Southern Alps domain are evidenced in black. They are, from west to east: Brescian Alps, Alto Vicentino, Valsugana, Dolomitic Area (identified by the circle), Carnia and Karawanken. (b) Simplified geological map of the Predazzo Intrusive Complex (PIC), showing the occurrence of lamprophyric dykes. SS: Shoshonitic Silica Saturated unit; SU: Shoshonitic Silica Undersaturated unit; GU: Granitic Unit. (c) Lamprophyric dyke intruded in the Granitic Unit (GU) syenogranite (sy-gr) at Predazzo. (d) Amphibole megacryst (indicated by the arrow) and (e) clinopyroxenitic xenolith included in the lamprophyric rocks.
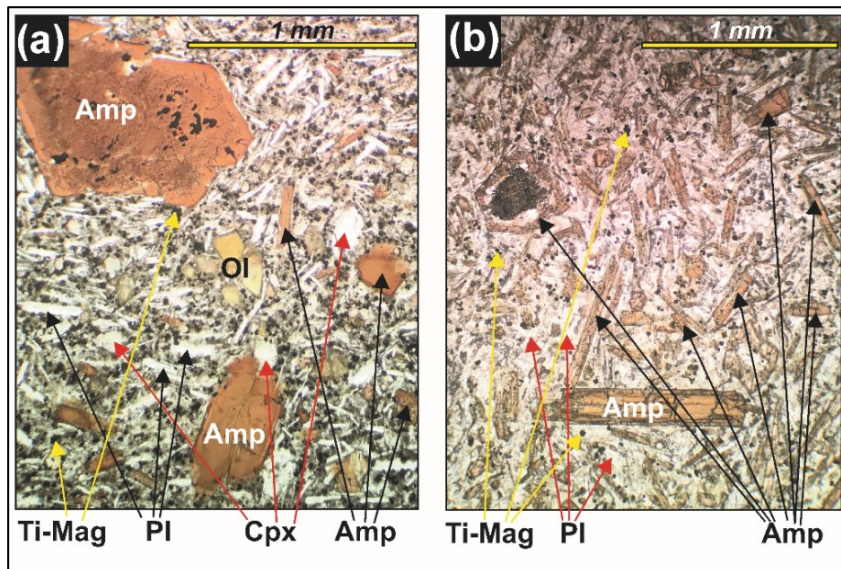
Fig. 36. Photomicrographs in transmitted plane-polarized light of (a) a less evolved and (b) a more evolved (sample MA1) camptonite. Amp: amphibole; Cpx: clinopyroxene; Ol: olivine; Pl: plagioclase; Ti-Mag: Ti-magnetite.
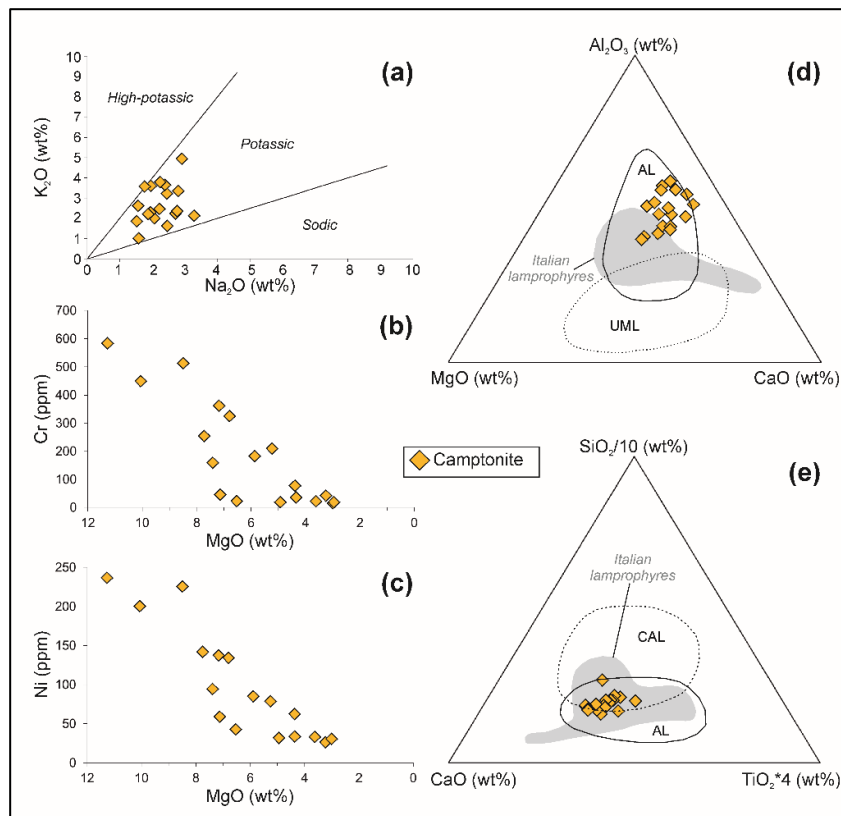
Fig. 37. (a) K_2O vs. Na_2O diagram, (b) Cr vs. MgO and (c) Ni vs. MgO variations diagrams for Predazzo camptonites. (d) Al_2O_3-MgO-CaO and (e) $SiO_2/10$-CaO-$TiO_2 \times 4$ ternary diagrams showing the composition of Predazzo camptonites compared to those of worldwide alkaline lamprophyres (AL), ultramafic lamprophyres (UML) and calc-alkaline lamprophyres (CAL). Data from Rock (1991). The compositional field of Cretaceous to Oligocenic Italian lamprophyres (grey field) is also reported for comparison (data from Stoppa et al., 2014).

6.2.2. Whole rock major and trace element chemistry

Predazzo camptonites are generally characterized by a SiO_2 range of 44.1 to 47.9 wt%, 1.6-3.2 Na_2O wt% and 1.0-3.7 K_2O wt%; an exception is constituted by sample MA1, which has higher silica (52.8 wt%) and alkali contents (2.9 Na_2O wt%; 5.0 K_2O wt%; Table A6.1). Mg# (calculated as MgO/[MgO+FeO] mol%, assuming Fe_2O_3/FeO ratio of 0.15 in agreement with a fO_2 around +1 FMQ buffer; Kress & Carmichael, 1991) is extremely variable, ranging from 70 to 37. These values strongly depend on the large MgO variations (from 3.0 to 11.3 wt%) at a narrower FeO interval (8.5-10.8 wt%). The lowest FeO content (6.5 wt%) is reported from sample MA1 (Mg# of about 47), whose compositional (and petrographic) features point towards a slightly differentiated nature. All lamprophyres have a K-affinity (Fig. 37), and their CaO contents span the range of 8.8-14.2 wt%, being sensitive to secondary alteration/hydrothermal processes and to the variable presence of carbonates. In the Al_2O_3-MgO-CaO and SiO_2/10-CaO-TiO_2×4 ternary diagrams, all samples plot in the alkaline lamprophyres field (Rock, 1987; 1991), resulting slightly enriched in Al_2O_3 with respect to the Cretaceous (110 Ma) to Oligocenic (29 Ma) Italian lamprophyres (Stoppa *et al.*, 2014, and references therein). CIPW norm calculations highlight the moderate to strong Si-undersaturation, with 1-13% normative nepheline for all samples and 3-5% normative leucite for two samples with high K/Si. MgO is negatively correlated with compatible elements, such as Ni (237-27 ppm) and Cr (585-14 ppm; Fig. 37).

Chondrite-normalized (Sun & McDonough, 1989) incompatible element patterns of Predazzo lamprophyres (Fig. 38) are characterized by Nb, Ta, LILE (especially Sr), Zr and Ti positive spikes, as well as by Th-U negative anomalies. These features are similar to those documented by Scarrow *et al.* (2011) for the Central Iberia lamprophyres. Predazzo lamprophyres patterns resemble that of alkaline rocks, but, when compared to the average composition of oceanic island basalts (OIB, Sun & McDonough, 1989), they are depleted in all elements except Rb, Ba and Sr. This feature is even more evident when compared to the worldwide camptonites (Fig. 38; Rock, 1991). Chondrite-normalized (Sun & McDonough, 1989) REE patterns are characterized by LREE enrichment (up to 200 times chondrite; La_N/Yb_N up to 11.0) and flat M-HREE profiles, with absence of Eu negative anomaly, consistent with the lack of significant plagioclase fractionation (Fig. 38). The less differentiated camptonite (Mg# 70) is slightly LREE-depleted with respect to the other camptonites, as evidenced by its lower La_N/Yb_N ratio of ~6.0. The Gd_N/Yb_N ratios of Predazzo camptonites range between 1.7 and 2.7, contrasting with the typical steep-sloping shape of OIB rocks in general, and of camptonites in particular (Fig. 38; Sun & McDonough, 1989; Rock, 1991). Compared to the other Italian lamprophyres (Galassi *et al.*, 1994; Vichi

et al., 2005; Stoppa, 2008; Stoppa *et al.*, 2014), Predazzo camptonites are generally depleted in all incompatible elements, except for Rb and K. Common feature is the absence of a Ta-Nb-Ti negative anomaly (Fig. 38). The HFSE distribution in the less differentiated Predazzo camptonites well fit the OIB field in the Th_N vs. Nb_N tectonic discrimination diagram (Fig. 39a; Saccani, 2015), highlighting a clear genetic link to a within-plate setting. The alkaline nature of Predazzo lamprophyres is clearly evidenced by the Ti/Y vs. Nb/Y and Zr/Y vs. Zr diagrams (Fig. 39b-c; Pearce & Norry, 1979; Pearce, 1982), as well as by the Th-Hf-Ta and Zr-Nb-Y ternary diagrams (Fig. 39e-f; Wood, 1980; Meschede, 1986).
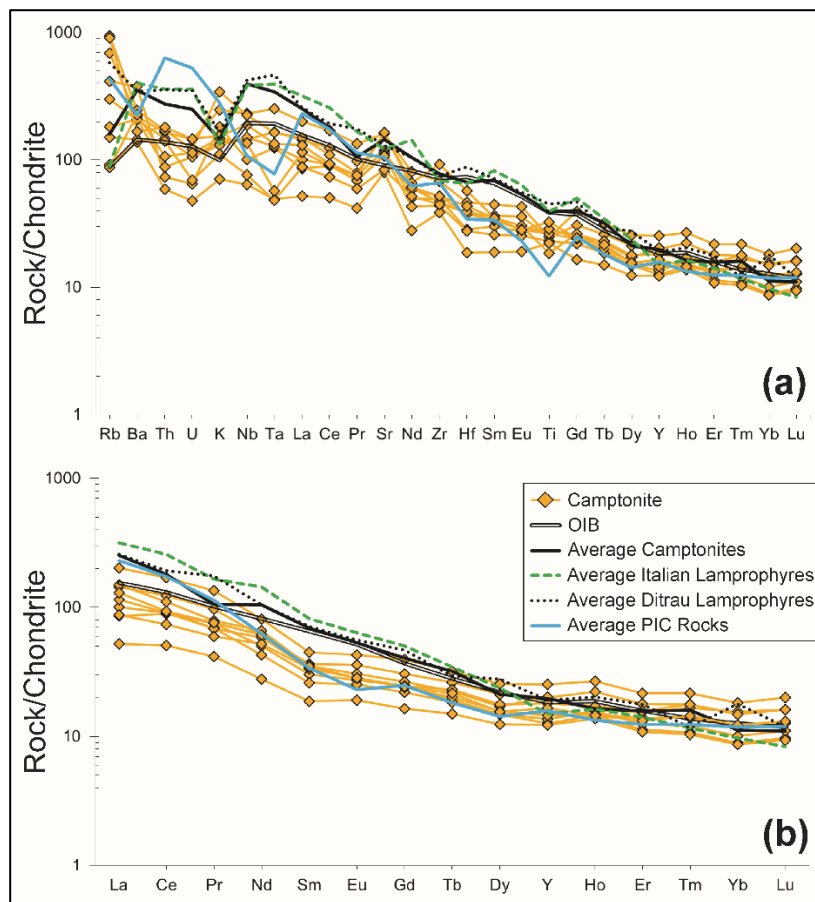
Fig. 38. Chondrite-normalized (Sun & McDonough, 1989) trace element (a) and REE patterns (b) of Predazzo camptonites. The OIB pattern (Sun & McDonough, 1989), the average composition of the worldwide camptonites (Rock, 1991), Italian lamprophyres (Galassi et al., 1994; Vichi et al., 2005; Stoppa et al., 2008; 2014), Ditrau lamprophyres (Batki et al., 2014) and Predazzo Intrusive Complex Shoshonitic Silica Saturated (SS) and Undersaturated (SU) rocks (Chapters 3 and 4) are reported for comparison.
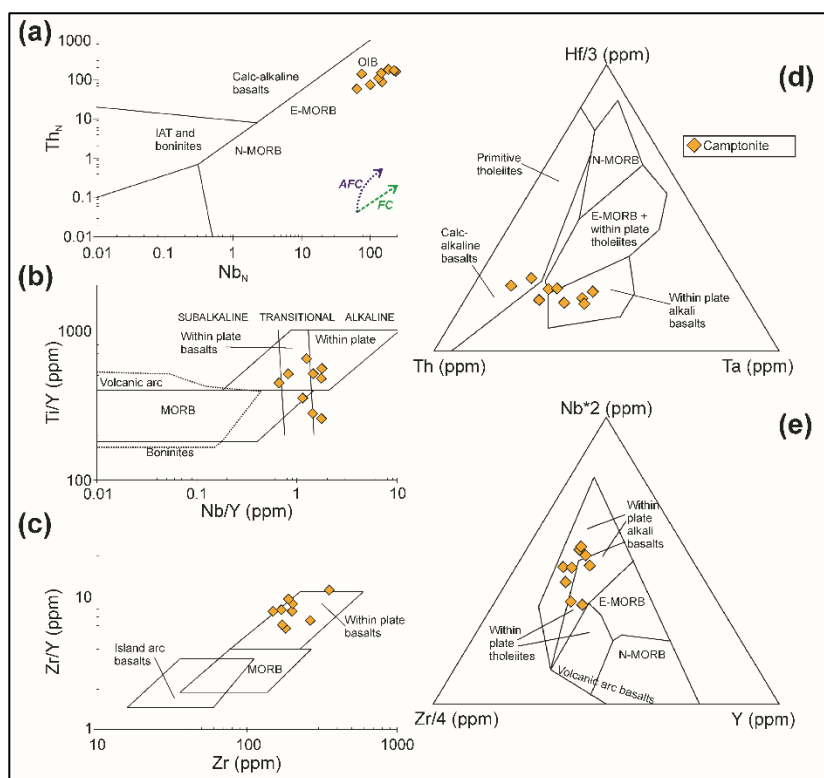
Fig. 39. Trace element discrimination diagrams for Predazzo camptonites: (a) Th_N vs. Nb_N diagram (Saccani, 2015); (b) Ti/Y vs. Nb/Y diagram (Pearce, 1982); (c) Zr/Y vs. Zr diagram (Pearce and Norry, 1979); (d) Th-Hf-Ta ternary diagram (Wood, 1980); (e) Zr-Nb-Y ternary diagram (Meschede, 1986). Fractional Crystallization (FC) and Assimilation and Fractional Crystallization (AFC) vectors reported in (a) are in accordance with Saccani (2015).

6.3. Mineral chemistry and textures

Major element composition of amphibole, clinopyroxene, feldspars, oxides and trace element analyses of amphibole and clinopyroxene were determined on representative lamprophyre samples. The intense state of alteration of olivine in pilite prevented its chemical analysis: according to Carraro & Visonà (2003), olivine phenocrysts in the less evolved Predazzo camptonites range in compostion from $Fo_{72.5}$ to $Fo_{87.5}$, suggesting a primitive, mantle-derived nature of these rocks.

6.3.1. Amphibole

Many amphibole classification schemes were proposed in literature (e.g. Tindle & Webb 1994; Leake *et al.*, 1997; Hawthorne *et al.*, 2012; Locock, 2014; Ridolfi *et al.*, 2018). Among the most recent classifications, we adopted the Locock (2014) a.p.f.u. computation, calculating the formula on the basis of 24 oxygens (OH, F, Cl, O), and assuming (OH, F, Cl) = (2 - 2Ti) and ^{W}O = 2Ti, according to the recommendations of the IMA-CNMNC subcommittee on amphiboles (Table A6.2; Hawthorne *et al.*, 2012; Oberti *et al.*, 2012). This

cation site distribution assignes the proper nomenclature while minimizing the OH and Fe^{3+} effects.

Amphiboles in Predazzo camptonites belong to both the ^{W}(OH, F, Cl)- and the ^{W}(O)-dominant (oxo-amphibole) groups, and to the Ca subgroup. Their composition is extremely variable between the less differentiated and the more differentiated samples, as testified by the Mg# (calculated as Mg/[Mg+Fe] mol% assuming all Fe as Fe^{2+}) range of 28-75. In the less evolved rocks amphibole ranges from pargasite to ferri-kaersutite, magnesio-hastingsite and Ti-rich magnesio-hastingsite, whereas in the more differentiated samples it varies from magnesio-hastingsite to Ti-rich magnesio-hastingsite, Ti-rich ferri-sadanagaite and Ti-rich ferro-ferri-sadanagaite (Table A6.2). The sadanagaitic composition is quite rare and represents the most Si-poor variety of amphibole reported from alkaline lamprophyres (Rock, 1991). On the basis of cation site distribution, the calculated maximum OH contents is 1.4 a.p.f.u. In terms of CaO/Na_2O and Al_2O_3/TiO_2 ratios, most of the analyzed amphiboles are similar to those reported by Rock (1991) in alkaline lamprophyres (Fig. 40). Some crystals have a quite high Al_2O_3/TiO_2 ratio, similar to those of the calc-alkaline hastingsites, but mantaining a CaO/Na_2O ratio comparable to the alkaline kaersutites (Fig. 40; Rock, 1991).
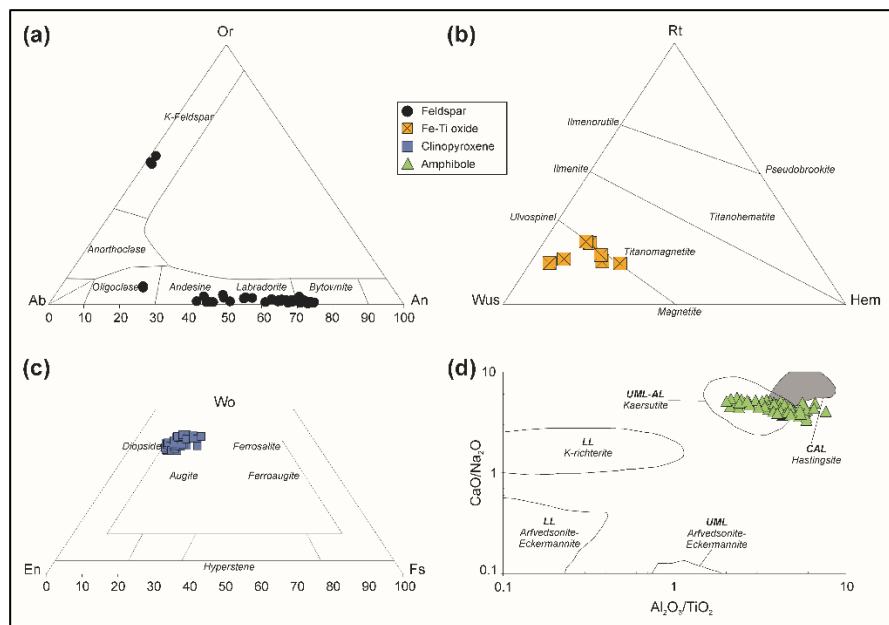
Fig. 40. Mineral phase classification diagrams showing the composition of the main crystals of Predazzo camptonites. (a) Orthoclase (Or)-Albite (Ab)-Anorthite (An) ternary diagram for plagioclase and K-Feldspar; (b) Rutile (Ru)-Wustite (Wu)-Hematite (Hm) ternary diagram for Fe-Ti oxide; (c) Wollastonite (Wo)-Enstatite (En)-Ferrosilite (Fs) diagram for clinopyroxene (after Morimoto, 1988). (d) CaO/Na_2O vs. Al_2O_3/TiO_2 diagram for amphibole crystals (after Rock, 1991). Compositional field of kaersutite in ultramafic (UML) and alkaline lamprophyres (AL), hastingsite in calc-alkaline lamprophyres (CAL), and K-richterite, arfvedsonite and eckermannite in lamproites (LL) are also reported in (d) for comparison (data from Rock, 1991).

6.3.1.1. Amphibole textural features and major element compositions

Optical and electron microscope observations, coupled with major element chemical data, enabled us to identify the occurrence of five distinct textural types of amphibole, following a scheme analogous to that proposed for plagioclase and clinopyroxene crystals at Mt. Etna by Giacomoni *et al.* (2014; 2016).

Type 1 amphiboles (Fig. 41a) are the most common and occur both phenocrysts and in the groundmass. They have euhedral contour with homogeneous pale brown to orange rounded dissolved cores; the more differentiated is the host rock, the more elongated is the crystal shape, becoming acicular in sample MA1. *Type 1* crystals are pargasitic to Ti-rich magnesio-hastingsitic (Mg# = 71-74), usually surrounded by a reddish ferri-kaersutitic rim (Mg# =59-66) with euhedral shape, in optical continuity with the cores. In *Type 1* crystals an intermediate magnesio-hastingsitic (Mg# = 72-74) overgrowth is often visible by means of electron microscope. Groundmass amphiboles reflect the composition of the outermost rims of the phenocrysts (ferri-kaersutite to Ti-rich magnesio-hastingsite).

Type 2 crystals (Fig. 41b), Ti-rich magnesio-hastingsitic in composition, have brown rounded cores (Mg# = 62-64), characterized by the presence of dispersed Fe-Ti oxides and melt pockets, and ferri-kaersutitic rims (Mg# = 60-68). The cores are often surrounded by magnesio-hastingsitic intermediate overgrowths analogous to those documented in *Type 1* amphiboles. Both the intermediate overgrowth and the external rim are in optical continuity with the core.

Type 3 crystals (Fig. 41c) have blackish dusty cores with euhedral edges. As in case of *Type 1* crystals, they are surrounded by Ti-rich magnesio-hastingsitic to ferri-kaersutitic rims (Mg# 53-70).

Type 4 amphiboles (Fig. 41d) are those previously defined xenocrysts. They usually are centimetric in size, black coloured and markedly altered, sometimes being resorbed in entire portions. Their Ti-rich magnesio-hastingsitic core (Mg# 51-62) is often pervaded by the incipient formation of fibrous minerals and micrometric veins bearing Fe-Ti oxides. The outer portions of the core present strongly dusty resorbed zones comparable to those recognized in *Type 3* crystals cores. *Type 4* xenocrysts are surrounded by a pale brown to reddish magnesio-hastingsitic to ferri-kaersutitic rim (Mg# ~68).

Type 5 amphiboles (Fig. 41e), documented only in sample MA1, occur both as phenocrysts and centimeter-scale megacrysts. They have dark brown Ti-rich ferri-sadanagaitic to Ti-rich ferro-ferri-sadanagaitic cores (Mg# = 29-39) and pale brown Ti-rich magnesio-hastingsitic rims (Mg# 68-72), grown in optical continuity. With respect to *Type 4* xenocrysts,

megacrysts are identified by their euhedral habitus and the absence of resorption/alteration features. It should be noticed that, although important indicators of the physico-chemical conditions of the magmatic system, *Type 2* to *Type 5* are much rarer than *Type 1* amphiboles, rarely exceeding 1-5 vol.% of the specimens.
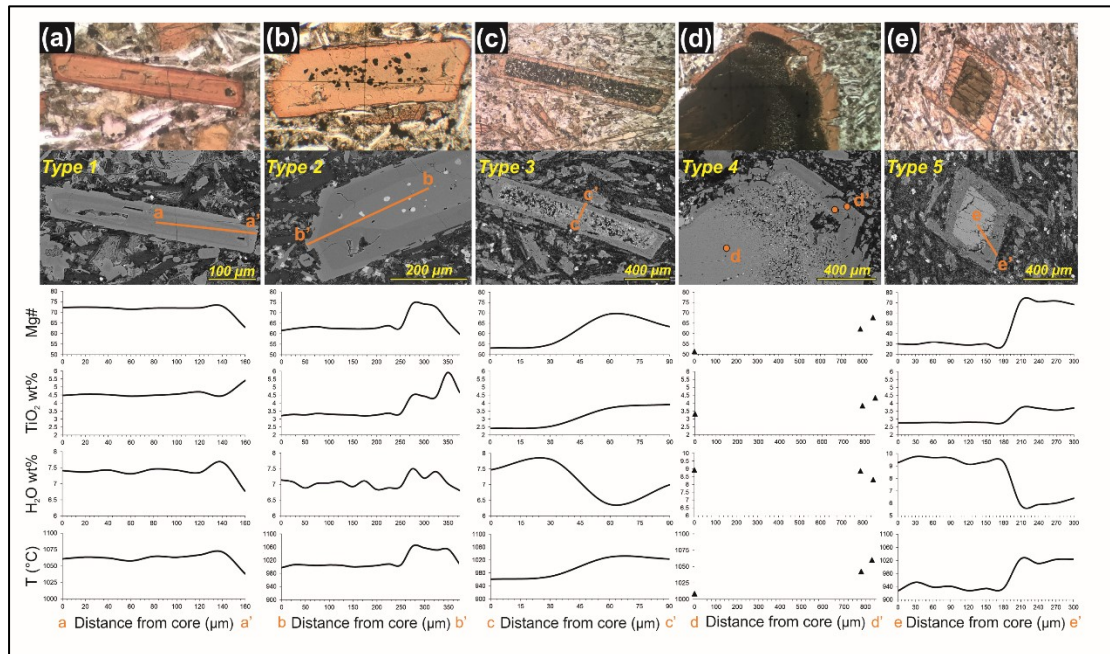
Fig. 41. Photomicrographs in transmitted plane-polarized light, back scattered SEM images and core-to-rim compositional (Mg# and TiO₂) profiles of (a) Type 1, (b) Type 2, (c) Type 3, (d) Type 4 and (e) Type 5 amphiboles recognized in Predazzo camptonites. For each amphibole type, the determination of the water content (H₂O wt%) dissolved in the melt obtained by the equation of Ridolfi et al. (2010) and the crystallization temperature (T °C) calculated by means of Putirka (2016) thermometer are also reported.

6.3.1.2. Amphibole trace element composition

Due to the small size and general alteration of most of the amphiboles, in situ trace element analyses were obtained only for *Type 1* (both core/rim of the larger phenocrysts and smaller groundmass specimens), *Type 2* (rim) crystals and *Type 4* (core/rim) xenocrysts (Table A6.4). Their chondrite-normalized (Sun & McDonough, 1989) incompatible element patterns are characterized by Ba, Sr positive spikes and Th, U and Zr negative anomalies (Fig. 42). Their REE content is markedly enriched with respect to the chondritic composition, as displayed by the convex-upward pattern (Fig. 42). *Type 4* amphibole core and *Type 1* groundmass crystals have the most Nb-, Zr-, Hf-, and REE-enriched (up to 30-70 chondrite) patterns. The less enriched patterns are from *Type 1* phenocrysts, relatively Zr-

Hf-Nb-depleted at the core and REE-depleted at the rim. Rims are generally REE-depleted with respect to the related cores (Fig. 42).
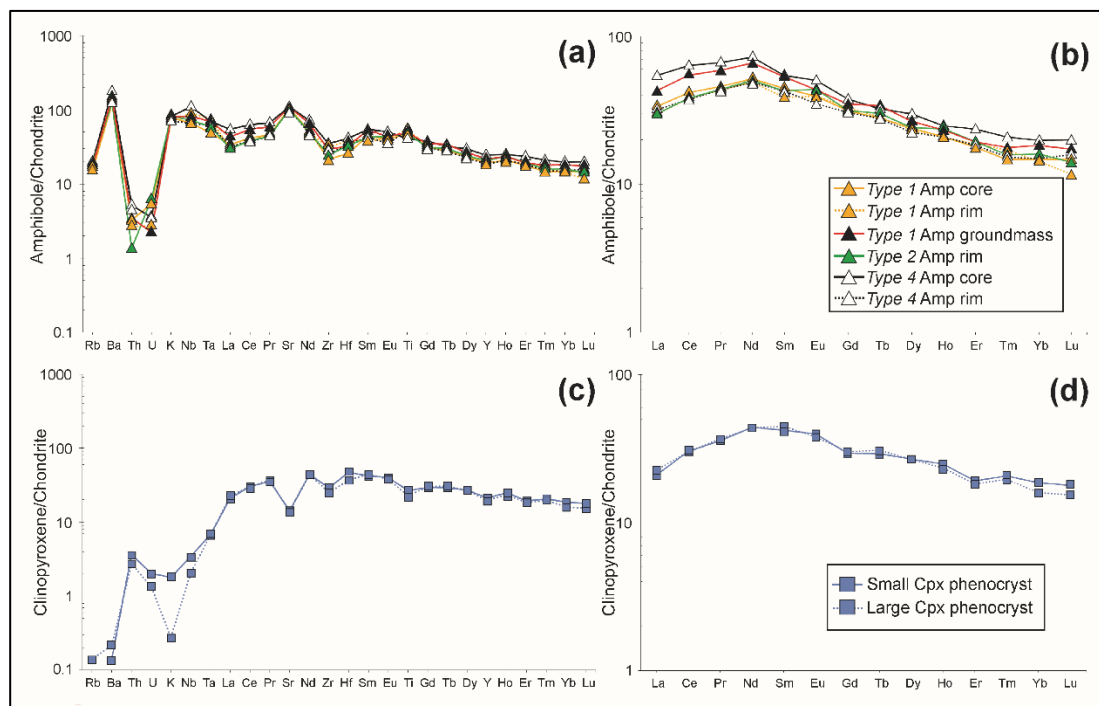
Fig. 42. Chondrite-normalized (Sun & McDonough, 1989) trace element (a, c) and REE (b, d) patterns of amphibole (Amp) and clinopyroxene (Cpx) crystals analysed in Predazzo camptonites. Solid lines: core composition; dotted lines: rim composition.

6.3.2. Clinopyroxene

Clinopyroxene is generally aluminian- to ferrian-titanian-diopside (Fig. 40; Table A6.3). The most magnesian compositions (Mg# ~82) are reported from the cores of the larger phenocrysts, whose rims have Mg# of 68-72. The less magnesian specimens (Mg# down to 64) are the smaller more homogeneous phenocrysts. The outermost rim of the larger "atoll-like" clinopyroxenes (Mg# ~74) is compositionally similar to the smaller euhedral crystals. Clinopyroxene TiO_2 content reaches high values (5.2 wt%), as already highlighted by Carraro & Visonà (2003). Al_2O_3 content ranges from 4.8 to 10.9 wt%, positively correlated with Na_2O (0.25-0.75 wt%; Table A6.3).

6.3.2.1. Clinopyroxene trace element chemistry

Clinopyroxene trace element analyses were performed on euhedral phenocrysts as well as on the outermost rims of the larger crystal with evident compositional zoning (Table A6.4). Chondrite-normalized (Sun & McDonough, 1989) incompatible element patterns resemble those of amphibole, except for the elements structurally prevented (Rb, Ba) or preferentially

partitioned into amphibole (Sr and Ti; Fig. 42). REE patterns also mimic those of amphibole, but with a gentler M-HREE-fractionated profiles (Fig. 42). No significant trace element compositional variations are present between the smaller phenocrysts and the rims of the larger crystals.

6.3.3. Feldspar

Plagioclase and K-Feldspar crystallization occur later than olivine, clinopyroxene and amphibole, as evidenced by their dimension and texture. Plagioclase compositions vary from bytownite to oligoclase (An_{74} to An_{23}; Fig. 40; Table A6.5). K-Feldspar, usually present as groundmass phase, becames modally and dimensionally significant in the sample MA1, where it ranges in composition from Or_{54} to Or_{57} (Fig. 40; Table A6.5).

6.3.4. Fe-Ti oxides

Fe-Ti oxides are widespread in the groundmass assemblage of all camptonites and are generally Ti-magnetitic in composition, with TiO_2 and Al_2O_3 contents ranging from 12.1 to 19.0 wt% and from 2.3 to 7.8 wt%, respectively (Fig. 40; Table A6.6). Micrometric Ti-magnetite crystals can be also found included in *Type 2* amphibole cores or within the reaction assemblages pervading some clinopyroxene crystals and *Type 4* amphibole xenocrysts.

6.4. Carbonate ocelli

Rounded ocellar structures with carbonatic composition were identified in many Predazzo camptonites. Unfortunately, the significant state of alteration of the dykes prevented any accurate evaluation of their distribution at the macro-scale. Sample MA1 is the only ocelli-free, as often happens for differentiated alkaline lamprophyres (Rock, 1991). Chemically, the carbonate crystals analyzed inside the ocelli can be subdivided in two groups (Fig. 43; Table A6.7): i) dolomite-ankerite type (FeO = 5.0-14.4 wt%; MgO = 12.7-18.7 wt%); ii) magnesite-siderite type, close to the breunneritic term (FeO = 27.5-39.0 wt%; MgO = 14.3-24.0 wt%). These compositions well fit those identified by Rock (1991) for the worldwide carbonate-bearing lamprophyres (Fig. 43). SrO content is low in all carbonate types, reaching the maximum values of 0.16-0.30 wt% in some dolomite-ankerite grains; BaO was often below the EMPA detection limit. MnO content varies from 0.24 to 0.62 wt%. Some of the ocelli are texturally composite, including both smaller dolomite-ankerite crystals and larger well-developed magnesite-siderite ones, the latters mainly occurring in the inner portions; some others are instead constituted of sole dolomite-ankerite crystals (Fig. 43).

An intriguing topic in the study of carbonates in magmatic rocks is the determination of their primary (carbonatitic) or late-stage (hydrothermal) origin. If the carbonate ocelli represent/belong to a primary melt, the intimate association between lamprophyric and carbonatitic melts would be strengthened by Predazzo camptonites, and liquid immiscibility processes probably drove the generation of the carbonate ocelli globular structures (Rock, 1991; Le Roex & Lanyon, 1998; Leat *et al.*, 2000; Vichi *et al.*, 2005). If not, their nature would be linked to the occurrence of late-stage hydrothermal processes. From a textural point of view, carbonate ocelli in Predazzo camptonites are characterized by: (i) spherical shape, easily distinguishable from secondary-filled amygdalae, elongated in shape; (ii) flow-aligned tangential growth of high-temperature-forming silicates (plagioclase, amphibole and/or clinopyroxene); (iii) lack of more typically hydrothermal minerals, such as zeolites (Fig. 9). According to Vichi *et al.* (2005) and Gozzi *et al.* (2014), all these features support the primary magmatic nature of the ocelli, and, therefore, the existence of carbonatitic-like droplets within the silicate melt.

To solve the primary vs. secondary nature of carbonates, some authors proposed that a low SrO contents (<0.6 wt%) are consistent with a late-stage origin (Hay & O'Neil, 1983; Hogarth, 1989; Leat *et al.*, 2000), whereas some others hypothesized that carbonates with SrO >0.3 wt% and MnO >0.2 wt% can be considered primary (Vichi *et al.*, 2005). On the other side, it should be noticed that magnesite-siderite series in carbonatitic complexes often have low SrO contents (Buckley & Woolley, 1990; Zaitsev *et al.*, 2004). Plotting our data in a CaO/MgO vs. SrO+MnO space, which discriminates between high temperature and late-stage secondary carbonates (Vichi *et al.*, 2005), a positive correlation is displayed by most of the magnesite-siderite crystals, whereas an almost constant CaO/MgO accompanies a large scattered (SrO+MnO) sum for the dolomite-ankerite grains (Fig. 43). Such a feature is consistent with a late-stage crystallization of the magnesite-siderite crystals, and a magmatic origin for the dolomite-ankerite grains. This hypothesis is also supported by the occurrence of magnesite-siderite-free ocelli in the analyzed camptonites. A similar combination has been also recognized by Leat *et al.* (2000) in carbonate ocelli inside the Middle Jurassic lamprophyres of the Ferrar region (Antarctica): according to these authors, an earlier formation of magmatic calcite-dolomite was followed by a late-stage deposition of Fe-rich, Sr-poor carbonates towards the core of the ocelli. Such an interpretation, well fitting both the chemical and textural features of the carbonate ocelli of Predazzo lamprophyres, lead us to hypothesize that magnesite-siderite precipitation probably occurred during late-stage hydrothermal fluid circulation, whereas dolomite-ankerite crystallization was primary (magmatic), likely derived from a carbonatitic-like melt that coexisted with the lamprophyric

one. In this respect, hotly debated is the association between carbonatitic and alkaline melts, and especially whether carbonatites are primary melts generated by partial melting of the mantle or formed by exsolution of immiscible carbonate fractions from alkaline magmas (Wallace & Green, 1988). This controversy applies also to the carbonatitic ocelli in Predazzo camptonites, which can be considered both as remnants of a mixing process between a denser silicate (lamprophyric) and a carbonatitic magma generated from the same mantle source, or as droplets of carbonatitic melt segregated at lower pressures via silicate-carbonate immiscibility from a common starting melt. Despite the almost perfectly rounded shape of the analyzed ocelli seems to favour this last theory, further studies are required to investigate the association between carbonatites and lamprophyres in the subcontinental lithospheric mantle beneath the Southern Alps.
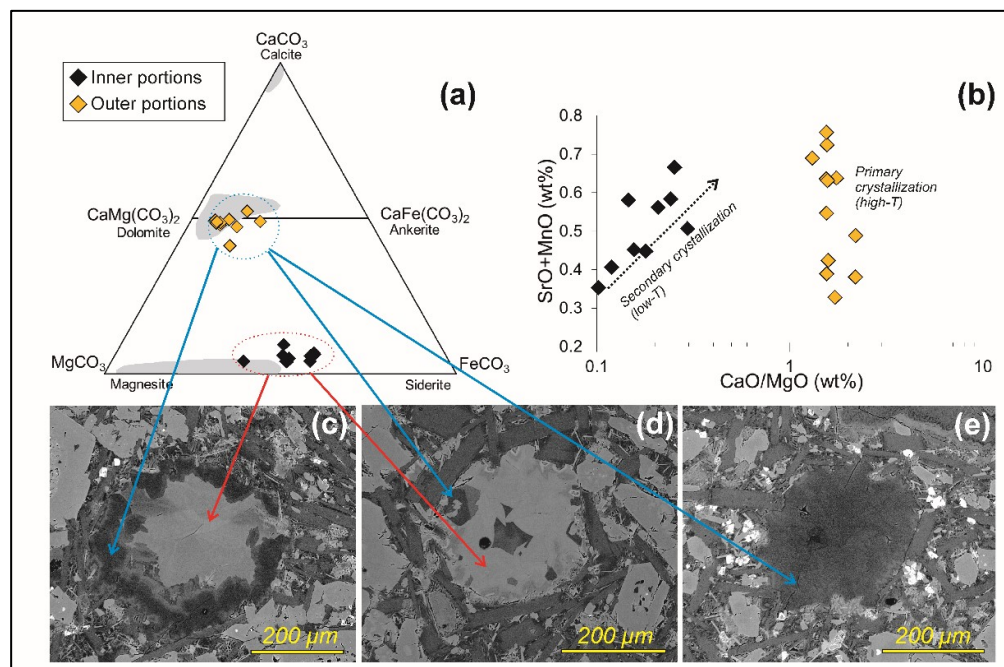
Fig. 43. Compositional and textural features of the carbonate ocelli inside Predazzo camptonites. (a) Calcite-magnesite-siderite ternary diagram and (b) SrO+MnO vs. CaO/MgO diagram (after Vichi et al., 2005) showing the composition of carbonates from the inner and outer portions of the ocelli. Grey fields in (a) are referred to the composition of carbonates documented in worldwide lamprophyres (data from Rock, 1991). Dotted arrow in (b) represent the positive correlation between SrO+MnO and CaO/MgO, typical of low-temperature (low-T) carbonates (Vichi et al., 2005). (c, d, e) Back scattered SEM images of carbonate ocelli composed of (c, d) both dolomite-ankerite/magnesite-siderite or (e) dolomite-ankerite crystals only. The flow-aligned tangential growth of amphibole, plagioclase and clinopyroxene is particularly evident in (d) and (e).

6.5. Age and isotopic signature of Predazzo camptonites

6.5.1. $^{40}Ar/^{39}Ar$ geochronology

The $^{40}Ar/^{39}Ar$ incremental heating method was applied to amphibole and plagioclase separates from two different camptonite samples (FF2 and FF37). Results, and age spectra are shown in Fig. 44. Sample FF2 (plagioclase): The data defined a plateau (>90% ^{39}Ar, n = 16, MSWD 0.9) with an age of 218.90 ± 0.59 Ma. The younger discordant steps in the age spectrum likely related to alteration of the plagioclase. Sample FF37 (amphibole): The data defined a plateau (>50% ^{39}Ar, n = 6, MSWD 1.98) with an age of 219.70 ± 0.73 Ma. Younger apparent ages in the early steps of amphibole age spectrum, concomitant with high K/Ca ratios, were probably due to secondary alteration. The plagioclase and amphibole age are in good agreement and define a crystallisation age for the Predazzo camptonites of 219.22 ± 0.46/0.73 Ma (2σ; analytical/full systematic uncertainties).
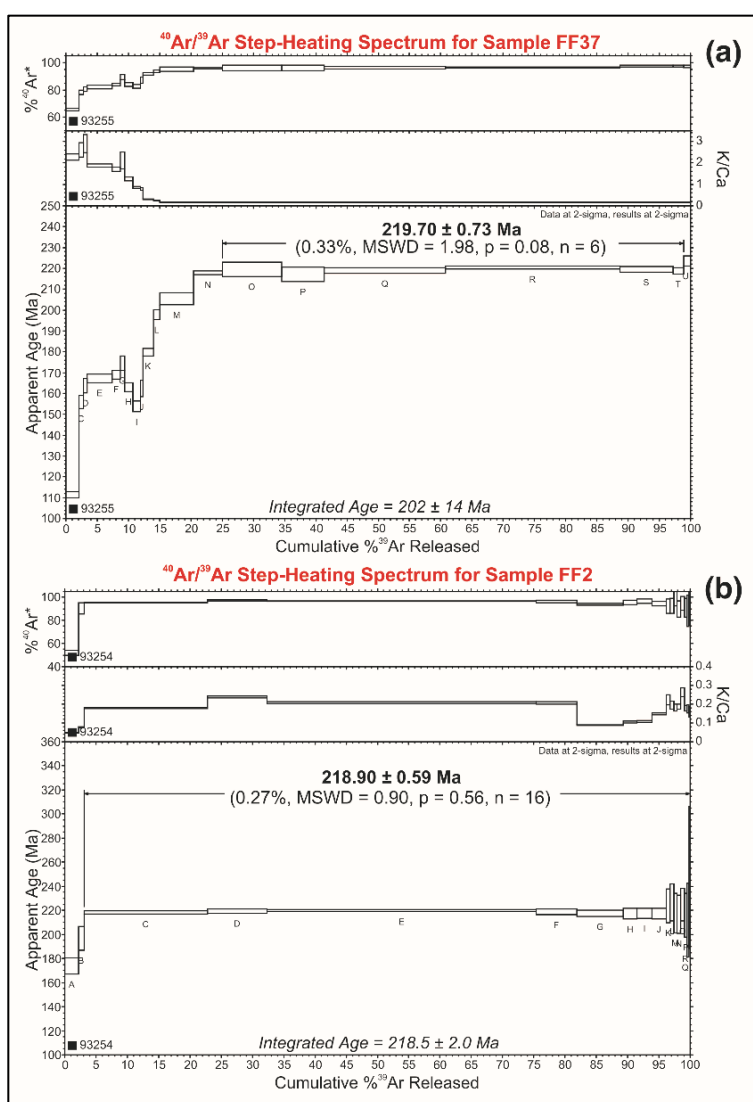
Fig. 44. $^{40}Ar/^{39}Ar$ Age spectra for mineral separates from Predazzo camptonites, with apparent ages and K/Ca ratios spectra plotted against the cumulative percentage of ^{39}Ar released. (a) Age spectrum yielded by amphibole crystals from sample FF37; (b) age spectrum yielded by plagioclase crystals from sample FF2. Plateau ages are indicated in bold.

6.5.2. $^{87}Sr/^{86}Sr$ and $^{143}Nd/^{144}Nd$ isotopes

Whole-rock $^{87}Sr/^{86}Sr$ and $^{143}Nd/^{144}Nd$ isotopic ratios were measured on representative samples among the Predazzo lamprophyres. Strontium isotopic ratios range between 0.7044 and 0.7064, whereas Nd isotopic compositions vary between 0.51277 and 0.51280 (Table A6.1). Initial isotopic ratios, respectively named $^{87}Sr/^{86}Sr_i$ and $^{143}Nd/^{144}Nd_i$, were corrected to an age of 220 Ma, in accordance with the $^{40}Ar/^{39}Ar$ dating results. The Predazzo samples are characterized by $^{87}Sr/^{86}Sr_i$ values ranging between 0.7033 and 0.7040, for a $^{143}Nd/^{144}Nd_i$ range of 0.51260-0.51265 (Fig. 45). The isotopic data, in accordance to what hypothesized by Marrocchino *et al.* (2002), highlight a discrepancy between the isotopic signature of the lamprophyres and their "hosting" Predazzo Intrusive Complex (see Chapter 4). The lamprophyres isotopic signature lies in fact between the DMM and the EM I mantle end-members, in contrast to that of the Predazzo Intrusive Complex, purely EM I-like (Fig. 45).
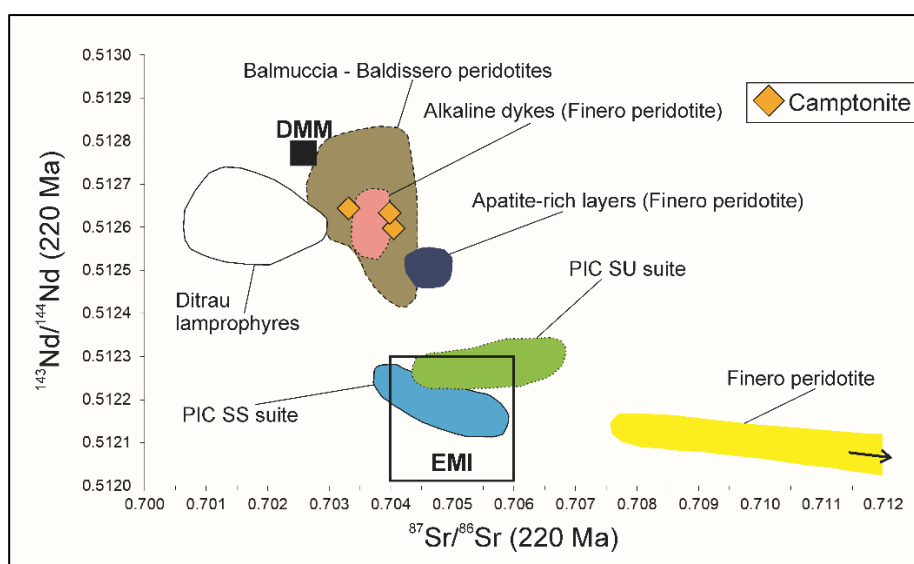
Fig. 45. $^{87}Sr/^{86}Sr$ vs. $^{143}Nd/^{144}Nd$ diagram showing the isotopic signature of Predazzo camptonites corrected to 220 Ma. Fields indicate the Sr-Nd isotopic signature of the: Finero (Voshage et al., 1987), Balmuccia and Baldissero peridotites (Mukasa & Shervais 1999; Mazzucchelli et al., 2009); alkaline dykes intruded in the Finero peridotite (220 Ma; Stahle et al., 2001); apatite-rich layers of the Finero peridotite (215 Ma; Morishita et al., 2008); Ditrau lamprophyres (220 Ma; Batki et al., 2014); Predazzo Intrusive Complex (PIC) Shoshonitic Silica Saturated (SS) and Undersaturated (SU) rocks (234 Ma; see Chapter 4). DMM (Workman & Hart, 2005) and EM I (Zindler & Hart, 1986) mantle end-members (corrected to 220 Ma) are also reported for comparison.
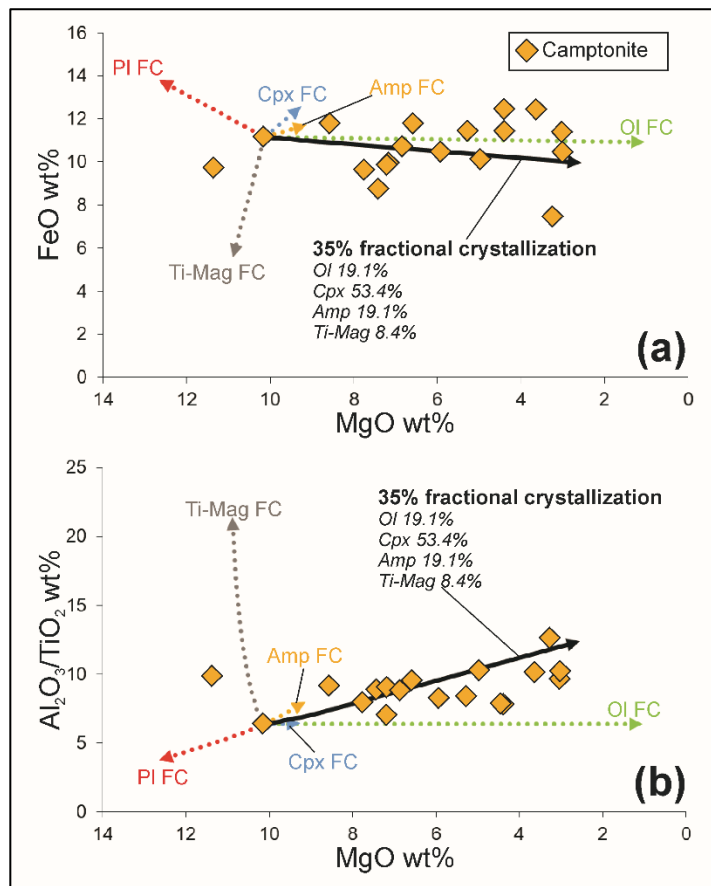
Fig. 46. (a) FeO vs. MgO and (b) Al_2O_3/TiO_2 vs. MgO diagrams showing the fractional crystallization (FC) vectors used to simulate the compositional trend of Predazzo camptonites. The dotted vectors represent the contribution of the single mineral phases during fractional crystallization; the black solid arrows represent the sum vector at 35% fractional crystallization. The relative percentages of fractionation of the single phases are also reported. Ol: olivine; Cpx: clinopyroxene; Pl: plagioclase; Amp: amphibole; Ti-Mag: Ti-magnetite.

6.6. Lamprophyres differentiation

The differentiation processes of worldwide alkaline lamprophyres are often testified by the occurrence, both at local (ocelli, veins, globules) and regional scale (coeval dykes/plutons), of co-magmatic intermediate/felsic rocks, mainly foid-syenitic in composition (Rock, 1987; 1991). The Ni, Cr decrease at decreasing MgO (Fig. 46), together with the mineral phase compositional variations, speak in favour of the occurrence of fractional crystallization processes in the Predazzo lamprophyres magmatic system. The absence of a significant interaction with crustal components during ascent/emplacement is supported by the high whole rock MgO, Cr and Ni contents, the presence of forsteritic olivine and the initial $^{87}Sr/^{86}Sr$ and $^{143}Nd/^{144}Nd$ values that approach the DMM isotopic component. These features point towards a mantle-derived origin for our samples, in accordance with most of the worldwide alkaline lamprophyres (Rock, 1991).

To roughly model the extent of fractional crystallization experienced by Predazzo lamprophyres, the Shaw (1970) equation $C_L = C_0 \times F^{(D-1)}$ was applied by considering the concentration of the most incompatible element (i.e. Zr) in the less and more evolved camptonites. In this equation, C_L indicates the composition (in our case Zr concentration) of the evolved melt, C_0 the composition of the primitive melt, F the residual melt percentage after fractional crystallization and D the sum of the mineral/melt partition coefficients weighted for the fractionation percentage. If we assume a complete incompatible behavior of Zr (D = 0), the residual melt percentage (F) can be estimated as C_0/C_L. According to such calculations, the more differentiated camptonite MA1 was generated by ~40% fractional crystallization of a starting primitive camptonitic melt. Further confirmation of such values was given by mass balance calculations. Major element vectors (Fig. 46) show that 35% fractional crystallization of an assemblage made of olivine (19.1%), clinopyroxene (53.4%), amphibole (19.1%) and Ti-magnetite (8.4%) from a starting primitive camptonitic magma is able to reproduce the composition of MA1 sample.

6.7. *T-P-f*O$_2$ conditions of crystallization and water content of lamprophyric melts

The determination of *T-P-f*O$_2$ parameters and water content of lamprophyric systems is challenging. A first assumption for the application of mineral-melt thermobarometers to natural samples is that the whole rock composition resembles that of a melt. The correspondence between lamprophyres and melts was intensively discussed by Rock (1987, 1991), who proposed that lamprophyres can be considered as "frozen samples" representing melt + suspended crystals + volatiles, thus "complete" magma systems which can alone retain some representative of the volatile phase. On this basis, the physico-chemical crystallization conditions of Predazzo camptonites were estimated by means of several thermo-, oxy-barometric and hygrometric equations applied to chosen mineral (clinopyroxene, Ti-magnetite, amphibole)-melt pairs. Errors related to each applied method are reported in Table A6.8.

Equilibrium between clinopyroxene phenocrysts and camptonitic melt was evaluated by means of their Fe-Mg partitioning, assuming a $^{Cpx-Liq}Kd_{Fe-Mg}$ of 0.26±0.05 (Akinin *et al.*, 2005), which ideally reflect clinopyroxene equilibrium conditions in an alkali-dominated basic melt (i.e. camptonites; Ubide *et al.*, 2014). Since the composition of lamprophyric melts is, by definition, anomalously rich in volatiles with respect to alkali basalts/basanites, P and T of clinopyroxene crystallization were determined by means of the H$_2$O-independent equations 32a and 32d of Putirka (2008), in turn derived by the *T*-dependent barometer and the P-independent thermometer of Putirka *et al.* (1996). Being these equations based on

clinopyroxene chemistry only, the dependency on the composition of the camptonitic melt was bypassed. The equilibrium between amphibole crystals and the camptonitic melts was evaluated by means of the T- and P-independent $^{Amp\text{-}Liq}Kd_{Fe\text{-}Mg}$ exchange coefficient, which should be 0.28 ± 0.11 in conditions of equilibrium (Putirka, 2016). The H_2O content of the melt from which amphibole crystallized was calculated by the single-mineral hygrometer of Ridolfi *et al.* (2010). Afterwards, the T-P conditions of amphibole crystallization were calculated by means of the amphibole-melt P-independent thermometer (Equation 5) and the T-independent, H_2O-dependent barometer (Equation 7b) of Putirka (2016). In this latter equation, the H_2O values obtained by the Ridolfi *et al.* (2010) hygrometer were used as input. The oxygen fugacity of the magmatic system was calculated by means of the oxy-barometer of Ishibashi (2013), based on the Fe^{2+}/Fe^{3+} partitioning between spinel and melt.

6.7.1. Clinopyroxene and Ti-magnetite crystallization conditions

Equilibrium check results indicated that most of the clinopyroxene phenocrysts were not in equilibrium with the high Mg# (59-65) camptonitic melts ($^{Cpx\text{-}Liq}Kd_{Fe\text{-}Mg}$ = 0.32-0.96), requiring instead a more evolved melt to attain equilibrium (Mg# 44-49). The disequilibrium is also supported by the compositional zoning between cores (Mg# 82) and rims (Mg# 68) of many crystals, as well as by the dusty reaction zones of the larger phenocrysts. The few crystals attaining equilibrium belong to slightly more evolved camptonitic samples ($^{Cpx\text{-}Liq}Kd_{Fe\text{-}Mg}$ = 0.17-0.40). Thermobarometric results indicate that clinopyroxene in equilibrium with their host rock composition crystallized at P of 490 ± 180 MPa and T of 1087 ± 27 °C (Table A6.8). According to these ranges, T-P values of 1100-1050°C and 500 MPa were considered to apply the Ishibashi (2013) oxy-barometer to Ti-magnetite crystals. Results yielded a fO_2 interval of -8.3/-10.0 log fO2 at 1100°C, and a -9.4/-11.0 log fO_2 range at 1050°C (between -1 and +1 FMQ; Table A6.8).

6.7.2. Amphibole crystallization conditions

Amphibole crystals in the less evolved camptonite resulted not in equilibrium with their host rock composition, having an $^{Amp\text{-}Liq}Kd_{Fe\text{-}Mg}$ of 0.42-0.89. On the other side, equilibrium was attained by some crystals in the more evolved MA1 sample ($^{Amp\text{-}Liq}Kd_{Fe\text{-}Mg}$ = 0.29-1.0). As expected, *Type 4* xenocrysts and *Type 5* amphiboles cores yielded extreme disequilibrium conditions, with $^{Amp\text{-}Liq}Kd_{Fe\text{-}Mg}$ values as high as 1.94.

The Ridolfi *et al.* (2010) hygrometer indicates that *Type 1*, *Type 2* and *Type 3* amphiboles crystallized at water contents of 7.3 ± 0.3 wt% in the less evolved camptonitic melt, and 6.8 ± 0.7 wt% in the more differentiated one (Table A6.8). Higher values were calculated for

Type 4 xenocrysts and *Type 5* amphibole cores, which yielded H_2O contents up to 9.8 wt%. By considering only the crystals in equilibrium with their host rock composition, a range of 6.4±0.3 H2O wt% is obtained. Putirka (2016) thermobarometers yielded *T-P* intervals of 1074-927°C and 1230-470 MPa for all amphibole crystals (Table A6.8). The highest *P* were calculated for *Type 4* xenocrysts (1190±50 MPa) and *Type 5* amphiboles cores (1030±50 MPa), at corresponding crystallization *T* of 1037±21°C and 952±21°C, respectively (Table A6.8). It is worth noting that, due to the significant disequilibrium between *Type 4* and *Type 5* crystals and the melt, these values should be considered with caution. By taking into account only the crystals in equilibrium with the host rock, *T-P* ranges of 1027±12°C and 600±60 MPa are obtained. These values can be likely represent the shallower crystallization conditions of amphibole in the magmatic system. The deeper crystallization conditions can be instead roughly approached by some *Type 1*, *Type 2* and *Type 3* crystals close to the equilibrium with the host camptonite ($^{Amp-Liq}Kd_{Fe-Mg}$ = 0.42-0.46), which yield P and T up to 1160 MPa and 1067°C. In any case, the obtained *T-P* ranges are consistent with the experimental simulations proposed by Pilet *et al.* (2010), who demonstrated that kaersutite crystallization can start at 1130°C and 1500 MPa in volatile-enriched (5-6 H_2O wt%) basanitic melts, thus in conditions similar to those of Predazzo camptonites. If combined to the thermobarometric results obtained by clinopyroxene, these *T-P* values suggest that crystallization in the lamprophyric system occurred continuously between 690 and 230 MPa, at *T* decreasing from 1124 to ~1000°C, with an H_2O content ≥ 6.4±0.3 wt%.

6.7.2.1. Interpretation of amphibole textures

A correlation between the obtained *T-P* and H_2O results and the previously identified textures enable us to infer amphibole crystallization processes. The homogeneous composition of *Type 1* amphibole cores, close to the equilibrium with the less evolved melt ($^{Amp-Liq}Kd_{Fe-Mg}$ = 0.42-0.58) records a growth at high *T-P* (1057±12°C; 980±50 MPa), and 7.5±0.3 H_2O wt% in the melt. The crystallization of *Type 1* crystals continued during differentiation of the melt towards more evolved compositions (MA1 sample), where crystals attain equilibrium ($^{Amp-Liq}Kd_{Fe-Mg}$ = 0.32-0.36), at *T-P* down to 1013±34°C and 740±120 MPa, and water content of 7.3±0.9 wt%. *Type 2* crystal cores, in marked disequilibrium with the melt ($^{Amp-Liq}Kd_{Fe-Mg}$ = 0.73-0.80), record crystallization *T* and *P* of 1004±3°C and 900±10 MPa, at 7.0±0.1 H_2O wt%. The rounded shape of both *Type 1* and *Type 2* cores reflects an event of simply dissolution after reaction with a melt phase undersaturated in amphibole. Subsequently, the melt differentiated and re-saturated in amphibole, allowing the precipitation of the rims at lower *T-P* (1048±15°C, 750±110 MPa

Type 1; 1029±24°C and 750±20 MPa *Type 2*) and H_2O content (6.9±0.3 wt%; Fig. 41). The magnesio-hastingsitic overgrowth in both *Type 1* and *Type 2* crystals, similar to the diopsidic bands identified by Petrone *et al.* (2018) in clinopyroxenes from Stromboli volcano (Aeolian Islands), probably formed in response of new pulse of primitive melts that introduced additional high *T* components (Mg and Ca) in the magmatic system. An abrupt *T* increase (from 1051 to 1071°C) is recorded in this intermediate overgrowth (Figg. 41a and 41b), which can provide the evidence of small-scale mixing dynamics between differentiated and primitive batches inside the magmatic system. Dusty zones of *Type 3* amphibole cores formed as result of pseudomorphic replacement by interface-coupled dissolution-precipitation processes, resulting in Ti-magnetite, plagioclase and clinopyroxene formation at the interface (Ruiz-Agudo *et al.*, 2014). The overgrowth of a newly formed rim in *Type 3* crystals is likely concomitant with the formation of *Type 1* and *Type 2* rims. *Type 3* rim, in fact, approaches the equilibrium towards the more evolved camptonitic melt ($^{Amp\text{-}Liq}Kd_{Fe\text{-}Mg}$ = 0.34-0.69). Its crystallization conditions are the following: T = 1017±40°C; P = 760±120 MPa; melt H_2O content = 7.2±0.4 wt%. *Type 4* xenocrysts probably represent relicts of larger crystals of deep crustal origin, brought to the surface by the ascent of lamprophyres. The incipient alteration and resorption features of their cores suggest disequilibrium with the hosting melt, as also confirmed by the high $^{Amp\text{-}Liq}Kd_{Fe\text{-}Mg}$ (1.22). Their dusty portions probably formed as consequence of interface-coupled dissolution-precipitation. The outermost rim, compositionally analogous to most phenocryst rims and groundmass crystals (*Type 1*, *Type 2* and *Type 3*) represent a late overgrowth approaching the equilibrium with the melt ($^{Amp\text{-}Liq}Kd_{Fe\text{-}Mg}$ down to 0.61), as evidenced by the crystallization T (1051±9°C), P (1180±50 MPa) and H_2O (8.6±0.3 wt%). The sharp edges and optical continuity between *Type 5* amphiboles core and rim, as well as the absence of resorption zones, suggest that this texture is a consequence of a magnesio-hastingsitic overgrowth around preexisting sadanagaitic (Mg# = 29-39) crystals (Fig. 41e). The high $^{Amp\text{-}Liq}Kd_{Fe\text{-}Mg}$ of the cores (1.18 to 1.94) indicates significant disequilibrium with respect to the host rock composition, implying that they would attain equilibrium only in an extremely differentiated melt. The related thermobarometric results, which should be considered with caution, suggest high P (1030±50 MPa) and low T (952±21°C) of crystallization, at high water content (up to 9.8 wt%). The peculiar composition of *Type 5* cores, rare even in lamprophyres (Rock, 1991), makes it difficult to clearly define their origin, deserving further studies. *Type 5* rims represent a subsequent growth in equilibrium with the melt ($^{Amp\text{-}Liq}Kd_{Fe\text{-}Mg}$ = 0.29-0.55), at T of 1015±18°C, P of 570±60 MPa and H_2O content down to 5.8 wt%.

The observed simple dissolution and pseudomorphic replacement textures indicate a very dynamic regime of the lamprophyres magmatic system. Chemical zoning associated with dissolution-reprecipitation textures suggest that amphibole stability was affected by T changes due to small scale mixing between variably differentiated and/or volatile rich melts. The repeated occurrence of such small-scale mixing processes resulted in fact in multiple and abrupt changes of amphibole liquidus conditions during lamprophyre differentiation.

6.8. Lamprophyre mantle source and melting model

An intriguing topic is the nature of the mantle source from which Predazzo lamprophyres were generated, especially in the light of their HFSE/REE distribution and Sr-Nd isotopic signature. Indirect evidence of the minimum depth of segregation is provided by the lherzolite xenoliths, which record a re-equilibration process at about 45 km of depth, in the spinel stability field (Carraro & Visonà, 2003). The Zr/Y (6-11), Lu/Hf (0.07-0.12) and Dy_N/Yb_N (1.1-1.7) ratios of Predazzo lamprophyres suggest that garnet played a significant role during melting in their mantle source, as also suggested by Pinzuti *et al.* (2013) for Asal Rift magmas. On the other side, the La_N/Yb_N and Gd_N/Yb_N ratios of the less evolved camptonites are not very high, suggesting that their source differs from those of the "typical" alkaline lamprophyres and OIB magmas (Sun & McDonough, 1989; Rock, 1991). According to the Sr-Nd isotopic data (Fig. 45), lamprophyres were generated by a depleted mantle, as also confirmed by the Nb/La vs. La/Yb diagram of Smith *et al.* (1999), which indicates that an asthenospheric contribution was required for their generation (Fig. 47a).

On the basis of these constraints, we tentatively modelled the nature of the mantle domain from which Predazzo lamprophyres were segregated by applying non-modal batch melting equations (Shaw, 1970). To account for the HFSE and REE budget of our samples, several mantle melting domains were used as starting point of our simulations. The modal composition and melting proportion of each of the considered mantle sources are reported in Table A6.9. A first discrimination between the role of spinel and garnet in the hypothetical source was put forward by using as starting mantle domains a spinel- and a garnet-bearing fertile lherzolites with Primordial Mantle (PM; Sun & McDonough, 1989) composition (curves II and III in Fig. 47). Consistently with the Sr-Nd isotopic data, a melting path was also proposed by using as starting source a depleted mantle composition (DMM; Workman & Hart, 2005; curve I in Fig. 47). According to the obtained melting curves, none of the chosen starting component was able to obtain the Sm/Yb ratio of Predazzo lamprophyres (Fig. 47). Their Gd/Yb ratio was better approximated by the melting curve of the garnet-bearing source, even if the match was not perfect (curve III in Fig. 47). Consequently,

amphibole and/or phlogopite were introduced as additional components of the starting mantle domains in our simulations. The calculated curves showed that both a garnet-amphibole- (curve V), a garnet-phlogopite- (curve VI) and a garnet-spinel-amphibole-bearing (curve IV) sources are able to account for the Sm/Yb and Gd/Yb ratios of our samples (Fig. 47). However, the REE patterns obtained by melting the garnet-phlogopite-lherzolite were anomalously HREE-enriched with respect to Predazzo lamprophyres, being therefore considered not suitable for our model. Among the melting trends of garnet-amphibole- and the garnet-spinel-amphibole-bearing sources, the former better reproduced the features of the less evolved camptonites, both in the Sm/Yb, La/Yb and Gd/Yb ratios and in the REE pattern (Fig. 47d). Accordingly, Predazzo lamprophyres could have been generated by low melting percentages (1.0 to 2.5%) of a garnet-amphibole-bearing lherzolite, with a fertile PM starting composition (Sun & McDonough, 1989).

Such mantle source modal composition and melting degrees are similar to those proposed by Batki *et al.* (2014) for the generation of Ditrau lamprophyres (1-4% partial melting). However, the mantle source composition required by Predazzo lamprophyres is more depleted than the Ditrau one, being this latter a REE-enriched mantle with significant contribution of asthenospheric HIMU-OIB-like components (EAM, Seghedi *et al.*, 2004; Batki *et al.*, 2014). The presence of a LILE- and volatiles-enriched garnet-bearing mantle source with an asthenospheric signature was also proposed by Stoppa *et al.* (2014) to model the genesis of the Cretaceous to Oligocenic alkaline/ultramafic lamprophyres of Central-Southern Italy, whose REE patterns are strongly LREE-enriched and HREE-depleted with respect to the Predazzo ones. The involvement of amphibole and garnet during melting was required to simulate the relatively low LREE/HREE ratios of Predazzo lamprophyres, as well as to get rid of their H_2O-CO_2-alkali-rich nature. Considering that the spinel-garnet transition in a continental lithospheric setting occurs at 60-90 km (2-3 GPa; Takahashi & Kushiro, 1983; Falloon & Green, 1988; Kinzler & Grove, 1992; Robinson & Wood, 1998; Pinzuti *et al.*, 2013), we can hypothesize that the melting region of Predazzo lamprophyres was located at depth >60 km. On the other side, amphibole stability in the mantle is limited to ~3 GPa (Frost, 2006; Fumagalli *et al.*, 2009; Tumiati *et al.*, 2013; Mandler & Grove, 2016), suggesting that the mantle source depth should be <90 km. For these reasons, an averaged depth of 70-80 km is considered likely for the source region of the studied camptonites. Similar depths are also consistent with those proposed by Hammouda & Keshav (2015), according to whom carbonatite and silicate melts can coexist between 2 and 2.6 GPa (ca. 60-80 km) along the convecting mantle adiabat (asthenosphere).
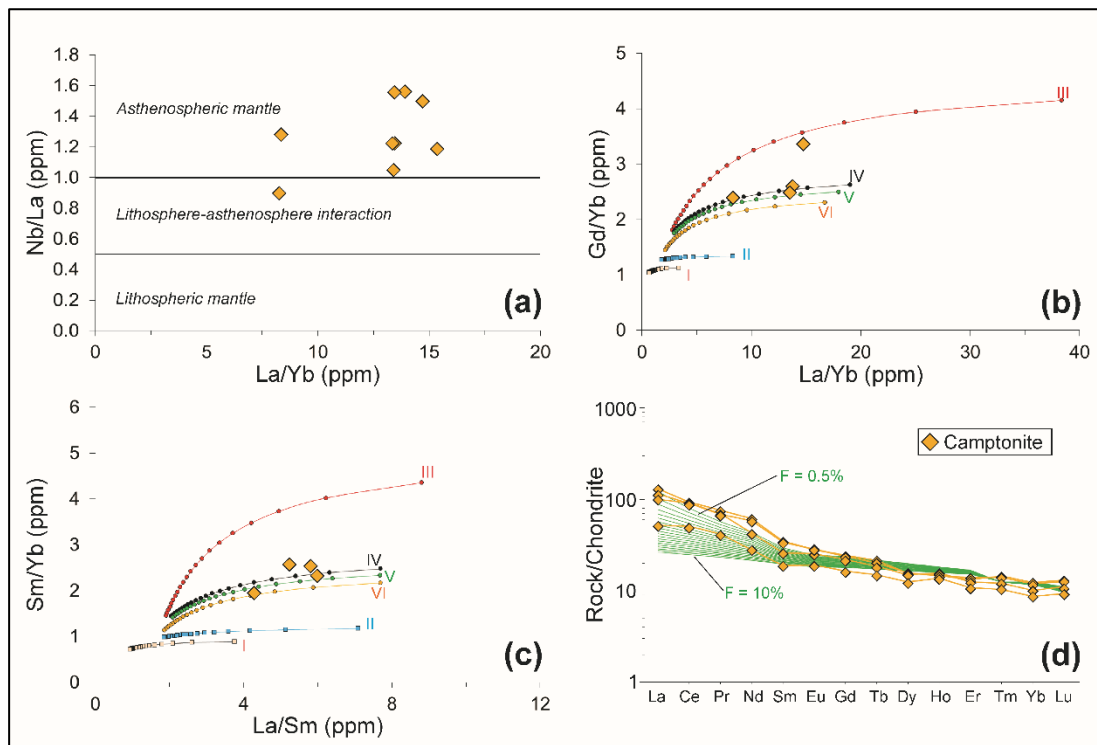
Fig. 47. (a) Nb/La vs. La/Yb diagram (Smith et al., 1999) used to discriminate between the contribution of lithosphere and asthenosphere in the mantle source of Predazzo camptonites. (b) Gd/Yb vs. La/Yb and (c) Sm/Yb vs. La/Sm diagrams for the less differentiated Predazzo camptonites. Melting curves in (b) and (c) are modelled using the non-modal batch melting equations of Shaw (1970). Starting mantle sources: I = Spl-lherzolite with DMM composition (Workman & Hart, 2005); II = Spl-lherzolite; III = Grt-lherzolite; IV = Spl-Grt-Amp-lherzolite; V = Grt-Amp-lherzolite; VI = Grt-Phl-lherzolite. Starting REE composition of II, III, IV, V and VI sources is fertile PM of Sun & McDonough (1989). Source modal composition, melting proportions and partition coefficients for olivine, orthopyroxene, clinopyroxene, spinel, garnet, amphibole and phlogopite are reported in Table A6.9. (d) Chondrite-normalized (Sun & McDonough, 1989) REE patterns of Predazzo less differentiated camptonites compared to those simulated by partial melting of a garnet-amphibole-lherzolite (curve V) at partial melting degrees of 0.5 to 10%.

6.9. Geodynamic implications

6.9.1. The magmatism of the Dolomitic Area

The late-stage occurrence of alkaline lamprophyric dykes in intrusive complexes often acquires a double significance, since they do not only act as younger chronological boundary of the magmatic episodes, but they also constitute the most primitive (and less contaminated by the crust) magma types (Rock, 1991). In the case of the Predazzo area, several authors suggested a strict relationship between the alkaline lamprophyres and the host pluton (Lucchini *et al.*, 1969; 1982; Carraro & Visonà, 2003). The new $^{40}Ar/^{39}Ar$ age results (from 218.90 ± 0.59/0.66 to 219.70 ± 0.73/0.85 Ma; Fig. 44) lead us to point out that the lamprophyric rocks belong to a distinct magmatic pulse that occurred about 17-20 Ma later than the emplacement of the Predazzo Intrusive Complex (U-Pb zircon age of 238.075 ±

0.087 Ma, Storck *et al.*, 2018). Moreover, since the entire Ladinian volcano-plutonic event in the Dolomitic Area has a limited duration (from 239.04±0.04 to 237.77±0.05 Ma; Brack *et al.*, 1996; Mundil *et al.*, 1996; Mietto *et al.*, 2012; Abbas *et al.*, 2018; Storck *et al.*, 2018; Wotzlaw *et al.*, 2018), it is evident that the lamprophyres represent a distinct and subsequent magmatic event. This chronological gap is also reinforced by the geochemical discrepancies: despite showing a K-affinity comparable to that of the high-K calc-alkaline to shoshonitic volcano-plutonic rocks of the entire Dolomitic Area (Bonadiman *et al.*, 1994; see also Chapters 3, 4 and 5), camptonites have peculiar trace element profiles and Sr-Nd isotopic signature (Figg. 38 and 45). In fact, whereas the Ladinian high-K calc-alkaline to shoshonitic rocks display the typical subduction-related incompatible element patterns, alkaline lamprophyres lack any Ta-Nb-Ti and U-Th negative anomaly, suggesting the involvement of an OIB-like component in their mantle source. The $^{87}Sr/^{86}Sr_i$ and $^{143}Nd/^{144}Nd_i$ signature of Predazzo camptonites points towards a genesis from a mantle source more depleted than the EM I-like source that produced the Ladinian high-K calc-alkaline to shoshonitic rocks. As shown in Fig. 45, in fact, they plot close to the DMM end-member (Workman & Hart, 2005), suggesting that a significant contribution of the asthenospheric mantle was involved in their genesis. This feature confirms a time-related progressive depletion of the mantle source beneath the Dolomitic Area during Middle-Late Triassic, as already hypothesized for the source of Predazzo Intrusive Complex in Chapter 4. Our study indicates that the magmatic activity in the Dolomitic Area was not confined to the Ladinian, but re-activated at about 218.5-220.5 Ma, with the emplacement of a small alkaline pulse generated from a $^{143}Nd/^{144}Nd$-enriched mantle domain. At shallow depth, the ascent of such small melts was probably favoured by extensional-trastensional dynamics, to which lamprophyres are often associated (e.g. Scarrow *et al.*, 2011, and reference therein). The (if any) relationships between Predazzo lamprophyres and the Triassic NE-SW transtensive-transpressive regimes of the Dolomitic Area (Doglioni, 2007; Doglioni & Carminati, 2008; Abbas *et al.*, 2018), however, has never been investigated, and requires further studies, especially in the light of the new age data. The occurrence of extensional dynamics during lamprophyres ascent is also testified by the amphibole and clinopyroxene *T-P* path of crystallization. In contrast to the Ladinian magmatic event, when the crystallization of the high-K calc-alkaline to shoshonitic melts occurred preferentially in batches located at shallow crustal depths (1.4-5.6 km; see Chapter 4), lamprophyres crystallization started at 24 km (considering a ΔP/Δz of 29 MPa/km) and continued towards the surface (at least until 8 km). Such a condition is consistent with the presence of a polybaric vertical plumbing system and suggests that the fractional crystallization and (small-scale) mixing processes recorded by amphibole crystals

took place en route to the surface, without implying the presence of a magma chamber. This hypothesis, fostered by the presence of mantle xenoliths in many Predazzo camptonites, further suggest that lamprophyres are unrelated to the host plutonic complex.

6.9.2. Late-stage magmas or alkaline precursors?

When considered at a geodynamic scale, the significance of Predazzo lamprophyres is intriguing, since several magmatic episodes with variable geochemical affinity shaped the Southalpine-Austroalpine and Carnic-Dinaric domains from Permian to Middle-Late Triassic. The most similar and chronologically closer magmatic occurrence was documented in the Ditrau Alkaline Massif (Carpathians), where late-stage alkaline lamprophyres (camptonites) intruded a Middle-Triassic (231-227 Ma) alkaline intrusion (Dallmeyer *et al.*, 1997; Morogan *et al.*, 2000; Pana *et al.*, 2000; Batki *et al.*, 2014; Pál-Molnár *et al.*, 2015). The major and trace elements and isotopic similarities between the Ditrau lamprophyres and the host pluton led to interpret them as the parental magmas of the intrusive suite (Batki *et al.*, 2014). Such a model cannot be applied to the Predazzo case, where the geochronological and geochemical discrepancies between the alkaline lamprophyres and the plutonic complex rule out any possible correlation between camptonites and the trachybasaltic/shoshonitic rocks. Notwithstanding a slight relative depletion in Th, U, Nb, Zr and LREE with respect to the Ditrau lamprophyres, Predazzo lamprophyres have comparable Sr-Nd isotopic signature (Figg. 38 and 45), suggesting that similar mantle sources were involved in their genesis. According to Batki *et al.* (2014), Ditrau lamprophyres were generated in an early extensional phase of the Middle Triassic to Jurassic rifting that separated the Getic microplate from the Bucovinian margin (Batki *et al.*, 2014), thus representing the Alpine Tethys rift portion located northward of the Meliata basin (Stampfli *et al.*, 2002; Stampfli, 2005). Precursors of the Tethyan opening were also documented in the Brescian Alps, not far from the Dolomitic Area, where intra-plate tholeiitic lavas and dykes with depleted Sr-Nd isotopic signature emplaced almost simultaneously with the Predazzo lamprophyres, at about 217±3 Ma (Cassinis *et al.*, 2008).

Coeval (220-225 Ma) magmatic occurrences were also recognized in the Western Alps, where alkaline dykes, generated by an upwelling mantle with significant asthenospheric contribution, emplaced in the Finero area (Stähle *et al.*, 1990; 2001). Moreover, ages of 215±35 Ma and 220±4 Ma were determined by Morishita *et al.* (2008) and Malitch *et al.* (2017), respectively, for the formation of the metasomatic apatite-rich and chromitite layers in the Finero peridotite. This time overlap, fostered by the Sr-Nd isotopic analogies between the alkaline dykes and the apatite-rich layers (Fig. 45), led several authors (Ferrario & Garuti,

1990; Morishita *et al.*, 2003; 2008; Zaccarini *et al.*, 2004) to associate all these occurrences to a unique alkaline-carbonatitic magmatic event. The generation of such H_2O-CO_2-rich fluids was attributed to mantle upwelling dynamics in a continental rifting setting (Zaccarini *et al.*, 2004).

The $219.22 \pm 0.46/0.73$ Ma occurrence of alkaline lamprophyres at Predazzo can be easily incorporated in such a context, taking into account that their Sr-Nd isotopic signature totally overlap those of the alkaline dykes and the apatite-rich layers at Finero (Fig. 45; Stähle *et al.*, 1990; 2001; Morishita *et al.*, 2008). The less differentiated alkaline dykes intruded at Finero (Stähle *et al.*, 2001) are also characterized by trace element patterns comparable to those of Predazzo lamprophyres, except for Nb, Ta and Zr, slightly enriched in the former. A marked U-Th depletion characterizes both Predazzo lamprophyres and the alkaline dykes at Finero, and their REE pattern almost totally overlap, as testified by the Gd_N/Yb_N (1.9) and Dy_N/Yb_N (1.4) ratios of the latters. Furthermore, the Sr-Nb enrichment of Predazzo lamprophyres well matches the main features of the apatite-bearing assemblages at Finero (Zanetti *et al.*, 1999), confirming the involvement of a carbonate-rich component in their genesis. This parallelism is also supported by the presence, in Predazzo camptonites, of carbonate ocelli with a dolomite-ankerite composition comparable to that of the interstitial dolomite grains in the Finero peridotite (Zanetti *et al.*, 1999).

According to our findings, Predazzo lamprophyres can be considered as an expression of the 215-225 Ma alkaline-carbonatitic magmatism that intruded the subcontinental mantle portion beneath the Southern Alps (Ferrario & Garuti, 1990; Stähle *et al.*, 1990; 2001; Zanetti *et al.*, 1999; Morishita *et al.*, 2003; 2008; Zaccarini *et al.*, 2004; Matsumoto *et al.*, 2005; Raffone *et al.*, 2006; Malitch *et al.*, 2017). This magmatic pulse, characterized by mantle-upwelling signature, is well distinguished from the previous, subduction-related, K- and LILE-rich metasomatic episode that produced amphibole and phlogopite in the Finero peridotite (Fig. 45; Coltorti & Siena, 1984; Morishita *et al.*, 2003; 2008; Malitch *et al.*, 2017). According to the U-Pb zircon ages (190-180 Ma and 230-180 Ma) proposed by Zanetti *et al.* (2016) and Langone *et al.* (2018), the alkaline-carbonatitic metasomatism affected the subcontinental mantle immediately prior to its exhumation, which was precisely related to the extensional stages of the Alpine Tethys rift.

Rather than to a late-stage episode connected to the Middle Triassic high-K calc-alkaline to shoshonitic (orogenic) magmatism, the generation of Predazzo lamprophyres should be therefore considered, together with the Ditrau lamprophyres, the Brescian Alps basalts and the Finero alkaline-carbonatitic magmas, as a Late Triassic precursor of the Alpine Tethys rifting event. This hypothesis is supported by their depleted Sr-Nd isotopic signature,

consistent with a genesis from a mantle source influenced by an asthenospheric contribution (Fig. 45). Further evidence is given by the incompatible elements pattern of the alkaline lamprophyres that, when compared to the Ladinian shoshonitic rocks of the Dolomitic Area, appear depleted in U, Th, K and La, more than enriched in Nb and Ta (Fig. 38). Such a feature is consistent with the progressive shift of the magmatism from orogenic-like to anorogenic, and thus to a progressive evolution of the subcontinental mantle source towards a more depleted, asthenospheric-related nature.

6.10. Conclusions

1. The petrological, geochronological and isotopic study of the Predazzo alkaline lamprophyres enabled us to provide new insights on the geodynamic evolution of the Dolomitic Area and the Southern Alps during Middle-Late Triassic. The most relevant findings can be summarized as follows:

2. The compositional spectrum of Predazzo alkaline lamprophyres (camptonites) can be explained by assuming 35-40% fractional crystallization of olivine, clinopyroxene, amphibole and Ti-magnetite from an initial primitive camptonitic melt.

3. Amphibole textural and compositional features suggest that the lamprophyre magmatic system was subjected to small scale mixing between variably differentiated and/or volatile rich melts during differentiation, as testified by the variable presence of dissolution-reprecipitation textures and pseudomorphic replacements. Moreover, the occurrence, composition and textural features of carbonate-bearing ocelli suggest that a carbonatitic melt was intimately associated to the alkaline lamprophyric one.

4. ^{40}Ar/^{39}Ar ages of Predazzo alkaline lamprophyres demonstrated that they emplaced between 218.90 ± 0.59/0.66 and 219.70 ± 0.73/0.85 Ma (Late Triassic; ^{40}Ar/^{39}Ar; 2σ; analytical/full systematic uncertainties), suggesting an origin unrelated to the short-lived Ladinian high-K calc-alkaline to shoshonitic magmatism of the Predazzo-Mt. Monzoni intrusions in the Dolomitic Area.

5. The difference between alkaline lamprophyres and the host Ladinian rocks is fostered by the absence of Ta-Nb-Ti negative anomalies, the presence of U-Th negative peaks, and their HFSE distribution, which point towards a genesis in an intra-plate geodynamic setting, from a garnet-bearing mantle source. This is also confirmed by their ^{87}Sr/^{86}Sr$_i$ and ^{143}Nd/^{144}Nd$_i$ depleted signature, consistent with a depleted mantle contribution in their source, in contrast to the pure EM I-like signature of the Predazzo-Mt.Monzoni Ladinian intrusions, which was ascribed to a subduction-modified mantle.

6. Thermo-, oxy-barometric and hygrometric calculations based on clinopyroxene, amphibole and Ti-magnetite composition suggest that the crystallization in the lamprophyres magmatic system occurred at least between 690 and 230 MPa, a T decreasing from 1124 to ~1000°C. The oxygen fugacity of the magmatic system varied between -1 and +1 FMQ, whereas the H_2O content of the lamprophyric melts resulted $\geq$ 6.4±0.3 wt%, decreasing with decreasing temperature. These results strengthen the distinction between lamprophyres and the Ladinian high-K calc-alkaline to shoshonitic magmatism: whereas the latter was dominated by crystallization processes at shallow crustal levels (1.4-5.6 km; see Chapter 4), lamprophyres started crystallizing at about 24 km and continued towards the surface, probably in an extensional-trastensional tectonic regime.

7. Mantle melting models suggest that low melting percentages (1.0-2.5%) of a fertile garnet-amphibole-bearing lherzolite can account for the generation of Predazzo lamprophyres. The melting region was probably located between 70 and 80 km of depth.

8. Predazzo lamprophyres are temporally, spatially and geochemically correlable to several magmatic occurrences of the Southern Alps-Carpathians area: i) the Ditrau alkaline lamprophyres (Batki *et al.*, 2014); ii) the Brescian Alps intra-plate tholeiitic lavas and dykes (Cassinis *et al.*, 2008); iii) the alkaline dykes, apatite-rich and chromitite layers in the Finero peridotite (Ferrario & Garuti, 1990; Stähle *et al.*, 1990; 2001; Morishita *et al.*, 2003; 2008; Zaccarini *et al.*, 2004; Malitch *et al.*, 2017). A further geochemical and geochronological comparison with the alkaline magmas at Karawanken (Austroalpine domain, Visonà & Zanferrari, 2000) is instead required, since the only available age data for this complex (230±9 Ma, Lippolt & Pidgeon, 1974) overlaps with both the ~237 Ma high-K calc-alkaline to shoshonitic and the 215-225 Ma alkaline lamprophyres of the Southern Alps.

9. Rather than a late-stage episode related to the Ladinian high-K calc-alkaline to shoshonitic magmatism of the Dolomitic Area, Predazzo lamprophyres should be considered part of the alkaline-carbonatitic magmatic pulse that intruded the Southern Alps subcontinental mantle at about 215-225 Ma. Such a magmatic event likely represents a precursor of the rifting stage connected to the Alpine Tethys opening, as also suggested by its astenospheric-influenced Sr-Nd isotopic signature. The generation of such H_2O-CO_2-rich alkaline-carbonatitic melts is therefore ascribable to mantle upwelling dynamics in a continental rifting setting (Stähle *et al.*, 1990; 2001; Zaccarini *et al.*, 2004; Batki *et al.*, 2014).

10. Predazzo alkaline lamprophyres can be considered as geochemical and geochronological markers of the shift from orogenic-like to anorogenic magmatism in the Southern Alps. Their Sr-Nd isotopic signature and incompatible elements pattern suggest that the mantle source that generated the Ladinian (~237 Ma) subduction-related magmas was progressively being depleted, during Late Triassic, by the asthenospheric influx related to the Alpine Tethys opening.

Appendix A6

Table A6.1. Whole rock major, trace element composition and $^{87}Sr/^{86}Sr$ and $^{143}Nd/^{144}Nd$ isotopes of representative Predazzo lamprophyres. Fe_2O_3 and FeO were calculated by considering a Fe_2O_3/FeO ratio of 0.15, in agreement with a fO_2 around FMQ buffer (Kress & Carmichael, 1991). Mg# = Mg/[Mg+Fe^{2+}] mol%; n.d. = not detected. All trace element (ppm) were analysed by ICP-MS except Pb, Zn, Ni, Co, Cr, V and Ba (XRF). The trace element composition of samples labelled with (*) was entirely determined by XRF. Sr-Nd isotopic ratios were corrected for 220 Ma of radiogenic ingrowth using the trace element abundances determined by ICP-MS, the decay rates of Rotenberg et al. (2012) and Lugmair & Marti (1978). Initial ratios (i) and uncertainties (2σ) were propagated according to Ickert (2013). Camp: Camptonite.

Lithology	Camp	Camp	Camp	Camp	Camp	Camp	Camp	Camp	Camp	Camp	Camp	Camp	Camp	Camp	Camp
Sample	A 71*	FF2*	FF17*	FF22*	FF37*	FF38*	EM97	EM99	FF14	EM20A	EM87	EM37A	FC80	MA5	MA1
Oxide (wt%)															
SiO₂	47.90	45.00	44.29	45.02	45.86	45.63	45.74	47.00	44.07	45.24	44.59	44.73	45.16	46.67	52.81
TiO₂	1.83	1.87	2.13	2.31	1.82	1.91	2.14	1.85	2.41	1.84	1.71	1.65	1.96	2.13	1.37
Al₂O₃	18.82	17.97	17.01	16.23	18.46	18.36	17.62	18.78	15.29	16.39	15.75	16.25	17.74	16.65	17.45
Fe₂O₃	1.33	1.49	1.26	1.30	1.63	1.55	1.37	1.37	1.46	1.41	1.55	1.29	1.31	1.50	0.98
FeO	8.83	9.91	8.45	8.65	10.83	10.32	9.15	9.10	9.74	9.38	10.30	8.54	8.71	10.02	6.53
MnO	0.19	0.23	0.19	0.23	0.18	0.15	0.20	0.20	0.18	0.22	0.20	0.20	0.18	0.17	0.16
MgO	4.93	2.99	7.72	7.15	3.60	6.53	5.88	3.00	10.06	6.80	8.49	11.28	7.13	4.37	3.23
CaO	9.71	13.88	13.43	14.24	10.73	10.26	13.03	12.49	11.92	13.81	13.21	12.86	11.80	13.95	8.83
Na₂O	1.95	2.45	2.73	1.92	2.23	2.20	1.56	1.75	1.89	2.08	1.54	1.59	3.27	2.47	2.90
K₂O	3.61	3.25	2.27	2.29	3.74	2.48	2.64	3.58	2.25	2.01	1.89	1.02	2.14	1.61	4.97
P₂O₅	0.90	0.95	0.51	0.65	0.92	0.60	0.65	0.86	0.73	0.81	0.78	0.60	0.60	0.44	0.77
Tot.	100.00	100.00	100.00	100.00	100.00	100.00	100.00	100.00	100.00	100.00	100.00	100.00	100.00	100.00	100.00
Mg#	49.90	34.97	61.94	59.58	37.20	52.99	53.41	36.96	64.77	56.34	59.52	70.19	59.33	43.75	46.88
LOI	3.72	6.39	4.92	5.41	5.53	4.81	5.33	6.53	5.70	6.11	5.13	6.68	5.17	7.36	5.94
Trace element (ppm)															
Pb	8.20	12.0	13.0	10.0	26.0	13.7	5.60	22.2	11.0	12.2	15.8	21.4	16.0	34.0	8.7
Zn	79.5	69.0	65.0	79.0	124	216	110	122	97.0	90.1	88.0	107	80.7	145	77.9
Ni	31.8	31.0	143	138	33.0	43.3	85.5	30.9	201	135	226	237	59.4	62.8	27.3
Co	28.8	28.0	40.0	43.0	34.0	43.0	30.3	34.5	45.0	32.4	44.4	48.4	40.6	41.6	25.8
Cr	19.8	14.0	254	364	23.0	24.9	185	16.0	449	326	514	585	46.8	78.9	42.2
V	112	124	238	231	130	187	222	125	220	167	170	212	191	223	92.8
Rb	82.8	239	114	48.0	238	54.0	146	242	318	105	63.9	32.0	30.5	52.7	331
Ba	790	528	542	510	522	576	910	525	405	496	504	334	546	350	590
Sr	1305	1247	661	807	1183	1069	862	1175	1190	829	795	581	780	609	1181
Nb	58.4	60.0	16.0	30.0	63.0	n.d.	24.9	56.9	46.2	35.8	37.2	15.8	33.3	18.8	55.2
Zr	321	309	211	241	333	212	190	264	201	182	170	150	202	173	356
Hf							3.03	4.96	4.62	4.08	2.95	1.99	4.02	4.19	6.11
U							0.52	1.16	1.18	0.86	0.85	0.38	0.91	0.56	0.98
Th							2.13	4.83	5.26	4.29	2.55	1.71	3.10	4.09	4.96
Y	31.6	25.0	24.0	23.0	27.0	30.3	19.9	39.8	26.0	31.4	21.5	19.4	22.8	28.5	31.9
Ta							1.74	3.53	1.88	2.32	1.80	0.69	0.80	0.68	2.30
La	71.5	38.0	11.0	27.0	37.0	48.4	20.4	47.7	30.9	34.0	23.8	12.3	27.2	20.8	35.4
Ce	121	125	64.0	42.0	86.0	49.5	54.8	105	57.2	76.2	55.9	31.1	55.6	45.1	67.5
Pr							7.17	12.8	7.21	9.27	6.61	3.96	6.53	5.65	7.51
Nd							23.4	37.8	28.7	28.1	20.0	13.0	27.2	24.3	31.0
Sm							4.62	6.86	5.32	5.58	3.98	2.88	5.19	5.13	5.37
Eu							1.58	2.50	1.64	2.08	1.48	1.11	1.65	1.65	1.77
Gd							5.10	8.08	5.01	6.29	4.54	3.39	4.92	5.05	5.45
Tb							0.72	1.20	0.81	0.98	0.69	0.56	0.76	0.86	0.84
Dy							3.76	6.53	3.96	5.39	3.81	3.16	3.99	4.53	4.34
Ho							0.82	1.52	0.83	1.26	0.89	0.78	0.84	0.98	0.91
Er							1.88	3.59	2.20	2.97	2.07	1.80	2.31	2.61	2.55
Tm							0.28	0.55	0.37	0.45	0.31	0.26	0.36	0.45	0.43
Yb							1.52	3.10	2.09	2.54	1.71	1.48	2.02	2.52	2.64
Lu							0.25	0.51	0.33	0.41	0.28	0.24	0.32	0.41	0.41
$^{87}Sr/^{86}Sr$									0.706376				0.704373		0.705787
$^{87}Rb/^{86}Sr$									0.7733				0.1129		0.8098
$^{87}Sr/^{86}Sr(i)$									0.703996				0.704025		0.703295
2σ									0.000031				0.000020		0.000030
$^{143}Nd/^{144}Nd$									0.512795				0.512765		0.512796
$^{147}Sm/^{144}Nd$									0.1118				0.1152		0.1047
$^{143}Nd/^{144}Nd(i)$									0.512634				0.512599		0.512645
2σ									0.000006				0.000006		0.000007

Table A6.2. Major element core to rim analyses and a.p.f.u. calculation of representative amphibole types from Predazzo lamprophyres. A.p.f.u. were calculated using the Lockock (2014) computation; the classification follows the recommendations of the IMA-CNMNC subcommittee on amphiboles (Hawthorne *et al.*, 2012; Oberti *et al.*, 2012).

Sample	FC80	FC80	FC80	FC80	FC80	FC80	FC80	FC80	FC80
Amphibole type	*Type 1*								
Name	Am1_c	Am1_tr1	Am1_tr2	Am1_tr3	Am1_tr4	Am1_tr5	Am1_tr6	Am1_tr7	Am1_r
Oxyde (wt%)									
SiO$_2$	39.456	39.460	39.315	39.213	39.224	39.412	39.345	38.865	39.353
TiO$_2$	4.475	4.548	4.522	4.426	4.487	4.553	4.696	4.450	5.407
Al$_2$O$_3$	15.137	15.130	15.154	15.117	15.197	15.145	15.034	15.553	12.907
Cr$_2$O$_3$	0.097	0.081	0.087	0.076	0.073	0.068	0.080	0.121	0.007
FeO$_{TOT}$	9.284	9.253	9.265	9.664	9.351	9.382	9.334	8.918	12.204
MnO	0.097	0.081	0.136	0.101	0.096	0.084	0.096	0.125	0.196
MgO	13.584	13.675	13.509	13.571	13.512	13.570	13.542	13.502	11.614
CaO	11.901	11.897	11.745	11.572	11.933	11.770	11.927	11.963	11.900
Na$_2$O	2.456	2.482	2.452	2.437	2.502	2.516	2.514	2.448	2.577
K$_2$O	1.164	1.142	1.162	1.115	1.147	1.119	1.135	1.182	1.053
NiO	0.003	0.011	0.004	0.000	0.015	0.000	0.046	0.034	0.000
F	0.339	0.265	0.178	0.360	0.290	0.270	0.379	0.327	0.585
Cl	0.000	0.028	0.000	0.041	0.000	0.030	0.066	0.020	0.036
Tot.	97.993	98.054	97.529	97.694	97.826	97.919	98.194	97.508	97.837
Mg#	**72.3**	**72.5**	**72.2**	**71.4**	**72.0**	**72.0**	**72.1**	**73.0**	**62.9**
Fe^{3+}/ΣFe used	0.904	0.91	0.903	0.904	0.909	0.898	0.912	0.926	0.618
Group	OH,F,Cl	oxo	oxo	OH,F,Cl	OH,F,Cl	oxo	oxo	OH,F,Cl	oxo
Subgroup of (OH,F,Cl)	Ca	B = Ca	B = Ca	Ca	Ca	B = Ca	B = Ca	Ca	B = Ca
Species	magnesio-hastingsite	ferri-kaersutite	ferri-kaersutite	magnesio-hastingsite	magnesio-hastingsite	ferri-kaersutite	ferri-kaersutite	magnesio-hastingsite	ferri-kaersutite
Formula Assignments									
(T) Si	5.794	5.789	5.792	5.778	5.771	5.791	5.782	5.736	5.941
(T) Al	2.206	2.211	2.208	2.222	2.229	2.209	2.218	2.264	2.059
(T) Ti	0	0	0	0	0	0	0	0	0
(C) Ti	0.494	0.502	0.501	0.491	0.497	0.503	0.519	0.494	0.614
(C) Al	0.413	0.405	0.423	0.403	0.406	0.414	0.386	0.442	0.237
(C) Cr	0.011	0.009	0.01	0.009	0.008	0.008	0.009	0.014	0.001
(C) Fe^{3+}	1.03	1.033	1.031	1.076	1.046	1.035	1.047	1.019	0.952
(C) Ni	0	0.001	0.001	0	0.002	0	0.005	0.004	0
(C) Mn^{2+}	0	0	0	0	0	0	0	0	0
(C) Fe^{2+}	0.077	0.06	0.068	0.04	0.078	0.068	0.067	0.056	0.583
(C) Mg	2.974	2.991	2.967	2.981	2.964	2.972	2.967	2.971	2.614
(B) Mn^{2+}	0.012	0.01	0.017	0.013	0.012	0.01	0.012	0.016	0.025
(B) Fe^{2+}	0.033	0.043	0.043	0.075	0.027	0.05	0.034	0.026	0.007
(B) Ca	1.872	1.87	1.854	1.827	1.881	1.853	1.878	1.892	1.925
(B) Na	0.083	0.077	0.087	0.086	0.08	0.087	0.076	0.067	0.043
(A) Ca	0	0	0	0	0	0	0	0	0
(A) Na	0.617	0.629	0.614	0.611	0.634	0.63	0.64	0.634	0.711
(A) K	0.218	0.214	0.218	0.21	0.215	0.21	0.213	0.223	0.203
O (non-W)	22	22	22	22	22	22	22	22	22
(W) OH	0.853	0.865	0.914	0.84	0.871	0.86	0.768	0.853	0.483
(W) F	0.157	0.123	0.083	0.168	0.135	0.125	0.176	0.153	0.279
(W) Cl	0	0.007	0	0.01	0	0.008	0.016	0.005	0.009
(W) O	0.99	1.005	1.003	0.982	0.994	1.007	1.039	0.989	1.229
Sum (T,C,B,A)	15.834	15.844	15.834	15.822	15.85	15.84	15.853	15.858	15.915

Table A6.2. (continued).

Sample	FC80	FC80	FC80	FC80	FC80	FC80	FC80	FC80	FC80	FC80
Amphibole type	*Type 2*									
Name	Am4_c	Am4_tr1	Am4_tr2	Am4_tr3	Am4_tr4	Am4_tr5	Am4_tr6	Am4_tr7	Am4_tr8	Am4_tr9
Oxyde (wt%)										
SiO_2	39.687	39.567	39.625	39.816	39.634	39.599	39.801	39.721	39.715	39.835
TiO_2	3.208	3.285	3.254	3.343	3.300	3.269	3.248	3.195	3.249	3.362
Al_2O_3	14.502	14.608	14.513	14.422	14.436	14.522	14.435	14.547	14.532	14.488
Cr_2O_3	0.000	0.009	0.001	0.000	0.000	0.002	0.001	0.000	0.002	0.000
FeO_{TOT}	13.256	12.909	12.811	12.658	12.748	12.854	13.007	12.910	12.864	12.407
MnO	0.159	0.169	0.136	0.126	0.137	0.154	0.109	0.178	0.164	0.156
MgO	11.909	12.036	12.258	12.291	12.007	12.016	12.078	11.991	12.153	12.317
CaO	11.360	11.429	11.461	11.459	11.448	11.441	11.544	11.481	11.347	11.473
Na_2O	2.549	2.612	2.591	2.548	2.637	2.605	2.551	2.583	2.607	2.609
K_2O	1.180	1.192	1.206	1.165	1.189	1.185	1.246	1.208	1.249	1.231
NiO	0.004	0.000	0.037	0.015	0.004	0.000	0.004	0.000	0.008	0.031
F	0.110	0.281	0.263	0.221	0.275	0.238	0.237	0.083	0.209	0.185
Cl	0.047	0.000	0.000	0.074	0.031	0.000	0.013	0.026	0.000	0.053
Tot.	97.970	98.097	98.155	98.137	97.846	97.885	98.274	97.923	98.098	98.149
Mg#	**61.6**	**62.4**	**63.0**	**63.4**	**62.7**	**62.5**	**62.3**	**62.3**	**62.7**	**63.9**
$Fe^{3+}/\Sigma Fe$ used	0.574	0.58	0.605	0.605	0.549	0.567	0.562	0.554	0.581	0.584
Group	OH,F,Cl	OH,F,Cl	OH,F,Cl	OH,F,Cl	OH,F,Cl	OH,F,Cl	OH,F,Cl	OH,F,Cl	OH,F,Cl	OH,F,Cl
Subgroup of (OH,F,Cl)	Ca	Ca	Ca	Ca	Ca	Ca	Ca	Ca	Ca	Ca
Species	Ti-rich magnesio-hastingsite	Ti-rich magnesio-hastingsite	Ti-rich magnesio-hastingsite	Ti-rich magnesio-hastingsite	Ti-rich magnesio-hastingsite	Ti-rich magnesio-hastingsite	Ti-rich magnesio-hastingsite	Ti-rich magnesio-hastingsite	Ti-rich magnesio-hastingsite	Ti-rich magnesio-hastingsite
Formula Assignments										
(T) Si	5.89	5.872	5.869	5.894	5.902	5.887	5.897	5.896	5.886	5.898
(T) Al	2.11	2.128	2.131	2.106	2.098	2.113	2.103	2.104	2.114	2.102
(T) Ti	0	0	0	0	0	0	0	0	0	0
(C) Ti	0.358	0.367	0.363	0.372	0.37	0.366	0.362	0.357	0.362	0.375
(C) Al	0.427	0.427	0.402	0.411	0.435	0.431	0.418	0.441	0.424	0.426
(C) Cr	0	0.001	0	0	0	0	0	0	0	0
(C) Fe^{3+}	0.944	0.929	0.961	0.949	0.871	0.906	0.906	0.888	0.926	0.897
(C) Ni	0	0	0.004	0.002	0.001	0	0	0	0.001	0.004
(C) Mn^{2+}	0	0	0	0	0	0	0	0	0	0
(C) Fe^{2+}	0.636	0.614	0.563	0.554	0.658	0.634	0.646	0.661	0.601	0.58
(C) Mg	2.635	2.663	2.707	2.713	2.666	2.663	2.668	2.653	2.685	2.719
(B) Mn^{2+}	0.02	0.021	0.017	0.016	0.017	0.019	0.014	0.022	0.021	0.02
(B) Fe^{2+}	0.065	0.059	0.063	0.064	0.059	0.059	0.06	0.054	0.067	0.059
(B) Ca	1.806	1.817	1.819	1.818	1.827	1.822	1.833	1.826	1.802	1.82
(B) Na	0.108	0.102	0.102	0.102	0.097	0.1	0.094	0.098	0.111	0.101
(A) Ca	0	0	0	0	0	0	0	0	0	0
(A) Na	0.625	0.649	0.643	0.629	0.664	0.651	0.639	0.645	0.639	0.648
(A) K	0.223	0.226	0.228	0.22	0.226	0.225	0.235	0.229	0.236	0.232
O (non-W)	22	22	22	22	22	22	22	22	22	22
(W) OH	1.219	1.134	1.151	1.133	1.123	1.156	1.161	1.24	1.177	1.151
(W) F	0.052	0.132	0.123	0.103	0.13	0.112	0.111	0.039	0.098	0.086
(W) Cl	0.012	0	0	0.019	0.008	0	0.003	0.006	0	0.013
(W) O	0.717	0.734	0.726	0.745	0.74	0.732	0.725	0.714	0.725	0.75
Sum (T,C,B,A)	15.847	15.875	15.872	15.85	15.891	15.876	15.875	15.874	15.875	15.881

157

Table A6.2. (continued).

Sample	FC80	FC80	FC80	FC80	FC80	FC80	MA1	MA1	MA1	MA1
Amphibole type	*Type 2*						*Type 3*			
Name	Am4_tr10	Am4_tr11	Am4_tr12	Am4_tr13	Am4_tr14	Am4_r	Am2_c	Am2_tr1	Am2_tr2	Am2_r
Oxyde (wt%)										
SiO_2	39.503	39.735	39.958	40.207	39.575	40.113	39.088	38.649	39.990	39.134
TiO_2	3.320	4.475	4.431	4.384	5.920	4.671	2.405	2.533	3.694	3.908
Al_2O_3	14.456	15.007	14.708	14.618	13.098	12.745	13.833	14.093	14.308	13.688
Cr_2O_3	0.000	0.129	0.120	0.016	0.012	0.000	0.004	0.000	0.029	0.024
FeO_{TOT}	12.899	8.558	8.650	9.197	11.280	13.322	15.794	15.274	10.384	12.324
MnO	0.159	0.096	0.091	0.116	0.148	0.241	0.399	0.351	0.134	0.174
MgO	12.191	13.842	13.973	13.753	12.134	11.133	10.018	10.383	13.287	11.999
CaO	11.542	12.205	12.128	12.027	12.359	11.833	11.721	11.951	11.602	11.791
Na_2O	2.544	2.430	2.434	2.529	2.433	2.570	2.660	2.466	2.610	2.735
K_2O	1.199	1.148	1.157	1.026	1.045	1.105	1.132	1.073	1.297	0.994
NiO	0.000	0.014	0.020	0.057	0.000	0.000	0.000	0.016	0.000	0.026
F	0.226	0.263	0.337	0.295	0.476	0.579	0.243	0.304	0.203	0.254
Cl	0.000	0.000	0.036	0.000	0.049	0.000	0.034	0.077	0.000	0.010
Tot.	98.039	97.905	98.042	98.225	98.528	98.310	97.330	97.167	97.538	97.061
Mg#	**62.7**	**74.2**	**74.2**	**72.7**	**65.7**	**59.8**	**53.1**	**54.8**	**69.5**	**63.4**
$Fe^{3+}/\Sigma Fe$ used	0.615	0.916	0.913	0.814	0.713	0.478	0.366	0.449	0.589	0.584
Group	OH,F,Cl	OH,F,Cl	OH,F,Cl	OH,F,Cl	oxo	oxo	OH,F,Cl	OH,F,Cl	OH,F,Cl	OH,F,Cl
Subgroup of (OH,F,Cl)	Ca	Ca	Ca	Ca	B = Ca	B = Ca	Ca	Ca	Ca	Ca
Species	Ti-rich magnesio-hastingsite	magnesio-hastingsite	magnesio-hastingsite	magnesio-hastingsite	ferri-kaersutite	ferri-kaersutite	magnesio-hastingsite	magnesio-hastingsite	Ti-rich magnesio-hastingsite	Ti-rich magnesio-hastingsite
Formula Assignments										
(T) Si	5.859	5.827	5.856	5.889	5.909	6.04	5.946	5.871	5.933	5.894
(T) Al	2.141	2.173	2.144	2.111	2.091	1.96	2.054	2.129	2.067	2.106
(T) Ti	0	0	0	0	0	0	0	0	0	0
(C) Ti	0.371	0.494	0.488	0.483	0.665	0.529	0.275	0.289	0.412	0.443
(C) Al	0.386	0.42	0.396	0.412	0.213	0.302	0.426	0.393	0.434	0.323
(C) Cr	0	0.015	0.014	0.002	0.001	0	0.001	0	0.003	0.003
(C) Fe^{3+}	0.984	0.961	0.968	0.917	1.005	0.802	0.736	0.87	0.759	0.906
(C) Ni	0	0.002	0.002	0.007	0	0	0	0.002	0	0.003
(C) Mn^{2+}	0	0	0	0	0.011	0	0.018	0.024	0	0
(C) Fe^{2+}	0.564	0.082	0.078	0.176	0.404	0.868	1.273	1.07	0.453	0.628
(C) Mg	2.696	3.026	3.053	3.003	2.701	2.499	2.272	2.351	2.938	2.694
(B) Mn^{2+}	0.02	0.012	0.011	0.014	0.007	0.031	0.034	0.021	0.017	0.022
(B) Fe^{2+}	0.052	0.006	0.014	0.033	0	0.008	0	0	0.077	0.018
(B) Ca	1.834	1.918	1.904	1.887	1.977	1.909	1.91	1.945	1.844	1.903
(B) Na	0.093	0.064	0.071	0.065	0.015	0.053	0.056	0.034	0.062	0.057
(A) Ca	0	0	0	0	0	0	0	0	0	0
(A) Na	0.638	0.627	0.621	0.653	0.689	0.698	0.729	0.692	0.688	0.741
(A) K	0.227	0.215	0.216	0.192	0.199	0.212	0.22	0.208	0.246	0.191
O (non-W)	22	22	22	22	22	22	22	22	22	22
(W) OH	1.152	0.89	0.858	0.897	0.433	0.666	1.323	1.255	1.08	0.99
(W) F	0.106	0.122	0.156	0.137	0.225	0.275	0.117	0.146	0.095	0.121
(W) Cl	0	0	0.009	0	0.012	0	0.009	0.02	0	0.002
(W) O	0.742	0.988	0.978	0.967	1.33	1.059	0.551	0.579	0.825	0.886
Sum (T,C,B,A)	15.865	15.842	15.836	15.844	15.887	15.911	15.95	15.899	15.933	15.932

Table A6.2. (continued).

Sample	FC80	FC80	FC80	MA1	MA1	MA1	MA1	MA1	MA1	MA1
Amphibole type	*Type 4*			*Type 5*						
Name	Am3_c	Am3_tr1	Am3_r	Am5_c	Am5_tr1	Am5_tr2	Am5_tr3	Am5_tr4	Am5_tr5	Am5_tr6
Oxyde (wt%)										
SiO_2	37.475	37.671	38.310	37.416	37.227	38.800	37.863	36.037	36.968	36.020
TiO_2	3.312	3.837	4.336	2.757	2.765	2.787	2.771	2.798	2.782	2.775
Al_2O_3	15.537	15.957	15.546	15.375	16.316	16.200	16.158	14.846	15.421	14.974
Cr_2O_3	0.000	0.021	0.000	0.009	0.011	0.001	0.000	0.000	0.010	0.003
FeO_{TOT}	15.449	12.154	10.548	22.091	22.060	21.710	22.044	22.038	21.979	21.989
MnO	0.193	0.139	0.115	0.420	0.426	0.415	0.423	0.442	0.400	0.425
MgO	9.137	11.240	12.446	5.341	5.217	5.696	5.397	5.033	5.324	4.949
CaO	11.771	12.079	11.779	10.377	10.230	10.279	10.283	10.387	10.395	10.341
Na_2O	2.730	2.417	2.513	2.682	3.145	2.994	2.950	2.548	2.732	2.720
K_2O	1.182	1.130	1.024	1.396	1.320	1.351	1.364	1.372	1.357	1.316
NiO				0.007	0.000	0.017	0.018	0.012	0.000	0.000
F	0.111	0.138	0.180	0.199	0.028	0.093	0.064	0.085	0.112	0.112
Cl	0.037	0.010	0.014	0.103	0.077	0.084	0.059	0.078	0.099	0.104
Tot.	96.933	96.793	96.799	98.172	98.821	100.426	99.391	95.674	97.578	95.727
Mg#	**51.3**	**62.2**	**67.8**	**30.1**	**29.6**	**31.9**	**30.4**	**28.9**	**30.2**	**28.6**
$Fe^{3+}/\Sigma Fe$ used	0.41	0.626	0.783	0.314	0.346	0.303	0.325	0.331	0.328	0.328
Group	OH,F,Cl	OH,F,Cl	OH,F,Cl	OH,F,Cl	OH,F,Cl	OH,F,Cl	OH,F,Cl	OH,F,Cl	OH,F,Cl	OH,F,Cl
Subgroup of (OH,F,Cl)	Ca	Ca	Ca	Ca	Ca	Ca	Ca	Ca	Ca	Ca
Species	Ti-rich magnesio-hastingsite	Ti-rich magnesio-hastingsite	magnesio-hastingsite	Ti-rich ferro-ferri-sadanagaite	Ti-rich ferro-ferri-sadanagaite	Ti-rich ferro-ferri-sadanagaite	Ti-rich ferro-ferri-sadanagaite	Ti-rich ferro-ferri-sadanagaite	Ti-rich ferro-ferri-sadanagaite	Ti-rich ferro-ferri-sadanagaite
Formula Assignments										
(T) Si	5.736	5.675	5.722	5.799	5.707	5.838	5.768	5.746	5.76	5.741
(T) Al	2.264	2.325	2.278	2.201	2.293	2.162	2.232	2.254	2.24	2.259
(T) Ti	0	0	0	0	0	0	0	0	0	0
(C) Ti	0.381	0.435	0.487	0.321	0.319	0.315	0.318	0.336	0.326	0.333
(C) Al	0.539	0.508	0.458	0.607	0.655	0.71	0.67	0.535	0.591	0.554
(C) Cr	0	0.003	0	0.001	0.001	0	0	0	0.001	0
(C) Fe^{3+}	0.81	0.958	1.032	0.899	0.979	0.826	0.913	0.972	0.94	0.962
(C) Ni	0	0	0	0.001	0	0.002	0.002	0.001	0	0
(C) Mn^{2+}	0.018	0	0	0	0.004	0	0	0	0	0.006
(C) Fe^{2+}	1.168	0.573	0.252	1.936	1.849	1.868	1.872	1.96	1.905	1.969
(C) Mg	2.085	2.524	2.771	1.234	1.192	1.278	1.226	1.196	1.237	1.176
(B) Mn^{2+}	0.007	0.018	0.015	0.055	0.052	0.053	0.055	0.06	0.053	0.052
(B) Fe^{2+}	0	0	0.034	0.028	0	0.037	0.024	0.007	0.019	0
(B) Ca	1.93	1.95	1.885	1.723	1.68	1.657	1.678	1.774	1.735	1.766
(B) Na	0.062	0.032	0.067	0.194	0.268	0.253	0.243	0.159	0.193	0.182
(A) Ca	0	0	0	0	0	0	0	0	0	0
(A) Na	0.748	0.673	0.661	0.612	0.667	0.62	0.628	0.628	0.632	0.658
(A) K	0.231	0.217	0.195	0.276	0.258	0.259	0.265	0.279	0.27	0.268
O (non-W)	22	22	22	22	22	22	22	22	22	22
(W) OH	1.173	1.061	0.936	1.232	1.328	1.302	1.318	1.264	1.266	1.25
(W) F	0.054	0.066	0.085	0.098	0.014	0.044	0.031	0.043	0.055	0.056
(W) Cl	0.01	0.003	0.004	0.027	0.02	0.021	0.015	0.021	0.026	0.028
(W) O	0.764	0.87	0.975	0.644	0.639	0.632	0.636	0.672	0.653	0.666
Sum (T,C,B,A)	15.979	15.891	15.857	15.887	15.924	15.878	15.894	15.907	15.902	15.926

Table A6.2. (continued).

Sample	MA1	MA1	MA1	MA1
Amphibole type	*Type 5*			
Name	Am5_tr7	Am5_tr8	Am5_tr9	Am5_r
Oxyde (wt%)				
SiO$_2$	40.965	41.475	40.666	40.164
TiO$_2$	3.727	3.681	3.561	3.706
Al$_2$O$_3$	13.539	13.258	13.611	13.514
Cr$_2$O$_3$	0.093	0.055	0.059	0.008
FeO$_{TOT}$	9.648	10.186	9.729	10.834
MnO	0.168	0.156	0.125	0.153
MgO	14.000	13.977	13.894	13.101
CaO	11.427	11.238	11.426	11.877
Na$_2$O	2.703	2.647	2.687	2.762
K$_2$O	1.189	1.127	1.153	1.071
NiO	0.046	0.038	0.009	0.014
F	0.267	0.270	0.178	0.384
Cl	0.016	0.029	0.011	0.026
Tot.	97.787	98.136	97.107	97.614
Mg#	**72.1**	**71.0**	**71.8**	**68.3**
Fe^{3+}/ΣFe used	0.592	0.677	0.58	0.548
Group	OH,F,Cl	OH,F,Cl	OH,F,Cl	OH,F,Cl
Subgroup of (OH,F,Cl)	Ca	Ca	Ca	Ca
Species	Ti-rich magnesio-hastingsite	Ti-rich magnesio-hastingsite	Ti-rich magnesio-hastingsite	Ti-rich magnesio-hastingsite
Formula Assignments				
(T) Si	6.043	6.078	6.033	5.986
(T) Al	1.957	1.922	1.967	2.014
(T) Ti	0	0	0	0
(C) Ti	0.414	0.406	0.397	0.416
(C) Al	0.397	0.368	0.412	0.36
(C) Cr	0.011	0.006	0.007	0.001
(C) Fe^{3+}	0.705	0.845	0.7	0.74
(C) Ni	0.005	0.004	0.001	0.002
(C) Mn^{2+}	0	0	0	0
(C) Fe^{2+}	0.389	0.317	0.41	0.571
(C) Mg	3.079	3.053	3.073	2.911
(B) Mn^{2+}	0.021	0.019	0.016	0.019
(B) Fe^{2+}	0.097	0.086	0.097	0.04
(B) Ca	1.806	1.765	1.816	1.897
(B) Na	0.076	0.13	0.071	0.044
(A) Ca	0	0	0	0
(A) Na	0.697	0.622	0.702	0.754
(A) K	0.224	0.211	0.218	0.204
O (non-W)	22	22	22	22
(W) OH	1.043	1.056	1.119	0.981
(W) F	0.124	0.125	0.083	0.181
(W) Cl	0.004	0.007	0.003	0.007
(W) O	0.828	0.812	0.795	0.832
Sum (T,C,B,A)	15.921	15.832	15.92	15.959

Table A6.3. Major element composition and a.p.f.u. calculation of representative clinopyroxene crystals from Predazzo lamprophyres.

Sample	FC80 - Camptonite											
Name	Cpx1_c	Cpx1_r	Cpx3_c	Cpx4_c	Cpx6_c	Cpx6_tr1	Cpx8_c	Cpx11_c	Cpx11_r	Cpx14_c	Cpx14_r	Cpx19_c
Oxide (wt%)												
SiO_2	49.604	42.278	48.742	47.089	44.324	45.773	43.078	45.583	48.050	45.548	45.762	46.792
TiO_2	1.108	4.031	1.206	2.126	2.065	2.136	3.164	2.266	2.012	2.151	1.974	1.744
Al_2O_3	5.005	9.933	5.847	5.462	10.878	9.710	10.085	9.836	5.581	9.582	9.247	9.208
FeO	5.751	8.483	6.028	8.099	8.532	6.142	7.942	6.680	7.971	6.469	6.756	6.383
MnO	0.138	0.139	0.130	0.180	0.176	0.118	0.143	0.125	0.200	0.126	0.126	0.116
MgO	14.534	10.291	14.344	12.714	10.378	12.376	11.069	12.295	12.714	12.290	12.161	12.765
CaO	22.176	22.555	21.673	22.676	21.990	22.073	22.669	22.133	22.611	22.259	22.334	21.958
Na_2O	0.502	0.594	0.505	0.410	0.754	0.641	0.471	0.621	0.448	0.624	0.597	0.650
K_2O	0.000	0.017	0.000	0.022	0.004	0.005	0.005	0.008	0.008	0.000	0.002	0.014
Cr_2O_3	0.133	0.000	0.155	0.010	0.041	0.142	0.025	0.194	0.000	0.258	0.047	0.205
NiO	0.000	0.019	0.020	0.013	0.009	0.022		0.012	0.007	0.000	0.010	0.015
Tot.	98.933	98.336	98.643	98.799	99.150	99.138	98.782	99.754	99.601	99.306	99.015	99.849
Mg#	**81.8**	**68.4**	**80.9**	**73.7**	**68.4**	**78.2**	**71.3**	**76.6**	**74.0**	**77.2**	**76.2**	**78.1**
A.p.f.u.												
(T) Si^{4+}	1.841	1.612	1.815	1.775	1.664	1.703	1.628	1.688	1.796	1.694	1.708	1.727
(T) Al^{3+}	0.159	0.388	0.185	0.225	0.336	0.297	0.372	0.312	0.204	0.306	0.292	0.273
(T) Fe^{3+}	0.000	0.000	0.000	0.000	0.000	0.000	0.000	0.000	0.000	0.000	0.000	0.000
(M1) Al^{3+}	0.060	0.058	0.072	0.017	0.146	0.128	0.077	0.118	0.041	0.114	0.115	0.127
(M1) Fe^{3+}	0.069	0.144	0.078	0.119	0.127	0.092	0.149	0.107	0.083	0.109	0.108	0.091
(M1) Ti^{4+}	0.031	0.116	0.034	0.060	0.058	0.060	0.090	0.063	0.057	0.060	0.055	0.048
(M1) Cr^{3+}	0.004	0.000	0.005	0.000	0.001	0.004	0.001	0.006	0.000	0.008	0.001	0.006
(M1) Ni^{2+}	0.000	0.001	0.001	0.000	0.000	0.001	0.000	0.000	0.000	0.000	0.000	0.000
(M1) Mg^{2+}	0.804	0.585	0.796	0.714	0.581	0.686	0.624	0.679	0.708	0.681	0.677	0.702
(M1) Fe^{2+}	0.032	0.097	0.015	0.089	0.086	0.029	0.060	0.027	0.111	0.028	0.043	0.025
(M2) Fe^{2+}	0.078	0.030	0.095	0.048	0.055	0.070	0.043	0.073	0.056	0.064	0.060	0.081
(M2) Mn^{2+}	0.004	0.004	0.004	0.006	0.006	0.004	0.005	0.004	0.006	0.004	0.004	0.004
(M2) Ca^{2+}	0.882	0.921	0.865	0.916	0.885	0.880	0.918	0.878	0.905	0.887	0.893	0.868
(M2) Na^+	0.036	0.044	0.036	0.030	0.055	0.046	0.035	0.045	0.032	0.045	0.043	0.046
(M2) K^+	0.000	0.001	0.000	0.001	0.000	0.000	0.000	0.000	0.000	0.000	0.000	0.001
Wo	47.18	51.72	46.67	48.42	50.87	49.96	51.07	49.68	48.44	50.01	50.04	49.02
En	43.03	32.84	42.98	37.78	33.41	38.98	34.70	38.40	37.90	38.42	37.92	39.65
Fs	9.78	15.44	10.35	13.80	15.73	11.06	14.22	11.92	13.67	11.57	12.04	11.33
Tot.	100.00	100.00	100.00	100.00	100.00	100.00	100.00	100.00	100.00	100.00	100.00	100.00

Table A6.3. (continued).

Sample	MA5 - Camptonite						FF14 - Camptonite				
Name	Cpx1_c	Cpx1_tr1	Cpx1_r	Cpx2_c	Cpx3_c	Cpx4_c	Cpx1_c	Cpx2_c	Cpx5_c	Cpx8_c	Cpx12_c
Oxide (wt%)											
SiO$_2$	47.658	47.176	43.272	43.518	47.591	42.472	44.043	44.549	42.305	47.141	48.427
TiO$_2$	1.461	1.491	3.773	3.844	2.089	4.049	3.343	2.614	3.633	1.947	1.536
Al$_2$O$_3$	8.612	9.028	10.068	9.320	5.270	9.178	9.003	8.648	10.510	5.790	4.823
FeO	5.394	5.476	7.874	8.073	8.106	9.655	6.928	6.474	7.052	8.213	6.620
MnO	0.110	0.119	0.110	0.133	0.146	0.139	0.112	0.130	0.096	0.168	0.170
MgO	13.600	13.384	11.329	11.037	13.487	10.405	11.393	12.179	11.164	12.814	14.086
CaO	22.045	21.903	22.618	22.829	21.650	22.464	22.758	22.967	22.873	22.475	22.767
Na$_2$O	0.555	0.558	0.414	0.533	0.322	0.524	0.408	0.406	0.416	0.332	0.283
K$_2$O	0.000	0.015	0.004	0.005	0.000	0.006	0.059	0.012	0.023	0.014	0.007
Cr$_2$O$_3$	0.462	0.510	0.249	0.202	0.121	0.002	0.442	0.830	0.463	0.025	0.159
NiO	0.036	0.034	0.017	0.000	0.006	0.000	0.020	0.000			
Tot.	99.932	99.695	99.727	99.494	98.788	98.893	98.510	98.804	98.557	98.983	98.933
Mg#	**81.8**	**81.3**	**71.9**	**70.9**	**74.8**	**65.8**	**74.6**	**77.0**	**73.8**	**73.5**	**79.1**
A.p.f.u.											
(T) Si^{4+}	1.751	1.738	1.621	1.636	1.791	1.616	1.667	1.674	1.600	1.774	1.810
(T) Al^{3+}	0.249	0.262	0.379	0.364	0.209	0.384	0.333	0.326	0.400	0.226	0.190
(T) Fe^{3+}	0.000	0.000	0.000	0.000	0.000	0.000	0.000	0.000	0.000	0.000	0.000
(M1) Al^{3+}	0.124	0.130	0.065	0.050	0.025	0.028	0.069	0.057	0.069	0.031	0.022
(M1) Fe^{3+}	0.071	0.075	0.124	0.130	0.086	0.164	0.093	0.127	0.142	0.110	0.097
(M1) Ti^{4+}	0.040	0.041	0.106	0.109	0.059	0.116	0.095	0.074	0.103	0.055	0.043
(M1) Cr^{3+}	0.013	0.015	0.007	0.006	0.004	0.000	0.013	0.025	0.014	0.001	0.005
(M1) Ni^{2+}	0.001	0.001	0.001	0.000	0.000	0.000	0.001	0.000	0.000	0.000	0.000
(M1) Mg^{2+}	0.745	0.735	0.633	0.619	0.757	0.590	0.643	0.682	0.630	0.719	0.785
(M1) Fe^{2+}	0.006	0.003	0.064	0.087	0.070	0.103	0.086	0.035	0.042	0.085	0.047
(M2) Fe^{2+}	0.089	0.091	0.059	0.037	0.099	0.041	0.041	0.041	0.038	0.064	0.062
(M2) Mn^{2+}	0.003	0.004	0.003	0.004	0.005	0.004	0.004	0.004	0.003	0.005	0.005
(M2) Ca^{2+}	0.868	0.865	0.908	0.920	0.873	0.916	0.923	0.925	0.927	0.906	0.912
(M2) Na^{+}	0.040	0.040	0.030	0.039	0.023	0.039	0.030	0.030	0.031	0.024	0.021
(M2) K^{+}	0.000	0.001	0.000	0.000	0.000	0.000	0.003	0.001	0.001	0.001	0.000
Wo	48.70	48.79	50.70	51.19	46.20	50.38	51.60	50.96	52.00	47.97	47.76
En	41.81	41.48	35.33	34.44	40.05	32.47	35.94	37.60	35.32	38.06	41.12
Fs	9.49	9.73	13.97	14.37	13.75	17.15	12.46	11.44	12.69	13.97	11.12
Tot.	100.00	100.00	100.00	100.00	100.00	100.00	100.00	100.00	100.00	100.00	100.00

162

Table A6.4. LA-ICP-MS trace element composition of representative amphibole and clinopyroxene crystals from Predazzo camptonite. Amp: amphibole; Cpx: clinopyroxene

Sample	FC80	FC80	FC80	FC80	FC80	FC80	FC80	FC80
Mineral	Amp	Amp	Amp	Amp	Amp	Amp	Cpx	Cpx
Type	*Type 1*_core	*Type 1*_rim	*Type 1*_groundmass	*Type 2*_rim	*Type 4*_core	*Type 4*_rim	Large phenoXX	Small phenoXX
Trace element (ppm)								
Sc	53.670	89.030	54.330	65.190	32.225	77.530	124.850	148.210
V	398.665	519.700	379.830	343.440	333.475	519.990	409.270	453.925
Cr	9.830	131.000	22.485	195.080	21.245	62.270	542.315	941.050
Co	58.415	55.180	57.550	55.115	52.450	54.550	30.240	31.635
Ni	55.205	95.635	55.720	80.480	23.930	94.380	65.720	71.360
Zn	n.d.	n.d.	n.d.	n.d.	n.d.	n.d.	n.d.	n.d.
Pb	0.441	0.550	0.372	0.569	0.744	0.474	0.234	0.196
Cs	0.050	0.260	n.d.	0.179	n.d.	0.169	n.d.	n.d.
Rb	5.340	6.195	6.055	6.705	6.990	6.510	0.049	n.d.
Ba	291.855	365.970	349.270	303.505	429.855	356.940	0.521	0.328
Th	0.095	0.078	0.101	0.040	0.151	0.131	0.080	0.106
U	0.043	0.022	0.018	0.050	0.029	<0.0118	0.011	0.016
Nb	16.310	22.335	20.005	17.685	27.125	16.080	0.511	0.854
Ta	0.681	1.054	0.973	0.826	0.981	0.862	0.095	0.096
La	7.960	7.080	10.195	7.095	12.860	7.590	5.390	4.985
Ce	25.540	23.345	33.460	23.420	38.760	22.910	18.490	18.585
Pr	4.355	4.130	5.590	4.170	6.320	4.130	3.510	3.410
Sr	767.490	763.915	786.870	728.255	796.760	735.690	100.915	103.345
Nd	24.160	22.885	30.780	23.530	33.730	22.780	20.475	20.580
Zr	83.480	120.945	112.995	96.095	134.655	97.380	98.605	113.245
Hf	2.760	4.085	3.500	3.475	4.425	3.710	3.915	5.030
Sm	6.815	5.905	8.160	6.520	8.315	6.540	6.865	6.465
Eu	2.290	2.295	2.530	2.550	2.925	2.033	2.205	2.310
Gd	6.470	6.760	7.150	6.450	7.750	6.290	6.200	6.065
Tb	1.047	1.069	1.274	1.130	1.214	1.042	1.155	1.095
Dy	6.090	5.895	6.755	6.130	7.600	5.690	6.820	6.835
Y	30.115	30.060	34.325	32.300	38.270	29.120	31.030	33.470
Ho	1.185	1.163	1.319	1.341	1.408	1.180	1.325	1.414
Er	2.955	3.105	3.200	3.220	3.910	3.040	3.030	3.185
Tm	0.375	0.433	0.454	0.403	0.531	0.390	0.501	0.529
Yb	2.525	2.430	3.105	2.730	3.370	2.520	2.720	3.170
Lu	0.373	0.298	0.440	0.358	0.507	0.405	0.391	0.455

Table A6.5. Major element composition and a.p.f.u. calculation of representative plagioclase and K-feldspar crystals from Predazzo lamprophyres. Pl: plagioclase; Kfs: K-Feldspar

Sample	FC80 - Camptonite									
Mineral	Pl	Pl	Pl	Pl	Pl	Pl	Pl	Pl	Pl	Pl
Name	Plag1_c	Plag1_tr1	Plag1_tr2	Plag1_tr3	Plag1_r	Plag4_c	Plag5_c	Plag5_r	PLag7_c	Plag7_r
Oxide (wt%)										
SiO$_2$	56.994	55.766	56.303	56.115	49.614	51.747	55.204	49.116	52.291	50.105
TiO$_2$	0.013	0.000	0.002	0.012	0.107	0.087	0.013	0.086	0.015	0.102
Al$_2$O$_3$	26.996	27.050	27.099	27.365	30.781	30.266	28.417	31.571	30.506	31.151
FeO$_{TOT}$	0.147	0.450	0.151	0.143	0.587	0.639	0.203	0.596	0.043	0.520
MnO	0.000	0.006	0.000	0.000	0.000	0.020	0.004	0.003	0.002	0.008
MgO	0.002	0.379	0.000	0.000	0.082	0.071	0.006	0.101	0.000	0.079
CaO	8.566	9.274	8.988	9.313	13.734	12.879	10.469	14.586	12.605	13.943
BaO	0.000	0.013	0.000	0.027	0.066	0.036	0.007	0.037	0.000	0.009
Na$_2$O	6.687	5.987	6.230	6.216	3.380	3.857	5.559	3.047	4.439	3.471
K$_2$O	0.240	0.189	0.220	0.174	0.265	0.289	0.247	0.211	0.190	0.246
Tot.	99.610	99.113	98.986	99.347	98.609	99.890	100.130	99.353	100.064	99.632
A.p.f.u.										
Si	2.558	2.526	2.551	2.533	2.292	2.356	2.482	2.256	2.363	2.289
Ti	0.000	0.000	0.000	0.000	0.004	0.003	0.000	0.003	0.001	0.004
Al	1.428	1.444	1.447	1.456	1.676	1.624	1.506	1.709	1.625	1.677
Cr	0.000	0.000	0.000	0.000	0.000	0.000	0.000	0.000	0.000	0.000
Fe^{3+}	0.000	0.000	0.000	0.000	0.000	0.000	0.000	0.000	0.000	0.000
Fe^{2+}	0.006	0.017	0.006	0.005	0.023	0.024	0.008	0.023	0.002	0.020
Mn	0.000	0.000	0.000	0.000	0.000	0.001	0.000	0.000	0.000	0.000
Mg	0.000	0.026	0.000	0.000	0.006	0.005	0.000	0.007	0.000	0.005
Ca	0.412	0.450	0.436	0.450	0.680	0.628	0.504	0.718	0.610	0.683
Ba	0.000	0.000	0.000	0.000	0.001	0.001	0.000	0.001	0.000	0.000
Na	0.582	0.526	0.547	0.544	0.303	0.341	0.485	0.271	0.389	0.307
K	0.014	0.011	0.013	0.010	0.016	0.017	0.014	0.012	0.011	0.014
Tot. cat.	5.000	5.000	5.000	5.000	5.000	5.000	5.000	5.000	5.000	5.000
Tot. oxy.	7.975	7.980	7.994	7.985	7.975	7.993	7.986	7.972	7.976	7.970
An	**40.88**	**45.61**	**43.79**	**44.84**	**68.10**	**63.75**	**50.28**	**71.67**	**60.41**	**67.96**
Ab	**57.75**	**53.28**	**54.93**	**54.16**	**30.33**	**34.55**	**48.31**	**27.09**	**38.50**	**30.61**
Or	**1.36**	**1.11**	**1.28**	**1.00**	**1.56**	**1.70**	**1.41**	**1.23**	**1.08**	**1.43**
Tot.	**100.00**	**100.00**	**100.00**	**100.00**	**100.00**	**100.00**	**100.00**	**100.00**	**100.00**	**100.00**

Table A6.5. (continued).

Sample	FF14 - Camptonite						MA5 - Camptonite		MA1 – Camptonite				
Mineral	Pl	Pl	Pl	Pl	Pl	Pl	Pl	Pl	Pl	Pl	Kfs	Kfs	Kfs
Name	Plag3_c	Plag4_c	Plag8_c	Plag10_c	Plag11_c	Plag14_c	Plag3_c	Plag5_c	Plag1_c	Plag3_c	Kf1_c	Kf2_c	Kf4_c
Oxide (wt%)													
SiO$_2$	53.309	51.735	49.748	55.984	49.369	50.193	49.209	49.275	61.624	56.077	64.624	65.065	65.340
TiO$_2$	0.148	0.127	0.091	0.126	0.067	0.121	0.081	0.071	0.024	0.041	0.012	0.000	0.014
Al$_2$O$_3$	29.209	29.855	30.713	27.734	31.030	30.352	31.688	32.093	23.858	26.491	19.408	19.523	19.125
FeO$_{TOT}$	0.595	0.614	0.631	0.560	0.770	0.676	0.619	0.554	0.309	0.418	0.271	0.195	0.207
MnO	0.013	0.000	0.007	0.006	0.014	0.000	0.009	0.000	0.009	0.009	0.010	0.000	0.005
MgO	0.050	0.067	0.112	0.029	0.131	0.125	0.111	0.104	0.008	0.032	0.012	0.000	0.010
CaO	11.550	12.615	13.904	9.586	14.186	13.688	15.000	15.240	4.748	8.586	0.294	0.350	0.244
BaO	0.049	0.071	0.000	0.143	0.000	0.029	0.000	0.000	0.000	0.000	0.000	0.000	0.000
Na$_2$O	4.736	4.084	3.131	5.529	3.186	3.453	3.025	2.841	7.941	6.184	4.700	5.019	5.021
K$_2$O	0.453	0.378	0.496	0.643	0.240	0.301	0.135	0.146	1.177	0.579	9.925	9.465	9.555
Tot.	100.110	99.537	98.825	100.341	98.980	98.938	99.875	100.323	99.696	98.417	99.255	99.618	99.561
A.p.f.u.													
Si	2.410	2.361	2.296	2.518	2.275	2.312	2.249	2.244	2.751	2.557	2.942	2.946	2.963
Ti	0.005	0.004	0.003	0.004	0.002	0.004	0.003	0.002	0.001	0.001	0.000	0.000	0.000
Al	1.557	1.606	1.671	1.470	1.685	1.648	1.707	1.722	1.255	1.424	1.041	1.042	1.022
Cr	0.000	0.000	0.000	0.000	0.000	0.000	0.000	0.000	0.000	0.000	0.000	0.000	0.000
Fe^{3+}	0.000	0.000	0.000	0.000	0.000	0.000	0.000	0.000	0.000	0.000	0.000	0.000	0.000
Fe^{2+}	0.022	0.023	0.024	0.021	0.030	0.026	0.024	0.021	0.012	0.016	0.010	0.007	0.008
Mn	0.000	0.000	0.000	0.000	0.001	0.000	0.000	0.000	0.000	0.000	0.000	0.000	0.000
Mg	0.003	0.005	0.008	0.002	0.009	0.009	0.008	0.007	0.001	0.002	0.001	0.000	0.001
Ca	0.560	0.617	0.688	0.462	0.700	0.675	0.734	0.744	0.227	0.419	0.014	0.017	0.012
Ba	0.001	0.001	0.000	0.003	0.000	0.001	0.000	0.000	0.000	0.000	0.000	0.000	0.000
Na	0.415	0.361	0.280	0.482	0.285	0.308	0.268	0.251	0.687	0.547	0.415	0.441	0.441
K	0.026	0.022	0.029	0.037	0.014	0.018	0.008	0.008	0.067	0.034	0.576	0.547	0.553
Tot. cat.	5.000	5.000	5.000	5.000	5.000	5.000	5.000	5.000	5.000	5.000	5.000	5.000	5.000
Tot. oxy.	7.973	7.976	7.980	7.998	7.970	7.977	7.967	7.978	8.002	7.980	7.967	7.974	7.977
An	**55.91**	**61.67**	**68.97**	**47.09**	**70.10**	**67.45**	**72.69**	**74.14**	**23.14**	**41.95**	**1.43**	**1.69**	**1.18**
Ab	**41.48**	**36.13**	**28.10**	**49.15**	**28.49**	**30.79**	**26.53**	**25.01**	**70.03**	**54.68**	**41.25**	**43.87**	**43.88**
Or	**2.61**	**2.20**	**2.93**	**3.76**	**1.41**	**1.77**	**0.78**	**0.84**	**6.83**	**3.37**	**57.32**	**54.44**	**54.94**
Tot.	**100.00**	**100.00**	**100.00**	**100.00**	**100.00**	**100.00**	**100.00**	**100.00**	**100.00**	**100.00**	**100.00**	**100.00**	**100.00**

Table A6.6. Major element composition and a.p.f.u. calculation of representative Fe-Ti oxides from Predazzo lamprophyres.

Sample	FC80 - Camptonite				MA1 - Camptonite
Name	Ox1	Ox2	Ox5	Ox7	Ox3
Oxides (wt%)					
SiO$_2$	0.524	0.097	0.788	0.514	2.106
TiO$_2$	17.615	12.139	18.982	18.339	12.260
Al$_2$O$_3$	7.851	2.330	5.533	7.381	4.283
FeO	61.332	77.084	63.173	62.735	69.367
MnO	0.783	0.976	0.907	0.756	1.451
MgO	2.331	0.219	0.950	2.418	0.196
CaO	0.166	0.119	0.562	0.198	0.219
Cr$_2$O$_3$	0.146	0.000	0.044	0.036	0.043
V$_2$O$_3$	0.455	0.086	0.363	0.469	0.097
NiO	0.000	0.000	0.000	0.000	0.030
ZnO	0.166	0.238	0.322	0.110	0.237
Tot.	91.364	93.269	91.615	92.956	90.288
A.p.f.u.					
Si	0.020	0.004	0.031	0.019	0.083
Ti	0.503	0.352	0.553	0.515	0.363
Al	0.351	0.106	0.253	0.325	0.199
Fe^{3+}	0.000	0.000	0.000	0.000	0.000
Fe^{2+}	1.947	2.487	2.046	1.961	2.283
Mn	0.025	0.032	0.030	0.024	0.048
Mg	0.132	0.013	0.055	0.135	0.011
Ca	0.007	0.005	0.023	0.008	0.009
Cr	0.004	0.000	0.001	0.001	0.001
V	0.011	0.002	0.009	0.012	0.003
Tot. Cat.	3.000	3.000	3.000	3.000	3.000
FeO (mol%)	**63.04**	**58.10**	**63.78**	**62.76**	**62.79**
Fe$_2$O$_3$ (mol%)	**13.63**	**26.24**	**12.33**	**13.60**	**20.67**
TiO$_2$ (mol%)	**23.32**	**15.66**	**23.90**	**23.65**	**16.55**

Table A6.7. Major element composition of representative carbonates in Predazzo lamprophyres.

Sample	FC80 - Camptonite														
Name	C1	C3	C4	C5	C6	C7	C9	C10	C11	C13	C14	C15	C16	C18	C19
Oxides (wt%)															
SiO₂	0.023	0.017	0.011	0.006	0.012	0.007	0.016	0.025	0.000	0.043	0.000	0.021	0.000	0.000	0.030
FeO	35.147	34.065	32.973	5.434	10.377	5.523	6.483	10.561	38.746	38.623	38.958	14.368	7.794	5.001	6.548
MnO	0.406	0.447	0.483	0.544	0.249	0.467	0.391	0.328	0.647	0.550	0.581	0.423	0.477	0.421	0.450
MgO	18.482	18.521	17.697	18.416	16.137	18.578	18.025	13.629	14.356	15.035	15.342	12.706	16.453	18.538	17.990
CaO	2.209	3.343	5.232	28.475	27.579	29.062	28.604	29.870	3.645	3.137	2.250	27.823	28.638	28.816	27.907
SrO	0.000	0.000	0.000	0.212	0.080	0.166	0.033	0.054	0.000	0.000	0.000	0.066	0.161	0.304	0.098
Tot.	56.266	56.393	56.397	53.087	54.435	53.803	53.552	54.465	57.394	57.388	57.131	55.405	53.522	53.080	53.023
CaCO₃ (%)	3.966	5.962	9.343	48.352	47.239	48.690	48.411	52.050	6.703	5.737	4.131	48.722	49.310	48.831	47.715
MgCO₃ (%)	46.167	45.958	43.971	43.510	38.457	43.306	42.446	33.043	36.728	38.254	39.194	30.957	39.416	43.708	42.798
FeCO₃ (%)	49.253	47.421	45.961	7.202	13.873	7.222	8.565	14.364	55.610	55.129	55.833	19.639	10.474	6.615	8.739
SrCO₃ (%)	0.000	0.000	0.024	0.197	0.075	0.152	0.031	0.051	0.018	0.012	0.000	0.063	0.152	0.281	0.091
MnCO₃ (%)	0.577	0.630	0.682	0.730	0.337	0.619	0.523	0.451	0.941	0.796	0.843	0.585	0.649	0.564	0.608

Table A6.8. *P, T, fO₂ and H₂O parameters obtained by mineral-melt and single mineral calculations on Predazzo lamprophyres. For each applied method, the corresponding reference and error on the single parameters are reported. T and P of clinopyroxene crystallization were obtained by means of the mineral-melt equations of Putirka (2008). Oxygen fugacity was calculated by means of the Ishibashi (2013) oxy-barometer. The water content of the melt during amphibole crystallization was calculated using the Ridolfi et al. (2010) single-mineral hygrometer. T and P of amphibole crystallization were obtained by means of the Putirka (2016) mineral-melt thermometer and H₂O-dependent barometer. This latter equation was applied by considering as input the H₂O content of the coexisting melt resulted from the hygrometer of Ridolfi et al. (2010). Cpx: clinopyroxene; Amp: amphibole.*

Sample	Type (Amp)	Method	Reference	T (°C)	Error (°C)	P (MPa)	Error (MPa)	H₂O (wt%)	Error (wt%)	logfO₂
MA5 - Camptonite	-	Cpx-melt	Putirka (2008), Eq. 32a/32d	1060-1124	±58	230-640	±310	-	-	-
FC80 - Camptonite	*Type 1_core*	Amp-only; Amp-melt	Ridolfi et al. (2010); Putirka (2016), Eq. 5/7b	1023-1069	±30	920-1160	±170	7.2-8.5	±0.8-1.2	-
FC80 - Camptonite	*Type 1_rim*	Amp-only; Amp-melt	Ridolfi et al. (2010); Putirka (2016), Eq. 5/7b	1038-1067	±30	740-900	±170	6.8-7.5	±0.8-1.2	-
FC80 - Camptonite	*Type 1_intermediate*	Amp-only; Amp-melt	Ridolfi et al. (2010); Putirka (2016), Eq. 5/7b	1071	±30	1050	±170	7.7	±0.8-1.2	-
FC80 - Camptonite	*Type 1_groundmass*	Amp-only; Amp-melt	Ridolfi et al. (2010); Putirka (2016), Eq. 5/7b	1025-1074	±30	850-1110	±170	6.7-8.1	±0.8-1.2	-
MA1 - Camptonite	*Type 1_core*	Amp-only; Amp-melt	Ridolfi et al. (2010); Putirka (2016), Eq. 5/7b	948-1042	±30	620-980	±170	6.5-7.7	±0.8-1.2	-
MA1 - Camptonite	*Type 1_rim*	Amp-only; Amp-melt	Ridolfi et al. (2010); Putirka (2016), Eq. 5/7b	1031-1032	±30	600-640	±170	6.2-6.6	±0.8-1.2	-
MA1 - Camptonite	*Type 1_groundmass*	Amp-only; Amp-melt	Ridolfi et al. (2010); Putirka (2016), Eq. 5/7b	1001-1029	±30	470-800	±170	6.5-7.6	±0.8-1.2	-
FC80 - Camptonite	*Type 2_core*	Amp-only; Amp-melt	Ridolfi et al. (2010); Putirka (2016), Eq. 5/7b	997-1009	±30	890-920	±170	6.8-7.1	±0.8-1.2	-
FC80 - Camptonite	*Type 2_rim*	Amp-only; Amp-melt	Ridolfi et al. (2010); Putirka (2016), Eq. 5/7b	1005-1053	±30	730-770	±170	6.8-7.0	±0.8-1.2	-
FC80 - Camptonite	*Type 2_intermediate*	Amp-only; Amp-melt	Ridolfi et al. (2010); Putirka (2016), Eq. 5/7b	1051-1063	±30	920-970	±170	7.2-7.4	±0.8-1.2	-
FC80 - Camptonite	*Type 3_rim*	Amp-only; Amp-melt	Ridolfi et al. (2010); Putirka (2016), Eq. 5/7b	1057-1063	±30	870-980	±170	7.2-7.3	±0.8-1.2	-
MA1 - Camptonite	*Type 3_rim*	Amp-only; Amp-melt	Ridolfi et al. (2010); Putirka (2016), Eq. 5/7b	961-1030	±30	630-750	±170	6.4-7.8	±0.8-1.2	-
FC80 - Camptonite	*Type4_core*	Amp-only; Amp-melt	Ridolfi et al. (2010); Putirka (2016), Eq. 5/7b	1008	±30	1220	±170	8.9	±0.8-1.2	-
FC80 - Camptonite	*Type4_rim*	Amp-only; Amp-melt	Ridolfi et al. (2010); Putirka (2016), Eq. 5/7b	1042-1060	±30	1120-1230	±170	8.3	±0.8-1.2	-
MA1 - Camptonite	*Type 5_core*	Amp-only; Amp-melt	Ridolfi et al. (2010); Putirka (2016), Eq. 5/7b	927-983	±30	960-1130	±170	8.8-9.8	±0.8-1.2	-
MA1 - Camptonite	*Type 5_rim*	Amp-only; Amp-melt	Ridolfi et al. (2010); Putirka (2016), Eq. 5/7b	977-1048	±30	490-690	±170	5.8-6.9	±0.8-1.2	-
FC80 - Camptonite	-	Ti-magnetite-melt	Ishibashi (2013)	1100 (input)	-	500 (input)	-	-	-	-8.4/-10.0
FC80 - Camptonite	-	Ti-magnetite-melt	Ishibashi (2013)	1050 (input)	-	500 (input)	-	-	-	-9.4/-11.0

Table A6.9. Modal composition, melting proportions and REE composition of the mantle sources used in the partial melting models. Ol: olivine; Cpx: clinopyroxene; Opx: orthopyroxene; Spl: spinel; Grt: garnet; Amp: amphibole; Phl: phlogopite. I = Spl-lherzolite with DMM composition (Workman & Hart 2005); II = Spl-lherzolite; III = Grt-lherzolite; IV = Spl-Grt-Amp-lherzolite; V = Grt-Amp-lherzolite; VI = Grt-Phl-lherzolite. Starting REE composition of II, III, IV, V and VI sources is fertile PM of Sun & McDonough (1989). REE partition coefficients used in the models are also reported. Ol, Opx, Cpx, Spl, Grt and Amp partition coefficients are from McKenzie & O'Nions (1991) and Schmidt *et al.* (1999), except for Tm in Cpx (Zack & Brumm 1998). Phl partition coefficients: La, Ce, Nd and Sm from Schmidt *et al.* (1999); Eu, Gd, Dy, Er, Yb and Lu from Fujimaki *et al.* (1984); Pr, Tb, Ho and Tm were extrapolated from the partition coefficients of the adjacent elements according to Barry *et al.* (2003).

Source modal composition							Source melting proportions							
Phase	I	II	III	IV	V	VI	Phase	I	II	III	IV	V	VI	
Ol	0.57	0.55	0.55	0.55	0.55	0.56	Ol	0.01	0.01	0.01	0.05	0.03	0.03	
Opx	0.28	0.25	0.25	0.19	0.2	0.19	Opx	0.09	0.09	0.07	0.05	0.05	0.05	
Cpx	0.13	0.15	0.15	0.15	0.15	0.15	Cpx	0.6	0.6	0.6	0.1	0.22	0.1	
Spl	0.02	0.05	-	0.02	-	-	Spl	0.3	0.3	-	0.1	0	-	
Grt	-	-	0.05	0.04	0.04	0.02	Grt	-	-	0.32	0.2	0.2	0.15	
Amp	-	-	-	0.05	0.06	0.02	Amp	-	-	-	0.5	0.5	0.37	
Phl	-	-	-	-	-	0.06	Phl	-	-	-	-	-	0.3	

Source REE composition							Partition coefficients							
	I	II	III	IV	V	VI		Ol	Opx	Cpx	Spl	Grt	Amp	Phl
La	0.192	0.687	0.687	0.687	0.687	0.687	La	0.0004	0.002	0.054	0.01	0.01	0.17	0.00002
Ce	0.55	1.775	1.775	1.775	1.775	1.775	Ce	0.0005	0.003	0.098	0.01	0.021	0.26	0.0002
Pr	0.107	0.276	0.276	0.276	0.276	0.276	Pr	0.0008	0.0048	0.15	0.01	0.054	0.35	0.0002
Nd	0.581	1.354	1.354	1.354	1.354	1.354	Nd	0.001	0.0068	0.21	0.01	0.087	0.44	0.0002
Sm	0.239	0.444	0.444	0.444	0.444	0.444	Sm	0.0013	0.01	0.26	0.01	0.217	0.76	0.0002
Eu	0.0096	0.168	0.168	0.168	0.168	0.168	Eu	0.0016	0.013	0.31	0.01	0.32	0.88	0.0218
Gd	0.358	0.596	0.596	0.596	0.596	0.596	Gd	0.0015	0.016	0.3	0.01	0.498	0.86	0.0205
Tb	0.07	0.108	0.108	0.108	0.108	0.108	Tb	0.0015	0.019	0.31	0.01	0.75	0.83	0.025
Dy	0.505	0.737	0.737	0.737	0.737	0.737	Dy	0.0017	0.022	0.33	0.01	1.06	0.78	0.0281
Ho	0.115	0.164	0.164	0.164	0.164	0.164	Ho	0.0016	0.026	0.31	0.01	1.53	0.73	0.028
Er	0.348	0.48	0.48	0.48	0.48	0.48	Er	0.0015	0.03	0.29	0.01	2	0.68	0.0303
Tm	-	0.074	0.074	0.074	0.074	0.074	Tm	0.0015	0.04	0.449	0.01	3	0.64	0.035
Yb	0.365	0.493	0.493	0.493	0.493	0.493	Yb	0.0015	0.049	0.28	0.01	4.03	0.59	0.0484
Lu	0.058	0.074	0.074	0.074	0.074	0.074	Lu	0.0015	0.06	0.28	0.01	5.5	0.51	0.0471

Chapter 7

Final remarks

Chapter 7. Final remarks

One of the most representative expressions of the magmatic event that affected the Southalpine and Austroalpine domains during Middle-Late Triassic is recorded in the Dolomitic Area. After being at the heart of the petrographic works of the '80s and '90s, this area has been poorly studied in the last couple of decades, notwithstanding the numerous unsolved questions about its tectono-magmatic history. At a larger scale, the features of the Triassic magmatism of the Dolomitic Area can provide a substantial contribution to the discovery and interpretation of the geodynamic evolution of the Southern Alps between the Hercynian orogeny and the opening of the Alpine Tethys. In this thesis, a petrological, geochemical and geochronological study of the intrusive/hypabyssal bodies cropping out at Predazzo, Mt. Monzoni and Cima Pape enabled to frame the Dolomitic Area in the complex evolution of the Southalpine-Austroalpine domains during Middle-Late Triassic.

In addition, the preservation of this area from the Alpine tectonics and the action of the erosion made it possible the nowadays exposure onto the surface of a continuous volcanic/volcanoclastic sequence, related dyke swarms and intrusive/hypabyssal complexes. As a result, many portions of the Dolomitic Area are "snapshots" of the ancient plumbing systems, completely preserved in their relationships with the sedimentary host rocks and the overlying volcanites. In the present thesis, the main chemico-physical features of these ancient plumbing systems were set out, and a good agreement between field evidence and thermobarometric estimates was achieved. According to our results, the features of these feeding systems can play a key role in the future development and/or test of the modern thermobarometric approaches to active volcanic systems, where the depth and nature of the magma chamber/s can be only determined by means of indirect methodologies.

Beyond the petrological, geochemical and geochronological characterization of the Middle-Late Triassic magmatism, summarized in the following lines, main goal of the present thesis is therefore reawakening the interest of the scientific community on the intriguing features of the Dolomitic Area, whose relevance at both local and global scale is paramount.

7.1. The Middle Triassic magmas of the Dolomitic Area: multiple intrusion of shoshonitic melts in a shallow crust

Within the Dolomitic Area, the Predazzo, Mt. Monzoni and Cima Pape volcano-plutonic complexes are the most intriguing expressions of the Middle Triassic magmatic event. The surface exposure of the relationships between intrusions, dyke swarms, host rocks and volcanic products make them perfect petrological laboratories. Detailed field surveys, sampling and geochemical/petrological/geochronological studies led to point out that the

three bodies are constituted by a SiO_2-saturated (SS) magmatic suite with K-affinity and orogenic-like (shoshonitic) features, as testified by the Nb-Ta-Ti negative anomalies and LILE enrichment, the widespread occurrence of biotite and amphibole, and the EM I-like $^{87}Sr/^{86}Sr$-$^{143}Nd/^{144}Nd$ isotopic signature. In contrast to the single-pulse Mt. Monzoni and Cima Pape bodies, the Predazzo Intrusive Complex has a multi-pulse nature. In this pluton, the emplacement of the main silica-saturated suite is followed by the intrusion of a SiO_2-oversaturated (granitic, GU) unit, and finally by the emplacement of a SiO_2-undersaturated (SU) batch (Fig. 48). SS and SU bodies are clearly distinguishable by means of petrography and mineral chemistry, as well as by their HFSE and LREE contents and their Sr-Nd isotopic signature. Their slight Nd isotopic range can be explained by low degree of crustal assimilation (5-6%), whereas the Sr isotopic variability is likely the results of syn-emplacement contamination processes at the intrusion edges, as clearly evident in the case of Mt. Monzoni. Fractional crystallization was the major (and almost only) process acting during the differentiation of SS and SU batches, confirming what hypothesized by Petersen *et al.* (1980), Gasparotto & Simboli (1991) and Bonadiman *et al.* (1994). In particular, fractional crystallization processes starting from SS/SU trachybasaltic magmas can model the occurrence of cumulitic gabbros and pyroxenites.

Despite petrography, whole-rock and mineral chemistry suggested an I-type affinity for GU granites/syenogranites, the wide range and the uncertainty on their isotopic signature leaves the question on the origin of GU suite still unsolved. The absence of similar effusive products in the surrounding area and the impossibility to model the genesis of GU granites/syenogranites via simple fractional crystallization from a starting SS magma points towards the absence of a link between SS and GU rocks. On the other side, the geochemical/petrographic similarities between GU rocks and the coheval calc-alkaline/high-K calc-alkaline rhyolites found in Carnia (Gianolla, 1992) and Alto Vicentino (De Vecchi *et al.*, 1974; Barbieri *et al.*, 1982; Bellieni *et al.*, 2010) suggest that a high-K calc-alkaline suite was also present in the Dolomitic Area during Middle Triassic.

Thermobarometric, oxybarometric and hygrometric estimates enabled to unravel the main chemico-physical conditions of emplacement of the Predazzo, Mt. Monzoni and Cima Pape intrusions. They intruded at similar shallow depth (1.0-3.6 km Mt. Monzoni pluton; 1.4-5.6 km Predazzo pluton), at *T* ranging from 1000-1100°C to 589-610°C. Despite similar *T-P* of magma emplacement of the SS, SU and GU batches, H_2O and fO_2 data indicated that SU primary magmas were characterized by slightly lower water contents and oxidizing conditions than the SS ones (1.0-1.5 *vs.* 2.0-2.5 H_2O wt%; -0.1/+0.33 vs. +0.2/+0.7 ΔFMQ, respectively). Plagioclase-melt, amphibole and K-feldspar-melt hygrometers indicated

highly hydrated conditions of magmas and progressive H_2O enrichment during differentiation, as also confirmed by the widespread presence of hydrous phases. At odds with what proposed in literature (Menegazzo Vitturi *et al.*, 1995), the calculated depth of emplacement is well in accordance with the field evidence. A magmatic contact between the Predazzo pluton and the overlying volcanites was in fact documented, similarly to what proposed by Sommavilla (1970) for the Cima Pape sill. Besides confirming the shallow nature of the intrusion/s, this grain size gradual transition, together with the lack of 'caldera-filling'-like materials, led to exclude the presence of a calderic collapse structure in the Predazzo area, invoked by several authors to explain the ring-shape of the plutonic complex. The EM I-like isotopic signature of the Dolomitic Area rocks speaks in favor of the presence of a subduction-signature in the mantle beneath Southern Alps during Middle Triassic, as already proposed by Bonadiman *et al.* (1994) and Zanetti *et al.* (2013). Even if the absence of primary products in the Dolomitic Area prevents to exactly quantify the role of the enriched mantle component in the magma genesis, its contribution was undoubtedly high. The slight Nd-isotopic enrichment of SU magmas with respect to SS ones could be ascribed to a time-related change in the mantle source, slightly moving towards a more depleted component. Finally, the signature of the Triassic magmas is consistent with the presence of an Ivrea-like basement beneath the Dolomitic Area.
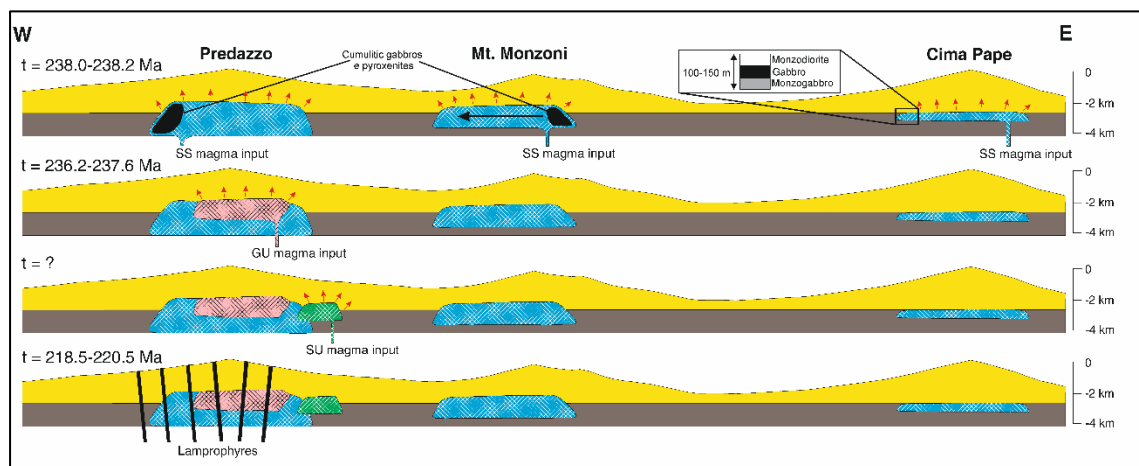
Fig. 48. West to East interpretative sketch of the evolutionary sequence of the Middle-Late Triassic magmatism in the Dolomitic Area. A first emplacement of the Shoshonitic Silica Saturated (SS) intrusive batches at Predazzo, Mt. Monzoni and Cima Pape (dated at 238.0-238.2 Ma, Storck et al., 2018) was followed by the intrusion of the Granitic Unit (GU, 236.2-237.6 Ma) and the Shoshonitic Silica Undersaturated (SU) batch (age unknown) at Predazzo. Finally, at 218.5-220.5 Ma, alkaline lamprophyres intruded in and around the Predazzo Intrusive Complex. The black arrow inside Mt. Monzoni pluton indicates the differentiation trend hypothesized by Bonadiman et al. (1994). Black bodies represent cumulitic gabbros and pyroxenites. Inset shows the stratigraphy of Cima Pape sill.

7.2. A Late Triassic magmatic pulse: the shift from orogenic to anorogenic magmas marked by the intrusion of lamprophyric dykes

Thought to represent a "fourth" magmatic pulse related to the Middle Triassic magmatic event, the alkaline lamprophyres (camptonites) cropping out in the Predazzo area were investigated by means of petrologic, geochemical and geochronological approaches.

Their wide Mg# range, together with the behaviour of compatible elements (such as Ni and Cr) and the small variations in the mineral phase abundances, enabled to hypothesize that differentiation processes took place inside the lamprophyres magmatic system. According to mass balance models, the more evolved camptonites were generated by 35-40% fractional crystallization of olivine, clinopyroxene, amphibole and Ti-magnetite from an initial primitive melt. On the other side, amphibole textures and composition record the occurrence of small scale mixing between variably evolved and/or volatile-rich melts during differentiation, as testified by the variable presence of dissolution-reprecipitation textures and pseudomorphic replacements. Moreover, the occurrence, composition and textural features of carbonate-bearing ocelli lead us to hypothesize that a carbonatitic melt was intimately associated to the alkaline lamprophyric one.

In contrast to what previously hypothesized, $^{40}Ar/^{39}Ar$ ages of Predazzo alkaline lamprophyres demonstrated that they emplaced at $219.22 \pm 0.46/0.73$ Ma (2σ; analytical/full systematic uncertainties), suggesting an origin unrelated to the short-lived (700 ka) Middle Triassic high-K calc-alkaline/shoshonitic magmatism of the Predazzo-Mt. Monzoni-Cima Pape intrusions (Fig. 48). The trace element distribution, Sr-Nd isotopes and mantle melting models of lamprophyres fostered this hypothesis, pointing towards a genesis in an intra-plate geodynamic setting, from a garnet-amphibole-bearing mantle source with a strong $^{87}Sr/^{86}Sr$-$^{143}Nd/^{144}Nd$ depleted component. Low melting percentages (1.0-2.5%) of a fertile lherzolite at a depth of 70-80 km can account for their generation. According to thermobarometric estimates, the crystallization of Predazzo lamprophyres occurred at least between 690 and 230 MPa, at T decreasing from 1124 to ~1000°C. The oxygen fugacity of the magmatic system varied between -1 and +1 ΔFMQ, whereas the H_2O content of the lamprophyric melt resulted of 5.8-6.8 wt%, decreasing with decreasing temperature. The T-P path of lamprophyres crystallization strengthens the distinction between them and the Ladinian high-K calc-alkaline to shoshonitic magmas. Whereas the crystallization of the latters occurred mainly at shallow depth (1-6 km), the former began crystallizing at about 24 km and continued towards the surface. Such a discrepancy can be explained by the major role played by the extensional-trastensional tectonics during lamprophyres intrusion.

Lamprophyres are temporally, spatially and geochemically correlable to several magmatic occurrences of the Southern Alps-Carpathians area, such as: (i) the Ditrau alkaline lamprophyres (Batki *et al.*, 2014); (ii) the Brescian Alps intra-plate tholeiitic lavas and dykes (Cassinis *et al.*, 2008); (iii) the alkaline dykes, the apatite-rich and the chromitite layers in the Finero peridotite (Ferrario & Garuti, 1990; Stähle *et al.*, 1990; 2001; Morishita *et al.*, 2003; 2008; Zaccarini *et al.*, 2004; Malitch *et al.*, 2017). More than a late-stage episode related to the Middle Triassic high-K calc-alkaline to shoshonitic magmatism of the Dolomitic Area, Predazzo lamprophyres should be now considered as part of the alkaline-carbonatitic magmatic pulse that intruded the subcontinental mantle portion of the Southern Alps at about 215-225 Ma (Fig. 48). Such a magmatic event likely represents a precursor of the rifting stage connected to the Alpine Tethys opening, as also suggested by its asthenospheric-influenced Sr-Nd isotopic signature. The generation of such H_2O-CO_2-rich alkaline-carbonatitic melts is therefore ascribable to mantle upwelling dynamics in a continental rifting setting (Stähle *et al.*, 1990; 2001; Zaccarini *et al.*, 2004; Batki *et al.*, 2014). In summary, the alkaline lamprophyres cropping out at Predazzo can be considered as markers of the geochemical/geochronological shift of the Southern Alps magmatism from orogenic-like to anorogenic nature. According to these data, the mantle source that generated the subduction-related Middle Triassic (~237 Ma) magmatism of the Predazzo, Mt. Monzoni and Cima Pape complexes was progressively being depleted, during Late Triassic, by the asthenospheric influx related to the Alpine Tethys opening.

References

Abbas, H., Michail, M., Cifelli, F., Mattei, M., Gianolla, P., Lustrino, M. & Carminati, E. (2018). Emplacement modes of the Ladinian plutonic rocks of the Dolomites: Insights from anisotropy of magnetic susceptibility. Journal of Structural Geology 113, 42-61.

Akinin, V. V., Sobolev, A. V., Ntaflos, T. & Richter, W. (2005). Clinopyroxene megacrysts from Enmelen melanephelinitic volcanoes (Chukchi Peninsula, Russia): application to composition and evolution of mantle melts. Contributions to Mineralogy and Petrology 150(1), 85-101.

Allahyari, K., Saccani, E., Rahimzadeh, B. & Zeda, O. (2014). Mineral chemistry and petrology of highly magnesian ultramafic cumulates from the Sarve-Abad (Sawlava) ophiolites (Kurdistan, NW Iran): New evidence for boninitic magmatism in intra-oceanic fore-arc setting in the Neo-Tethys between Arabia and Iran: Journal of Asian Earth Sciences 79, 312-328.

Anderson, J. L. (1996). Status of thermobarometry in granitic batholiths. Geological Society of America Special Papers 315, 125-138.

Anderson, J. L. & Smith, D. R. (1995). The effects of temperature and fO_2 on the Al-in-hornblende barometer. American Mineralogist 80(5-6), 549-559.

Armienti, P., Corazzato, C., Groppelli, G., Natoli, E. & Pasquarè, G. (2003). Geological and petrographical study of Montecampione Triassic subvolcanic bodies (Southern Alps, Italy): preliminary geodynamic results. Italian Journal of Geosciences 2, 67-78.

Barbieri, G., De Vecchi, G. P., De Zanche, V., Mietto, P. & Sedea, R. (1982). Stratigrafia e petrologia del magmatismo triassico nell'area di Recoaro. Guida alla geologia del Sudalpino centro-orientale. Società Geologica Italiana - Guide Geologiche Regionali, 179-187.

Barfod, D. N., Mark, D. F., Tait, A., Dymock, R. C. & Imlach, J. (2014). Argon extraction from geological samples by CO_2 scanning laser step-heating. In: Jourdan, F., Mark, D.F., & Verati, C. (eds.) Advances in $^{40}Ar/^{39}Ar$ dating: from archaeology to planetary sciences. Geological Society of London Special Publication 378, 79-90.

Barry, T. L., Saunders, A. D., Kempton, P. D., Windley, B. F., Pringle, M. S., Dorjnamjaa, D. & Saandar, S. (2003). Petrogenesis of Cenozoic basalts from Mongolia: evidence for the role of asthenospheric versus metasomatized lithospheric mantle sources. Journal of Petrology 44(1), 55-91.

Barth, S., Oberli, F., Meier, M., Blattner, P., Bargossi, G. M. & Di Battistini, G. (1993). The evolution of a calc-alkaline basic to silicic magma system: geochemical and Rb-Sr, Sm-Nd, and $^{18}O/^{16}O$ isotopic evidence from the Late Hercynian Atesina-Cima d'Asta volcanoplutonic complex, northern Italy. Geochimica et Cosmochimica Acta 57, 4285-4300.

Batki, A., Pál-Molnár, E., Dobosi, G. & Skelton, A. (2014). Petrogenetic significance of ocellar camptonite dykes in the Ditrău Alkaline Massif, Romania. Lithos 200, 181-196.

Bébien, J., Blanchet, R., Cadet, J.P., Charvet, J., Chorowicz, J., Lapierre, H. & Rampnoux, J.P. (1978). Le volcanisme Triassique des Dinarides en Yougoslavie: sa place dans l'évolution geotectonique peri-mediterraneenne. Tectonophysics 47(1-2), 159-176.

Beccaluva, L., Coltorti, M., Saccani, E., Siena, F. & Zeda, O. (2005). Triassic Magmatism and Jurassic Ophiolites at the Margins of the Adria Plate. In: Finetti I. R. (ed.) Crop Project: Deep Seismic Exploration of the Central Mediterranean and Italy. Elsevier 28, 607-622.

Beccaluva, L., Dal Piaz, G.V. & Macciota, G. (1984). Transitional to normal MORB affinities in ophiolitic metabasites from the Zermatt-Saas, Combin and Antrona units, Western Alps: implications for the paleogeographic evolution of the Western Tethyan Basin: Geologie en Mijnbouw 63, 165-177.

Bellieni, G., Fioretti, A. M., Marzoli, A. & Visonà, D. (2010). Permo-Paleogene magmatism in the eastern Alps. Rendiconti Lincei 21, S51-S71.

Beltrán-Triviño, A., Winkler, W., von Quadt, A. & Gallhofer, D. (2016). Triassic magmatism on the transition from Variscan to Alpine cycles: evidence from U–Pb, Hf, and geochemistry of detrital minerals. Swiss Journal of Geosciences 109(3), 309-328.

Bernoulli, D. & Lemoine, M. (1980). Birth and Early Evolution of the Tethys: the Overall Situation. Mémoires du Bureau de recherches géologiques et minières 115, 168-179.

Bertotti, G., Picotti, V., Bernoulli, D. & Castellarin, A. (1993). From rifting to drifting: tectonic evolution of the South-Alpine upper crust from the Triassic to the Early Cretaceous: Sedimentary Geology 86, 53-76.

Bianchini, G., Natali, C., Shibata, T. & Yoshikawa, M. (2018). Basic dykes crosscutting the crystalline basement of Valsugana (Italy): new evidence of early Triassic volcanism in the Southern Alps. Tectonics 37(7), 2080-2093.

Blendinger, W., Lohmeier, S., Bertini, A., Meißner, E. & Sattler, C. D. (2015). A new model for the formation of Dolomite in the Triassic dolomites, Northern Italy. Journal of Petroleum Geology 38(1), 5-36.

Bohrson, W. A. & Spera, F. J. (2001). Energy-constrained open-system magmatic processes II: application of energy-constrained assimilation–fractional crystallization (EC-AFC) model to magmatic systems. Journal of Petrology 42(5), 1019-1041.

Bonadiman, C., Coltorti, M. & Siena, F. (1994). Petrogenesis and T-fO$_2$ estimates of Mt. Monzoni complex (Central Dolomites, Southern Alps): a Triassic shoshonitic intrusion in a trascurrent geodynamic setting. European Journal of Mineralogy 6, 943-966.

Bonin, B. (1988). From orogenic to anorogenic environments: evidence from associated magmatic episodes. Schweizerische Mineralogische und Petrographische Mitteilungen 68, 301-311.

Brack, P., Mundil, R., Oberli, F., Meier, M. & Rieber, H. (1996). Biostratigraphic and radiometric age data question the Milankovitch characteristics of the Latemar cycles (Southern Alps, Italy). Geology 24(4), 371-375.

Brack, P., Mundil, R., Oberli, F., Meier, M. & Rieber, H. (1997). Biostratigraphic and radiometric age data question the Milankovitch characteristics of the Latemar cycles (Southern Alps, Italy): Reply. Geology 25(5), 471-472.

Brack, P., Rieber, H., Nicora, A. & Mundil, R. (2005). The Global boundary Stratotype Section and Point (GSSP) of the Ladinian Stage (Middle Triassic) at Bagolino (Southern Alps, Northern Italy) and its implications for the Triassic time scale. Episodes 28(4), 233-244.

Brady, J. B. & McCallister, R. H. (1983). Diffusion data for clinopyroxenes from homogenization and self-diffusion experiments. American Mineralogist 68, 95-105.

Brondi, A., Mittempergher, M., Panizza, M., Rossi, D., Sommavilla, E. & Vuillermin, F. (1977). Note Illustrative della Carta Geologica d'Italia, Foglio 028 La Marmolada. Servizio Geologico d'Italia, Roma, scale 1:50.000, 1 sheet.

Buckley, H. A. & Woolley, A. R. (1990). Carbonates of the magnesite-siderite series from four carbonatite complexes. Mineralogical Magazine 54(376), 413-418.

Burkhard, D. J. M. (1991). Temperature and redox path of biotite-bearing intrusives: a method of estimation applied to S- and I-type granites from Australia. Earth and Planetary Science Letters 104, 89-98.

Burnham, D. J. M., Holloway, J. R. & Davis, N. F. (1969). Thermodynamic properties of water to 1000°C and 10,000 bars. Geological Society of America Special Papers 132, 96.

Calanchi, N., Lucchini, F. & Rossi, P. L. (1977). M. Agnello: un apparato a condotto centrale delle Dolomiti. Mineralogica et Petrografica Acta 21, 221-229.

Calanchi, N., Lucchini, F. & Rossi, P. L. (1978). The volcanic rocks from the Mount Agnello area (Fiemme Valley, Italy): a contribution to the knowledge of the Mid-Triassic magmatism of the Southern Alps. Tschermaks Mineralogische und Petrographische Mitteilungen, 25.

Carraro, A. & Visonà, D. (2003). Mantle xenoliths in Triassic camptonite dykes of the Predazzo Area (Dolomites, Northern Italy). European Journal of Mineralogy 15(1), 103-115.

Cassinis, G., Cortesogno, L., Gaggero, L., Perotti, C. R. & Buzzi, L. (2008). Permian to Triassic geodynamic and magmatic evolution of the Brescian Prealps (eastern Lombardy, Italy): Italian Journal of Geosciences 127(3), 501-518.

Castellarin, A. (1983). Alpi Meridionali. Magmatismo e tettonica triassica: Memorie della Società Geologica Italiana, 24, 5-7.

Castellarin, A., Lucchini, F., Rossi, P. L., Sartori, L., Simboli, G. & Sommavilla, E. (1982). Note geologiche sulle intrusioni di Predazzo e dei M. Monzoni. Guida alla geologia del Sudalpino centro-orientale. Guide geologiche regionali S.G.I., 211-219.

Castellarin, A., Lucchini, F., Rossi, P. L., Selli, L. & Simboli, G. (1988). The Middle Triassic magmatic-tectonic arc development in the Southern Alps. Tectonophysics 146(1-4), 79-89.

Castellarin, A., Lucchini, F., Rossi, P. L., Simboli, G., Bosellini, A. & Sommavilla, E. (1980). Middle Triassic magmatism in Southern Alps II: A geodynamic model. Rivista Italiana di Paleontologia e Stratigrafia 85(3-4), 1111-1124.

Chappell, B. W. & White, A. J. R. (2001). Two contrasting granite types: 25 years later. Australian Journal of Earth Sciences 48(4), 489-499.

Cherniak, D. J. & Liang, Y. (2012). Ti diffusion in natural pyroxene. Geochimica et Cosmochimica Acta 98, 31-47.

Coltorti, M. & Siena, F. (1984). Mantle tectonite and fractionate peridotite at Finero (Italian Western Alps). Neues Jahrbuch für Mineralogie-Abhandlungen 149(3), 225-244.

Coltorti, M., Siena, F. & Visonà, D. (1996). Aspetti petrologici del magmatismo Triassico dell'area di Predazzo78° Riunione estiva Soc. Geol. It: Geologia delle Dolomiti. San Cassiano (1996), Conference Abstract.

Cornelius, H. P. & Cornelius-Furlani, M. (1924). Zur Geologie der Tuffbildungen im Marmolatagebiet (Südtirol). Zentralblatt für Geologie und Paläontologie 12, 366-373.

Cruden, A. R., McCaffrey, K. J. W. & Bunger, A. P. (2018). Geometric Scaling of Tabular Igneous Intrusions: Implications for Emplacement and Growth. In Breitkreuz, C. & Rocchi, S. (eds.) Physical Geology of Shallow Magmatic Systems. Springer, 11-38.

Dal Negro, A., Cundari, A., Piccirillo, E. M., Molin, G.M. & Uliana, D. (1986). Distinctive Crystal-chemistry and Site Configuration of the Clinopyroxene from Alkali Basaltic Rocks - the Nyambeni Clinopyroxene Suite, Kenya: Contributions to Mineralogy and Petrology 92, 35-43.

Dal Piaz, G. (1993). Evolution of Austro-Alpine and Upper Penninic basement in the northwestern Alps from Varisican convergence to post-Variscan extension. In Pre-Mesozoic geology in the Alps. Springer-Verlag, 327-344.

Dal Piaz, G., Bistacchi, A. & Massironi, M. (2003). Geological outline of the Alps. Episodes 26(3), 175-180.

Dal Piaz, G., Bistacchi, A., Gianotti, F., Monopoli, B., Passeri, L., … & Toffolon, G. (2015). Carta Geologica d'Italia-Foglio 070 Monte Cervino. Carta Geologica d'Italia, 1:50.000 scale: 70.

Dallai, L., Cioni, R., Boschi, C. & D'Oriano, C. (2011). Carbonate-derived CO_2 purging magma at depth: influence on the eruptive activity of Somma-Vesuvius, Italy. Earth and Planetary Science Letters 310(1), 84-95.

Dallmeyer, D.R., Kräutner, H.G. & Neubauer, F. (1997). Middle-late Triassic $^{40}Ar/^{39}Ar$ hornblende ages for early intrusions within the Ditrau alkaline massif, Rumania: Implications for Alpine rifting in the Carpathian orogen. Geologica Carpathica 48(6), 347-352.

De Vecchi, G., De Zanche, V. & Sedea, R. (1974). Osservazioni preliminari sulle manifestazioni magmatiche triassiche nelle Prealpi Vicentine (area di Recoaro-Schio-Posina). Italian Journal of Geosciences 93(2), 397-409.

Della Lucia, A. (1997). Aspetti vulcanologici e petrologici del complesso vulcano-plutonico Triassico di Cima Pape (Pale di San Lucano, BL). Unpublished master thesis, University of Ferrara.

Di Matteo, V., Carroll, M. R., Behrens, H., Vetere, F. & Brooker, R. A. (2004). Water solubility in trachytic melts. Chemical Geology 213(1-3), 187-196.

Dimanov, A., Jaoul, O. & Sautter, V. (1996). Calcium self-diffusion in natural diopside single crystals. Geochimica et Cosmochimica Acta 60(21), 4095-4106.

Doglioni, C. (1984). Triassic diapiric structure in the central Dolomites (Northen Italy). Eclogae Geologicae Helvetiae 77, 2.

Doglioni, C. (1987). Tectonics of the Dolomites (Southern Alps, Northern Italy). Journal of Structural Geology 9, 181-193.

Doglioni, C. (2007). Tectonics of the Dolomites. Bulletin für angewandte Geologie 12(2), 11-15.

Doglioni, C. & Bosellini, A. (1987). Eoalpine and Mesoalpine tectonics in the Southern Alps: Geologische Rundschau 76(3), 735-754.

Doglioni, C. & Carminati, E. (2008). Structural styles and Dolomites field trip. Memorie Descrittive della Carta Geologica d'Italia 82, 301.

Dymek, F. R. (1983). Titanium, aluminium and interlayercalation substitution in biotite from high-grade gneisses, West Greenland: American Mineralogist, 68, 880-899.

Ellis, B. S., Mark, D. F., Pritchard, C. J. & Wolff, J. A. (2012). Temporal dissection of the Huckleberry Ridge Tuff using the $^{40}Ar/^{39}Ar$ dating technique. Quaternary Geochronology 9, 34-41.

Eppelbaum, L., Kutasov, I. & Pilchin, A. (2014). Thermal properties of rocks and density of fluids. In: Applied geothermics. Springer Berlin Heidelberg, 99-149.

Ewart, A. (1982). The mineralogy and petrology of Tertiary-Recent orogenic volcanic rocks: with special reference to the andesitic-basaltic compositional range. In Thorp, R. S. (ed.) Andesites: Orogenic Andesites and Related Rocks. John Wiley and Sons, New York, 724, 25-95.

Falloon, T. J. & Green, D. H. (1988). Anhydrous partial melting of peridotite from 8 to 35 kb and the petrogenesis of MORB. Journal of Petrology 1, 379-414.

Ferrario, A. & Garuti, G. (1990). Platinum-group mineral inclusions in chromitites of the Finero mafic-ultramafic complex (Ivrea-Zone, Italy). Mineralogy and Petrology 41(2-4), 125-143.

Ferry, J. M., Wing, B. A., Penniston-Dorland, S. C. & Rumble, D. (2002). The direction of fluid flow during contact metamorphism of siliceous carbonate rocks: new data for the Monzoni and Predazzo aureoles, northern Italy, and a global review. Contributions to Mineralogy and Petrology 142(6), 679-699.

Frizzo, P., Peruzzo, L. & Dellantonio, E. (2010). The copper-wolfram deposit of Bedovina (Trento, Italy): Geo.Alp, 7, 55-70.

Frost, D. J. (2006). The stability of hydrous mantle phases. Reviews in Mineralogy and Geochemistry 62(1), 243-271.

Fujimaki, H., Tatsumoto, M. & Aoki, K. I. (1984). Partition coefficients of Hf, Zr, and REE between phenocrysts and groundmasses. Journal of Geophysical Research: Solid Earth 89(S02), B662-B672.

Fumagalli, P., Zanchetta, S. & Poli, S. (2009). Alkali in phlogopite and amphibole and their effects on phase relations in metasomatized peridotites: a high-pressure study. Contributions to Mineralogy and Petrology 158(6), 723.

Galassi, B., Monese, A., Ogniben, G., Siena, F. & Vaccaro, C. (1994). Age and nature of lamprophyric dykes at Calceranica (Trento). Mineralogica et Petrographica Acta 37, 163-171.

Gallien, F., Abart, R. & Wyhlidal, S. (2007.) Contact metamorphism and selective metasomatism of the layered Bellerophon Formation in the eastern Monzoni contact aureole, northern Italy. Mineralogy and Petrology 91(1), 25-53.

Gasparotto, G. & Simboli, G. (1991). Mineralogia, petrografia e schemi evolutivi delle magmatiti triassiche del complesso di Cima Pape (Dolomiti Orientali). Mineralogica et Petrografica Acta 34, 205-234.

GERM, Partition Coefficient (Kd) Database, development and maintenance by the EarthRef.org Database Team, Data contribution by Roger Nielsen. Earthref.org/KDD.

Giacomoni, P. P., Coltorti, M., Bryce, J. G., Fahnestock, M. F. & Guitreau, M. (2016). Mt. Etna plumbing system revealed by combined textural, compositional, and thermobarometric studies in clinopyroxenes. Contributions to Mineralogy and Petrology 171(4), 34.

Giacomoni, P. P., Ferlito, C., Coltorti, M., Bonadiman, C. & Lanzafame, G. (2014). Plagioclase as archive of magma ascent dynamics on "open conduit" volcanoes: The 2001-2006 eruptive period at Mt. Etna. Earth-Science Reviews 138, 371-393.

Gianolla, P. (1992). Evoluzione mediotriassica del vulcanismo di Rio Freddo (Api Giulie, Italia). Memorie di Scienze Geologiche 44, 193-209.

Gianolla, P., Avanzini, M., Breda, A., Kustatscher, E., Preto, … & Stefani, M. (2010). Dolomites, 7th International Triassic Field Workshop, Field trip to the World Heritage Site of the Tethyan Triassic. September 5-10 2010, Dolomites, Southern Alps, Italy. With the adesion of Fondazione Dolomiti-Dolomiten-Dolomites-Dolomitis Unesco.

Gozzi, F., Gaeta, M., Freda, C., Mollo, S., Di Rocco, T., ... & Pack, A. (2014). Primary magmatic calcite reveals origin from crustal carbonate. Lithos 190, 191-203.

Grove, T. L., Baker, M. B. & Kinzler, R. J. (1984). Coupled CaAl-NaSi diffusion in plagioclase feldspar: Experiments and applications to cooling rate speedometry. Geochimica et Cosmochimica Acta 48, 2113-2121.

Gualda, G. A. R., Ghiorso, M. S., Lemons, R. V. & Carley, T. L. (2012). Rhyolite-MELTS: a Modified Calibration of MELTS Optimized for Silica-rich, Fluid-bearing Magmatic Systems: Journal of Petrology 53, 875-890.

Hammarstrom, J. M. & Zen, E. A. (1986). Aluminum in hornblende: an empirical igneous geobarometer. American Mineralogist 71(11-12), 1297-1313.

Hammouda, T. & Keshav, S. (2015). Melting in the mantle in the presence of carbon: Review of experiments and discussion on the origin of carbonatites. Chemical Geology 418, 171-188.

Hawthorne, F. C., Oberti, R., Harlow, G. E., Maresch, W. V., Martin, R. F., Schumacher, J. C. & Welch, M.D. (2012). Nomenclature of the amphibole supergroup. American Mineralogist 97(11-12), 2031-2048.

Hay, R. L. & O'Neil, J. R. (1983). Carbonatite tuffs in the Laetolil Beds of Tanzania and the Kaiserstuhl in Germany. Contributions to Mineralogy and Petrology 82(4), 403-406.

Henry, D. J., Guidotti, C. V. & Thomson, J. A. (2005). The Ti-saturation surface for low-to-medium pressure metapelitic biotites: Implications for geothermometry and Ti-substitution mechanisms. American Mineralogist 90(2-3), 316-328.

Hogarth, D. D. (1989). Pyrochlore, apatite and amphibole: distinctive minerals in carbonatite. In: Bell, K. (ed.) Carbonatites: Genesis and Evolution. Unwin Hyman, London, 103-148.

Holland, T. & Blundy, J. (1994). Non-ideal interactions in calcic amphiboles and their bearing on amphibole-plagioclase thermometry. Contributions to Mineralogy and Petrology 116(4), 433-447.

Huebner, J. S. & Sato, M. (1970). The oxygen fugacity-temperature relationships of manganese oxide and nickel oxide buffers. American Mineralogist 55, 934-952.

Ickert, R. B. (2013). Algorithms for estimating uncertainties in initial radiogenic isotope ratios and model ages. Chemical Geology 340, 131-138.

Ishibashi, H. (2013). Spinel-melt oxygen barometry: a method and application to Cenozoic alkali basaltic magmas from the Higashi-Matsuura district, NW Kyushu. Japan Geoscience Reports 40, 21-32.

Kinzler, R. J. & Grove, T. L. (1992). Primary magmas of mid-ocean ridge basalts 1. Experiments and methods. Journal of Geophysical Research: Solid Earth 97(B5), 6885-6906.

Kohn, S. C. (2000). The dissolution mechanisms of water in silicate melts; a synthesis of recent data. Mineralogical Magazine 64(3), 389-408.

Kress, V. C. & Carmichael, I. S. (1988). Stoichiometry of the iron oxidation reactions in silicate melts. American Mineralogist 73, 1267-1274.

Kress, V. C. & Carmichael, I. S. (1991). The compressibility of silicate liquids containing Fe_2O_3 and the effect of composition, temperature, oxygen fugacity and pressure on their redox states. Contributions to Mineralogy and Petrology 108(1-2), 82-92.

Lange, R. A., Frey, H. M. & Hector, J. (2009). A thermodynamic model for the plagioclase-liquid hygrometer/thermometer. American Mineralogist 94(4), 494-506.

Langone, A., Zanetti, A., Daczko, N. R., Piazolo, S., Tiepolo, M. & Mazzucchelli, M. (2018). Zircon U-Pb Dating of a Lower Crustal Shear Zone: A Case Study From the Northern Sector of the Ivrea-Verbano Zone (Val Cannobina, Italy). Tectonics 37(1), 322-342.

Laurenzi, M. A. & Visonà, D. (1996). $^{40}Ar/^{39}Ar$ Chronology of Predazzo magmatic complex (Southern Alps, Italy). 78° Riunione estiva Società Geologica Italiana: Geologia delle Dolomiti. San Cassiano (1996), 16-18.

Le Maitre, R. W., Bateman, P., Dudek, A., Keller, J., Lameyre, L., ... & Zanettin, B. (1989). A classification of igneous rocks and glossary of terms: recommendations of the IUGS Commission on the Systematics of Igneous Rocks.

Le Maitre, R. W., Streckeisen, A., Zanettin, B., Le Bas, M. J., Bonin, B., ... & Lameyre, J. (2002). Igneous rocks. A classification and glossary of terms. Recommendations of the IUGS Subcomission on the Systematics of Igneous Rocks. Cambridge University Press.

Le Roex, A. P. & Lanyon, R. (1998). Isotope and trace element geochemistry of Cretaceous Damaraland lamprophyres and carbonatites, northwestern Namibia: Evidence for plume-lithosphere interactions. Journal of Petrology 39(6), 1117-1146.

Leake, B. E., Woolley, A. R., Arps, C. E. S., Birch, W. D., Gilbert, M. C., ... & Linthout, K. (1997). Nomenclature of amphiboles: report of the subcommittee on amphiboles of the International Mineralogical Association Commission on New Minerals and Mineral Names. Mineralogical Magazine 61, 295-321.

Leat, P. T., Riley, T. R., Storey, B. C., Kelley, S. P. & Millar, I. L. (2000). Middle Jurassic ultramafic lamprophyre dyke within the Ferrar magmatic province, Pensacola Mountains, Antarctica. Mineralogical Magazine 64(1), 95-111.

Lee, J-Y., Marti, K., Severinghaus, J. P., Kawamura, K., Yoo, H. S., Lee, J. B., & Kim, J. S. (2006). A redetermination of the isotopic abundances of atmospheric Ar. Geochimica et Cosmochimica Acta 70, 4507-4512.

Lemoine, M., Tricart, P. & Boillot, G. (1987). Ultramafic and gabbroic ocean floor of the Ligurian Tethys (Alps, Corsica, Appennines). In search of a genetic model. Geology 15, 622-625.

Leonardi, P. (1968). Centro eruttivo di Predazzo. In Le Dolomiti, Geologia dei monti tra Isarco e Piave 52.

Lippolt, H. & Pidgeon, R. (1974). Isotopic mineral ages of a diorite from the Eisenkappel intrusion, Austria. Zeitschrift für Naturforschung 29a.

Liu, Y., Zhang, Y. & Behrens, H. (2005). Solubility of H_2O in rhyolitic melts at low pressures and a new empirical model for mixed H_2O-CO_2 solubility in rhyolitic melts. Journal of Volcanology and Geothermal Research 143(1-3), 219-235.

Locock, A. J. (2014). An Excel spreadsheet to classify chemical analyses of amphiboles following the IMA 2012 recommendations. Computers & Geosciences 62, 1-11.

Lu, Y. J., McCuaig, T. C., Li, Z. X., Jourdan, F., Hart, C. J., Hou, Z. Q. & Tang, S.H. (2015). Paleogene post-collisional lamprophyres in western Yunnan, western Yangtze Craton: mantle source and tectonic implications. Lithos 233, 139-161.

Lucchini, F. & Morten, L. (1977). An example of flow differentiation: clinopyroxenite of the Predazzo igneous complex (north Italy). Lithos, 10, 39-47.

Lucchini, F., Mezzetti, R. & Simboli, G. (1969). The lamprophyres of the area Predazzo-Monzoni: camptonites. Mineralogica et Petrografica Acta 15, 109-145.

Lucchini, F., Rossi, P. L. & Simboli, G. (1982). Il magmatismo triassico dell'area di Predazzo (Alpi Meridionali, Italia). In: Castellarin, A. & Vai, G. B. (eds.). Guida alla Geologia del Sudalpino centro-orientale. Guide Geologiche Regionali Società Geologica Italiana, 221-230.

Lugmair, G. W. & Marti, K. (1978). Lunar initial $^{143}Nd/^{144}Nd$: differential evolution of Lunar crust and mantle. Earth and Planetary Science Letters 39, 349-357.

Malitch, K. N., Belousova, E. A., Griffin, W. L., Badanina, I. Y., Knauf, V. V., O'Reilly, S. Y. & Pearson, N.J. (2017). Laurite and zircon from the Finero chromitites (Italy): New insights into evolution of the subcontinental mantle. Ore Geology Reviews 90, 210-225.

Mandler, B. E. & Grove, T. L. (2016). Controls on the stability and composition of amphibole in the Earth's mantle. Contributions to Mineralogy and Petrology 171(8-9), 68.

Manzotti, P., Ballèvre, M. & Dal Piaz, G. V. (2017). Continental gabbros in the Dent Blanche Tectonic System (Western Alps): from the pre-Alpine crustal structure of the Adriatic palaeo-margin to the geometry of an alleged subduction interface. Journal of the Geological Society 174(3), 541-556.

Mark, D. F., Rice, C. M., Lee, M. R., Fallick, A. E., Boyce, A., Trewin, N. H. & Lee, J. K. W. (2011a). $^{40}Ar/^{39}Ar$ dating of hydrothermal activity, biota and gold mineralization in the Rhynie hot-spring system, Aberdeenshire, Scotland. Geochimica et Cosmochimica Acta 75, 555-569.

Mark, D. F., Stuart, F. M. & De Podesta, M. (2011b). New high-precision measurements of the isotopic composition of atmospheric argon. Geochimica et Cosmochimica Acta 75(23), 7494-7501.

Marocchi, M., Morelli, C., Mair, V., Klötzli, U. & Bargossi, G. M. (2008). Evolution of large silicic magma systems: new U–Pb zircon data on the NWPermian Athesian Volcanic Group (Southern Alps, Italy). Journal of Geology 116, 480-498.

Marrocchino, E., Coltorti, M., Visonà, D. & Thirwall, M. F. (2002). Petrology of Predazzo magmatic complex (Trento, Italy). Geochimica et Cosmochimica Acta 66(15a), A486-A486.

Martin, E. E. & Macdougall, J. D. (1995). Sr and Nd isotopes at the prmian/triassic boundary: A record of climate change. Chemical Geology 125(1-2), 73-99.

Marzari Pencati, G. (1820). Notizia sopra un granito in massa terziario sovrapposto al calcare secondario nel fiume Avisio. Supplemento al "Nuovo Osservatorio Veneziano", 118-127.

Marzocchi, C. (1987). Petrologia e metallogenesi del complesso eruttivo di Predazzo (TN): con particolare riguardo al settore meridionale. Unpublished master thesis, University of Ferrara.

Masotta, M., Mollo, S., Freda, C., Gaeta, M. & Moore, G. (2013). Clinopyroxene–liquid thermometers and barometers specific to alkaline differentiated magmas. Contributions to Mineralogy and Petrology 166(6), 1545-1561.

Matsumoto, T., Morishita, T., Matsuda, J. I., Fujioka, T., Takebe, M., Yamamoto, K. & Arai, S. (2005). Noble gases in the Finero phlogopite-peridotites, western Italian Alps. Earth and Planetary Science Letters 238(1-2), 130-145.

Mazzucchelli, M., Rivalenti, G., Brunelli, D., Zanetti, A. & Boari, E. (2009). Formation of highly refractory dunite by focused percolation of pyroxenite-derived melt in the Balmuccia peridotite massif (Italy). Journal of Petrology 50(7), 1205-1233.

McKenzie, D. A. N. & O'nions, R. K. (1991). Partial melt distributions from inversion of rare earth element concentrations. Journal of Petrology 32(5), 1021-1091.

Menegazzo Vitturi, L., Visonà, D. & Zantedeschi, C. (1995). Amphibole composition in rocks from Predazzo volcano-plutonic complex (Southern Alps, Italy). Memorie di Scienze Geologiche 47, 87-94.

Meschede, M. (1986). A method of discriminating between different types of mid-ocean ridge basalts and continental tholeiites with the Nb-Zr-Y diagram. Chemical geology 56(3-4), 207-218.

Mietto, P., Manfrin, S., Preto, N., Rigo, M., Roghi, G., ... & Bowring, S.A. (2012). The Global Boundary Stratotype Section and Point (GSSP) of the Carnian Stage (Late Triassic) at Prati di Stuores/ Stuores Wiesen Section (Southern Alps, NE Italy). Episodes 35(3), 414-430.

Mollo, S., Masotta, M., Forni, F., Bachmann, O., De Astis, G., Moore, G. & Scarlato, P. (2015). A K-feldspar–liquid hygrometer specific to alkaline differentiated magmas. Chemical Geology 392, 1-8.

Mollo, S., Putirka, K., Iezzi, G., Del Gaudio, P. & Scarlato, P. (2011). Plagioclase–melt (dis) equilibrium due to cooling dynamics: implications for thermometry, barometry and hygrometry. Lithos 125(1), 221-235.

Monjoie, P., Bussy, F., Schaltegger, U., Mulch, A., Lapierre, H. & Pfeifer, H. R. (2007). Contrasting magma types and timing of intrusion in the Permian layered mafic complex of Mont Collon (Western Alps, Valais, Switzerland): evidence from U/Pb zircon and $^{40}Ar/^{39}Ar$ amphibole dating. Swiss Journal of Geosciences 100(1), 125-135.

Moore, J. M., Kuhn, B. K., Mark, D. F. & Tsikos, H. (2011). A sugilite-bearing assemblage from the Wolhaarkop breccia, Bruce iron-ore mine, South Africa: Evidence for alkali metasomatism and ^{40}Ar-^{39}Ar dating. European Journal of Mineralogy 23(4), 661-673.

Morgan, L. E., Mark, D. F., Imlach, J., Barfod, D. & Dymock, R. (2014). FCs-EK: a new sampling of the Fish Canyon Tuff $^{40}Ar/^{39}Ar$ neutron flux monitor. Geological Society of London Special Publications 378(1), 63-67.

Morimoto, N. (1988). Nomenclature of pyroxenes. Mineralogy and Petrology 39(1), 55-76.

Morishita, T., Arai, S. & Tamura, A. (2003). Petrology of an apatite-rich layer in the Finero phlogopite–peridotite, Italian Western Alps; implications for evolution of a metasomatising agent. Lithos 69(1-2), 37-49.

Morishita, T., Hattori, K. H., Terada, K., Matsumoto, T., Yamamoto, K., ... & Arai, S. (2008). Geochemistry of apatite-rich layers in the Finero phlogopite–peridotite massif (Italian Western Alps) and ion microprobe dating of apatite. Chemical Geology 251(1-4), 99-111.

Morogan, V., Upton, B. G. J., & Fitton, J. G. (2000). The petrology of the Ditrau alkaline complex, Eastern Carpathians. Mineralogy and Petrology 69(3-4), 227-265.

Morse, S. A. & Brady, J. B. (2017). Thermal History of the Upper Zone of the Kiglapait Intrusion. Journal of Petrology 58(7), 1319-1332.

Morten, L. (1980). Mineral chemistry of ultramafic inclusions from the Predazzo volcanic rocks. Dolomite Region, north Italy. Journal of Mineralogy and Geochemistry 138, 259-273.

Mukasa, S.B. & Shervais, J. W. (1999). Growth of subcontinental lithosphere: evidence from repeated dike injections in the Balmuccia lherzolite massif, Italian Alps. Lithos 48, 287-316.

Müller, T., Dohmen, R., Becker, H. W., Ter Heege, J. H. & Chakraborty, S. (2013). Fe-Mg interdiffusion rates in clinopyroxene: experimental data and implications for Fe-Mg exchange geothermometers. Contributions to Mineralogy and Petrology 166(6), 1563-1576.

Mundil, R., Brack, P. & Laurenzi, M. A. (1996). High resolution U/Pb single zircon age determinations: new constraints on the timing of Middle Triassic magmatism in the Southern Alps. 78° Riunione estiva della Società Geologica Italiana. Geologia delle Dolomiti. San Cassiano (1996), Conference Abstract.

Mundil, R., Brack, P., Meier, M., Rieber, H. & Oberli, F. (1996). High resolution U-Pb dating of middle Triassic volcaniclastics: time-scale calibration and verification of tuning parameters for carbonate sedimentation: Earth and Planetary Science Letters 141, 137-151.

Myers, J. T. & Eugster, H. P. (1983). The system Fe-Si-O: Oxygen buffer calibrations to 1500 K. Contributions to Mineralogy and Petrology 82(1), 75-90.

Namur, O. & Humphreys, M. C. S. (2018). Trace Element Constraints on the Differentiation and Crystal Mush Solidification in the Skaergaard Intrusion, Greenland. Journal of Petrology, 1-31.

Nardini, N. (2018). Studio petrografico e geochimico della sequenza vulcano-plutonica di Cima Pape. Unpublished bachelor thesis, University of Ferrara.

Németh, K. & Budai, T. (2009). Diatremes cut through the Triassic carbonate platforms in the Dolomites? Evidences from and around the Latemar, northern Italy. Episodes 32(2), 74.

Nielsen, T. F. D. (2004). The Shape and Volume of the Skaergaard Intrusion, Greenland: Implications for Mass Balance and Bulk Composition. Journal of Petrology 45(3), 507-530.

Nimis, P., Omenetto, P., Giunti, I., Artioli, G. & Angelini, I. (2012). Lead isotope systematics in hydrothermal sulphide deposits from the central-eastern Southalpine (northern Italy): European Journal of Mineralogy 24, 23-37.

Oberti, R., Cannillo, E. & Toscani, G. (2012). How to name amphiboles after the IMA2012 report: rules of thumb and a new PC program for monoclinic amphiboles. Periodico di Mineralogia 81(2), 257-267.

Paganelli, L. & Tiburtini, R. (1964). The Predazzo granite, North Italy. Mineralogica et Petrographica Acta 10, 57-79.

Pál-Molnár, E., Batki, A., Almási, E., Kiss, B., Upton, B. G., ... & Harangi, S. (2015). Origin of mafic and ultramafic cumulates from the Ditrău Alkaline Massif, Romania. Lithos 239, 1-18.

Pamic, J. J. (1984). Triassic magmatism of the Dinarides in Yugoslavia. Tectonophysics 109(3-4), 273-307.

Pană, D., Balintoni, I. & Heaman, L. (2000). Precise U-Pb zircon dating of the syenite phase from the Ditrau alkaline igneous complex. Studia UBB Geologia 45(1), 79-90.

Pandey, A., Rao, N. C., Chakrabarti, R., Pandit, D., Pankaj, P., Kumar, A. & Sahoo, S. (2017a). Petrogenesis of a Mesoproterozoic shoshonitic lamprophyre dyke from the Wajrakarur kimberlite field, eastern Dharwar craton, southern India: geochemical and Sr-Nd isotopic evidence for a modified sub-continental lithospheric mantle source. Lithos 292, 218-233.

Pandey, A., Rao, N. C., Pandit, D., Pankaj, P., Pandey, R., Sahoo, S. & Kumar, A. (2017b). Subduction–tectonics in the evolution of the eastern Dharwar craton, southern India: Insights from the post-collisional calc-alkaline lamprophyres at the western margin of the Cuddapah basin. Precambrian Research 298, 235-251.

Pearce, J. A. (1982). Trace elements characteristics of lavas from destructive plate boundaries. In Thorpe, E. S. (ed.) Andesites. New York, John Wiley and Sons, 525-548.

Pearce, J. A. & Norry, M. J. (1979). Petrogenetic implications of Ti, Zr, Y, and Nb variations in volcanic rocks. Contributions to Mineralogy and Petrology 69(1), 33-47.

Pe-Piper, G. (1982). Geochemistry, tectonic setting and metamorphism of mid-Triassic volcanic rocks of Greece. Tectonophysics 85(3-4), 253-272.

Pe-Piper, G. (1983). Triassic shoshonites and andesites, Lakmon Mountains, western continental Greece: Differences in primary geochemistry and sheet silicate alteration products. Lithos 16(1), 23-33.

Pe-Piper, G. (1998). The nature of Triassic extension-related magmatism in Greece: evidence from Nd and Pb isotope geochemistry. Geological Magazine 135(3), 331-348.

Petersen, J. S., Morten, L., Simboli, G. & Lucchini, F. (1980). REE abundances in the Predazzo-Monzoni intrusive complex, Dolomites, North Italy. Rivista Italiana di Paleontologia e Stratigrafia 85, 1065-1080.

Petrone, C. M., Braschi, E., Francalanci, L., Casalini, M. & Tommasini, S. (2018). Rapid mixing and short storage timescale in the magma dynamics of a steady-state volcano. Earth and Planetary Science Letters 492, 206-221.

Piccardo, G. B., Rampone, E., Vannucci, R. & Cimmino, F. (1994). Upper mantle evolution of ophiolitic peridotites from the Northern Apennine: Petrological constraints to the geodynamic processes. Memorie della Società Geologica Italiana 8, 137-148.

Pilet, S., Ulmer, P. & Villiger, S. (2010). Liquid line of descent of a basanitic liquid at 1.5 GPa: constraints on the formation of metasomatic veins. Contributions to Mineralogy and Petrology 159(5), 621-643.

Pin, C. & Sills, J. D. (1986). Petrogenesis of layered gabbros and ultramafic rocks from Val Sesia, the Ivrea Zone, NW Italy: trace element and isotope geochemistry. Geological Society, London, Special Publications 24, 231-249.

Pinzuti, P., Humler, E., Manighetti, I. & Gaudemer, Y. (2013). Petrological constraints on melt generation beneath the Asal Rift (Djibouti) using quaternary basalts. Geochemistry, Geophysics, Geosystems 14(8), 2932-2953.

Pisa, G., Castellarin, A., Lucchini, F., Rossi, P.L., Simboli, G., Bosellini, A. & Sommavilla, E. (1979). Middle Triassic magmatism in Southern Alps. I: a review of general data in the Dolomites. Rivista Italiana di Paleontologia e Stratigrafia, 85(3-4), 1093-1110.

Pouchou, J. L. & Pichoir, F. (1991). Quantitative analysis of homogeneous or stratified microvolumes applying the model "PAP". In: Electron probe quantitation. Springer US, 31-75.

Povoden, E., Horacek, M. & Abart, R. (2002). Contact metamorphism of siliceous dolomite and impure limestones from the Werfen formation in the eastern Monzoni contact aureole. Mineralogy and Petrology 76(1), 99-120.

Princivalle, F., Della Giusta, A., De Min, A. & Piccirillo, E. M. (1999). Crystal chemistry and significance of cation ordering in Mg-Al rich spinels from high-grade hornfels (Predazzo-Monzoni, NE Italy). Mineralogical Magazine 63(2), 257-257.

Putirka, K. D. (2008). Thermometers and barometers for volcanic systems. Reviews in Mineralogy and Geochemistry 69(1), 61-120.

Putirka, K. D. (2016). Amphibole thermometers and barometers for igneous systems and some implications for eruption mechanisms of felsic magmas at arc volcanoes. American Mineralogist 101(4), 841-858.

Putirka, K. D., Johnson, M., Kinzler, R., Longhi, J. & Walker, D. (1996). Thermobarometry of mafic igneous rocks based on clinopyroxene-liquid equilibria, 0-30 kbar. Contributions to Mineralogy and Petrology 123(1), 92-108.

Putirka, K., Mikaelian, H., Ryerson, F. & Shaw, H. (2003). New clinopyroxene-liquid thermobarometers for mafic, evolved, and volatile-bearing lava compositions, with applications to lavas from Tibet and the Snake River Plain, Idaho. American Mineralogist 88, 1542-1554.

Quick, J. E., Sinigoi, S., Peressini, G., Demarchi, G., Wooden, J. L. & Sbisà, A. (2009). Magmatic plumbing of a large Permian caldera exposed to a depth of 25 km. Geology 37, 603-606.

Quick, J. E., Sinigoi, S., Snoke, A.W., Kalakay, T. J., Mayer, A. & Peressini, G. (2003). Geologic map of the Southern Ivrea-Verbano Zone, Northwestern Italy: U.S. Geological Survey.

Raffone, N., Le Fèvre, B., Ottolini, L., Vannucci, R. & Zanetti, A. (2006). Light-lithophile element metasomatism of Finero peridotite (W Alps): a secondary-ion mass spectrometry study. Microchimica Acta 155(1-2), 251-255.

Rampone, E. & Piccardo, G.B. (2000). The ophiolite-oceanic lithosphere analogue: new insights from the Northern Apennines (Italy), In Dilek, J., Moores, E., Elthon, D. & Nicolas, A. (eds.) Ophiolites and Oceanic

Crust: New Insights from Field Studies and Ocean Drilling Program. Geological Society of America Memoir, Special Paper 349, 21-34.

Renne, P. R., Balco, G., Ludwig, K. R., Mundil, R. & Min, K. (2011). Response to comment by W.H. Schwarz et al. on 'Joint determination of ^{40}K decay constants and ^{40}Ar*/^{40}K for the Fish Canyon sanidine standard, and improved accuracy for ^{40}Ar/^{39}Ar geochronology' by P.R. Renne et al., 2010. Geochimica et Cosmochimica Acta 75, 5097-5100.

Renne, P. R., Deino, A. L., Hames, W. E., Heizler, M. T., Hemming, S. R., … & Wijbrans, J.R. (2009). Data Reporting Norms for ^{40}Ar/^{39}Ar Geochronology. Quaternary Geochronology 4, 346-352.

Renne, P. R., Mundil, R., Balco, G., Min, K. & Ludwig, K. R. (2010). Joint determination of ^{40}K decay constants and ^{40}Ar*/^{40}K for the Fish Canyon sanidine standard, and improved accuracy for ^{40}Ar/^{39}Ar geochronology. Geochimica et Cosmochimica Acta 74, 5349-5367.

Ridolfi, F. & Renzulli, A. (2012). Calcic amphiboles in calc-alkaline and alkaline magmas: thermobarometric and chemometric empirical equations valid up to 1,130° C and 2.2 GPa. Contributions to Mineralogy and Petrology 163(5), 877-895.

Ridolfi, F., Renzulli, A. & Puerini, M. (2010). Stability and chemical equilibrium of amphibole in calc-alkaline magmas: an overview, new thermobarometric formulations and application to subduction-related volcanoes. Contributions to Mineralogy and Petrology 160(1), 45-66.

Ridolfi, F., Zanetti, A., Renzulli, A., Perugini, D., Holtz, F. & Oberti, R. (2018). AMFORM, a new mass-based model for the calculation of the unit formula of amphiboles from electron microprobe analyses. American Mineralogist 103, 1112-1125.

Robinson, J. A. C. & Wood, B. J. (1998). The depth of the spinel to garnet transition at the peridotite solidus. Earth and Planetary Science Letters 164(1-2), 277-284.

Rocchi, S. & Breitkreuz, C. (2018). Physical Geology of Shallow Magmatic Systems-An Introduction. In Breitkreuz, C. & Rocchi, S. (eds.) Physical Geology of Shallow Magmatic Systems. Springer, 1-10.

Rock, N. M. S. (1987). The nature and origin of lamprophyres: an overview. Geological Society of London, Special Publications 30(1), 191-226.

Rock, N. M. S. (1991). Lamprophyres. Springer.

Rossi, P.L., Viel, G. & Simboli, G. (1976). Significato paleogeografico e magmatico-tettonico della serie vulcano-clastica ladinica superiore nell'area del Monte Civetta: Italian Journal of Geosciences 95, 433-458.

Rotenberg, E., Davis, D. W., Amelin, Y., Ghosh, S. & Bergquist, B. A. (2012). Determination of the decay-constant of ^{87}Rb by laboratory accumulation of ^{87}Sr. Geochimica et Cosmochimica Acta 85, 41-57.

Rottura, A., Bargossi, G. M., Caggianelli, A., Del Moro, A., Visonà, D. & Tranne, C. A. (1998). Origin and significance of the Permian high-K calc-alkaline magmatism in the central-eastern Southern Alps, Italy. Lithos 45, 329-348.

Rottura, A., Del Moro, A., Caggianelli, A., Bargossi, G. M. & Gasparotto, G. (1997). Petrogenesis of the Monte Croce granitoids in the context of Permian magmatism in the Southern Alps, Italy. European Journal of Mineralogy 9(6), 1293-1310.

Ruiz-Agudo, E., Putnis, C. V. & Putnis, A. (2014). Coupled dissolution and precipitation at mineral–fluid interfaces. Chemical Geology 383, 132-146.

Saccani, E. (2015). A new method of discriminating different types of post-Archean ophiolitic basalts and their tectonic significance using Th-Nb and Ce-Dy-Yb systematics. Geoscience Frontiers 6(4), 481-501.

Salomon, W. (1895). Geologische und palaontologische Studien fiber die Marmolata. Palaeontographica 42(1), 210.

Sarti, M. & Ardizzoni, F. (1984). Tettonica Triassica nel gruppo di Cima Pape-Pale di Sanson (Dolomiti Bellunesi). Memorie di Scienze Geologiche 36, 353-370.

Scandone, P. (1975). Triassic seaways and the Jurassic Thethis Ocean in the central Mediterranean area. Nature 256, 5513.

Scarrow, J. H., Molina, J. F., Bea, F., Montero, P. & Vaughan, A. P. (2011). Lamprophyre dikes as tectonic markers of late orogenic transtension timing and kinematics: A case study from the Central Iberian Zone. Tectonics, 30(4).

Schaltegger, U. & Brack, P. (2007). Crustal-scale magmatic systems during intracontinental strike-slip tectonics: U, Pb and Hf isotopic constraints from Permian magmatic rocks of the Southern Alps. International Journal of Earth Sciences 96(6), 1131-1151.

Schmid, M. S., Bernoulli, D., Fügenschuh, B., Georgiev, N., Kounov, A., ... & Van Hinsbergen, D. (2016). Tectonic units of the Alpine collision zone between Eastern Alps and Western Turkey: Unpublished map.

Schmid, S. M., Bernoulli, D., Fügenschuh, B., Matenco, L., Schefer, S., ... & Ustaszewski, K. (2008). The Alpine-Carpathian-Dinaridic orogenic system: correlation and evolution of tectonic units. Swiss Journal of Geosciences 101(1), 139-183.

Schmidt, K. H., Bottazzi, P., Vannucci, R. & Mengel, K. (1999). Trace element partitioning between phlogopite, clinopyroxene and leucite lamproite melt. Earth and Planetary Science Letters 168(3), 287-299.

Seghedi, I., Downes, H., Vaselli, O., Szakács, A., Balogh, K. & Pécskay, Z. (2004). Post-collisional Tertiary-Quaternary mafic alkalicmagmatism in the Carpathian–Pannonian region: a review. Tectonophysics 393, 43–62.

Shaw, D. M. (1970). Trace element fractionation during anatexis. Geochimica et Cosmochimica Acta 34(2), 237-243.

Silver, L. & Stolper, E. (1985). A thermodynamic model for hydrous silicate melts. The Journal of Geology 93(2), 161-177.

Sinigoi, S., Quick, J. E., Demarchi, G. & Klotzli, U. (2011). The role of crustal fertility in the generation of large silicic magmatic systems triggered by intrusion of mantle magma in the deep crust: Contributions to Mineralogy and Petrology 162, 691-707.

Sinigoi, S., Quick, J. E., Demarchi, G. & Klotzli, U. (2016). Production of hybrid granitic magma at the advancing front of basaltic underplating: Inferences from the Sesia Magmatic System (south - western Alps, Italy). Lithos 252-253, 109-122.

Sloman, L. E. (1989). Triassic shoshonites from the dolomites, northern Italy: Alkaline arc rocks in a strike-slip setting. Journal of Geophysical Research: Solid Earth 94(B4), 4655-4666.

Smith, E. I., Sanchez, A., Walker, J. D. & Wang, K. (1999). Geochemistry of mafic magmas in the Hurricane Volcanic field, Utah: implications for small-and large-scale chemical variability of the lithospheric mantle. The Journal of Geology 107(4), 433-448.

Soder, C. & Romer, R. L. (2018). Post-collisional potassic–ultrapotassic magmatism of the Variscan Orogen: implications for mantle metasomatism during continental subduction. Journal of Petrology 59(6), 1007-1034.

Sommavilla, E. (1970). Monzonite con differenziazioni basiche e alkaline, e passaggio graduale a lava latitica, a nord delle Pale di S. Martino (Dolomiti, Italia). Studi Trentini di Scienze Naturali, 47(1), 135-160.

Spera, F. J. (1980). Thermal evolution of plutons: a parameterized approach. Science 207, 299-301.

Spera, F. J. (2000). Physical properties of magmas. In Sigurdsson H (ed.) Encyclopedia of Volcanoes. New York: Academic Press, 171-190.

Spera, F. J. & Bohrson, W. A. (2001). Energy-constrained open-system magmatic processes I: General model and energy-constrained assimilation and fractional crystallization (EC-AFC) formulation. Journal of Petrology 42(5), 999-1018.

Stahle, V., Frenzel, G., Hess, J. C., Saupé, F., Schmidt, S. T. & Schneider, W. (2001). Permian metabasalt and Triassic alkaline dykes in the northern Ivrea zone: clues to the post-Variscan geodynamic evolution of the Southern Alps. Schweizerische Mineralogische und Petrographische Mitteilungen 81(1), 1-21.

Stähle, V., Frenzel, G., Kober, B., Michard, A., Puchelt, H. & Schneider, W. (1990). Zircon syenite pegmatites in the Finero peridotite (Ivrea zone): evidence for a syenite from a mantle source. Earth and Planetary Science Letters 101(2-4), 196-205.

Stampfli, G.M. (2005). Plate Tectonics of the Apulia-Adria Microcontinents. In: Finetti, I. R. (ed.) Crop Project: Deep Seismic Exploration of the Central Mediterranean and Italy. Elsevier 28, 747-766.

Stampfli, G. M. & Borel, G. D. (2002). A plate tectonic model for the Paleozoic and Mesozoic constrained by dynamic plate boundaries and restored synthetic oceanic isochrones. Earth and Planetary Science Letters 196(1), 17-33.

Stampfli, G. M. & Borel, G. D. (2004). The TRANSMED transects in space and time: constraints on the paleotectonic evolution of the Mediterranean domain. In: The TRANSMED Atlas: The Mediterranean region from crust to mantle, 53-80.

Stampfli, G. M., Borel, G. D., Marchant, R. & Mosar, J. (2002). Western Alps geological constraints on western Tethyan reconstructions. Journal of the Virtual Explorer 8, 77.

Stolper, E. (1982). The speciation of water in silicate melts. Geochimica et Cosmochimica Acta 46(12), 2609-2620.

Stoppa, F. (2008). Alkaline and ultramafic lamprophyres in Italy: Distribution, mineral phases, and bulk rock data. Deep-Seated Magmatism, Its Sources and Plumes. Publishing House of the Institute of Geography, SB RAS, 209-238.

Stoppa, F., Rukhlov, A.S., Bell, K., Schiazza, M. & Vichi, G. (2014). Lamprophyres of Italy: early cretaceous alkaline lamprophyres of southern Tuscany, Italy. Lithos 188, 97-112.

Storck, J-C., Brack, P., Wotzlaw, J-F & Ulmer, P. (2018). Timing and evolution of Middle Triassic magmatism in the Southern Alps (Northern Italy). Journal of the Geological Society 123.

Sun, S. & McDonough, W. F. (1989). Chemical and isotopic systematics of oceanic basalts: implication for mantle and processes. In: Saunders A. D. & Norry M. J. (eds.) Magmatism in the Ocean Basins. Geological Society, Special Publications, 42, 313-345.

Takahashi, E. & Kushiro, I. (1983). Melting of a dry peridotite at high pressures and basalt magma genesis. American Mineralogist 68(9-10), 859-879.

Tiepolo, M., Bottazzi, P., Palenzona, M. & Vannucci, R. (2003). A laser probe coupled with ICP–double-focusing sector-field mass spectrometer for in situ analysis of geological samples and U-Pb dating of zircon. The Canadian Mineralogist 41(2), 259-272.

Tindle, A. G. & Webb, P. C. (1994). PROBE-AMPH - a spreadsheet program to classify microprobe-derived amphibole analyses. Computer and Geosciences 20, 1201-1228.

Traill, R. J. & Lachance, G. R. (1966). A practical solution to the matrix problem in X-ray analysis. II. Application to a multicomponent alloy system. Canadian Spectroscopy 11(3), 63-71.

Tumiati, S., Fumagalli, P., Tiraboschi, C. & Poli, S. (2013). An experimental study on COH-bearing peridotite up to 3.2 GPa and implications for crust–mantle recycling. Journal of Petrology 54(3), 453-479.

Ubide, T., Galé, C., Arranz, E., Lago, M. & Larrea, P. (2014). Clinopyroxene and amphibole crystal populations in a lamprophyre sill from the Catalonian Coastal Ranges (NE Spain): a record of magma history and a window to mineral-melt partitioning. Lithos 184, 225-242.

Vardabasso, S. (1929). Rapporti tra attività magmatica e vicende tettoniche nella provincia petrografica di Predazzo. Studi Trentini di Scienze Naturali 11.

Vardabasso, S. (1930). Carta geologica del territorio eruttivo di Predazzo e Monzoni: Ufficio Idrografico del Magistrato alle Acque di Venezia, PD, scale 1:25000, 2 sheet.

Velde, D. (1968). Les transformations de l'olivine dans les lamprophyres et lamproites; une etude de la pilite. Bulletin de la Société Géologique de France 7(5), 601-612.

Vichi, G., Stoppa, F. & Wall, F. (2005). The carbonate fraction in carbonatitic Italian lamprophyres. Lithos 85(1-4), 154-170.

Visonà, D. (1997). The Predazzo multipulse intrusive body (Western Dolomites, Italy). Field and mineralogical studies. Memorie di Scienze Geologiche 49, 117-125.

Visonà, D. & Zanferrari, A. (2000). Some constraints on geochemical features in the Triassic mantle of the easternmost Austroalpine-Southalpine domain: evidence from the Karawanken pluton (Carinthia, Austria). International Journal of Earth Sciences 89(1), 40-51.

Voshage, H., Hofmann, A. W., Mazzucchelli, M., Rivalenti, G., Sinigoi, S., Raczek, I. & Demarchi, G. (1990). Isotopic evidence from the Ivrea Zone for a hybrid lower crust formed by magmatic underplating. Nature 347(6295), 731-736.

Voshage, H., Hunziker, J. C., Hofmann, A. W. & Zingg, A. (1987). A Nd and Sr isotopic study of the Ivrea zone, Southern Alps, N-Italy. Contributions to Mineralogy and Petrology 97, 31-42.

Waldbaum, D. R. & Thompson, J. B. (1969). Mixing properties of sanidine crystalline solutions: IV. Phase diagrams from equations of state. American Mineralogist 54, 1274-1298.

Wallace, M. E. & Green, D. H. (1988). An experimental determination of primary carbonatite magma composition. Nature 335, 343-346.

Whitney, D. L. & Evans, B.W. (2010). Abbreviations for names of rock-forming minerals. American Mineralogist 95, 185-187.

Willcock, M. A. W., Bargossi, G. M., Weinberg, R. F., Gasparotto, G., Cas, R. A. F., Giordano, G. & Marocchi, M. (2015). A complex magma reservoir system for a large volume intra-to extra-caldera ignimbrite: Mineralogical and chemical architecture of the VEI8, Permian Ora ignimbrite (Italy). Journal of Volcanology and Geothermal Research 306, 17-40.

Wood, D.A. (1980). The application of a Th-Hf-Ta diagram to problems of tectonomagmatic classification and to establishing the nature of crustal contamination of basaltic lavas of the British Tertiary Volcanic Province. Earth and Planetary Science Letters 50(1), 11-30.

Woolley, A. R., Bergman, S. C., Edgar, A. D., Le Bas, M. J., Mitchell, R. H., Rock, N. M. S. & Scott Smith, B. H. (1996). Classification of lamprophyres, lamproites, kimberlites, and the kalsilitic, melilitic, and leucitic rocks. The Canadian Mineralogist 34(2), 175-186.

Workman, R. K. & Hart, S. R. (2005). Major and trace element composition of the depleted MORB mantle (DMM). Earth and Planetary Science Letters 231(1), 53-72.

Wotzlaw, J. F., Brack, P. & Storck, J. C. (2018). High-resolution stratigraphy and zircon U–Pb geochronology of the Middle Triassic Buchenstein Formation (Dolomites, northern Italy): precession-forcing of hemipelagic carbonate sedimentation and calibration of the Anisian-Ladinian boundary interval. Journal of the Geological Society 175(1), 71-85.

Zaccarini, F., Stumpfl, E. F. & Garuti, G. (2004). Zirconolite and Zr–Th–U minerals in chromitites of the Finero complex, Western Alps, Italy: evidence for carbonatite-type metasomatism in a subcontinental mantle plume. The Canadian Mineralogist 42(6), 1825-1845.

Zack, T. & Brumm, R. (1998). Ilmenite/liquid partition coefficients of 26 trace elements determined through ilmenite/clinopyroxene partitioning in garnet pyroxene. In: Gurney, J. J., Gurney, J. L., Pascoe, M. D. & Richardson, S. H. (eds.) 7th International Kimberlite Conference. Red Roof Design, Cape Town, 986-988.

Zaitsev, A. N., Sitnikova, M. A., Subbotin, V. V., Fernández-Suárez, J., Jeffries, T. E. & Wall, F. (2004). Sallanlatvi complex: a rare example of magnesite and siderite carbonatites. Phoscorites and carbonatites from mantle to mine: the key example of the Kola Alkaline Province. Mineralogical Society of London, 201-245.

Zanetti, A., Giovanardi, T., Langone, A., Tiepolo, M., Wu, F. Y., Dallai, L. & Mazzucchelli, M. (2016). Origin and age of zircon-bearing chromitite layers from the Finero phlogopite peridotite (Ivrea-Verbano Zone, Western Alps) and geodynamic consequences. Lithos 262, 58-74.

Zanetti, A., Mazzucchelli, M., Rivalenti, G. & Vannucci, R. (1999). The Finero phlogopite-peridotite massif: an example of subduction-related metasomatism. Contributions to Mineralogy and Petrology 134(2-3), 107-122.

Zanetti, A., Mazzucchelli, M., Sinigoi, S., Giovanardi, T., Peressini, G. & Fanning, M. (2013). SHRIMP U–Pb Zircon Triassic intrusion age of the Finero mafic complex (Ivrea–Verbano zone, Western Alps) and its geodynamic implications. Journal of Petrology 54(11), 2235-2265.

Ziegler, P. A. & Stampfli, G. M. (2001). Late Palaeozoic-Early Mesozoic plate boundary reorganization: collapse of the Variscan orogen and opening of Neotethys. Natura Bresciana 25, 17-34.

Zindler, A. & Hart, S. R. (1986). Chemical geodynamics. Annual Review of Earth and Planetary Sciences 14, 493-571.